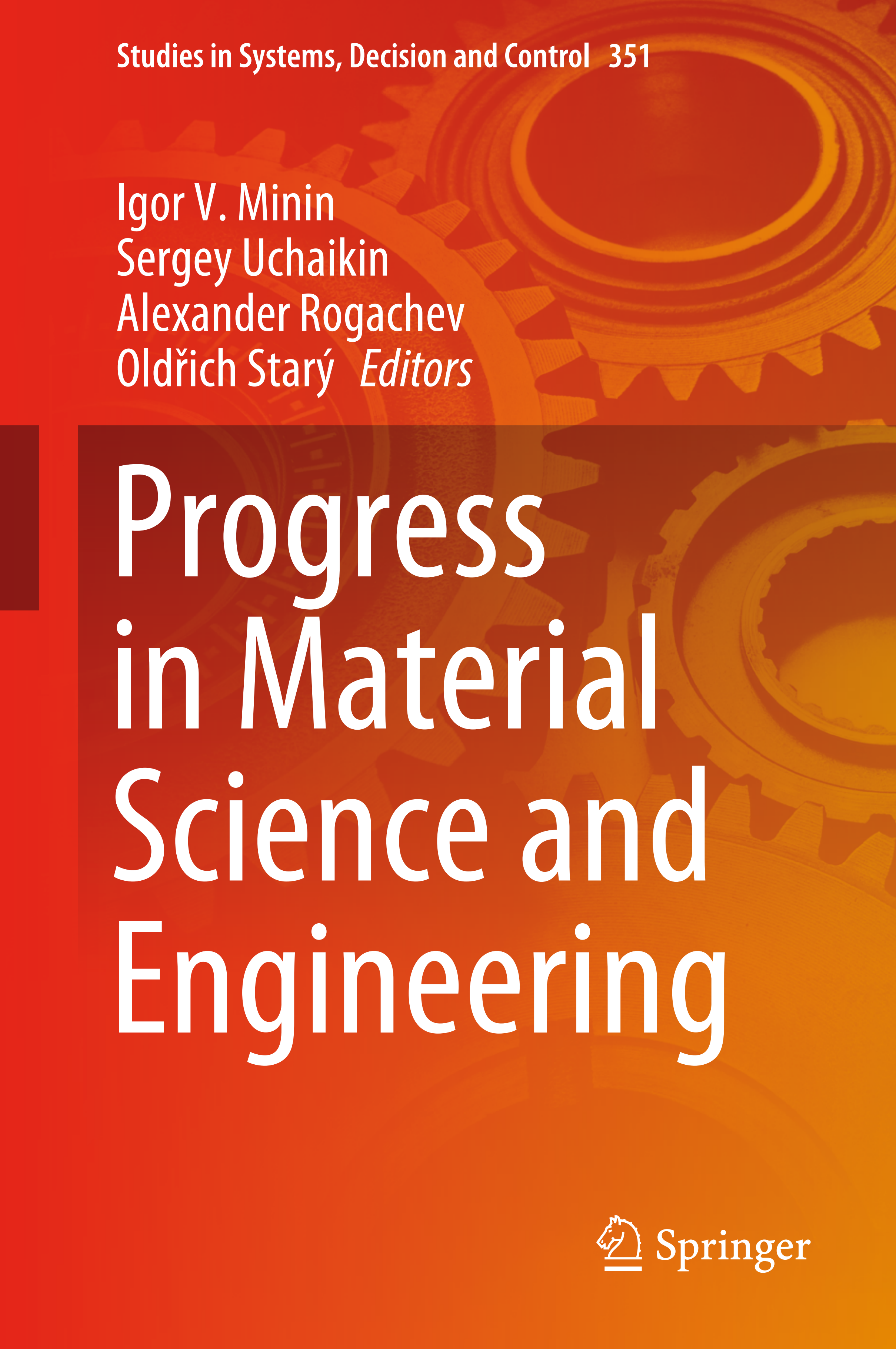

Studies in Systems, Decision and Control 351

Igor V. Minin
Sergey Uchaikin
Alexander Rogachev
Oldřich Starý *Editors*

Progress in Material Science and Engineering

Springer

Studies in Systems, Decision and Control

Volume 351

Series Editor

Janusz Kacprzyk, Systems Research Institute, Polish Academy of Sciences, Warsaw, Poland

The series "Studies in Systems, Decision and Control" (SSDC) covers both new developments and advances, as well as the state of the art, in the various areas of broadly perceived systems, decision making and control–quickly, up to date and with a high quality. The intent is to cover the theory, applications, and perspectives on the state of the art and future developments relevant to systems, decision making, control, complex processes and related areas, as embedded in the fields of engineering, computer science, physics, economics, social and life sciences, as well as the paradigms and methodologies behind them. The series contains monographs, textbooks, lecture notes and edited volumes in systems, decision making and control spanning the areas of Cyber-Physical Systems, Autonomous Systems, Sensor Networks, Control Systems, Energy Systems, Automotive Systems, Biological Systems, Vehicular Networking and Connected Vehicles, Aerospace Systems, Automation, Manufacturing, Smart Grids, Nonlinear Systems, Power Systems, Robotics, Social Systems, Economic Systems and other. Of particular value to both the contributors and the readership are the short publication timeframe and the world-wide distribution and exposure which enable both a wide and rapid dissemination of research output.

Indexed by SCOPUS, DBLP, WTI Frankfurt eG, zbMATH, SCImago.

All books published in the series are submitted for consideration in Web of Science.

More information about this series at http://www.springer.com/series/13304

Igor V. Minin · Sergey Uchaikin ·
Alexander Rogachev · Oldřich Starý
Editors

Progress in Material Science and Engineering

Springer

Editors
Igor V. Minin
Tomsk Polytechnic University
Tomsk, Russia

Alexander Rogachev
Research Institute of Physics and Chemistry
Francisk Skorina Gomel State University
Gomel, Belarus

Sergey Uchaikin
IBS Center for Axion and Precision Physics Research
Institute for Basic Science
Daejeon, Korea (Republic of)

Oldřich Starý
Czech Technical University in Prague
Dejvice, Czech Republic

ISSN 2198-4182 ISSN 2198-4190 (electronic)
Studies in Systems, Decision and Control
ISBN 978-3-030-68102-9 ISBN 978-3-030-68103-6 (eBook)
https://doi.org/10.1007/978-3-030-68103-6

© The Editor(s) (if applicable) and The Author(s), under exclusive license to Springer Nature Switzerland AG 2021
This work is subject to copyright. All rights are solely and exclusively licensed by the Publisher, whether the whole or part of the material is concerned, specifically the rights of translation, reprinting, reuse of illustrations, recitation, broadcasting, reproduction on microfilms or in any other physical way, and transmission or information storage and retrieval, electronic adaptation, computer software, or by similar or dissimilar methodology now known or hereafter developed.
The use of general descriptive names, registered names, trademarks, service marks, etc. in this publication does not imply, even in the absence of a specific statement, that such names are exempt from the relevant protective laws and regulations and therefore free for general use.
The publisher, the authors and the editors are safe to assume that the advice and information in this book are believed to be true and accurate at the date of publication. Neither the publisher nor the authors or the editors give a warranty, expressed or implied, with respect to the material contained herein or for any errors or omissions that may have been made. The publisher remains neutral with regard to jurisdictional claims in published maps and institutional affiliations.

This Springer imprint is published by the registered company Springer Nature Switzerland AG
The registered company address is: Gewerbestrasse 11, 6330 Cham, Switzerland

Foreword

Non-destructive testing technology methods are usually used for detection, location and sizing of both surface and internal defects of different nature. The School of Non-Destructive Testing of the Tomsk Polytechnic University, Russia, is promoting scientific research and industrial applications of non-destructive testing technology, which includes microwave, acoustical (ultrasonic), infrared, magnetic, vibration, radiography, visual and other testing and related methods, for safety of operation of medical and industrial processes.

Today, there is a need for educational materials that will help in the formation and continuous training of their specialists in non-destructive testing. This tutorial can be used as a complementary technical document to enhance the skills of NDT professionals and as a basic resource to educate managers and decision makers in the industry about the future of NDT.

The current timely book presents recent advantages and perspective directions in scientific investigations and industrial applications of non-destructive testing in different areas including medicine, quality assurance, sensors and engineering systems: ultrasionic tomography, infrared inspection and spectral analysis, surface material control, diagnostics of metal nanopowders, biomedical engineering.

NDT takes centre stage in our technological world, books that highlight what is possible are both welcome and instructive. I am delighted to see this comprehensive book take shape and promote the field to the next generation of researchers looking for new avenues to explore.

March 2021

Prof. Oleg V. Minin, Ph.D., D.Sc. (Hab)
Academician
Tomsk Polytechnic University
Tomsk, Russia

Contents

Innovation in Non-destructive Testing

Innovations in Technical Diagnostics and Materials Science

Innovations in Biomedical Engineering

Innovation in Non-destructive Testing

Informative Potential of Eddy Current Tomography

Aleksandr Goldshtein and Evgeny Yakimov

Abstract Applicability of methods used in tomography for reconstruction of electrically conductive objects of complex structure to increase the information content of eddy current testing is evaluated based on physical modeling of the interaction of the eddy current transducer magnetic field with electrically conductive objects. Methods considered imply scanning the surface of an object using an eddy current transducer with a local test area and obtaining measurement information at different angles of mutual spatial orientation of the excitation magnetic field strength vector and the test object.

1 Introduction

Tomography is one of the most informative methods in non-destructive testing and diagnostics, which provides data on each elementary volume of the object under study.

Tomography (Greek *tomos* slice, section + *graphō* write, describe) is layer-by-layer imaging of the internal structure of an object.

The application scope includes medical tomography (as a type of medical imaging and medical diagnostics), industrial tomography (as a type of defectoscopy), and tomography of macro-objects (e.g., a significant part of the atmosphere).

With regard to the type of the physical field used, tomography can be divided into radiation, optical, ultrasonic, radio wave, and magnetic resonance imaging. Radiation imaging [1] uses high-energy electromagnetic waves with frequency exceeding 3 × 10^{16} Hz, optical imaging [2] uses electromagnetic waves of the visual range,

---

A. Goldshtein · E. Yakimov (✉)
Division for Testing and Diagnostics, National Research Tomsk Polytechnic University,
30, Lenin Avenue, Tomsk, Russia 634050
e-mail: shishkovka@mail.ru

A. Goldshtein
e-mail: algol54@yandex.ru

I. V. Minin et al. (eds.), *Progress in Material Science and Engineering*,
Studies in Systems, Decision and Control 351,
https://doi.org/10.1007/978-3-030-68103-6_1

ultrasonic imaging [3] uses ultrasonic waves, radio wave imaging [4, 5] uses ultra-high frequency electromagnetic waves, and magnetic resonance imaging [6] uses high-frequency electromagnetic waves in combination with strong constant magnetic fields.

In [5], it is shown that eddy current testing based on excitation of eddy currents in the electrically conductive parts of the test object by low-frequency magnetic fields in the range of (10^1 to 10^7) Hz can be effectively used to solve a number of tomography problems in engineering.

These methods can be used to obtain detailed data on the structure of composite metal objects. Eddy current testing is superior to other physical methods used in tomography due to high test performance, safety and ability to obtain data with one-way access to the test object (compared to radiation methods), higher penetrating power and ability to obtain data on electromagnetic properties of the object (compared to optical and radio wave methods), ability to obtain data on the object structure with gaps (compared to acoustic methods), and ability to test objects made of high electrically conductive materials (compared to magnetic resonance tomography).

Reconstruction of objects of a complex structure (design) based on the data obtained in eddy current testing is performed similarly to that used in the tomography types listed above, employing mainly two methods to increase the information content of testing.

The first method implies scanning the object surface when detecting the interaction zone of the exciting magnetic field of the eddy current transducer (ECT) and the test object.

In the second method, data are obtained at different angles of mutual spatial orientation of the field strength vector of the exciting magnetic field and the test object. In contrast to the first method, the second method employs an ECT with high uniform sensitivity to the object in the entire test area.

Thus, in terms of tomography, we can assert that ‘multi-angle’ interaction of a physical field with an object can be used to increase the information content.

We agree with the authors of the monograph [5] on the fundamental applicability of low-frequency magnetic fields for tomography of technical objects, however, we suggest the term ‘magnetic tomography’ for this type of tomography. With regard to the specifics of the physical interaction of the exciting field and the test object, it is more logical to use the term ‘eddy current tomography’. The conclusions of the authors of the monograph should be supplemented on the applicability of this type of tomography for reconstruction of primarily plane objects using only the first method of increasing the information content of testing. Further, the effectiveness of the second method to increase the information content for reconstruction of volumetric local objects of a complex structure will be shown.

2 Experiments and Results

Consider the problem of reconstructing a plane electrically conductive object via scanning the surface of an ECT object with a local zone of interaction between the exciting magnetic field and the test object as an example.

Figure 1 shows a removable ECT over three metal plates located close to each other as a composite object: duralumin plate of (60 × 60 × 1) mm, duralumin plate of (60 × 60 × 2) mm and steel plate of (60 × 60 × 0.3) mm. The upper surfaces of the plates are in the same *XY* plane.

The design parameters of the removable transformer differential ECT used in the experiment were as follows: the diameter of the excitation winding (EW) middle turn was 36 mm; the diameter of the measuring winding (MW) and compensation winding (CW) middle turn was 32 mm; the distance between the planes of the middle turns of the MW and CW located symmetrically relative to the EW was 22 mm. The gap between the ECP and the *XY* plane was 8 mm. The excitation current frequency was 250 Hz.

The eddy current measuring system used in the experiment was based on the IVN-03 applied voltage meter developed in the Laboratory for Electromagnetic Testing, TPU, which enables measuring the amplitudes of the complex components of the ECT applied voltage with a relative error not exceeding ± 1%.

Before the experiment, the initial ECT voltage was automatically compensated for in the absence of the test object. During the experiment, the ECT was moved parallel to the *XY* plane in the range of (−105 to 105) mm along the *Y* axis and in the range of (−45…45) mm along the *X* axis with an increment of 5 mm.

Figure 2 shows the dependences of the amplitude A^* and phase φ of the relative applied voltage of the ECT on the X and Y coordinates. The maximum value of the amplitude A^* was 0.08. The phase variation range was (–19 to 86)°.

The analysis of the obtained results on the interaction of the ECT magnetic field and the composite plane object (the results of direct eddy current transformation) shows that the test object can be reconstructed with a certain degree of reliability (the inverse problem of eddy current transformation has been solved). In particular, the pattern of the dependences in Fig. 2 indicates that the test object consists of three

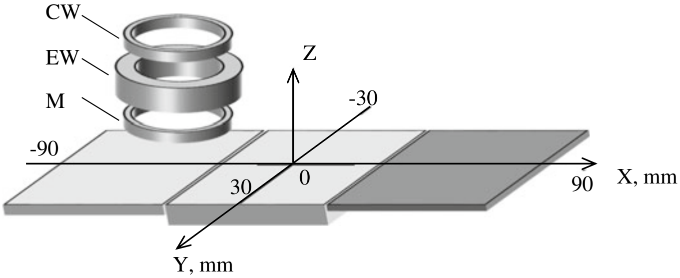

Fig. 1 A removable ECT over a plane composite metal object

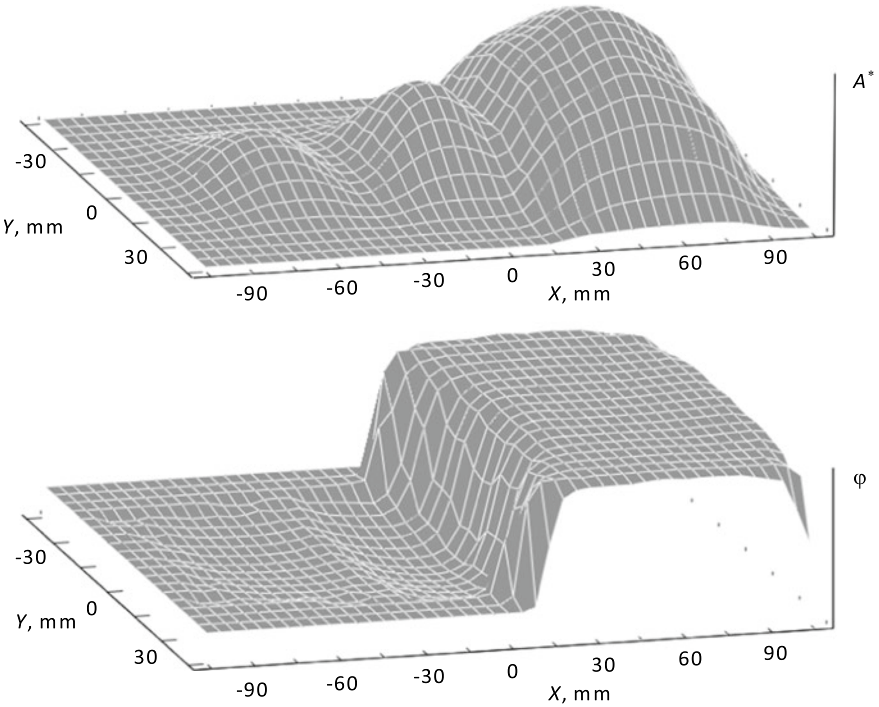

Fig. 2 Dependence of the amplitude A^* and phase φ of the relative applied voltage of the ECT on the X and Y coordinates

plane square-shaped components, two of which are made of non-magnetic material, and one is made of magnetic one. In this case, it can be concluded that, although non-magnetic parts are located relative to each other gapless, they are not one whole.

If necessary, the distance from the ECT to the metal plates and the thickness and electrical conductivity of non-magnetic components can be determined using conventional methods of eddy current testing, for example, the three-frequency method of eddy current testing of non-magnetic metal objects described in [7, 8]. According to this method, the first frequency is selected as a negligibly small value of the penetration depth of the magnetic field in comparison with the plane object thickness. The second frequency is selected from the condition that the penetration depth of the magnetic field is approximately equal to half the thickness of the object The third frequency is selected from the condition that the penetration depth of the magnetic field exceeds the object thickness. In this case, the applied voltage of the ECT at the first frequency depends on the gap h between the transducer and the test object only. The applied voltage at the second frequency depends on the gap h and the specific electrical conductivity σ of the material. The applied voltage at the third frequency depends on the gap h, the specific electrical conductivity σ of the material and the object thickness T.

The h value is determined by the value of the applied voltage amplitude of the first frequency. The values of the complex components of the applied voltage of the second frequency and the calculated gap value are used to determined the σ value. The values of the complex components of the applied voltage of the third frequency and the calculated values of the gap h and the material specific electrical conductivity σ are used to determine the object thickness T. The functions of the inverse transformation obtained in the numerical analysis of the functional dependences of the applied voltages of the ECT on the specified parameters of the object are used to determine the test object parameters: the gap h, the material specific electrical conductivity σ and the object thickness T.

Thus, a detailed reconstruction of the composite test object can be carried out. Moreover, testing can be performed even if there is an electrically conductive shield between the ECT and the test object (reconstruction of a multilayer object).

Figure 3 shows the dependences of the amplitude A^* and phase φ of the relative applied voltage of the ECP on the X and Y coordinates for the object in Fig. 1 in the presence of a duralumin plate 1.2 mm thick located directly above the XY plane. The

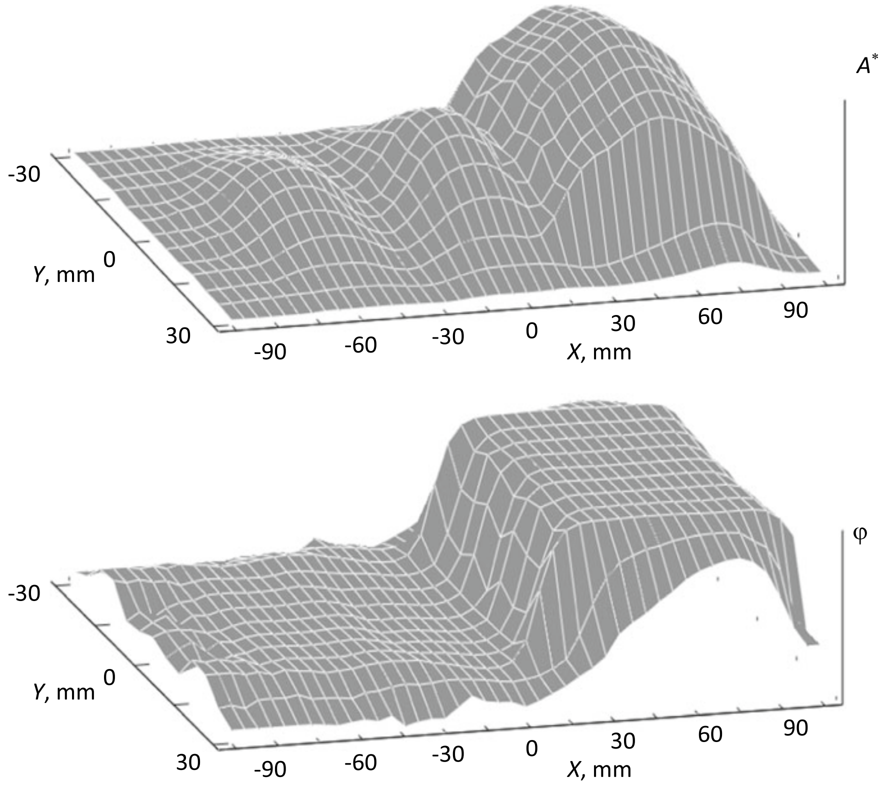

Fig. 3 Dependence of the amplitude A^* and phase φ of the relative applied voltage of the ECT on the X and Y coordinates when using the shield

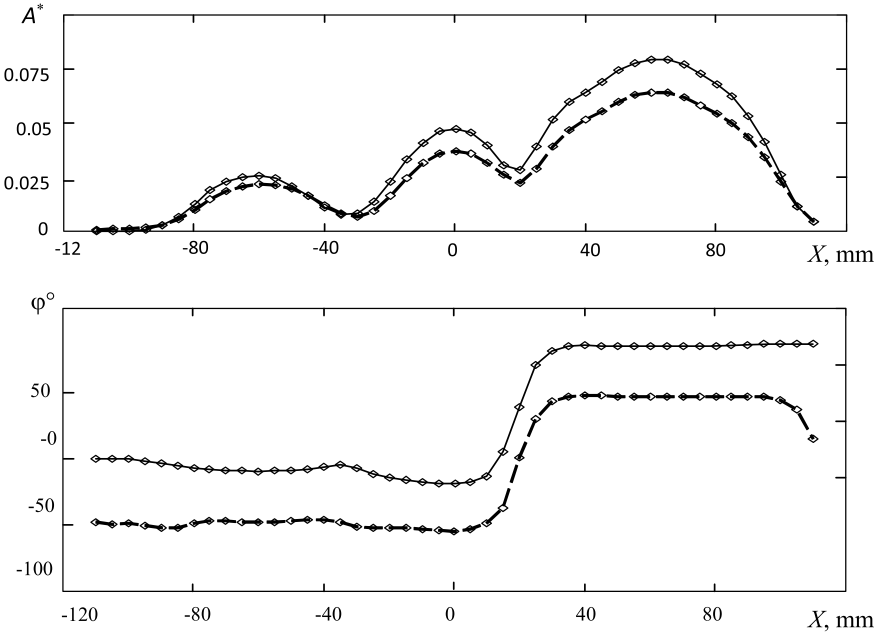

Fig. 4 Dependences of the amplitude A* and phase φ of the relative applied voltage of the ECT on the X coordinate at Y = 0 without (solid line) and with (dashed line) the shield

effect of the shield was minimized by balancing the ECT in the absence of the test object but in the presence of the shield.

The maximum amplitude A^* in this case was 0.065. The phase variation range was (–57 to 48)°.

A comparative analysis of the interaction results for the cases of absence and presence of the shield shows that the results are qualitatively similar. Figure 4 illustrates the quantitative difference between the results. It shows the dependences of the amplitude A^* and phase φ of the relative input voltage of the ECT on the X coordinate at $Y = 0$ for the cases of absence and presence of the shield. The differences in the values of the amplitude and phase are of natural character and can be compensated in the first case by multiplicative corrections, and in the second case by additive ones.

It should be noted that the decreased diameter of the ECT windings can enlarge the test area and, accordingly, provide more data on the properties of an electrically conductive test object. However, in this case, the maximum distance from the ECT to the object reduces.

Another way to increase the information value of eddy current testing and to provide more data on the results of eddy current tomography is measurement at different angles of mutual spatial orientation of the field strength vector of the exciting magnetic field and the test object [9]. As an example, consider the problem of reconstructing volumetric local electrically conductive objects in the form of rotating body for single objects located in the test area, and for pairs of objects with coaxial and non-coaxial orientation. The appearance and characteristics of the objects are shown in Fig. 5.

Figure 6 illustrates the transformer ECT with a two-section EW *w*1 and MW *w*2 located coaxially with the EW sections and at similar distance from them. The diameter of the middle turn of the windings is 320 mm, and the distance between the

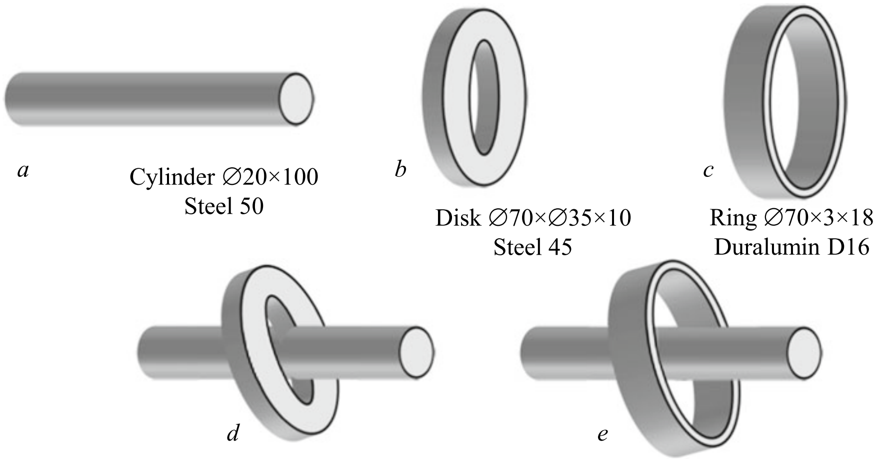

Fig. 5 Volumetric local electrically conductive objects: rotation bodies (**a**–**c**) and their pair combinations in the non-axial orientation (**d**, **e**)

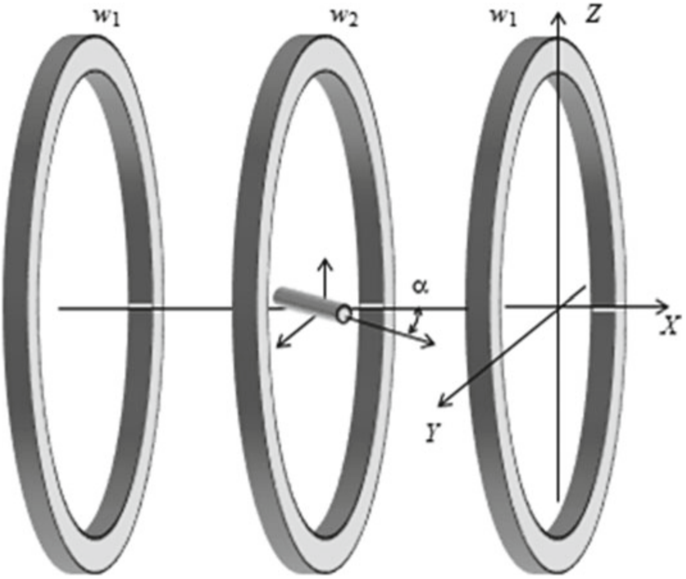

Fig. 6 Electrically conductive object in the ECT test area

windings is 120 mm. This ratio of the ECT geometric parameters in the middle zone of the test area ensures highly uniform sensitivity of the transducer to an electrically conductive object. Thus, when an electrically conductive object of a spherical shape moves within a spherical region with a diameter of 160 mm located in the center of the ECT, the relative change in the applied voltage amplitude does not exceed 5%.

The ECT comprises a special device for rotating the object in the XY plane and fixing the rotation angle α to ensure measurement at different mutual orientations of the exciting magnetic field (directed along the X axis) and the test object. The orientation angle α was changed in the range of (0–180)° with an increment of 15°.

During the experiments, the excitation current frequency was 1 kHz. The amplitudes of the complex components of the applied voltage of the ECT were measured using the previously mentioned IVN-03 meter.

Figure 7 shows the hodographs of the relative applied voltage for changes in the orientation with respect to the force lines of the magnetic field of objects in the form of rotation bodies. Hodographs of $\dot{U}^*_{\mathrm{INS}}$ for changes in the orientation of these objects with respect to the force lines of the ECT magnetic field are straight lines with the ends corresponding to the longitudinal and transverse orientations in the magnetic field.

Thus, the reflection of the parameters of the rotation bodies are two complex values $\dot{A}$ and $\dot{B}$ equal to the values $\dot{U}^*_{\mathrm{INS}}$ for the longitudinal ($\alpha = 0$) and transverse. ($\alpha = 90°$) orientations of the object in the magnetic field, respectively. As shown in [10], modules of complex values $\dot{A}$ and $\dot{B}$ are proportional to the cube of the characteristic size of the test object. These are the size of the object in the corresponding direction of the magnetizing field for ferromagnetic objects and the size of the object in the plane orthogonal to the direction of the magnetizing field for nonmagnetic objects. The ratio of the moduli of $\dot{A}$ and $\dot{B}$ shows the ratio of the longitudinal and transverse dimensions of the object, and the phase values indicate the electromagnetic properties of the material.

Figure 8 shows the hodographs of the relative applied voltage for changes in the orientation relative to the force lines of the magnetic field of pairs of objects in the form of rotation bodies in their coaxial orientation. In this case, the hodographs of $\dot{U}^*_{\mathrm{INS}}$ for changes in the orientation of these composite objects relative to the force lines of the ECT magnetic field are straight lines with the ends corresponding to the longitudinal and transverse orientations in the magnetic field.

Figure 9 shows the hodographs of the relative applied voltage for changes in the orientation with respect to the force lines of the magnetic field of the same pairs of rotation bodies in non-axial orientation (angle β between the direction of the longitudinal axes was set equal to 30°). Hodographs for changes in the orientation of such composite objects with respect to the force lines of the ECT magnetic field are not straight lines but ellipses.

The ratio of the axes of the ellipses shows the degree of non-axiality of the test objects. To illustrate this, we experimentally determined the dependence of the ratio of the axes of the ellipse ε on the angle β for a pair of rotation bodies—a ferromagnetic cylinder and a duralumin ring (Fig. 10). Analysis of this dependence shows that for coaxial ($\beta = 0°$) and orthogonal ($\beta = 90°$) mutual orientation of rotation bodies, the

Fig. 7 Hodographs of $\dot{U}^{*}_{\text{INS}}$ for rotation of the objects in the form of rotation bodies

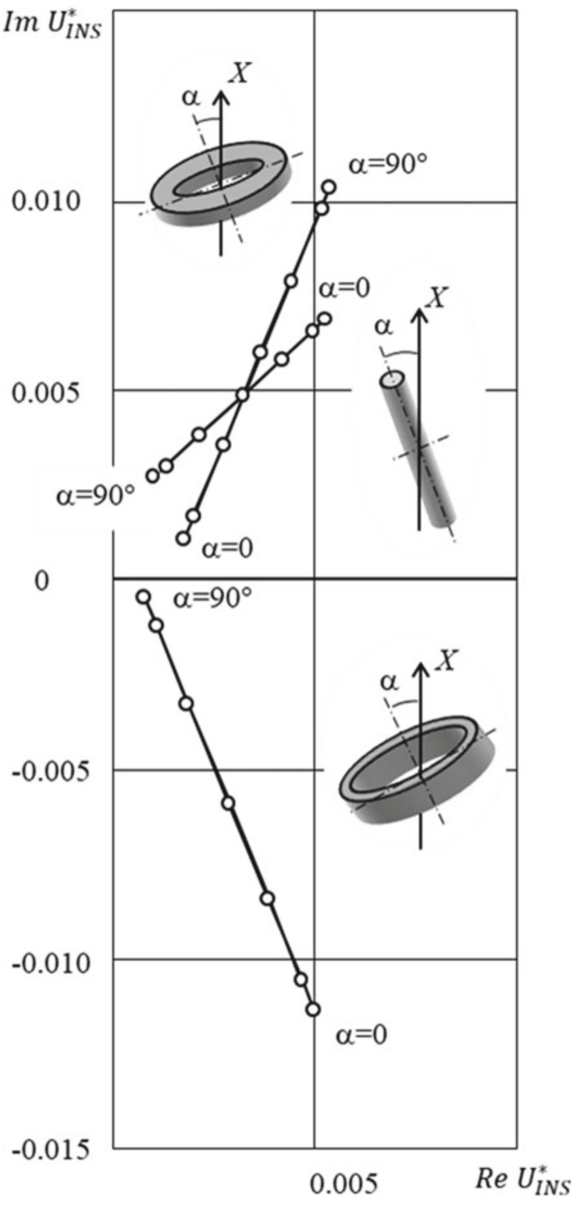

ratio of the ellipse axes (the minor axis-to large axis length ratio) is zero. When the angle β changes in the range of (0–90)°, the ratio ε for this asymmetric object changes in the range of (0–0.5). The maximum value ε corresponds to the non-axiality angle $\beta \approx 40°$. The ε(β) dependence is almost cosinusoidal one.

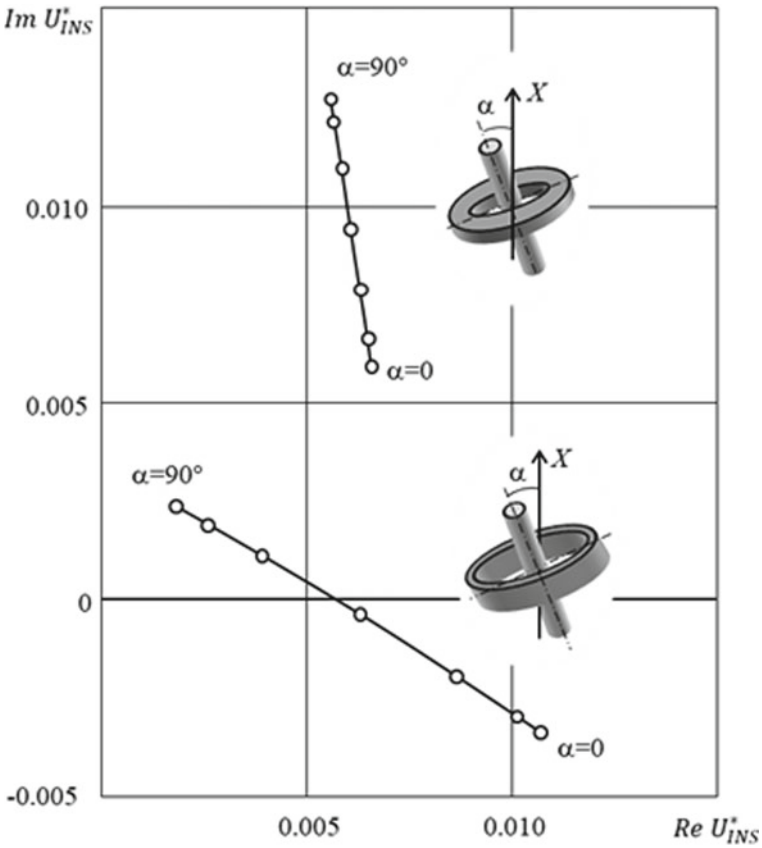

Fig. 8 Hodographs of $\dot{U}^*_{\mathrm{INS}}$ for rotation of the composite objects in the form of rotation bodies in coaxial orientation

Thus, measurements of $\dot{U}^*_{\mathrm{INS}}$ in different mutual orientations of the exciting magnetic field and the test object provide more data on the shape, material, dimensions, and orientation of the electrically conductive object in space. For asymmetric objects, a quantitative assessment of the asymmetry can be carried out.

The described example is a particular case of the orientation of the longitudinal axes of the test objects in the *XY* plane. In the case of arbitrary orientation, the objects should be rotated in at least two orthogonal planes to achieve reliable results of reconstruction.

In addition, practical implementation of the multi-angle interaction of the physical field with the object should be considered. In the first case considered, the ECT was mechanically displaced relative to the plane object, and in the second case, the most local electrically conductive object was mechanically rotated in the ECT magnetic field. However, as shown in [9], electrical methods of scanning objects are more

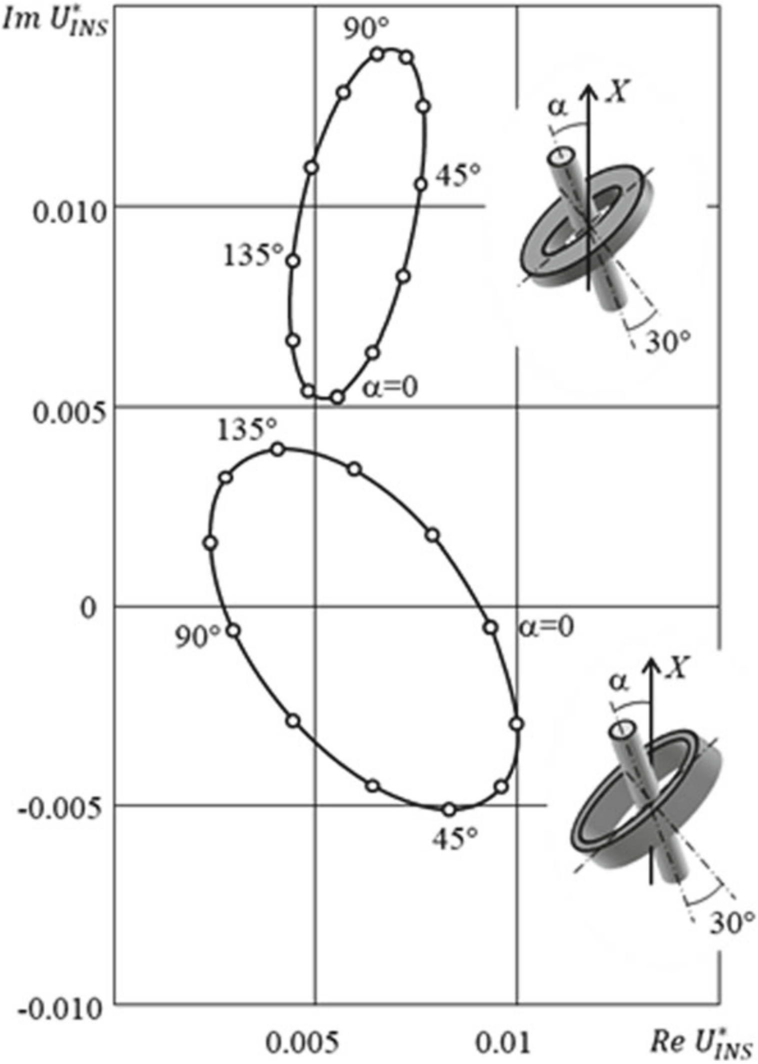

Fig. 9 Hodographs of $\dot{U}^{*}_{\text{INS}}$ for rotation of the composite objects in the form of rotation bodies in non-axial orientation

suitable due to the appropriate control of the field winding currents and signals of the measuring windings of a multi-winding ECT. These are matrix ECTs [11] and transducers of systems for selective detection of metal objects.

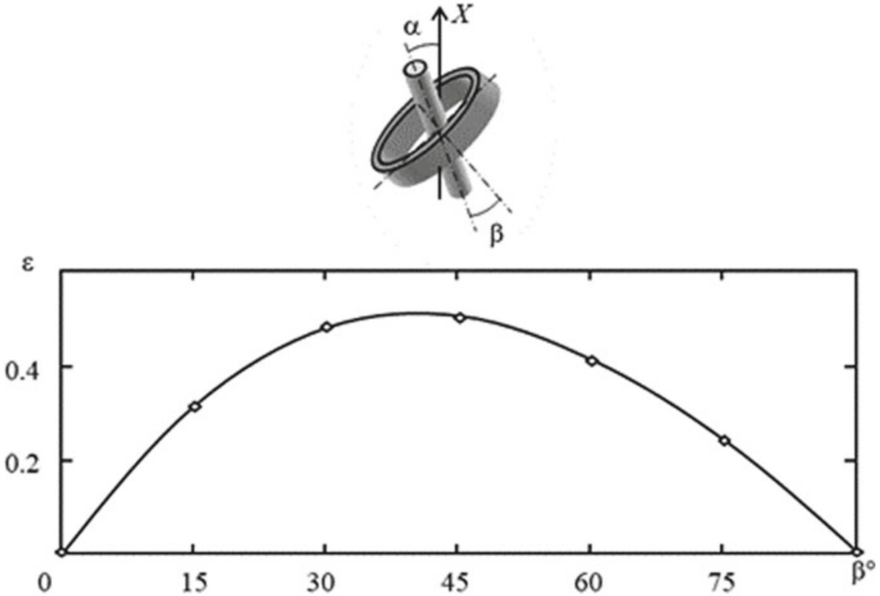

Fig. 10 Dependence of the ratio of the axes of the ellipse ε on the angle β for a pair of rotation bodies—a ferromagnetic cylinder and a duralumin ring

3 Conclusion

Thus, eddy current testing methods can be effectively used to solve a number of technical tomography problems associated with obtaining detailed information about the structure of composite metal objects.

The reconstruction of complex objects can be carried out based on the results of eddy current testing using two methods for increasing the information content of testing. The first method implies scanning the object surface when detecting the interaction zone of the exciting magnetic field of the ECT and the test object, and can be used for monitoring mainly plane electrically conductive objects. The second method provides measurement information at different angles of mutual spatial orientation of the excitation magnetic field strength vector and the test object, and can be used for reconstruction of volumetric local electrically conductive objects.

In the first case, information about the shape, material, dimensions, and continuity of the parts of a plane metal object can be obtained. In the second case, the shape, material, size, and space orientation of an electrically conductive object can be determined. For asymmetric objects, quantitative information can be obtained on the degree of their asymmetry, which can be used, in particular, to control the relative position of the parts.

References

1. Fuchs, T., Keßling, P., Firsching, M., Nachtrab, F., Scholz, G.: Industrial applications of dual X-ray energy computed tomography (2X-CT). RILEM Bookseries **6**, 97–103 (2012). https://doi.org/10.1007/978-94-007-0723-8_13
2. Wang, Z.-B., Shi, G.-H., He, Y., Ding, Z.-H., Zhang, Y.-D.: Application of optical coherence tomography to distance measurement of optical surface. Guangxue Jingmi Gongcheng/Opt. Precision Eng. **20**(7), 1469–1474 (2012). https://doi.org/10.3788/OPE.20122007.1469
3. Barkhatov, V.A.: Development of methods of ultrasonic nondestructive testing of welded joints. Russ. J. Nondestruct. Test **39**(1), 23–47 (2003). https://doi.org/10.1023/A:1024588920109
4. Monte, L., Erricolo, D., Ansari, R., et al: Underground imaging using RF tomography: the effect of lateral waves. In: Proceeding of the 2009 International Conference on Electromagnetics in Advanced Applications, pp. 873–876 (2009). https://doi.org/10.1109/ICEAA.2009.5297354
5. Minin, O.V., et al.: Ultra-wideband radio tomographic imaging with resolution near the diffraction limit. Opt. Quant. Electron. **49**(10), 339 (2017). https://doi.org/10.1007/s11082-017-1172-7
6. Bray, C.L., Hornak, J.P.: Unilateral MRI using a rastered projection. J. Magn. Reson. **188**(1), 151–159 (2007). https://doi.org/10.1016/j.jmr.2007.06.010
7. Tajima, N., Yusa, N., Hashizume, H.: Low frequency eddy current testing to measure thickness of double layer plates made of nonmagnetic steel. Stud. Appl. Electromagn. Mech. **42**, 131–138 (2017). https://doi.org/10.3233/978-1-61499-767-2-131
8. Yakimov, E.V., Urazbekov, E.I., Goldshtein, A.E., Bulgakov, V.F.: Computational transformation of signals of a measuring information system for eddy-current flaw detection. Russ. J. Nondestruct. Test **49**(11), 657–663 (2013). https://doi.org/10.1134/S1061830913110107
9. Goldstein, A.E., Belyankov, V.Y.: An eddy-current gauge for measuring the wall thickness of light-alloy drill pipes. Russ. J. Nondestruct. Test **53**(8), 588–595 (2017). https://doi.org/10.1134/S1061830917080022
10. Ammari, H., Chen, J., Chen, Z., Garnier, J., Volkov, D.: Target detection and characterization from electromagnetic induction data. J. des Mathematiques Pures et Appliquees **101**(1), 54–75 (2014). https://doi.org/10.1016/j.matpur.2013.05.002
11. Chady, T.: A family of matrix type sensors for detection of slight flaws in conducting plates. IEEE Trans. Magn. **35**(5), 3655–3657 (1999). https://doi.org/10.1109/20.800621

Application of Elliptical Properties in Building a Tomographic Image of an Inspected Object Using Multi-Element Ultrasonic Sensor Data

Yuliya Shulgina, Evgeny Shulgin, Ahmed Abouellail, Mariya Kostina, Oksana Terentyeva, and Jianglei Chang

Abstract The article discusses a proposed method that allows to reduce the amount of transmitted data from the receiving and data preprocessing to a personal computer, as well as the amount of digitized information and the time of its processing. The method is based on the main property of the ellipse. The developed data processing algorithm for a system with a multi-element sensor was tested in the MatLab software package. A block diagram and data processing algorithm have been developed for practical implementation on FPGAs. The amount of digitized information has been reduced by more than 10 times.

Y. Shulgina · E. Shulgin · A. Abouellail · M. Kostina (✉) · O. Terentyeva · J. Chang
Division for Electronic Engineering, School of Non-Destructive Testing, National Research Tomsk Polytechnic University, 30 Lenin Avenue, Tomsk, Russia 634050
e-mail: mashenkasoldatova@mail.ru

Y. Shulgina
e-mail: shulgina@tpu.ru

E. Shulgin
e-mail: sembox@mail.ru

A. Abouellail
e-mail: demo092@tpu.ru

O. Terentyeva
e-mail: oksanaterenteva95@mail.ru

J. Chang
e-mail: vastchan@mail.ru

M. Kostina
Department of Innovation Management, Tomsk State University of Control Systems and Radioelectronics, 40 Lenin Avenue, Tomsk, Russia 634050

I. V. Minin et al. (eds.), *Progress in Material Science and Engineering*,
Studies in Systems, Decision and Control 351,
https://doi.org/10.1007/978-3-030-68103-6_2

1 Introduction

Currently, ultrasonic non-destructive testing has entered a new stage of development. The possibility of obtaining a three-dimensional image of the test object with a high scanning speed in real time has been developed due to the use of multi-element sensors. Recently, the sampling phased array method (SPA), developed at the Fraunhofer Institute of nondestructive testing in Germany, is actively used to solve many problems of nondestructive testing. The essence of this method is the alternate excitation of the elements that make up the sensor, and the parallel reception of signals by all elements. The received ultrasonic signals are stored for each element of the phased array and serve as the initial data for 2D and 3D visualization of the test object. Thus, even after one cycle of transmission and reception, all angles of propagation of ultrasonic signals over the entire probing depth can be carried out, which will make it possible to reproduce the image of the object under study. Since the focusing of the ultrasonic beam is carried out not physically, but during the processing of the received data, a high scanning speed can be achieved.

The complexity of the development of devices containing multi-element sensors involves the need to transfer and process a large amount of data. Therefore, reducing the amount of recorded and transmitted information is an urgent task. With the increase in the number of the antenna array elements, the system becomes more complex and the amount of transmitted information increases. Conversion of an analog signal from an acoustic sensor into a digital sequence with a different sampling clock cycle can significantly reduce the amount of information transmitted to a personal computer or display device, as well as reduce the processing time.

2 The Principle of Constructing an Image of the Tested Object

The scanned area of the test object, located under the phased antenna array, is determined by the distance between adjacent radiating elements, the radiation pattern of the array and the frequency of the ultrasonic signal.

At the first step of the device operation, the first emitter is excited (Fig. 1), after which all elements of the array begin to receive the reflected signal [1, 2]. The received signals are fed through an amplifier to an analog-to-digital converter (ADC). The ADC, in the classic method, operates at a constant frequency clock. In this case, as will be shown below, the device memory is filled with information, some of which will not participate in image reconstruction. At the second step, the second element of the sensor is excited, after which all elements of the array receive the reflected signals. This procedure continues until all the elements of the array have been iterated over. In this case, with the increase in the number of elements in the acoustic array [3], the amount of digitized information increases in proportion to the square of their quantity.

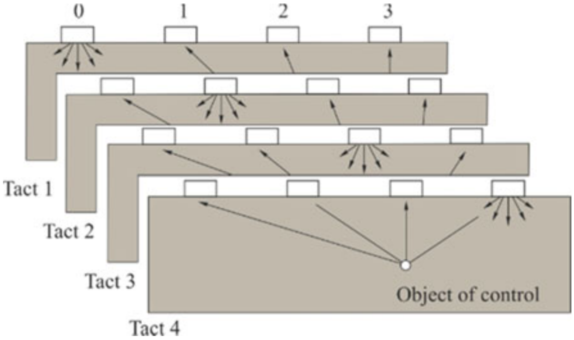

Fig. 1 The operational cycle of a 4 element sensor

To scan the area under the sensors, only four cycles of ultrasound "transmission-reception" are required for a phased array consisting of four elements, which increases the scanning speed compared to focusing the beams at each point of the tested object.

The recorded signal amplitudes at discrete times of A-scans for all emitter-receiver combinations are used in imaging. According to the calculated propagation time of the signal to the current calculated point of the tested object, the required amplitudes are sampled from each A-scan. The amplitudes for a point from all A-scans are summed together and interpreted as an image.

It is more convenient to set the point of the inspected object *N* by its *x*–*y* coordinates. To process one of the recorded A-scans, with the help of the emitter number N_e and the receiver number N_r, the ultrasound propagation time from the emitter to the receiver through the calculated point is calculated [4–7].

$$t_{N(x,y)\sum} = t_{ERN(x,y)} + t_{REN(x,y)}; \tag{1}$$

where $t_{\mathrm{ERN(x,y)}}$—propagation time of ultrasound from the emitter to the point *j*; $t_{\mathrm{REN(x,y)}}$—propagation time of ultrasound from point j to the receiver.

For the classical implementation of the SPA method, all distances calculated from each sensor to each point and from each point to each receiver are (Fig. 2). As a result, there is a table that contains information about the distances traveled by the ultrasound, depending on the point number, the number of the emitting sensor and the number of the receiving sensor [8]. Such a matrix will have the form shown in Table 1. In fact, there is a three-dimensional matrix for physical storage, but a two-dimensional matrix is used in this case, where the numbers of receivers and emitters are encoded by one variable.

The high demand for information processing speed leads to the necessity to perform a large number of operations simultaneously [9]. Either several high-performance processes for solving problems in parallel, or using programmable matrices, can allow for a large number of operations to be carried out in parallel on one chip.

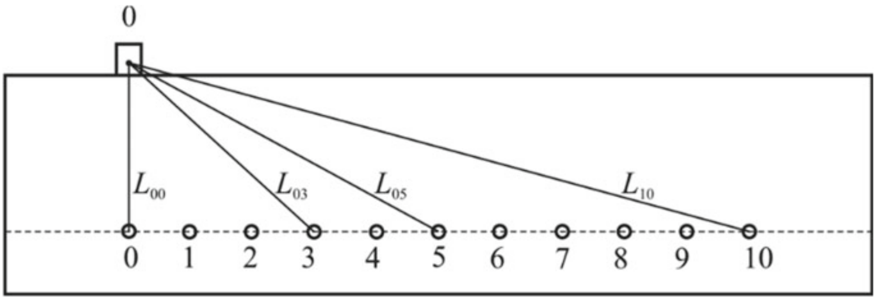

Fig. 2 Determination of the distance traveled by the signal from the source to the receiver through the calculated point

For the formation of a tomographic image of the tested object, a long post-processing time is required, because of the large number of distances determinations of signal reception and transmission by piezoelectric transducers through each digital focal point of the unltasonic signal. For example, to construct a tomographic image of the internal structure of a tested object with a size of 100 × 100 focal points of the ultrasonic signal and using an antenna array of 16 piezoelectric transducers, it is necessary to determine 2,560,000 distances.

To build an image of the tested object, it is necessary to calculate the resulting matrix, in rows and columns of which the total values of the amplitudes at a given point will be located [10–13].

The dimension of the matrix designed to store the resulting amplitude for each given point of the tested object coincides with the dimension of the image of the tested object. Therefore, with an increase in the resolution of the inspected area, the amount of stored and transmitted information increases proportionally.

3 Application of Ellipse Properties in Processing, Storing and Transmitting Information of a Tested Object

To implement the proposed processing algorithm, it is necessary to divide the scanned area of the tested object into separate scan points, as shown in Fig. 3. In this case, the same number of scanned points must be placed between adjacent sensors [14].

The essence of shortening the matrix is that the ultrasonic signal propagates radially, therefore, for any pair of emitter/receiver, there will be a set of points located at the same distances. These points will lie on the ellipse, as shown in Fig. 4. In this case, the selected transmitter and receiver will be in the focus of the ellipse. The distance between the selected emitter and receiver will determine the focal distance. The semi-minor axis of the ellipse will determine the probing depth [15].

Table 1 Complete matrix of distances for 10 points and three transmitters and receivers

Point No	Emitter 0 Receiver 0	Emitter 0 Receiver 1	Emitter 0 Receiver 2	Emitter 1 Receiver 0	Emitter 1 Receiver 1	Emitter 1 Receiver 2	Emitter 2 Receiver 0	Emitter 2 Receiver 1	Emitter 2 Receiver 2
0	L_{00}	L_{05}	L_{10}	L_{00}	L_{05}	L_{10}	L_{00}	L_{05}	L_{10}
1	L_{01}	L_{04}	L_{09}	L_{01}	L_{04}	L_{09}	L_{01}	L_{04}	L_{09}
2	L_{02}	L_{03}	L_{08}	L_{02}	L_{03}	L_{08}	L_{02}	L_{03}	L_{08}
3	L_{03}	L_{02}	L_{07}	L_{03}	L_{02}	L_{07}	L_{03}	L_{02}	L_{07}
4	L_{04}	L_{01}	L_{06}	L_{04}	L_{01}	L_{06}	L_{04}	L_{01}	L_{06}
5	L_{05}	L_{00}	L_{05}	L_{05}	L_{00}	L_{05}	L_{05}	L_{00}	L_{05}
6	L_{06}	L_{01}	L_{04}	L_{06}	L_{01}	L_{04}	L_{06}	L_{01}	L_{04}
7	L_{07}	L_{02}	L_{03}	L_{07}	L_{02}	L_{03}	L_{07}	L_{02}	L_{03}
8	L_{08}	L_{03}	L_{02}	L_{08}	L_{03}	L_{02}	L_{08}	L_{03}	L_{02}
9	L_{09}	L_{04}	L_{01}	L_{09}	L_{04}	L_{01}	L_{09}	L_{04}	L_{01}
10	L_{10}	L_{05}	L_{00}	L_{10}	L_{05}	L_{00}	L_{10}	L_{05}	L_{00}

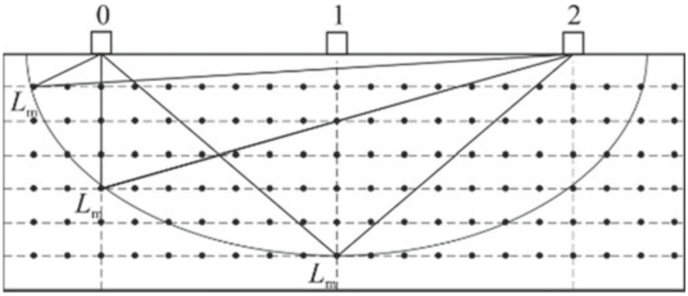

Fig. 3 The location of the pixels in the testing aria

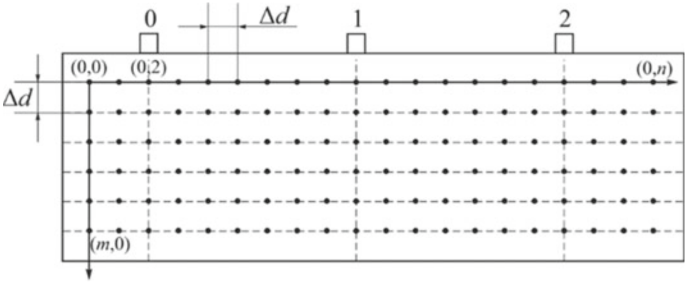

Fig. 4 Sample capture of pixels in the testing aria by using the ellipse method

It is possible to store information about the signal amplitude only for points that are a small radius of the ellipse (Fig. 5). In this case, it is possible to carry out analog-to-digital conversion of the received signal only at fixed points in time corresponding to a distance equal to the minor axis (Fig. 6).

Equally spaced points for a given combination of emitter and receiver lie on the line of the ellipse, therefore, by dividing the image of the tested object not into points, but rather into sectors of the ellipse, it is possible to sample the amplitudes from the

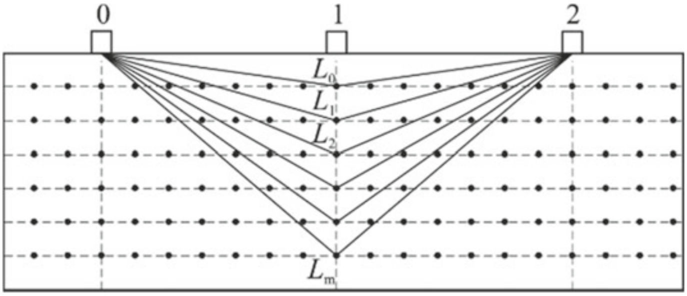

Fig. 5 Sample capture of pixels located on a small radius of an ellipse

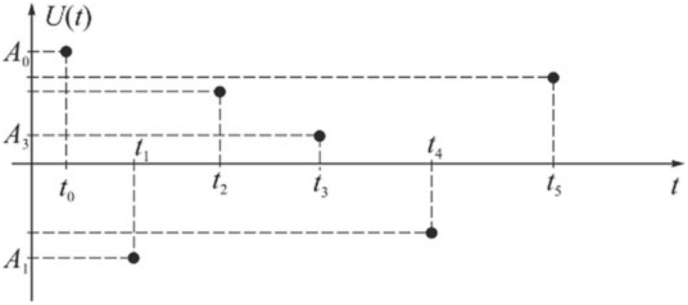

Fig. 6 An example of sample capture amplitudes of pixels located on a small radius of an ellipse

Table 2 Abbreviated matrix of distances (times) by the method of ellipses

Point number	Distance
0	L_0
1	L_1
2	L_2
3	L_3
4	L_4
5	L_5
…	…
m	L_m

A-scan memory only for points that are at an equal distance from the centers of the ellipse [16, 17].

As a result, we will have a matrix-column (Table 2), which will be completed to a complete picture of the tested object in the image processing unit.

For the data storage system, the use of the ellipse properties is very convenient, as the load on the transmitting channel is also reduced by a large factor. However, it is required to develop an imaging unit that implements an algorithm for calculating the coordinates of points located on the ellipse line.

The main difficulty in implementing the described method involves organizing the ADC clock, which requires calculating the time coordinates of the next sample and initializing the clock signal at the right time.

The clock generator, connected to the analog-to-digital conversion start unit, sets the frequency of the circuit. However, the use of programmable logic integrated circuits allows these calculations to be carried out in parallel with the recording and processing of the acoustic signal, which will make it possible to implement a system for constructing an image of the tested object in real time [18, 19].

4 Results of the Implementation of Ellipse Properties

Real signals from the antenna array were used to debug the data processing algorithm and build the image. For information processing and image construction, MATLAB programming and mathematical modeling package was selected.

The algorithm for obtaining an image using the MATLAB package is as follows (Fig. 7).

For each emitter-receiver pair, the propagation time of the ultrasonic pulse from the emitter to the receiver through the calculated point of the tested object, located on the minor axis of the ellipse, is calculated and summed.

Based on the calculated time, a column matrix is formed that stores information about the signal amplitudes at points located on the minor axis of the ellipse corresponding to the calculated row [20].

The next step is to form the image matrix, which is filled with the amplitude values by the points located on the ellipse.

After receiving image matrices from all pairs of sensors, they are summed up. The resulting matrix is displayed as an image using the images function.

Plexiglas was used as an object of control. The main data for the construction of the image was the distance between the sensors (0.75 mm), the sampling frequency (40 MHz), the ultrasound speed (2800 m/s), the number of sensors (16).

As a result of information processing in the MATLAB environment, a cross-sectional image of the examined object was built.

5 Experiment

Plexiglas with internal defects was used as an object of inspection and information was taken from a grid consisting of 16 elements, where the distance between the 16 sensors is 0.75 mm, the sampling frequency is 40 MHz, and the ultrasound speed is 2800 m/s. After one cycle of operation of the multielement sensor, 512 A-scans are obtained: 256 A-scans with constant sampling time (16 MHz) and 256 A-scans with variable sampling time.

The data was processed in two ways: the classical method and the ellipse method. Comparison of the two results was performed numerically and visually. When the imaging zone was limited by the main lobe of the sensor directional pattern, the discrepancies were observed only on the sides and amounted to less than 5%. Visually, the images obtained by the two methods did not differ. The results were visualized in the MathLab software package.

The resulting cross-sectional image of the examined object (Fig. 8) completely coincides with the image obtained using the existing algorithm, which confirms the adequacy and applicability of the developed method.

Fig. 7 Algorithm of the program in MatLab

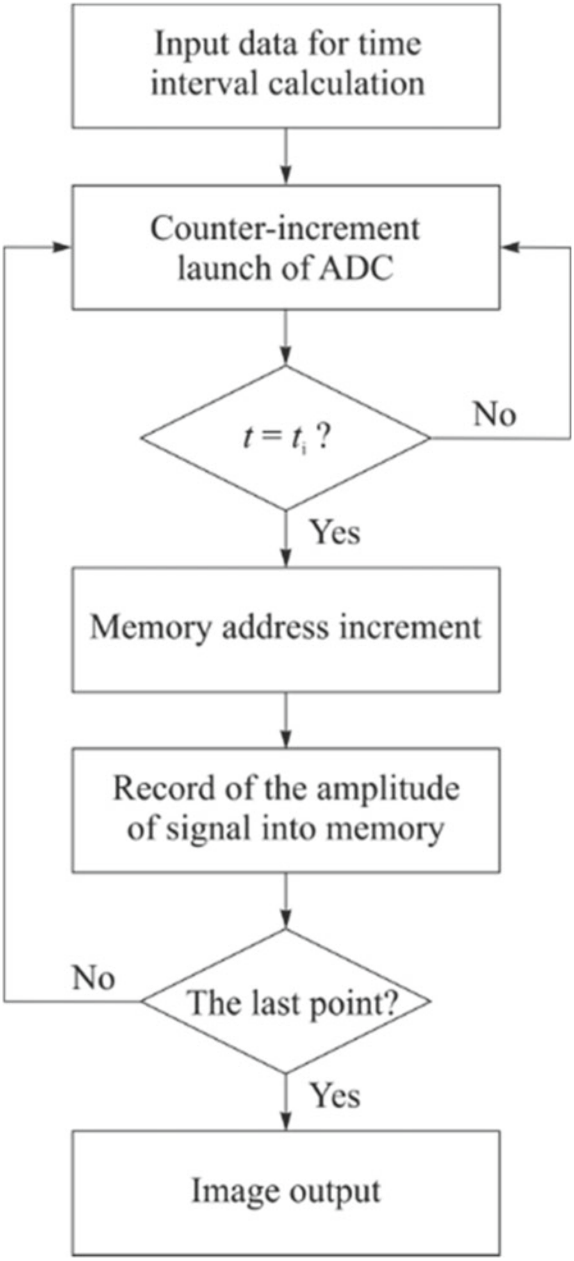

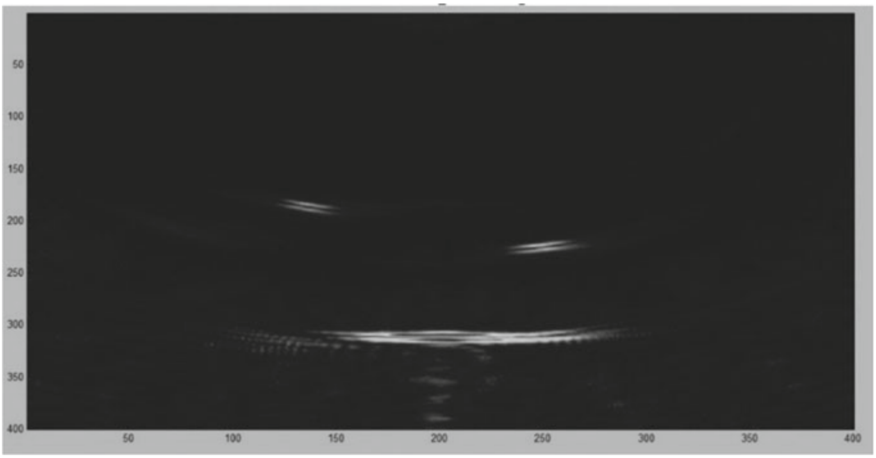

Fig. 8 Cross-sectional image of the examined object

6 Conclusion

The number of A-scan points significantly influences the processing time. When using the classical method for the object under study (plexiglass), 7818 A-scan points are required in order to satisfy all angles of the acoustic signal propagation for the selected resolution. However, when using the ellipse method, only 500 A-scan points are required, which means that the memory size for storing one A-scan will decrease 15.5 times.

The number of clock cycles per ADC cycle when processing one A-scan using the ellipse method has decreased 15.5 times, therefore, ADCs can be used operating at a lower frequency without losing image quality.

This significantly reduces the information that will be transmitted to the display system or the connected computer. The load on the information channel with the implementation of preprocessing in the programmable logic matrix will decrease by N^2 times, where N is the number of emitters in the sensor.

References

1. Bazulin, E.G., Sadykov, M.S.: Determining the speed of longitudinal waves in an isotropic homogeneous welded joint using echo signals measured by two antenna arrays. Russ. J. Nondestruct. Test. **54**(5), 303–315 (2018). https://doi.org/10.1134/S1061830918050029
2. Bazulin, E.G.: Allowing for inhomogeneous anisotropy of a welded joint when reconstructing reflector images from echo signals received by an ultrasonic antenna array. Russ. J. Nondestruct. Test. **53**(1), 9–22 (2017). https://doi.org/10.1134/S1061830917010028
3. Le Jeune, L., Robert, S., Lopez Villaverde, E., Prada, C.: Wave Imaging for ultrasonic non-destructive testing: Generalization to multimodal imaging. Ultrasonics **64**, 128–138 (2016).

https://doi.org/10.1016/j.ultras.2015.08.008

4. Camacho, J., Atehortua, D., Cruza, J.F., Brizuela, J., Ealo, J.: Ultrasonic crack evaluation by phase coherence processing and TFM and its application to online monitoring in fatigue tests. NDT E Int. **93**, 164–174 (2018). https://doi.org/10.1016/j.ndteint.2017.10.007
5. Brath, A.J., Simonetti, F.: Phased array imaging of complex-geometry composite components. IEEE Trans. Ultrason. Ferroelectr. Freq. Control **64**(10), 1573–1582 (2017). https://doi.org/10.1109/TUFFC.2017.2726819
6. Malkin, R.E., Franklin, A.C., Bevan, R.L., Kikura, H., Drinkwater, B.W.: Surface reconstruction accuracy using ultrasonic arrays: application to non-destructive testing. NDT E Int. **96**, 26–34 (2018). https://doi.org/10.1016/j.ndteint.2018.03.004
7. Haupert, S., Renaud, G., Schumm, A.: Ultrasonic imaging of nonlinear scatterers buried in a medium. NDT E Int. **87**, 1–6 (2017). https://doi.org/10.1016/j.ndteint.2016.12.010
8. Bazulin, E.G.: Decreasing the structural-noise level when performing ultrasonic testing using antenna arrays. Russ. J. Nondestruct. Test. **51**(9), 525–539 (2015). https://doi.org/10.1134/S1061830915090038X
9. Bazulin, E.G.: Determination of the reflector type from an image reconstructed using echo signals measured with ultrasonic antenna arrays. Russ. J. Nondestruct. Test. **50**(3), 141–149 (2014). https://doi.org/10.1134/S1061830914030036
10. Bazulin, A.E., Bazulin, E.G., Ismailov, G.M.: The calculation of DGS diagrams for ultrasound testing systems with the use of phased arrays. Russ. J. Nondestruct. Test. **50**(1), 29–37 (2014). https://doi.org/10.1134/S1061830914010033
11. Shah, P.N., White, A., Hensley, D., Papamoschou, D., Vold, H.: Continuous-scan phased array measurement methods for turbofan engine acoustic testing. J. Eng. Gas Turbines Power **141**(8), 081201 (2019). https://doi.org/10.1115/1.4042395
12. Dupont-Marillia, F., Jahazi, M., Lafreniere, S., Belanger, P.: Design and optimisation of a phased array transducer for ultrasonic inspection of large forged steel ingots. NDT E Int. **103**, 119–129 (2019). https://doi.org/10.1016/j.ndteint.2019.02.007
13. Moreau, L., Hunter, A.J., Drinkwater, B.W., Wilcox, P.D.: Efficient imaging techniques using an ultrasonic array. Proc SPIE Int. Soc. Opt. Eng. **7650**, 765037 (2010). https://doi.org/10.1117/12.847294
14. Soldatov, A.I., et al.: Dynamic imaging acoustic fields in research practice. In: Proceedings of the 7th International Forum on Strategic Technology (IFOST 2012), pp. 1–4 (2012). https://doi.org/10.1109/IFOST.2012.6357734
15. Soldatov, A. A., Soldatov, P. V., Soldatov, A. I., Kostina, M. A., Shul'gina, Y. V.: Small-angle acoustic tomography under shadow testing with antenna arrays. Russ. J. Nondestruct. Test. **54**(7), 463–468 (2018). https://doi.org/10.1134/S106183091807007
16. Soldatov, A.I., Kozhemyak, O.A., Soldatov, A.A., Shulgina, Y.V.: Measurement error reducing in the ultrasound time-pulse systems. IOP Conf. Ser. Mater. Sci. Eng. **81**(1), 012117 (2015). https://doi.org/10.1088/1757-899X/81/1/012117
17. Asochakov, A. S., Shulgina, Y. V., Soldatov, A. I., Shulgin, E. M., Ogorodnikov, D. N.: Method of processing of ultrasonic signal of phased array. In: Proceedings of 2015 International Conference on Mechanical Engineering, Automation and Control Systems (MEACS 2015) 7414874 (2016). https://doi.org/10.1109/MEACS.2015.7414874
18. Davy, M., Minonzio, J.-G., de Rosny, J., Prada, C., Fink, M.: Influence of noise on subwavelength imaging of two close scatterers using time reversal method: theory and experiments. Prog. Electromagn. Res. **98**, 333–358 (2009). https://doi.org/10.2528/PIER09071004
19. Asgedom, E.G., Gelius, L.-J., Austeng, A., Holm, S., Tygel, M.: Time-reversal multiple signal classification in case of noise: a phase-coherent approach. J. Acoust. Soc. Am. **130**(4), 2024–2034 (2011). https://doi.org/10.1121/1.3626526
20. Xiao, G., Xiong, C., Hou, Y.: Analyzing phased arrays with basis functions associated with characteristic modes. PIERS-Toyama 2018-August, pp. 208–212 (2018). https://doi.org/10.23919/PIERS.2018.8598107

Gaussian Filtered Small-Angle Ultrasonic Computed Tomography Using Linear Arrays

Jianglei Chang, Aleksey Soldatov, Pavel Sorokin, Mariya Kostina, Andrey Soldatov, Shupeng Xu, and Anatoly Chiriev

Abstract This paper describes the use of the Gauss filter to improve the quality of the tomogram with the shadow method of ultrasonic testing. The use of a window with different parameters was investigated on a model and tested on experimental data, and its optimal size was determined. The simulation and experimental results are given for one and two reflectors located in the testing zone. The resolution of the system consisting of receiving and transmitting antenna arrays with 16 elements is determined.

J. Chang · A. Soldatov (✉) · P. Sorokin · M. Kostina · A. Soldatov · S. Xu
Electronic Engineering Division, School of Non-Destructive Testing, National Research Tomsk Polytechnic University, 30 Lenin Avenue, Tomsk, Russia 634050
e-mail: asoldatof@mail.ru

J. Chang
e-mail: vastchan@mail.ru

P. Sorokin
e-mail: spv2003@mail.ru

M. Kostina
e-mail: mashenkasoldatova@mail.ru

A. Soldatov
e-mail: Soldatov.88@bk.ru

S. Xu
e-mail: isxusp@gmail.com

A. Chiriev
General Surgery Department, Siberian State Medical University, 30 Moskovslii highway, Tomsk, Russia 634050
e-mail: Chiradoc@yandex.ru

A. Soldatov · M. Kostina · A. Soldatov
Innovation Management Department, Tomsk State University of Control Systems and Radioelectronics, 40 Lenin Avenue, Tomsk, Russia 634050

I. V. Minin et al. (eds.), *Progress in Material Science and Engineering*,
Studies in Systems, Decision and Control 351,
https://doi.org/10.1007/978-3-030-68103-6_3

1 Introduction

The shadow method has a higher sensitivity and noise immunity, and also has no dead zone, in comparison with the pulse echo method. This method is especially effective when testing multilayer structures, which are currently widely used in various fields of technology [1–3]. Traditionally, a pair of transducers is placed on both sides of the test object. When these transducers are used to scan objects, the shadow imaging of the internal structure of the scanning area can be obtained. In this way, the internal defects of the test object and the projection size of the defect on the receiving transducer can be detected. However, this method cannot determine the location coordinates of the defect. To solve this problem, a set of different angle projections can be used, which is widely used in X-ray tomography [4–6]. Since the 1970s, devices based on linear antenna arrays have also been developed, and tested [7, 8]. In many works, the shadow method has been studied, which aims to test rubber products. In this case, the transmitting and receiving linear antenna arrays are perpendicular to each other. This reconstructed image pixel is obtained at the intersection of the transmitting element and the receiving element. This method was further developed in bearing inspection. This method is used to detect burnt areas during bearing heat treatment. In the past few years, papers on small-angle ultrasonic tomography for controlling composite materials have been published [9–13]. The acoustic wave path is shown in Fig. 1.

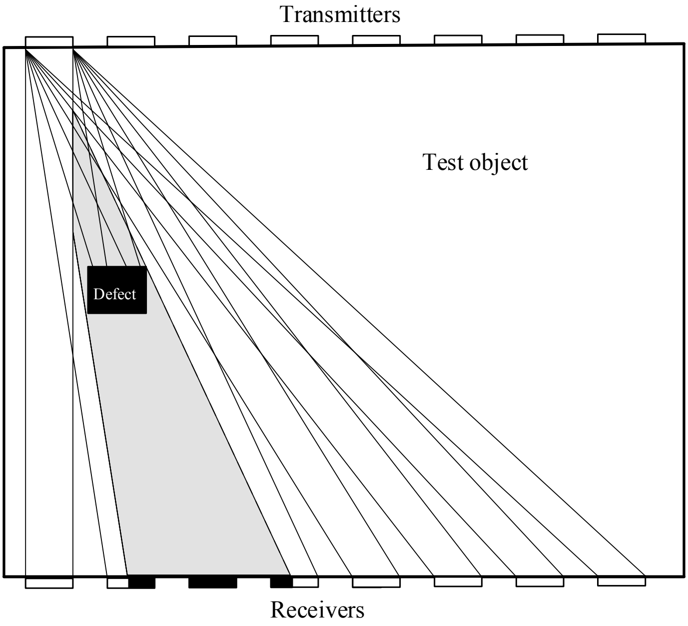

Fig. 1 Acoustic path of the test zone using shadow method

The tested object is located between the two ultrasonic receiving and transmitting arrays. The data matrix consists of m^2 measurement values, where m is the number of sensors in the linear array.

Detection of defects is determined by the coefficient k$_D$, which is determined by the ratio:

$$k_D = A_D/A_0 \tag{1}$$

where A_D is the amplitude of the acoustic signal at the receiver in the presence of a defect A_0 is the amplitude of the signal at the receiver in the absence of a defect.

For linear arrays, the coefficient is determined by the formula:

$$k_D = 1 - S_D/S \tag{2}$$

where S_D is the area of the acoustic shadow from the defect on the receiver; S is the area of receiver.

For a two-dimensional model, length is used instead of area. It can be seen from the figure that the first element of the receiving array is not in the acoustic shadow of the defect when the first element of the radiating array is probed. The second receiving element is partially located in the acoustic shadow, the size of which is equal to (S_D). The third element of the receiving array is completely in the acoustic shadow. The fourth element of the receiving array is partially in the acoustic shadow. Similarly, a shadow pattern of the defect is obtained on the plane of the receiving array for each element of the radiating array.

The algorithm for calculating of the coefficients k_D is shown in Fig. 2.

The reconstruction of tomogram consists of the following two stages. The first step is to obtain a data matrix from the receiving array. The second stage is the reconstruction of the tomogram based on these data [9, 10]. The shape of the defect is disc. The coordinate system is shown in Fig. 3.

According to the described algorithm (Fig. 3), a model was developed based on the MathCad software package. The simulation results are presented as a two-dimensional image, and the signal amplitude is color-coded (Fig. 4). To improve the image quality of the reconstructed test area, Gaussian filtering was applied. Specific Gaussian filtering operation uses convolution as shown in the following formula to scan each pixel in the image, and uses the weighted average of the pixels in the neighborhood defined to replace the central pixel.

$$(\mathrm{u}, \mathrm{v}) = \frac{1}{2\pi\sigma^2} e^{-(u^2+v^2)/(2\sigma^2)} \tag{3}$$

where u is the distance from the origin on the abscissa, v is the distance from the origin on the ordinate, and σ is the standard deviation of the Gaussian distribution, u and v are defined as the coordinate of the pixel with the maximum amplitude, σ is determined from the average amplitude around the maximum amplitude.

Fig. 2 Algorithm for calculating of the coefficients k_D in the presence of defects in the test zone

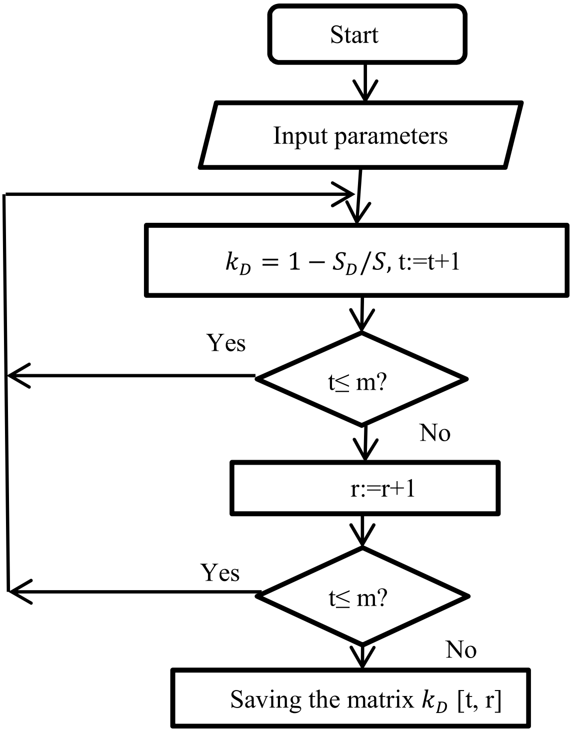

In Fig. 4 shows the simulation result. The simulation used a model of a disk-shaped defect with a radius of 3 mm. The coordinates and sizes of defects on the tomogram are determined automatically using a program written in MathCad, and its algorithm is shown in Fig. 3. It is difficult to determine the size and location of the defect from the initial data, so we apply Gaussian filtering.

After that, we have got a more focused image of the defect, which makes it possible to more accurately determine the coordinates and dimensions of the defect (Fig. 5).

In the range of 3σ distribution, the area of the defect is 99.7% of the total area, that is, 3σ < h, where h is the length of the test zone (in the presented example, $h = 160$).

The normal distribution function is:

$$f(x) = \frac{1}{\sigma\sqrt{2\pi}} e^{-(x-\mu)^2/(2\sigma^2)} \tag{4}$$

where μ is the mathematical expectation, x is the current coordinate, σ is the deviation from the mathematical expectation.

For x = μ, the Gauss function (4) is: $f(x)_{MAX} = \frac{1}{\sigma\sqrt{2\pi}}$.

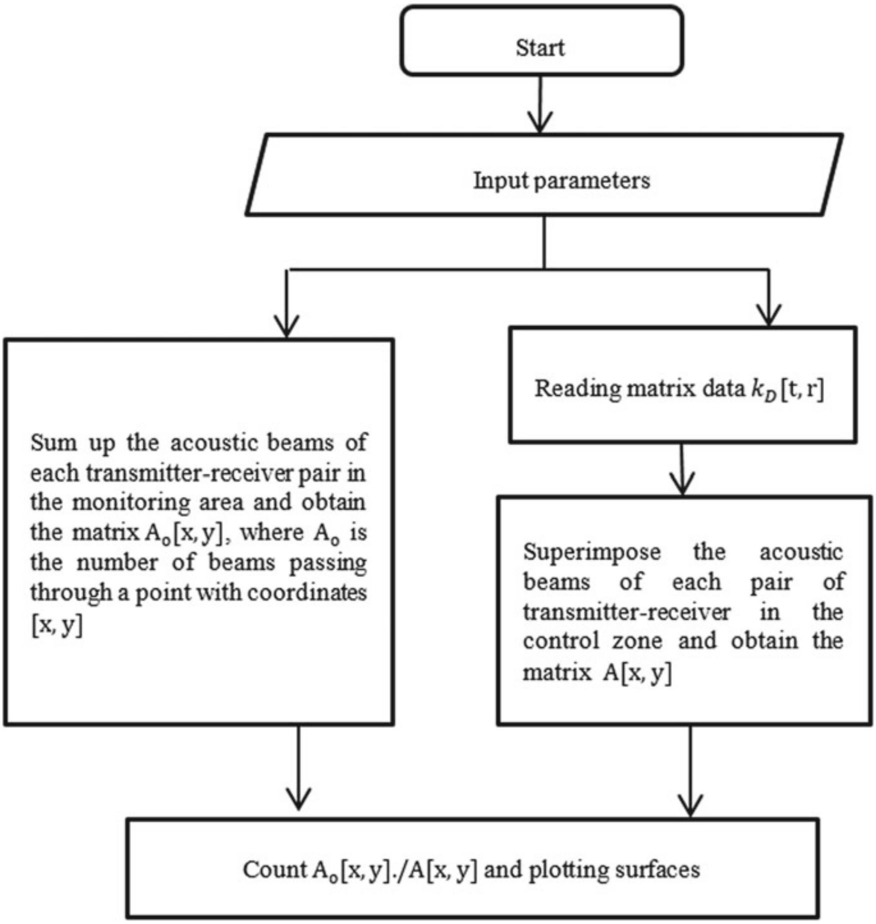

Fig. 3 Algorithm for reconstruction of the test zone

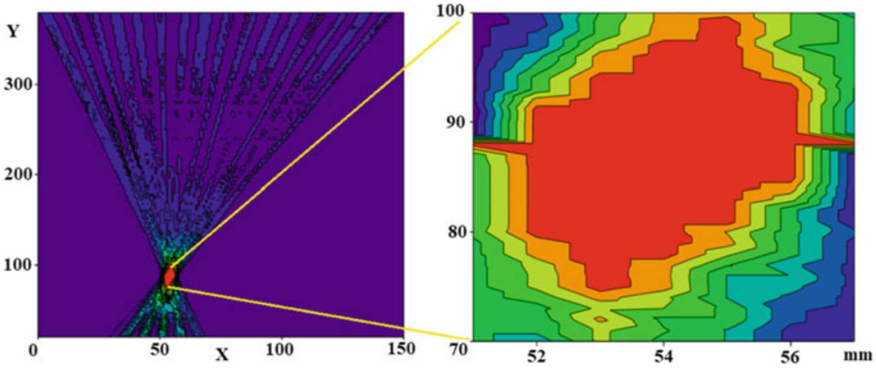

Fig. 4 The calculated result of the position of a defect with a radius of 3 mm

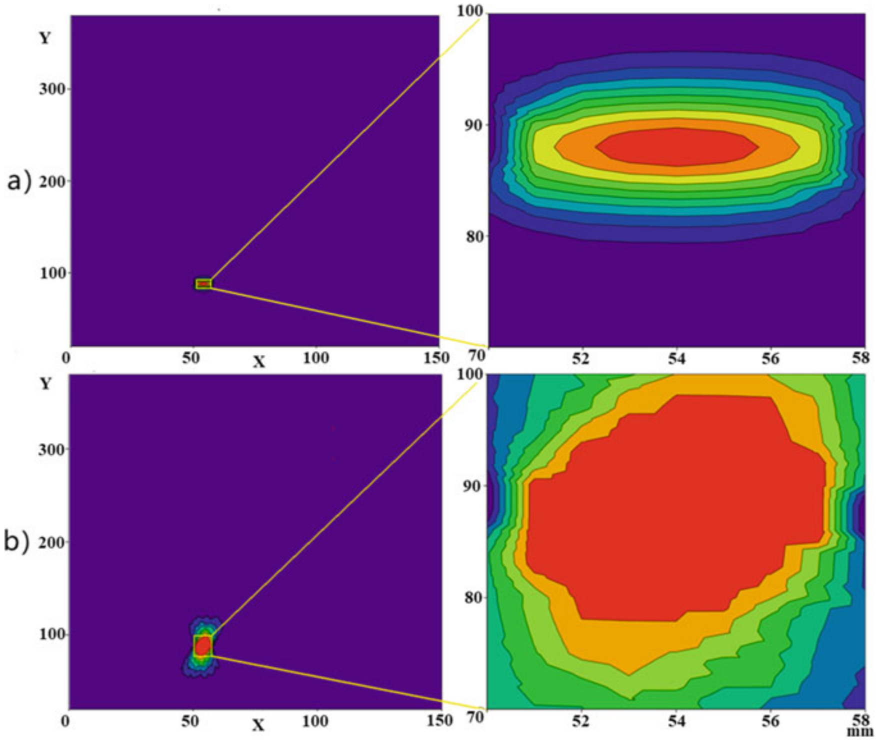

Fig. 5 The calculated result of the position of a defect after Gaussian filtration: **a** σ = 4; **b** σ = 20

For a relative filter coefficient: $\frac{f(x)}{f(x)_{MAX}} = \frac{\sqrt{2}}{2}$ we obtain the distribution of the radius equal to 0.833σ, that is, $0.833\sigma > \text{SEN}$ where SEN is the sensitivity (in the given example, SEN = $\lambda/2$).

Therefore $0.333\text{h} > \sigma > 0.6\lambda$. For the considered example h = 160, λ = 5 mm, we get $53.3 > \sigma > 3$.

This is the theoretical range of variation if the defect has the shape of a disk with a radius of 3.75 mm, that is, $0.833\sigma > 3.75$, we obtain $53.3 > \sigma > 4.5$.

Figure 5 shows that, when σ = 4.5, the dimensions of the reflector on the tomogram are very different from the real size. At the same time, when σ = 20, the effect of good filtration is achieved. Therefore, we chose σ = 20 for processing the experimental data.

2 Experimental Results

In the experimental setup, the emitting and receiving arrays were chosen to be the same, consisting of 16 circular piezoelectric elements 3 mm thick and 6 mm in

Fig. 6 Linear antenna arrays: 1—transmitter, 2—receiver

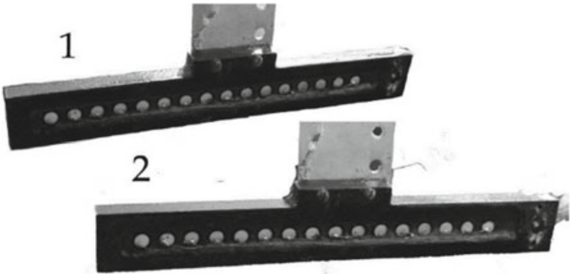

diameter (Fig. 6). The distance between the centers of adjacent piezoelectric elements is 10 mm.

These piezoelectric elements (Fig. 6) operate at a frequency of 300 kHz, at a temperature of 25 °C, the velocity of an elastic wave in a water is 1497 m/s. Radiation wavelength:

$$\lambda = \frac{v}{f} = \frac{1497\ \text{m/s}}{300\ \text{kHz}} = 5\ \text{mm}$$

The experimental setup contains an immersion bath and a system for moving antenna arrays fixed on the immersion bath (Fig. 7). One or two metal cylinders 50 mm long and 7.5 mm in diameter were used as defects.

A tomogram of the inspection area with one reflector is shown in Fig. 8.

Figure 8a shows a tomogram reconstructed from the initial data, and Fig. 8b—based on Gaussian filtering. From the result of theoretical analysis, we used σ = 20 to process the experimental data (Fig. 8b).

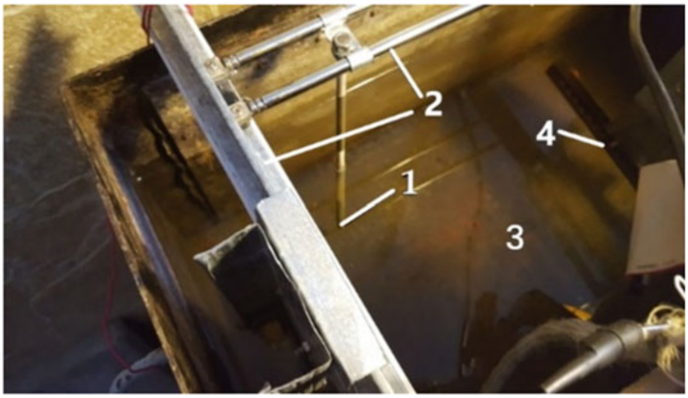

Fig. 7 Experimental setup: 1—defect, 2—travaling mechanism, 3—bath, 4—linear array

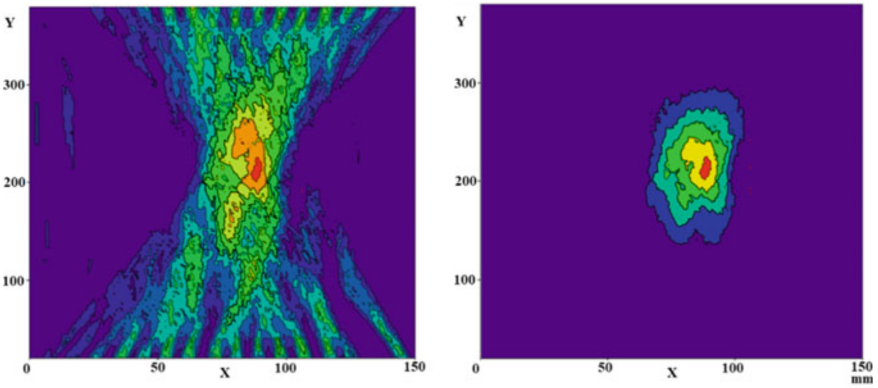

a) b)

Fig. 8 Tomogram of the test zone with one reflector, 7.5 mm in size: **a** initial data; **b** after Gaussian filtration

Table 1 Dependence of the error in determining the coordinates of the defect in different areas of the inspection zone

Distance between reflector and transmitter	40	60	80	100	120	140	160	200	240
Coordinate determination error (%)	11.3	9.7	6.8	8.4	7.7	6.4	3.5	4.3	5.2

Comparative analysis of Fig. 8 showed that the tomogram, reconsructed from the initial data (Fig. 8a), has a more blurred image compared to the tomogram after Gaussian filtering (Fig. 8b). Therefore, the coordinates of the reflector can be determined more accurately. The closer to the border of the test zone, will have the bigger error. The results of experimental studies to determine the coordinates of the reflector in different areas of the inspection zone are presented in Table 1.

It can be seen from the table that the closer reflector to the center of the test zone, the better result, and at a distance greater than 60 mm, the error does not exceed 10%.

Resolution is one of the main characteristics of testing method. An experimental study of the resolution of the ultrasonic flaw detector was carried out by placing two identical reflectors in different places of the test zone (Figs. 9 and 10). Figure 9 shows two reflectors spaced 12 mm apart. On both tomograms, both reflectors are clearly visible. Gaussian filtering of the initial data made it possible to reduce the level of noise in the test zone (Fig. 9b), which are observed on the initial data (Fig. 9a).

In the case of two reflectors, the sum of two Gaussian convolutions, which is used for data processing and the convolution kernel is determined through the coordinates of two pixels with the maximum amplitude, made it possible to obtain good results and improve the resolution.

In Fig. 10 shows the results of experimental studies of the resolution. It is impossible to detect two defects on a tomogram based on the initial data (Fig. 10a). After Gaussian filtering, two defects are detected separately, with a resolution of 12 mm with a 400 mm distance between arrays.

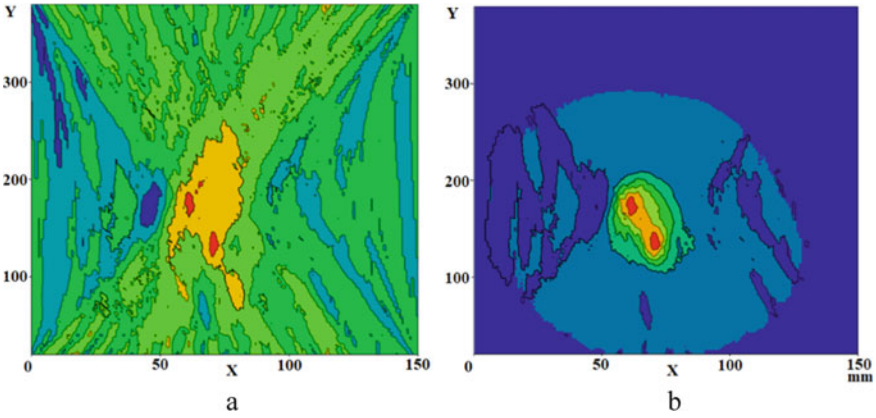

a b

Fig. 9 Tomogram of the test zone with two reflectors, 7.5 mm in size: **a** initial data; **b** after Gaussian filtering

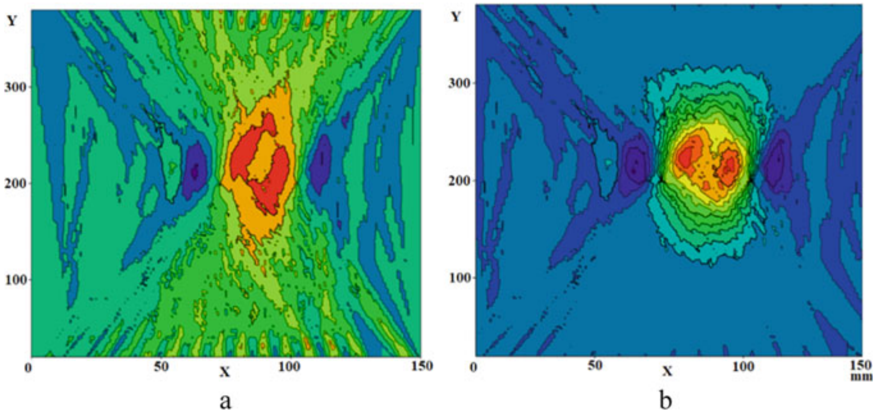

a b

Fig. 10 Tomogram of the test zone with two reflectors: **a** initial data; **b** after Gaussian filtering

3 Conclusions

This work presented a study of Gaussian filtering applied to ultrasonic computed tomography. The limits of changing the radius of the Gaussian filtering window have been determined, and when choosing the optimal window size, the proposed Gaussian filtering algorithm allows for increasing the resolution by about 10% and increasing the accuracy of determining the coordinates of the defect. In addition, Gaussian filtering can reduce noise.

References

1. Kak, A.C.: Principles of computerized tomographic imaging. Engineering (33.1), 327 (1988)
2. Amenabar, I., Mendikute, A., López-Arraiza, A., Lizaranzu, M., Aurrekoetxea, J.: Comparison and analysis of non-destructive testing techniques suitable for delamination inspection in wind turbine blades. Compos. B Eng. **42**(5), 1298–1305 (2011). https://doi.org/10.1016/j.compositesb.2011.01.025
3. Zhang, Y., Hong, H., Cai, W.: Photoacoustic imaging. Cold Spring Harb. Protoc. **6**(9), 1015–1025 (2011). https://doi.org/10.1101/pdb.top065508
4. Terzi, S., Daudin, R., Villanova, J., Srirangam, P., Lhuissier, P., Salvo, L., Boller, E., Schweins, R., Lindner, P., Blandin, J.-J., Lee, P., Lemmel, H.: X-ray tomography and small-angle neutron scattering characterization of nano-composites: static and in situ experiments. Light Metals **2014**(9781118889084), 1389–1393 (2014). https://doi.org/10.1002/9781118888438.ch232
5. Huang, H., Shu, D., Zeng, J., Bian, F., Fu, Y., Wang, J., Sun, B.: In situ small angle X-ray scattering investigation of ultrasound induced nucleation in a metallic alloy melt. Scripta Mater. **106**(9), 21–25 (2015). https://doi.org/10.1016/j.scriptamat.2015.04.011
6. Davis, T., Gao, D., Gureyev, T., Stevenson, A., Wilkins, S.: Phase contrast imaging of weakly absorbing materials using hard x-rays. Nature **373**(6515), 595–598 (1995). https://doi.org/10.1038/373595a0
7. Steiner, G., Wegleiter, H., Watzenig, D.: A dual mode ultrasound and electrical capacitance process tomography sensor. Sensors **2005**, 696–699 (2005). https://doi.org/10.1109/ICSENS.2005.1597794
8. Huang, S.-W., Li, P.-C.: Ultrasonic computed tomography reconstruction of the attenuation coefficient using a linear array. IEEE Trans. Ultrason. Ferroelectr. Freq. Control **52**(11), 2011–2022 (2005). https://doi.org/10.1109/TUFFC.2005.1561670
9. Medina-Valdes, L., Camacho, J., González-Salido, N., Cruza, J.F.: Resolution of image compounding with a ring array transducer. Phys. Procedia **63**, 141–146 (2015). https://doi.org/10.1016/j.phpro.2015.03.023
10. Nakagawa, Y., Nakagawa, M., Yoneyama, M., Kikuchi, M.: Nonlinear parameter imaging computed tomography by parametric acoustic array. IEEE Ultrasonics Sympos. **1984**, 673–676 (1984). https://doi.org/10.1109/ULTSYM.1984.198384
11. Dong, M., Ma, H., Chen, Y., Zhang, X., Cao, X.: Simulation of ultrasonic fields radiated by transducer through a wedge. Zhendong Yu Chongji/J. Vibr. Shock **36**(6), 152–156 (2017). https://doi.org/10.13465/j.cnki.jvs.2017.06.023
12. Chang, J., Soldatov, A. I., Abouellail, A. A., Soldatov, A. A., Obach I. I.: The resolution capability of the through-transmission method of testing of composites using linear array. In: Proceedings of the 2019 International Siberian Conference on Control and Communications (SIBCON 2019), 8729632 (2019). https://doi.org/10.1109/SIBCON.2019.8729632
13. Ahmed, S.R., Saka, M.: New ultrasonic angle-beam technique for sensitive evaluation of closed cracks. NDT E Int. **33**(4), 261–271 (2000). https://doi.org/10.1016/S0963-8695(99)00049-3

Inspection of Transformer Mechanical Integrity Using Sweep Frequency Response Method

Youssef Abouellail, Ahmed Abouellail, Aleksey Soldatov, and El-Saady Gaber

Abstract Power Transformers are the most critical and hig-hcost elements of power network systems. They play an essential role in power transmission to the users. They require continuous and regular monitoring and assessment, in order to increase the power supply reliability and to avoid hazardous breakdowns. The transformer is ordinarily exposed to high current surges in the course of service, mainly due to short circuit, which impacts the mechanical winding formation. The proposed a diagnostic technique, in this paper, performs a sweep frequency response analysis on the inspected transformer. Although it is considered a highly responsive and powerful inspection method, the critical challenge relies in the appropriate interpretation of the measured frequency response, which remains a gray zone left for professional experts to detect the type and location of defects. An experimental setup has been developed for the proposed testing technique and an analytical digital simulation of the built transformer is carried out. The simulation results could detect the defect type and its location in the transformer winding.

Y. Abouellail · E.-S. Gaber
Electrical Engineering Department, Faculty of Engineering, Assiut University, Assiut 71515, Egypt
e-mail: youssef.ali@eng.aun.edu.eg

E.-S. Gaber
e-mail: gaber.taha@eng.au.edu.eg

A. Abouellail · A. Soldatov (✉)
Electronic Engineering Division, School of Non-Destructive Testing, National Research Tomsk Polytechnic University, 30 Lenin Avenue, Tomsk, Russia 634050
e-mail: asoldatof@mail.ru

A. Abouellail
e-mail: demo092@tpu.ru

A. Soldatov
Innovation Management Department, Tomsk State University of Control Systems and Radioelectronics, 40 Lenin Avenue, Tomsk, Russia 634050

I. V. Minin et al. (eds.), *Progress in Material Science and Engineering*,
Studies in Systems, Decision and Control 351,
https://doi.org/10.1007/978-3-030-68103-6_4

1 Introduction

Sweep frequency response analysis (SFRA) technique measures the input impedance or the driving-point impedance (DPI) of transformer windings over a wide frequency range and compares the results with reference data and shows physical alterations [1]. The SFRA signature of the transformer is considered as a fingerprint, which helps in the detection of mechanical deformations [2]. However, the critical challenge in this method is to properly interpret the measured frequency response in the detection of the defect type, whether it is a radial or axial deformation [2–4]. This paper suggests a method of a genetic optimization algorithm to obtain a transformer equivalent circuit, based on a given direct measurement.

2 Experimental Setup and Results

The SFRA approach is known for its accuracy, and has several advantages over other inspection methods, such as the dissolved gas analysis method, reactance comparison method, and low voltage impulse method [1–5].

The configuration of the inspection setup is shown in Fig. 1, which is responsible of the measurement of the input voltage and output current to obtain input admittance or the driving point impedance (DPI) using an LCR meter [6].

When the DPI magnitude (Fig. 2) is maximum and the corresponding phase at the same frequency is zero (at an inverse from positive to negative), the certain frequencies in this peak can be called open-circuit natural frequencies (OCNF). When the DPI magnitude is at its minimum and the corresponding phase at the same

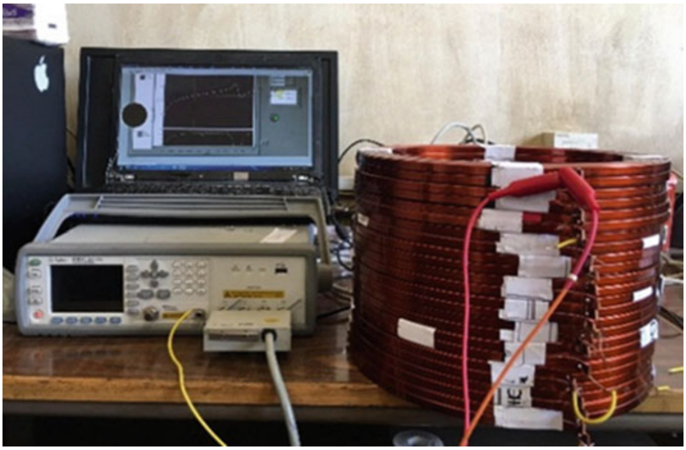

Fig. 1 LCR Meter obtaining magnitude and phase of the DPI of a single continuous winding transformer, response frequency from 20 Hz to 2 MHz

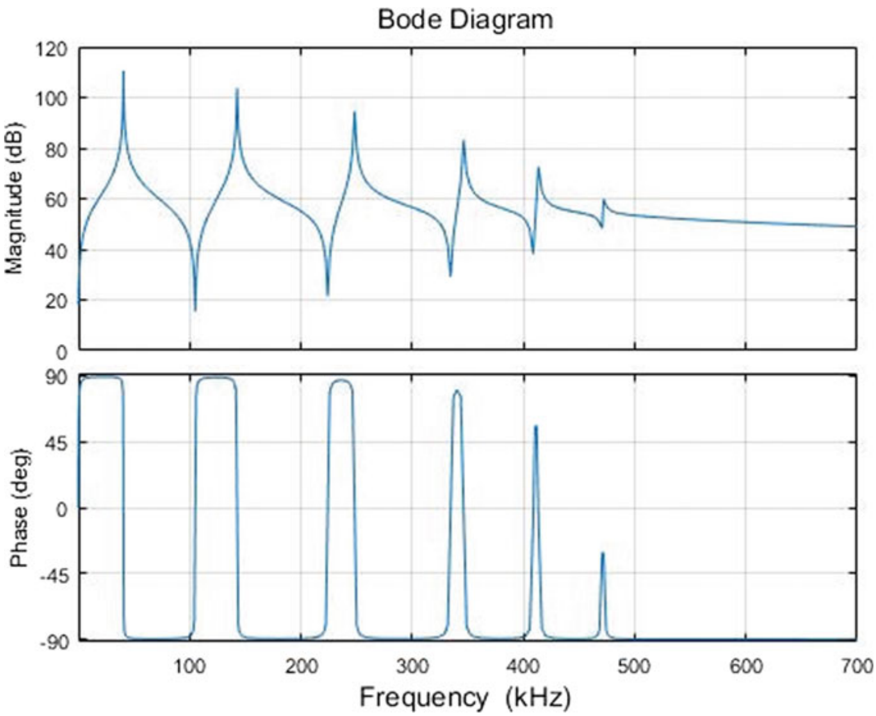

Fig. 2 Test results by the LCR meter showing magnitude and phase of the DPI

frequency is zero (at an inverse from negative to positive), the frequencies at these troughs can be called short-circuit natural frequencies (SCNF).

Determining OCNF as well as SCNF will help in forming pole-zero DPI-function [7]. The natural frequencies changes if the transformer mechanical integrity has been exposed to any harm [8].

3 Model of the Transformer Ladder Network

The transformer physical continuous winding can be symbolized by an electrical network, which consists of stray capacitance (C_s) between the conductor blocks, and ground capacitance (C_g) between conductors and ground, as shown in Fig. 3.

This network can be represented by an electrical circuit of serial discrete nodes, starting from the line end to the neutral end as shown in Fig. 4, where (l_s) is the self-inductance and in series with the conductor resistance, (r) while (m) is the mutual inductance between two discs (n) is the number of ladder network section which can be determined by the number of OCNFs [9].

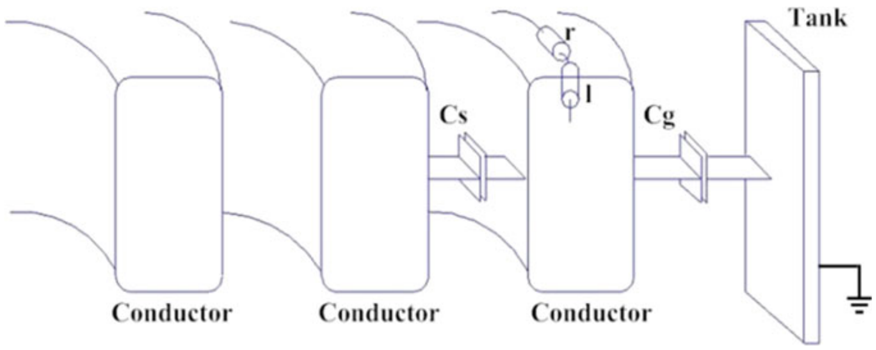

Fig. 3 Transformer windings represented by an electrical network

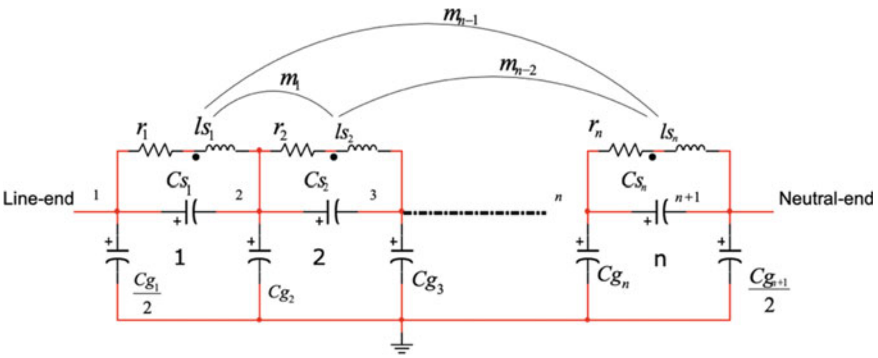

Fig. 4 Ladder network model with n network sections

4 Proposed Algorithm for Reference Ladder Network

The SFRA test in this research is performed on a discarded isolated high voltage winding in a transformer of a continuous winding design (phase: 3-φ, power capacity: 70 kVA, frequency: 25 Hz). The transformer winding is divided to nodes and it consists of 23 double-disks and 19 turns per disk.

Ladder network parameters can be determined by the proposed genetic algorithm (GA) following procedures in Fig. 5 [10–15].

Algorithm 1 At first, the following parameters are measured: DC resistance (R_{DC}) [7], equivalent air-core inductance (L_{eq})(Leq) [16], effective shunt capacitance to ground $\left(C_{g,eff}\right)$ [17]. Then SFR test is performed while neutral is grounded to obtain DPI. Hence, the value of OCNFs (q) and SCNFs ($q-1$) of the winding are determined by swept frequency measurements, and the number of sections (n) of the equivalent circuit is defined [7]:

$$n \leftarrow q \tag{1}$$

Fig. 5 Proposed operational genetic algorithm

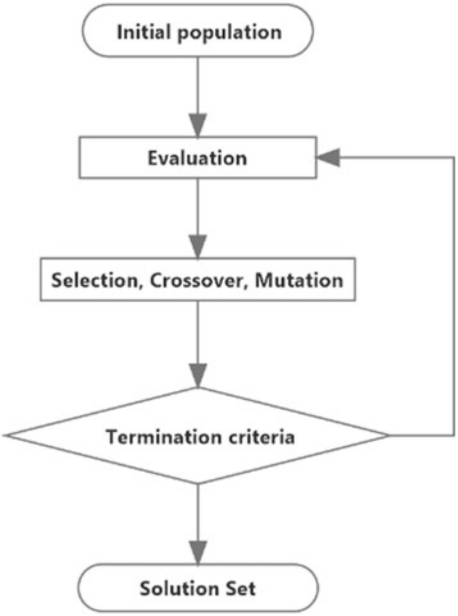

Resistance diagonal matrix $\left[R_{ref}\right]$ is built with diagonal element $\left(\frac{R_{DC}}{N}\right)$ [18]:

$$R(i, i) = r, \quad 1 \leq i \leq n \tag{2}$$

$$[R] = \begin{bmatrix} r_1 & 0 & \ldots & 0 \\ 0 & r_2 & \ldots & 0 \\ \vdots & \vdots & \ddots & \vdots \\ 0 & 0 & \ldots & r_n \end{bmatrix}$$

The search ranges of $(l_s, m_1, m_5, \ldots, m_{N-1})$ are decided considering the following constraints [18]:

$$0.3\frac{L_{eq}}{n} \leq l_s \leq 0.5\frac{L_{eq}}{n} \tag{3}$$

$$0.4l_s < m_1 < 0.8l_s \tag{4}$$

$$0.4m_{i-1} < m_i < 0.8m_{i-1}, \quad \forall i = 2, \ldots, n-1 \tag{5}$$

Inductance matrix $\left[L_{ref}\right]$ is, therefore, constructed:

$$\left[\boldsymbol{L_{ref}}\right] = \begin{bmatrix} \boldsymbol{l_1} & \boldsymbol{m_1} & \boldsymbol{m_2} & \ldots & \boldsymbol{m_n} \\ \boldsymbol{m_1} & \boldsymbol{l_2} & \boldsymbol{m_1} & \ldots & \boldsymbol{m_{n-1}} \\ \vdots & \vdots & \ddots & \ldots & \vdots \\ \boldsymbol{m_{n-1}} & \boldsymbol{m_{n-2}} & \boldsymbol{m_{n-3}} & \ddots & \vdots \\ \boldsymbol{m_n} & \boldsymbol{m_{n-1}} & \boldsymbol{m_{n-2}} & \ldots & \boldsymbol{l_n} \end{bmatrix} \tag{6}$$

The search range of C_s is calculated and the range of voltage distribution constant (α) is estimated from similar designs [7].

$$\boldsymbol{C_g = \frac{C_{g,eff}}{n}} \tag{7}$$

$$\boldsymbol{C_{s,min}} = \frac{\boldsymbol{N} \times \boldsymbol{C_{g,eff}}}{\boldsymbol{\alpha^2_{min}}}, \quad \boldsymbol{C_{s,max}} = \frac{\boldsymbol{N} \times \boldsymbol{C_{g,eff}}}{\boldsymbol{\alpha^2_{max}}} \tag{8}$$

Node capacitance matrix $\left[K_{ref}\right]$ is built as such:

$$\left[\boldsymbol{K_{ref}}\right] = \begin{bmatrix} \boldsymbol{C_{s_1}} + \frac{\boldsymbol{C_{g_1}}}{2} & -\boldsymbol{C_{s_1}} & \cdots & 0 \\ -\boldsymbol{C_{s_1}} & \boldsymbol{C_{s_1}} + \boldsymbol{C_{g_2}} + \boldsymbol{C_{s_2}} & \cdots & 0 \\ \vdots & \vdots & \vdots & \vdots \\ 0 & 0 & -\boldsymbol{C_{s_{n-1}}} & \boldsymbol{C_{s_{n-1,n}}} + \boldsymbol{C_{g_n}} + \boldsymbol{C_{s_n}} \end{bmatrix} \tag{9}$$

All of the aforementioned calculations are applied to the ladder network state space model. Winding parameter values can be obtained by GA in MATLAB, which produces highly correlated simulated DPI to the measured one by minimizing the GA objective function (OF) as in the next formula [11].

$$\boldsymbol{OF} = \frac{\sum_{i=0}^{P} \boldsymbol{w_i} \cdot \sqrt{\left[\frac{\boldsymbol{s_i} + \left(\frac{\boldsymbol{s_i}+\boldsymbol{r_i}}{2}\right)}{\frac{\boldsymbol{s_i}+\boldsymbol{r_i}}{2}}\right]^2 + \left[\frac{\boldsymbol{r_i} + \left(\frac{\boldsymbol{s_i}+\boldsymbol{r_i}}{2}\right)}{\frac{\boldsymbol{s_i}+\boldsymbol{r_i}}{2}}\right]^2}}{\sum_{i=0}^{P} \boldsymbol{w_i}} \tag{10}$$

where P is the number of points w_i is the weight factor of point i. r_i is the measured point and s_i is the simulated point.

5 Proposed Algorithm for Axial Deformation Detection

Single disk symmetrical uniformed axial deformation is detected in the transformer winding. This type of deformation dominantly alters mutual-inductance and ground capacitance of the symmetrical ladder network. Assuming that the space between two double-disks (upper and lower) increased after mapping winding disks to a number of nodes in the electrical circuit. The altered mutual inductance and ground capacitance parameters can be identified by the following functions:

$$\dot{\boldsymbol{M}} = \sum_{i=1}^{k} \sum_{j=k+1}^{n} \boldsymbol{m}_{i,j}, \boldsymbol{m}_{j,i} \tag{11}$$

$$\dot{\boldsymbol{C}}_{g} = \boldsymbol{C}_{g_{k+1}} + \boldsymbol{C}_{g_{k+2}} \tag{12}$$

where (k) is the upper-node number in the electrical circuit, (n) is the number of sections, $(\dot{M})$ defines the altered mutual inductance parameters,$\left(m_{i,j}, m_{ji}\right)$ is the altered mutual inductance between node (i) and node (j), and $(C_g))$ is the altered ground capacitance [19, 20].

The proposed diagnostic method will identify which node has been altered and to what extent the axial deformation has occurred.

Algorithm 2 The reference ladder network circuit is prepared in order to compare it to the altered ladder network, which will be calculated, and all the measuring procedures that have been mentioned in the reference ladder network algorithm will be repeated after a uniform axial deformation is introduced to one of the transformer double-disk continuous windings.

The defected mutual inductance parameters are identified for all axial deformation cases for disk $i = 1 : n$ and inductance matrix (n) is reconstructed considering all cases, so that the identified defected mutual-inductance is multiplied into axial deformation coefficient (γ), which is figured out by GA estimation, will be less than 1, when the distance between the two disks increases, and greater than 1, if the distance decreases.

The identification the defected two ground capacitance parameters in $\left[K_{ref}\right]$ is estimated using GA. GA minimum objective function of all (n) ladder networks is found.

Different values for ladder network parameters are calculated, although they are not physically capable of detecting the defect, which occurs to the transformer [11]. Therefore, this diagnostic algorithm will help in the flaw detection weather the transformer winding has exposed to an axial deformation or not.

6 Case Study and Simulation

Two cases will be discussed in detail. Case A is a reference model circuit and Case B is the axial deformation circuit.

Case A: Reference Ladder Network Circuit

In this case, the reference circuit model is built based on terminal measurement of some quantities such as DC resistance, equivalent air-core inductance, ground effective shunt capacitance, natural frequencies from DPI, and initial voltage distribution

Table 1 Calculated values of the reference model parameters

Parameters	GA limit		GA estimation
	Lower	Upper	
l_s	0.42817	0.434041	0.4297
m_1	0.22875	0.234617	0.2341
m_2	0.14077	0.146635	0.1421
m_3	0.08798	0.093846	0.0898
m_4	0.05572	0.061586	0.0604
m_5	0.04692	0.052788	0.0469
C_s	0.149	8.5	0.5976

constant for similar designs, assuming all the self-inductances (L_s), mutual inductances of (M_{ji}) and (M_{ij}), ground capacitance (C_g) and series capacitance (C_s) are identical.

Based on the previously mentioned measurement procedure, the following results have been achieved.

$$R_{DC} = 8\ \Omega, \quad L_{eq} = 6.98\ \text{mH}, \quad C_{g,eff} = 5.6\ \text{nF}, \quad \alpha_{max,min} = 5 : 15 \tag{13}$$

$$C_{s_{min}} = 0.149\ \text{nF}, \quad C_{s_{max}} = 8.4\ \text{nF} \tag{14}$$

The GA variables of upper and lower limits have been arranged in Table 1, which indicates self and mutual-inductances and stray capacitances.

From the GA parameter calculated values in Table 1, as well as the parameters that have been determined by reference measurement values in formulas (13) and (14), an estimated DPI plot (dotted line) is produced nearly same as actual DPI plot (solid line) with best fit value 0.0193 with only the last resonance missing in Fig. 6.

Case B: Axial Deformation Ladder Network

The introduced axial deformation flaws affect Node 2 and Node 3 of the 6-node ladder network circuit. For $k = 2$, the affected mutual inductances is $\dot{M} = M_{23}, M_{32}, M_{24}, M_{42}, M_{25}, M_{52}, M_{26}, M_{62}, M_{13}, M_{31}, M_{14}, M_{41}, M_{15}, M_{51}, M_{16}, M_{61}$. The algorithm proposes the minimum GA objective function error of all 5 axial deformation cases for any two consecutive nodes ($n_1 - n_2, n_2 - n_3, n_3 - n_4, n_4 - n_5, n_5 - n_6$) with their effected mutual inductance multiplied by γ, as well as the effected capacitance for each certain axial location. ($n_2 - n_3$) has the lest objective function error in Table 2, which produces the most correlated frequency response for the measured axial deformed winding as shown in Fig. 7.

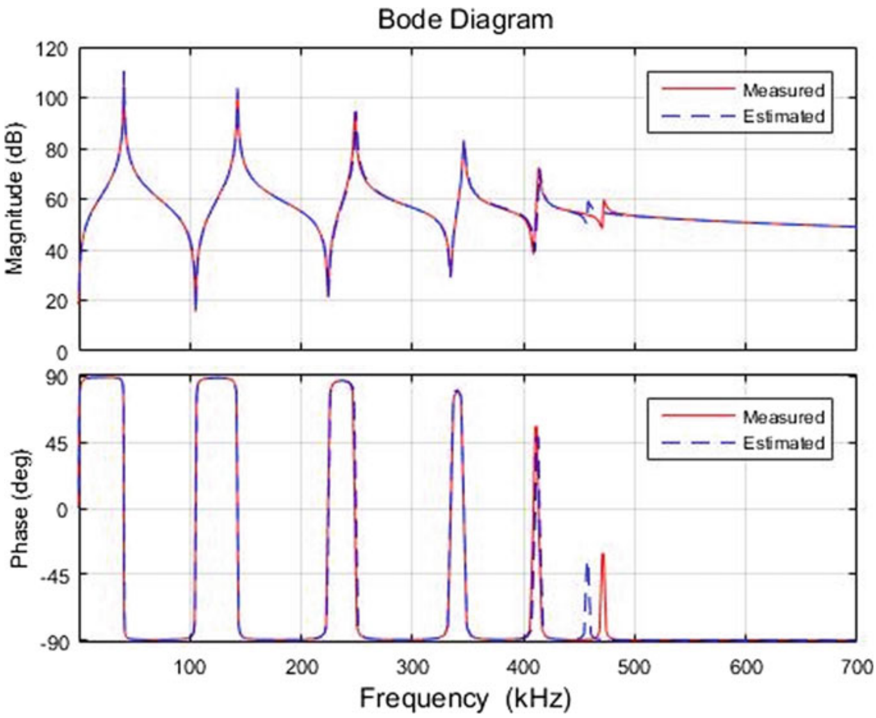

Fig. 6 Comparison of actual magnitude and phase of DPI to those of the GA ladder network

Table 2 Objective function error of all possible axial deformation locations

Axial location	Objective function	Axial location	Objective function
$n_1 - n_2$	0.056	$n_4 - n_5$	0.050
$n_2 - n_3$	6.328E−4	$n_5 - n_6$	0.040
$n_3 - n_4$	0.030		

7 Conclusion

GA is proceeded by the acquired reference measurement to obtain transformer reference circuit model. With the help of objective function, the variables such as mutual-inductances, series-capacitance are estimated. Furthermore, the GA localizes and diagnoses axial deformations by detecting the node number of the defect with the help of the ladder network reference. The proposed GA calculated parameters are approximately equal to both, the actual reference and deformation ladder networks with minimal error.

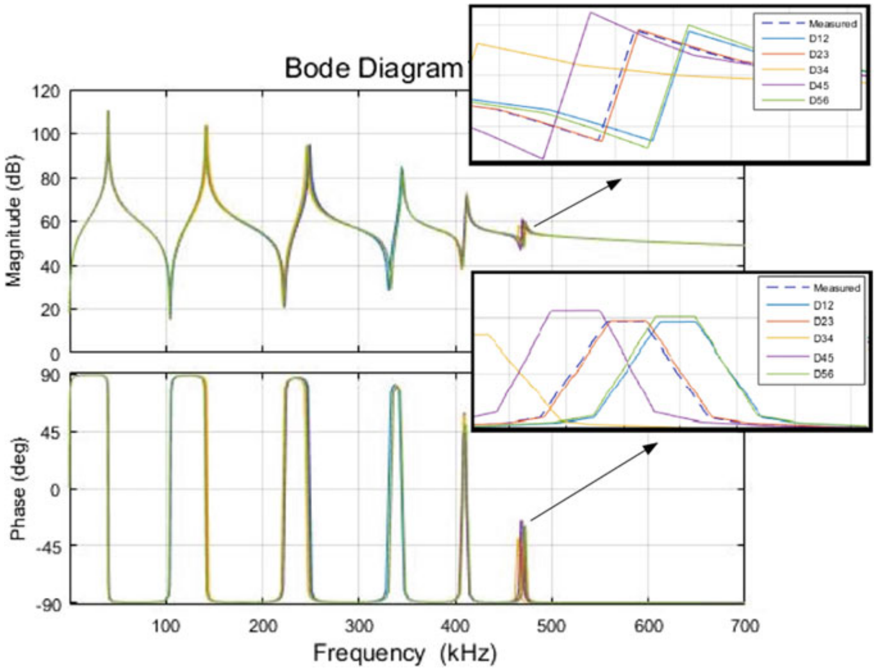

Fig. 7 Comparison of actual axial magnitude and phase of DPI to those of the GA ladder network

References

1. Dick, E.P., Erven, C.C.: Transformer diagnostic testing by frequuency response analysis. IEEE Trans. Power Apparatus Syst. **PAS-97**(6), 2144–2153 (1978). https://doi.org/10.1109/TPAS.1978.354718
2. Hashemnia, N. et al.: Characterization of transformer FRA signature under various winding faults. In: IEEE International Conference on Condition Monitoring and Diagnosis, pp. 446–449 (2012). https://doi.org/10.1109/CMD.2012.6416174
3. Zhao, X., et al.: Toward reliable interpretation of power transformer sweep frequency impedance signatures: experimental analysis. IEEE Electr. Insul. Mag. **34**(2), 40–51 (2018). https://doi.org/10.1109/MEI.2018.8300443
4. Gite, P., Sindekar, A.: Interpretation of sweep frequency response data (SFRA) using graphical and statistical technique. In: Proceedings of the International conference of Electronics, Communication and Aerospace Technology (ICECA), pp. 251–255, Jan 2017. https://doi.org/10.1109/ICECA.2017.8212810
5. Patil, S.S., Chaudhari, S.E.: An attempt to investigate the transformer failure by using DGA and SFRA analysis. In: Proceedings of the IEEE International Conference on the Properties and Applications of Dielectric Materials, 6318985 (2012). https://doi.org/10.1109/ICPADM.2012.6318985
6. Jayasinghe, J.A.S.B., et al.: Winding movement in power transformers: a comparison of FRA measurement connection methods. IEEE Trans. Dielectr. Electr. Insul. **13**(6), 1342–1349 (2006). https://doi.org/10.1109/TDEI.2006.258206

7. Ragavan, K., Satish, L.: Localization of changes in a model winding based on terminal measurements: Experimental study. IEEE Trans. Power Delivery **22**(3), 1557–1565 (2007). https://doi.org/10.1109/TPWRD.2006.886789
8. Tenbohlen, S., et al.: Diagnostic measurements for power transformers. Energies **9**(5), 347 (2016). https://doi.org/10.1109/TPWRD.2006.886789
9. Ragavan, K., Satish, L.: Construction of physically realizable driving-point function from measured frequency response data on a model winding. IEEE Trans. Power Delivery **23**(2), 760–767 (2008). https://doi.org/10.1109/TPWRD.2008.915815
10. Man, K.-F., Tang, K.S., Kwong, S.: Genetic algorithms: concepts and applications. IEEE Trans. Industr. Electron. **43**(5), 519–534 (1996). https://doi.org/10.1109/41.538609
11. Shabestary, M.M., et al.: Ladder network parameters determination considering nondominant resonances of the transformer winding. IEEE Trans. Power Delivery **29**(1), 108–117 (2014). https://doi.org/10.1109/TPWRD.2013.2278784
12. Prajapati, N., et al.: Driving-point impedance and particle swarm optimization based circuit synthesis of power transformer winding. In: Proceedings of the 3rd International Conference for Convergence in Technology (I2CT), 8529508 (2018). https://doi.org/10.1109/I2CT.2018.8529508
13. Rajendra, S.K., Ragavan, K.: Locating mechanical deformations in electromagnetic model of transformer winding. In: Proceedings of the Eighteenth National Power Systems Conference (NPSC). 7103783 (2014). https://doi.org/10.1109/NPSC.2014.7103783
14. Patel, S. et al.: Utilising genetic algorithm and driving point impedance data to synthesize high frequency circuit model of power transformer winding. In: Proceedings of the 5th International Conference on Signal Processing and Integrated Networks (SPIN), 407–412 (2018). https://doi.org/10.1109/SPIN.2018.8474058
15. Ren, F., et al.: Ladder network parameters identification of an isolated winding by combining the intelligent optimisation algorithm and GNIA. IET Gener. Transm. Distrib. **13**(2), 296–304 (2018). https://doi.org/10.1049/iet-gtd.2018.6414
16. Mukherjee, P., Satish, L.: Estimating the equivalent air-cored inductance of transformer winding from measured FRA. IEEE Trans. Power Delivery **33**(4), 1620–1627 (2017). https://doi.org/10.1109/TPWRD.2017.2735627
17. Shah, K., Ragavan, K.: Estimation of transformer winding capacitances through frequency response analysis–an experimental investigation. Int. J. Emerg. Electr. Power Syst. **14**(6), 549–559 (2013). https://doi.org/10.1515/ijeeps-2013-0098
18. Satish, L., Sahoo, S.K.: Locating faults in a transformer winding: an experimental study. Electric Power Syst. Res. **79**(1), 89–97 (2009). https://doi.org/10.1016/j.epsr.2008.05.020
19. Mukherjee, P., Satish, L.: Construction of equivalent circuit of a transformer winding from driving-point impedance function–analytical approach. IET Electr. Power Appl. **6**(3), 172–180 (2012). https://doi.org/10.1049/iet-epa.2011.0150
20. Mukherjee, P., Satish, L.: Diagnosing axial displacement in an actual, single, isolated transformer winding: experimental results. IEEE Trans. Dielectr. Electr. Insul. **24**(2), 1280–1287 (2017). https://doi.org/10.1109/TDEI.2017.006211

Detection of Damages in Electrically Dead Power Lines

Victor Sergeev, Vladislav Yurchenko, Galina Vavilova, Michael Belik, and Pavel Bezkorovainy

Abstract The analysis of damages at power lines has been carried out. The tasks of power lines status monitoring have been determined. The solving techniques of tasks in hand have been proposed. The proposed monitoring system will let quickly detect and locate damages at power lines. The system technical requirements have been quoted. The characteristics of reflectometer REIS-105 have been considered. Test results have been quoted.

1 Introduction

The ever-increasing competition in the field of energy supply leads to increased consumer requirements for the quality and reliability of electricity supply from the manufacturer and distributor of electricity flows. At the same time, outdated equipment is still used for power supply in Kazakhstan and Russia. The most unreliable part of electric power supply equipment is overhead power transmission lines. However,

---

V. Sergeev · V. Yurchenko · M. Belik
Department of Information Technology and Security, Karaganda Technical University,
56 Nursultan Nazarbayev Avenue, 100027 Karaganda, Republic of Kazakhstan
e-mail: vitya.sergeev.56@mail.ru

V. Yurchenko
e-mail: jurchenkovv@mail.ru

M. Belik
e-mail: m_belik@inbox.ru

G. Vavilova (✉)
Division for Testing and Diagnostics, National Research Tomsk Polytechnic University,
30 Lenin Avenue, Tomsk, Russia 634050
e-mail: wgw@tpu.ru

P. Bezkorovainy
Department of Mechanics, Karaganda Technical University, 56 Nursultan Nazarbayev Avenue,
Karaganda, Republic of Kazakhstan 100027
e-mail: bpg82_karlion@mail.ru

I. V. Minin et al. (eds.), *Progress in Material Science and Engineering*,
Studies in Systems, Decision and Control 351,
https://doi.org/10.1007/978-3-030-68103-6_5

they are the main element of the transmission of energy and in addition they cover vast territories both in Kazakhstan and Russia.

On this basis automatic control of power lines condition monitoring including damage is a critical task facing the designers and operators of modern power transmission lines [1, 2]. The greatest number of damages is due to wire breakage and a short circuit which usually occurs due to adverse weather conditions as well as unapproved dismantling of wires.

Wirebreaks due atmospheric forcing include coating of ice, breakages of power transmission line pole and breaks caused by broken tree limbs. In addition, when ice and hoarfrost appears on the wires functional failure of high-frequency carrier is possible and the signals from the automatic control of emergency situations and relay protection may be incorrectly encoded, incorrect transmission of technological information or its absence is possible [3–5].

Unapproved removal of wires accomplish through creating an artificial short circuit and electric transmission line cut-off from electrical power supply system or already electrically dead power line during fault clearance.

For technical control it is necessary to develop an operational control automated method of the appearance of ice coating on the wires with the ability to work remotely with sufficient sensitivity and reliability herewith an especially dedicated communication channel was not needed to transmit information and command signals to the control room. This method should maintain control of breaks absence in these power lines in case of a power outage on the power line wires [6–8].

The tasks that need to be solved to create this method are as follows [9–11]:

- to find the dependence of the delay period and changes in the signal amplitude in the form of reflected pulses during sounding by the power line location method on the thickness and length of ice accretion on the power transmission lines;
- to find support points that define the transmission lines obstacles such as high frequency shields, cable inserts, connection points to branch lines and other elements;
- to find responses to the transmission lines obstacles having both active and reactive characteristics when conducting a location by applying pulses;
- to create a technique for decoding the response when impulses are applied during sounding for real power lines;
- to develop a subsystem that implements the method of operational detection of various types of ice on power lines.

One of the ways to find the location of the area with a malfunction is a method of control using location and consists in the fact that the temperature of the wires is indirectly determined by the load current, temperature and the speed of air movement, and thus it is possible to find both wire breakage and short circuit [12].

Probing by the location method allows in a timely manner with high quality with a high degree of reliability and sensitivity not only to detect ice on the power lines but also to ensure the prompt organization of ice removal by the melting method. It also becomes possible to carry out operational control of short circuits and breaks on power lines which reduces the time for non-supply of electricity to consumers, quickly respond to possible actions for unauthorized removal of wires which reduces the material and financial costs of energy supplying organizations for emergency recovery work and for consumers for possible downtime.

Tools providing direct or indirect measurement of live parts temperature allow to prevent cases of vandalism and can be mounted on the section of a power transmission line passing through the substation territory near the connection point of the communication capacitors.

One of the effective principles of telemechanics is the "one - N" principle when use of the location method makes it possible using a commutation switch from a substation to connect all branch power transmission lines to reflection-coefficient meter and by the same one equipment at short intervals determine the presence of ice-coated occurrence or damage such as a short circuit or a break.

Costs of the probing system using the location method required to rime ice control is significantly less than the cost of the telemetry equipment used at present which is used to determine ice-coated occurrence. Moreover, the economic efficiency is the more significant the more power lines that are connected to the substation will be controlled by a location device complete with a commutation switch.

Thereby main technical requirements for the system are suggested:

(1) Structure requirements:
    Functional structure of the equipment can be represented following manner: high-voltage connection unit and line monitoring unit.
    High-voltage connection unit should be made as communication condensers for corresponding voltage and having external design.
    High-voltage connection unit should be intended for voltage limiting supplied to the control unit when the line is running and to supply control voltage to deenergized line.
    Line monitoring unit should be made as device controlling rate of change of electrical parameters of a de-energized 3-phase power line in order to determine short circuit of wires around each other or to ground [13].
(2) Technical characteristics requirements:
    It is known that electrical parameters of power transmission lines can be fluently vary during the day depending on environment temperature and humidity changes. Abrupt parameters changes can be caused by wire tangles caused by wind or by special jumpers for disabling line in order to quickly remove wires.
    Considering the foregoing main technical requirements that should apply to specific line monitoring equipment has been given in Table 1:
(3) Requirements of performed functions:

Equipment of location method for ice coating detection should be digital suitable for placing it in substation premises [10].

The equipment should generate following remote signaling signals:

- high voltage on power lines;
- equipment turning on in line monitoring mode;

Table 1 Technical characteristics of the line monitoring equipment

	Name of parameter	Normal value
1	Version	General purpose industrial
2	Level and type of ambient impact protection	JP 43
3	Number of monitored lines, at most	1
4	Number of wires in the line, at most	3
5	Minimum length of electric transmission line, at least, km	3
6	Maximum length of electric transmission line, at most, (km)	30
7	Electric transmission line voltage, at most (kV)	35
8	Line monitoring equipment supply voltage (V)	220 ± 15%
9	Number of output signals	3 remote signaling

- alarm at wire breakage, line or one line wire is shorted to ground, short circuit of wires around each other;
- presence ice coating on wires.

The equipment should generate following remote-control signal:

- activation of antiicing mode for wires.

These signals should be transmitted over telemechanics or other transmission systems (GSM or otherwise) to control center for control. When condition monitoring of power transmission lines it can be used Russian-manufactured digital reflectometers REIS-105P and REIS-205. These reflectometers have a sufficiently high sensitivity to record ice and frost deposits on conductive lines with a thickness of 5 mm or more, with a section with ice of 3% of the total length of the wires.

Reflectometers are connected to monitored power transmission lines with a voltage of 6–10 kV when they are de-energized with a piece of cable or two-wire line up to 200 m long, in order to enable the passage of location pulses with a duration of 0.3 μs and more [14, 15].

If the line is under a voltage of 6–10 kV then the reflectometer is connected through an industrial filter with a bandwidth from 400 to 900 kHz which ensures the passage of probing pulses with a length of 1 μs. Industrial filters used to carry out probing by the pulsed method should be tuned to a stop band of at least 400–900 kHz.

The new generation of impulse reflectometers is represented by the portable digital reflectometer REIS which was created by STELL for the purpose of using it in practical power engineering to detect damage and diagnose power cable lines as well as communication lines, power transmission, monitoring and control of all types. For use in the production and transmission of electricity they can be used instead of a significant number of obsolete reflectometers, for example, uniformity tester P5-10, P5-13 and P5-17.

All information from the memory of the REIS-105 M1 device can be quickly transferred to the computer memory via this interface. And then the necessary information is registered in the computer in the database which can be sorted, supplemented and saved in the form of reflectograms “library” of the lines serviced in due time. It is possible to transfer back to the device from the computer.

The formed data “library” of serviced lines ensures the promptness of finding the place of incorrect functioning by comparing data characterizing parameters of damage with information about the same line located in the “library"[16]. In addition it is possible to automatically calibrate the device by comparing data from the “library” all other things being equal.

For information exchange and the ability to work with a computer the REIS -105M1 device is supplied with software, in particular REID -7.

2 Results

Tests of experimental prototypes of power lines monitoring equipment were carried out in accordance with the program and methodology for preliminary tests of lines monitoring equipment at feeder No. 8 of the “Reproductor” substation, Kurlus settlement, Karaganda region.

The line control unit (LCU) of power lines monitoring equipment was installed in the substation premises. Instead of high-voltage connection unit a simulator was used which consist of LCU -3 type capacitors, it also installed in the substation premises.

The line control unit was connected to the power line and supply voltage of 220 V in accordance with the diagram shown in Fig. 1.

Tests were carried out on a de-energized power line. The signal level on receive line of LCU was additionally monitored by an oscilloscope (marked “H”).

The following types of damage were produced at the object:

1. Power line break at “Reproductor” substation. The break was made by removing wire from the line to the coupling capacitor.

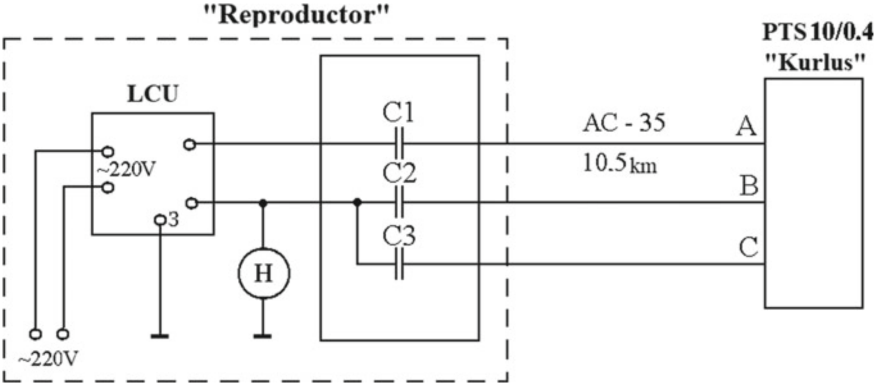

Fig. 1 Connection diagram of line control unit to power line

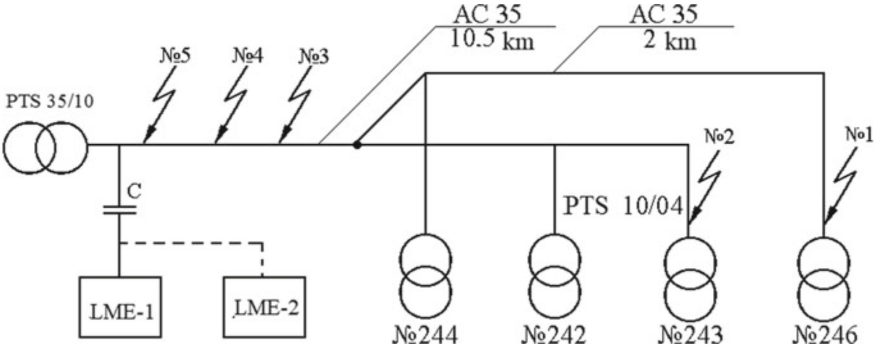

Fig. 2 Connection diagram

2. Closure of any phases pair with each other or all phases together at the “Reproductor” substation.
3. Closure of one phase or any phases pair to ground or all phases to ground at the “Reproductor” substation.
4. Closure of any phases pair or all phases to each other on buses of PTS 10/0.4 “Kurlus".
5. Closure of one phase or any phases pair to ground or all phases to ground on buses of PTS 10/0.4 “Kurlus".
6. Disconnection or connection of PTS 10/0.4 “Kurlus”.

Feeder No. 8 of the “Reproductor” substation feeds four package transformer substation (PTS) supplying Kurlus settlement with electricity as shown in Fig. 2.

3 Conclusion

The tests were carried out with two sets of line monitoring equipment. According to the test results following conclusions were made.

The tests were carried out without use of reflectometers but based upon their characteristics it is possible to use them for monitoring power lines in winter and summer conditions.

The considered monitoring system provides timely identification of damage type and location such as a short circuit and an open circuit from one control point - an electrical substation in addition it allows to suppress possible cases of vandalism, including unauthorized removal of wires [17].

The use of the proposed control method makes it possible to reduce the likelihood of the most severe, so-called ice-coated accidents, and thereby increase the reliability of power supply to enterprises and the population, as well as reduce the costs of restoring and repairing power lines.

References

1. Shaban, H.A., Seeber, A.: Monitoring global chromatin dynamics in response to DNA damage. Mutation Res. Fundamental Mol. Mech Mutagenesis **821**, 111707 (2020). https://doi.org/10.1016/j.mrfmmm.2020.111707
2. Maurel, V., Guipont, V., Theveneau, M., et al.: Thermal cycling damage monitoring of thermal barrier coating assisted with LASAT (LAser Shock Adhesion Test). Surf. Coat. Technol. **380**, 125048 (2019). https://doi.org/10.1016/j.surfcoat.2019.125048
3. Aggarwal, R.K., Johns, A.T., Jayasinghe, J.A.S.B., Su, W.: An overview of the condition monitoring of overhead line. Electric Power Syst. Res. **53**(1), 15–22 (2000). https://doi.org/10.1016/S0378-7796(99)00037-1
4. Lévesque, F., Goudreau, S., Cloutier, L., Cardou, A.: Finite element model of the contact between a vibrating conductor and a suspension clamp. Tribol. Int. **44**(9), 1014–1023 (2011). https://doi.org/10.1016/j.triboint.2011.04.006
5. Venkatasubramanian, V.: Process fault detection and diagnosis: past, present and future. IFAC Proc. **34**(27), 1–13 (2001). https://doi.org/10.1016/S1474-6670(17)33563-2
6. Ferreira, E.F., Barros, J.D.: Faults monitoring system in the electric power grid of medium voltage. Procedia Comput. Sci. **130**, 696–703 (2018). https://doi.org/10.1016/j.procs.2018.04.123
7. Kim, J.-D., Lee, J.-H., Ham, Y.-K. et al.: Sensor-Ball system based on IEEE 1451 for monitoring the condition of power transmission lines. Sens. Actuators, A: Phys. **154**(1), 157–168 (2009). https://doi.org/10.1016/j.sna.2009.06.009
8. Nizhegorodov, A.I., Gavrilin, A.N., Moyzes, B.B.: Application and production technology of thermal activation products of serpentine minerals from industrial wastes. Bull. Tomsk Polytechnic Univ. Geo Assets Eng **329**(5), 67–75 (2018)
9. Parsi, M., Crossley, P., Dragotti, P.L., Cole, D.: Wavelet based fault location on power transmission lines using real-world travelling wave data. Electric Power Syst. Res. **186**, 106261 (2020). https://doi.org/10.1016/j.epsr.2020.106261
10. Abu-Siada, A., Mir, S.: A new on-line technique to identify fault location within long transmission lines. Eng. Failure Anal. **105**, 52–64 (2019). https://doi.org/10.1016/j.engfailanal.2019.06.071
11. Vavilova, G.V., Gol'dshtein, A.E.: Instrument for in-process control of capacitance per unit length of an electrical wire. Meas. Tech. **61**(3), 278–283 (2018). https://doi.org/10.1007/s11018-018-1421-6
12. Hussain, S., Osman, A.H.: Fault location on series and shunt compensated lines using unsynchronized measurements. Electric Power Syst. Res. **116**, 166–173 (2014). https://doi.org/10.1016/j.epsr.2014.06.003
13. Jianwen, Z., Hui, H., Yu, G., et al.: Single-phase ground fault location method for distribution network based on traveling wave time-frequency characteristics. Electric Power Syst. Res. **186**, 106401 (2020). https://doi.org/10.1016/j.epsr.2020.106401
14. Prasad, Ch.D., Srinivasu, N.: Fault detection in transmission lines using instantaneous power with ED based fault index. Procedia Technol. **21**, 132–138 (2015). doi: https://doi.org/10.1016/j.protcy.2015.10.020
15. Goldshtein, A., Vavilova, G., Rumkin, A., Starý, O.: Detection of insulation defects in automated in-process testing of electric wire during its extrusion. Mater. Sci. Forum **942**, 141–150 (2019). https://doi.org/10.4028/www.scientific.net/MSF.942.141
16. Rathinam, A., Vanila, S., Harika, C.: Phasor measurement unit based wide area backup protection scheme for power transmission lines. Energy Procedia **117**, 1172–1181 (2017). https://doi.org/10.1016/j.egypro.2017.05.243
17. Calderaro, V., Galdi, V., Piccolo, A., Siano, P.: Adaptive relays for overhead line protection. Electric Power Syst. Res. **77**(12), 1552–2155 (2007). https://doi.org/10.1016/j.epsr.2006.11.001

Thermoelectric Quality Control of the Application of Heat-Conducting Compound

Ivan Vasiliev, Aleksey Soldatov, Ahmed Abouellail, Mariya Kostina, Andrey Soldatov, Dmitry Soldatov, and Svetlana Bortalevich

Abstract The article presents the results of experiments to determine the dependence of thermopower on the quality of applying a heat-conducting compound. The data of deposition quality of the heat-conducting compound, which is obtained by thermocouples, coincides with the data, which is obtained using thermopower, but with a slight deviation due to the intrinsic inertia of thermocouples and fluctuations in the ambient temperature. The analysis of the data revealed that the value of the emerging thermopower increases linearly with the deterioration of the quality of the thermal interface application.

I. Vasiliev
Polyus Research and Production Center, 56 Kirov Avenue, Tomsk, Russia 634050
e-mail: vasiliev_ivan91@mail.ru

A. Abouellail
Electronic Engineering Division, School of Non-Destructive, Testing of Tomsk Polytechnic University, 30 Lenin Avenue, Tomsk, Russia 634050
e-mail: demo092@tpu.ru

S. Bortalevich
Market Economy Institute of Russian Academy of Sciences, Nahimovskii av. 47, Moskow 117418, Russian Federation
e-mail: 680097@inbox.ru

A. Soldatov (✉) · M. Kostina · A. Soldatov · D. Soldatov
Electronic Engineering Division, School of Non-Destructive Testing, National Research Tomsk Polytechnic University, 30 Lenin Avenue, Tomsk, Russia 634050
e-mail: asoldatof@mail.ru

Innovation Management Department, Tomsk State University of Control Systems and Radioelectronics, 40 Lenin Avenue, Tomsk, Russia 634050

M. Kostina
e-mail: mashenkasoldatova@mail.ru

A. Soldatov
e-mail: soldatov.88@bk.ru

D. Soldatov
e-mail: dimasoldatov@sibmail.ru

I. V. Minin et al. (eds.), *Progress in Material Science and Engineering*,
Studies in Systems, Decision and Control 351,
https://doi.org/10.1007/978-3-030-68103-6_6

1 Introduction

Heat generation during the operation of semiconductor devices can lead to many negative consequences. For example, a decrease in performance, reliability of the device, or even its failure [1–3]. Today, most powerful semiconductor technology is used in tandem with a heatsink, which allows some of the power generated in the form of heat to be removed from the semiconductor device. The heatsink is attached to the body of the semiconductor device through a layer of a heat-conducting compound, which is also called thermal interface and has heat-conducting properties that are much higher than that of air. Displacing it from the microcracks of two connected surfaces, consequently increases the thermal conductivity from the semiconductor device to the heatsink. The contribution of the thermal interface to the total value of the "crystal-heatsink" thermal resistance can range from 20 to 65%, so the paste layer should be as thin as possible, while the minimum acceptable value is limited by the size of air cavities [4]. The available methods of ensuring the quality of the thermal interface have a common drawback, which is the difficulty of applying quality control after attaching the heatsink to the device [5–7].

2 Statement of Problem

The thermal resistance R_T between the semiconductor device case and the heatsink characterizes the quality of the thermal interface. Whereas, the thermal resistance of the body is characterized by the temperature difference in different parts of the body caused by the passage of a heat flux through it. Thermal resistance between the body of the semiconductor device and the heatsink is determined by the formula [8]:

$$R_S = \frac{\Delta T}{P} = \frac{\mu}{\lambda \times S} \tag{1}$$

where ΔT is the temperature difference, P is the power flow through the body, λ is the thermal conductivity coefficient of thermal interface, and S—the area of the adjacent surfaces of the semiconductor device and the heatsink.

Information about the thermal resistance of the applied thermal interface is provided by the temperature difference at the boundaries of the thermal interface layer at known values of the contact area of the semiconductor device and the cooling heatsink. It is necessary to install the temperature sensors to measure the temperature difference at the boundaries of the thermal interface. It should be noted that they should touch the body of the semiconductor device and the heatsink as close as possible to the thermal interface.

3 Problem Solution

In case of the contacting case, the composition of which is different from the material of the heatsink, thermopower will appear at the junction of the semiconductor device and the heatsink. This happens due to the difference in the number of charge carriers at the external level between dissimilar conductors [9]. Due to the effect of the conductor temperature on the concentration of charge carriers at the external level, the value of the electromotive force, in this case, will directly depend on the temperature according to the formula [10]:

$$E = (T_2 - T_1)\frac{k}{e} ln \frac{n_2}{n_1}; \tag{2}$$

where k is Boltzmann constant, $T_{1,2}$ are hot and cold junction temperatures, e is electron charge, and $n_{1,2}$ are carrier concentrations of the first and second conductor material.

The quantity $\frac{k}{e} \ln \frac{n_2}{n_1}$ is constant for two conductors, and is called the thermopower coefficient or the Seebeck coefficient. It is denoted by α [11, 12]. Formula (2) can be shortened to:

$$E = (T_2 - T_1) \times \alpha; \tag{3}$$

In order to calculate the Seebeck coefficient, in addition to the above physical constants, it is necessary to know the values of the concentration of charge carriers of the first and second conductor materials, respectively. For metals, the concentration of carriers depends on the number of electrons at the outer level of an atom of a substance according to the formula [13]:

$$n = \frac{\rho \times Na}{Ma};$$

where n is concentration of charge carriers, ρ is the density of the substance, Na—Avogadro's number, and Ma is the molar mass of a substance.

However, when the Fermi energy level is exceeded, the carrier concentration can increase in accordance with the Fermi–Dirac distribution [14]; for ease of use in popular literature sources, the main values of the Seebeck coefficient are given relative to lead, as lead does not create a potential difference between its cold and hot ends [15, 16].

At the point of contact between the heatsink and the semiconductor device, a thermopower will also appear, in case the device has a surface covered in conductive material of a composition that is different to that of the heatsink. By shortening T_2–T_1 into ΔT form formula (3) and substituting it in formula (1), the following formula can be obtained:

$$R_S = \frac{E}{\alpha \times P}; \tag{4}$$

From formula (4), it is revealed that the value of thermal resistance depends on the value of thermopower between different contacting metals from the device body and the cooling heatsink. The value of thermal resistance can be obtained by measuring the thermopower between the device case and the heatsink if the power flux P through the body is declared.

The heat flux power represents the amount of heat passing through a certain area of the body per unit of time and it is determined by the basic heat transfer equation for a stationary mode [17]:

$$P = KS\Delta T; \tag{5}$$

where P is the heat flux (amount of heat) transferred during heat transfer, S—is the area of the contacting surfaces of the power device and the heatsink, F—heat exchange surface, and K—is the heat transfer coefficient.

When transferring heat in the simplest case through a single-layer flat wall, the heat transfer coefficient K is calculated by the formula [18]:

$$K = \frac{1}{\frac{1}{\alpha_1} + \frac{h}{\lambda} + \frac{1}{\alpha_2}}; \tag{6}$$

For a body consisting of several n layers of different materials, the heat transfer coefficient K is calculated by the formula:

$$K = \frac{1}{\frac{1}{\alpha_1} + \sum_{i=1}^{n} \frac{h_i}{\lambda_i} + \frac{1}{\alpha_2}}; \tag{7}$$

where h is thermal interface thickness, λ is the thermal conductivity coefficient of the thermal interface, and $\alpha_{1,2}$ are the heat transfer coefficients, respectively, from the heatsink to the thermal interface and from the thermal interface to the body of the semiconductor device.

Thus, taking into account formula (6), the thermal resistance of a homogeneous body calculated by formula (4) can be presented as:

$$R_S = \frac{E\left(\frac{1}{\alpha_1} + \frac{h}{\lambda} + \frac{1}{\alpha_2}\right)}{\alpha \times S}; \tag{8}$$

The thermal resistance of several connected bodies with different thermal conductivity, taking into account formula (7), is determined as:

$$R_S = \frac{E\left(\frac{1}{\alpha_1} + \sum_{i=1}^{n} \frac{h_i}{\lambda_i} + \frac{1}{\alpha_2}\right)}{\alpha \times S}; \tag{9}$$

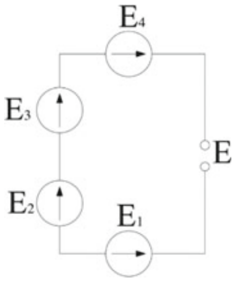

Fig. 1 Equivalent circuit for measuring thermopower

Based on formulas (8) and (9), the temperature difference at the boundaries of the thermal interface provides the value of thermal resistance of the applied thermal interface between the clamped semiconductor device and the heatsink. This temperature difference can be indicated through the thermopower, arising between the dissimilar materials of the semiconductor device and the heatsink, at known values of their contact area, thermal conductivity of the thermal interface, composition of the coating material of the body of the semiconductor device and the coating of the heatsink material, and their thermal conductivity [19, 20].

It should be taken into account that when monitoring thermopower, upon measuring the potential difference between two dissimilar conductors relative to each other, and not relative to temperature 0 °C, the resulting thermopower according to the additivity rule [21, 22] is determined by summing up all thermopower included in the measurement circuit. For instance, upon connecting a copper conductor to the body of the semiconductor device and to the heatsink, a thermopower will also appear at the connection points. In this case, it is necessary to take into account the direction of the thermopower forming a closed measurement loop (Fig. 1).

The resulting thermopower in this case is calculated by the formula:

$$E = \sum_i E_i; \tag{10}$$

4 Experimental Results

Experimental research is vital to verify the proposed method for the measurement of thermal resistance using thermopower. The objects of study were an aluminum cylinder-shaped heatsink and a power semiconductor device in a TO-220 casing, which is very often used in semiconductor technology. Platinum and platinum–rhodium thermocouples DT1 and DT2 were attached to the cylinder-shaped heatsink and to the TO-220 casing. The distance from the thermocouple to the border of the TP-220 case and the heatsink was made minimal. In the course of the experiment, boiling water influences to the body through the heatsink, which is placed in such a way that water cannot reach the instrument body. The thermopower and the voltage difference between the installed thermocouples were measured with the Agilent 34461A instrument in the data recording mode. The data received from the measuring devices were transferred to a personal computer. The experimental scheme is shown in Fig. 2.

The temperature difference characterizing the thermal resistance during the application of the KPT-8 thermal paste, is provided by thermocouples and using thermopower from the dissimilar case and the heatsink metals according to formula (2). It should be noted that the coating of the substrate of the power element body is made of stannum, and the heatsink is made of aluminum, as shown in Figs. 3 and 4. When partially applying the heat-conducting paste KPT-8, a polyethylene film preliminarily fixed on the surface of the power device casing was used, which prevented the paste from getting on the closed part of the case. Three film sizes were prepared that covered 25, 50 and 75% of the power tool housing surface. In the course of the research, for each variation of applying the heat-conducting paste,

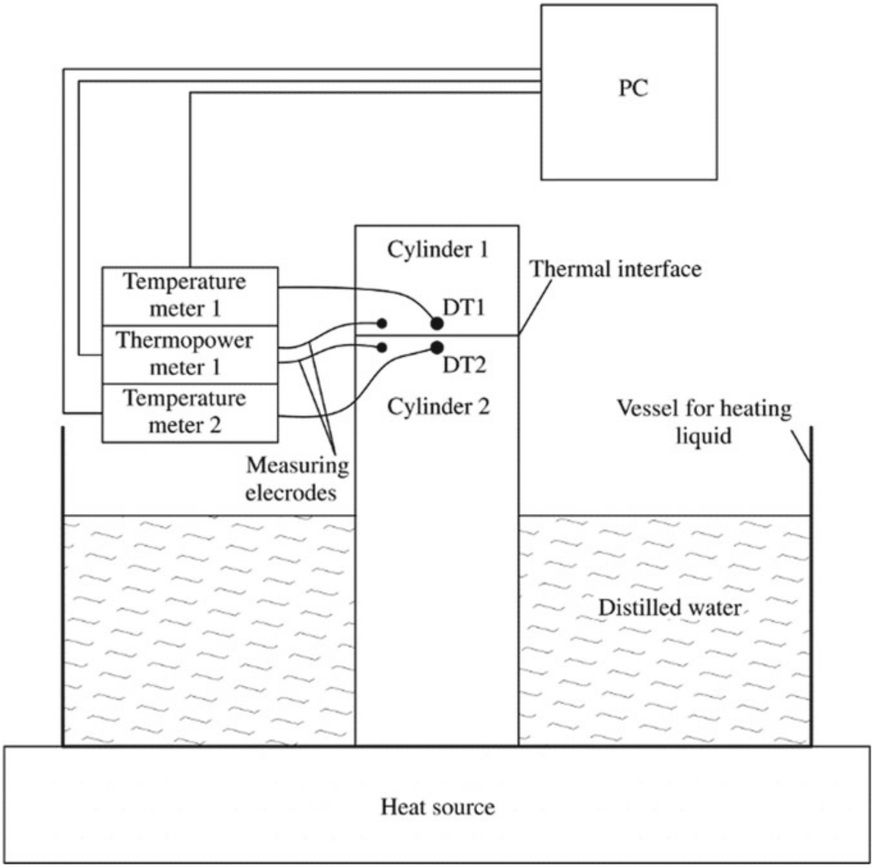

Fig. 2 Schematic representation of the experimental setup

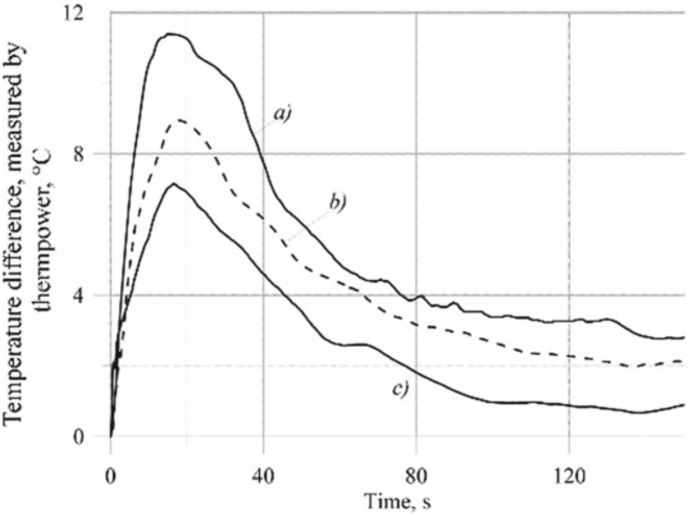

Fig. 3 The dependence of the temperature difference on time, as the temperature difference is identified to be between the case and the heatsink and obtained by thermocouples: **a** without thermal interface, **b** with partially applied thermal interface (50%), **c** with applied thermal interface (100%)

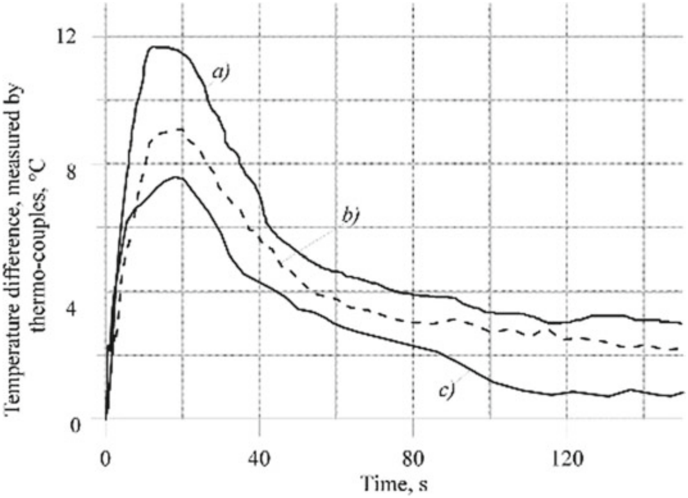

Fig. 4 The dependence of the temperature difference on time, as the temperature difference is identified to be between the case and the heatsink and obtained by the thermopower of the case and the heatsink. **a** without a thermal interface, **b** with partially applied thermal interface (50%), **c** with applied thermal interface (100%)

a series of 10 experiments were carried out, and for all experiments the same mass of the heat-conducting paste was used. Weighing was carried out on the laboratory scale AS 310/C/2. Averaging by the linear filtering method was used to build the graphs. The confidence interval does not exceed 8%.

Figures 3 and 4 show that at the initial moment of time, the temperature difference between the case of the power element and the cooling heatsink increases for each variation of applying the thermal interface due to the rapid heating of the heatsink placed in boiling water and slow heating of the case of the power element. After the heatsink has completely warmed up, the power element body begins to heat up smoothly and the temperature difference begins to gradually decrease, reaching a steady-state value. The duration of the transient process for each case of applying a thermal interface is constant. That is because this value is characterized by the heat capacity of the heatsink and the device body, and the influence of the thermal resistance of the heat-conducting layer is extremely small. The oscillatory nature of the change in temperature differences, shown in Fig. 3, is caused by small fluctuations in the ambient temperature and the presence of uncontrolled air flows in the experimental zone, which mainly affects the cold junction of thermocouples. These fluctuations are also observed in Fig. 4, but they are less pronounced due to the large thermal inertia of the body of the power element. The analysis of Figs. 3 and 4 shows that the temperature graphs, obtained in the course of experiments using thermocouples and thermopower, differ slightly. Small deviations are most likely caused by incorrect calculation of the Seebeck coefficient of the materials used.

Experimental studies of the dependence of thermopower on the coverage area of the body of a power element with a heat-conducting layer are shown in Fig. 5. When fixing a semiconductor device on a cooling heatsink, a part of the heat-conducting paste falls on the uncovered area of the body of a semiconductor device, therefore, the coverage area was measured after removing the semiconductor device from the cooling heatsink. The measurement was carried out on a 10× magnified photograph of the body of the power device, on which a transparent palette with a grid was applied. The area measurement error did not exceed 5%.

From Fig. 4 it can be seen that there is an almost linear dependence. With an increase in the coverage area, the thermopower decreases linearly. The confidence interval does not exceed 7%.

5 Conclusion

The obtained linear dependence of the thermopower on the coverage area of the body of the power element with a heat-conducting layer makes it possible to use the thermoelectric method to test the quality of the application of a heat-conducting compound. When using heatsinks or power devices in housings made of other alloys, it is necessary to first obtain a calibration dependence of the thermopower on the area of the power element housing with a heat-conducting layer. It should be taken

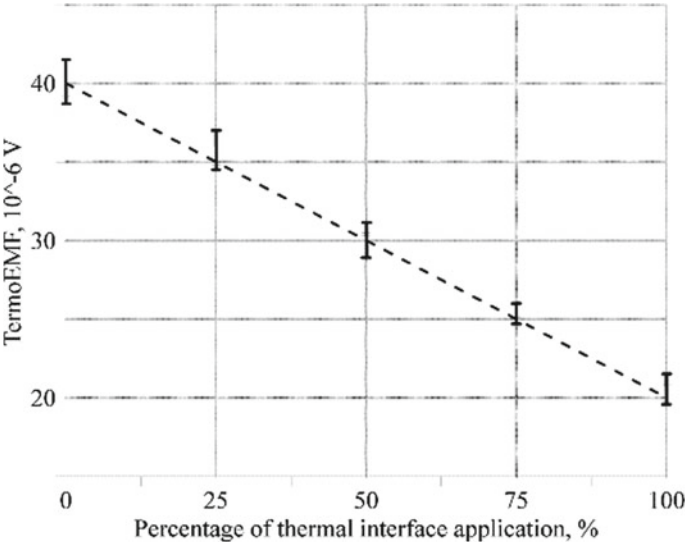

Fig. 5 The dependence of thermopower on the coverage area of the body of the power element with a heat-conducting layer

into account that the thermoelectric testing method can be used directly during the operation of electronic equipment.

References

1. Wintrich, A., Nicolai, U., Tursky, W., Reimann, T.: Application manual power semiconductors, 2nd edn. ISLE Verlag, Germany (2015)
2. Hopfe, S.: Technical Explanation Thermal Interface Materials, Rev. 01, Semikron International, GmbH (2016)
3. Weiss, R.: High voltage testing, Rev. 00, Semikron International, GmbH (2016)
4. Drexhage, P, Beckedahl, P.: Thermal Paste Application, Semikron (2018)
5. Esau, D.: Thermal Paste Application. Semikron (2010)
6. Chandler, G., Zimmer, J.: SOD substrates: the next step in electronics thermal management. In: Workshop on thermal management, Palo Alto USA (2006)
7. Maruta, A., Tabata, M.: 2500 A/1200 V Dual IGBT Module. PCIM Europe (2009).
8. JEDEC Standard JESD51–14: Transient dual interface test method for the measurement of the thermal resistance junction to case of semiconductor devices with heat flow through a single path
9. Schulz, M.: Thermal interface—an inconvenient truth. Article Bodo's Power Systems (2010)
10. Ioffe, A.: Semiconductor Thermoelements and Thermoelectric Cooling. Infosearch Limited (1957)
11. Eisele, R., Rudzki, J., Kock, M.: Pressure Sintering for Thermal Stack Assembly. PCIM Europe (2007)
12. Ashcroft, N., Mermin, D.: Solid State Physics. Holt, Rinehart and Winston, New York (1976)
13. Cutler, M., Mott, N.: Observation of Anderson localization in an electron gas. Phys. Rev. **181**(3), 1336–1340 (1969). https://doi.org/10.1103/PhysRev.181.1336

14. Joseph, R., Duck, Y., Mercouri, G.: New and old concepts in thermoelectric materials. Angewandte Chemie – International Edition **48** (46), 8616–8639 (2009). https://doi.org/10.1002/anie.200900598
15. Rhee, J., Danek, C., Moffat, R.: Adiabatic heat transfer coefficient on the faces of a cube in an electronics cooling situation. Am. Soc. Mech. Eng. **4–2**, 619–629 (1993)
16. Nakayama, W., Park, S.: Conjugate heat transfer from a single surface-mounted block to forced convective air flow in a channel. J. Heat Transfer **118**(2), 301–309 (1996). https://doi.org/10.1115/1.2825845
17. Park, R., Carroll, R., Bliss, P., Burns, G., Desmaris, R., Hall, F., et al.: Manual on the Use of Thermocouples in Temperature Measurement. ASTM International, West Conshohocken (1993)
18. Soldatov, A. I., Soldatov, A. A., Sorokin, P. V., Abouellail, A. A., Obach, I. I., Bortalevich, V. Y., Shinyakov, Y. A., Sukhorukov, M. P.: An experimental setup for studying electric characteristics of thermocouples. In: Proceeding of the International Siberian Conference on Control and Communications (SIBCON), 7998534 (2017). https://doi.org/10.1109/SIBCON.2017.7998534
19. Carreon, H.: Thermoelectric detection of spherical tin inclusions in copper by magnetic sensing. J. Appl. Phys. **88**(11), 6495–6500 (2000). https://doi.org/10.1063/1.1322591
20. Abouellail, A.A., Obach, I.I., Soldatov, A.A., Soldatov, A.I.: Surface inspection problems in thermoelectric testing. MATEC Web Conf. **102**, 01001 (2017). https://doi.org/10.1051/matecconf/201710201001
21. Stuart, C.M.: The Seebeck effect as used for the nondestructive evaluation of metals. Adv. Nondestr. Test. **9** (1983)
22. Soldatov, A.I., Soldatov, A.A., Sorokin, P.V., Loginov, E.L., Abouellail, A.A., Kozhemyak, O.A., Bortalevich, S.I.: Control system for device «thermotest». In: Proceeding of the International Siberian Conference on Control and Communications (SIBCON), pp. 1–5 (2016). https://doi.org/10.1109/SIBCON.2016.7491869

Simulation Study of an Ultrasonic Signal Compression

Olesya Kozhemyak, Oleg Stukach, and Alexey Soldatov

Abstract The paper presents three algorithms of an ultrasonic signal compressing. First one is a compression with linear time quantization. Second algorithm of signal compression calculates the rate of signal change and proportionally to it sets the sampling rate. Third algorithm of compression takes some number of random uniformly distributed samples from the original ultrasonic signal. The results of simulations for all three compressing algorithms are presented in the paper. An absolute error and mean square deviations for a wide range of compression ratios are calculated and compared for different compressing algorithms.

1 Introduction

Ultrasonic phased arrays are widely used in different fields of non-destructive testing. Higher accuracy of defect detection demands grater resolution of the ultrasonic installation, which necessitates the increase in the array element number. The increase in

---

O. Kozhemyak
Electronic Engineering Department, National Research Tomsk Polytechnic University, 30 Lenin Avenue, Tomsk, Russia 634050
e-mail: kozhemyak@tpu.ru

A. Soldatov (✉)
Electronic Engineering Division, School of Non-Destructive Testing, National Research Tomsk Polytechnic University, 30 Lenin Avenue, Tomsk, Russia 634050
e-mail: asoldatof@mail.ru

Innovation Management Department, Tomsk State University of Control Systems and Radioelectronics, 40 Lenin Avenue, Tomsk, Russia 634050

O. Stukach
School of Electronic Engineering, Higher School of Economics, 20 Myasnitskaya ulitsa, Moscow, Russia 10100
e-mail: tomsk@ieee.org

Information Secutiry Department, Novosibirsk State Technical University, 20 Marks Avenue, Novosibirsk, Russia 630073

I. V. Minin et al. (eds.), *Progress in Material Science and Engineering*,
Studies in Systems, Decision and Control 351,
https://doi.org/10.1007/978-3-030-68103-6_7

the element number, however, leads to larger amounts of data obtained and transmitted from sensors to processor unit. Large data arrays require higher transmission capacity of communication channels, as well as higher capacity of memory devices.

The solution to the problem of reducing the amount of data without distorting the results of testing is the use of a signal compression algorithm. Nowadays, different algorithms of data compression are developed [1–8]. Wavelet transforms are widely used to compress and filter signals [1–3]. A review of the use of wavelets for processing the ultrasonic signals showed that the wavelet transform was used mainly to improve the detection of defects by increasing the signal-to-noise ratio.

In the last decade, a new approach to signal processing, called compressive sensing [4–7], has become popular. This approach proposes measuring only the significant parts of the signal instead of obtaining its values on all samples. Thus, if the significant part of the signal is small when compared to the entire signal, then you can significantly reduce the amount of data processed and transmitted. Moreover, the approach allows filtering out unnecessary information already at the measurement stage, i.e. before the stages of data transmission and processing. Filtering procedure is executed at the physical level, with no use of computing resources and, therefore, with no time delays associated with computations [6].

In the works [7, 9] compression algorithms are described, in which inflection points and extremes are used as significant parts of the signal. Such algorithms have been used for processing and transmitting ultrasound data in medicine.

The compressive sensing problem arises in design of modern telecommunication systems of transfer of telemetry information through borehole pipe as evanescent waveguide that is not on the basic signal mode [10]. The information transfer problem through such communication channel is initially stage of development. Sand and drilling agent lead to sharp increase of attenuation. For deepest boreholes up to 2.5–3 km the overcoming of strong attenuation is the urgent technical problem. Radiophysical investigations show that frequency should be above to receive the maximum power of radiation and at the same time less for attenuation decrease in the filling media. Therefore, ultrasonic signal is the only suitable for the considered communication channel. But the use of the ultrasonic signal for telemetry transfer leads to low rate transfer. It leads to necessity of investigation of algorithms and ways of ultrasonic signal compression with losses that transferring all necessary data in real time.

2 Compression Ratio and Quality of Signal Reconstruction

The effectiveness of the compressing algorithm is characterized, first of all, by the compression ratio $\boldsymbol{k}$, which determines the ratio of the number of bit symbols of the original $\boldsymbol{N}$ and compressed signal M:

$$k = \frac{M}{N} \tag{1}$$

To estimate the quality of the reconstructed signal, the reduced error is calculated:

$$\gamma = \frac{x(n) - y(n)}{X} \times 100\% \tag{2}$$

where $n = 1 \ldots N$; N is the number of signal samples in the interval; $x(n)$ are samples of the original signal, $y(n)$ are samples of the recovered signal; X is the upper limit of the scale.

Also, to estimate the accuracy of signal reconstruction, the mean square deviation is used:

$$\delta = \sqrt{\frac{\sum_{n=1}^{y} [x(n) - y(n)]}{N}} \tag{3}$$

3 Signal Compression with Linear Time Quantization Algorithm

Fist algorithm to compress an acoustic signal is a linear time quantization compressing, i.e. sampling the signal with equivalent time intervals and fixed sampling frequency. When decreasing sampling frequency the number of samples also decreases and sampled signal is getting more and more compressed.

Let's now simulate this algorithm of regular compressing using MatLab Simulink. For this purpose we generate example signal of sinusoidal shape to demonstrate the proposed algorithm of compressing. Than we sample this signal with a help of pulse generator, the pulse frequency of which we can vary. Figure 1 shows the regular compressing algorithm: sin-wave signal, sampled sin-wave signal, reconstructed signal, absolute error of reconstruction.

This algorithm of regular compression was applied to compress an ultrasonic echo-signal, the model of which is presented in Fig. 2. Resulting signal is presented in Fig. 3.

The number of samples M was varied from 8000 to 400 which corresponded to a change of compression ratio in the range from 1 to 20. After modeling the graphs of absolute error and mean square deviation σ of the reconstructed signal versus compression ratio k were obtained (Fig. 4). Absolute error was calculated as a difference between compressed and original echo-signals signals.

The results of simulation show proportional increase in absolute error and mean square deviation with increasing compression ration $\boldsymbol{k}$ from. Therefore, the compressing algorithm based on linear time quantization of ultrasonic signal is inappropriate for signal compression with high ratios (more than 5) since the error exceeds 10% value.

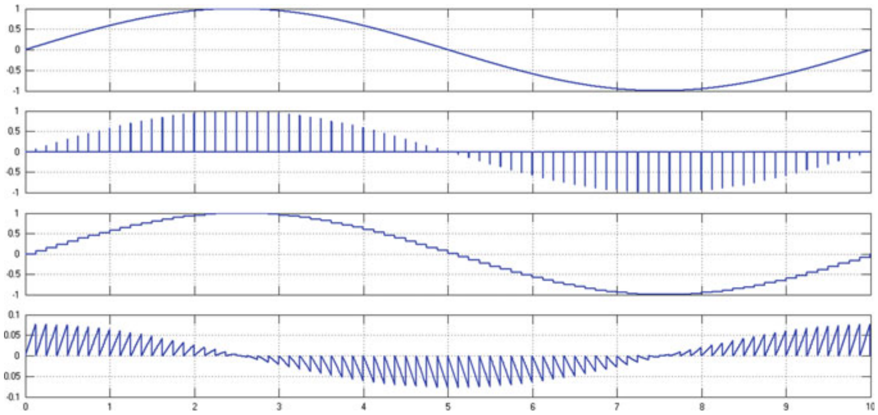

Fig. 1 Regular compressing of sin-wave input signal: input sin-wave signal, sampled sin-wave signal, reconstructed signal, absolute error of reconstruction

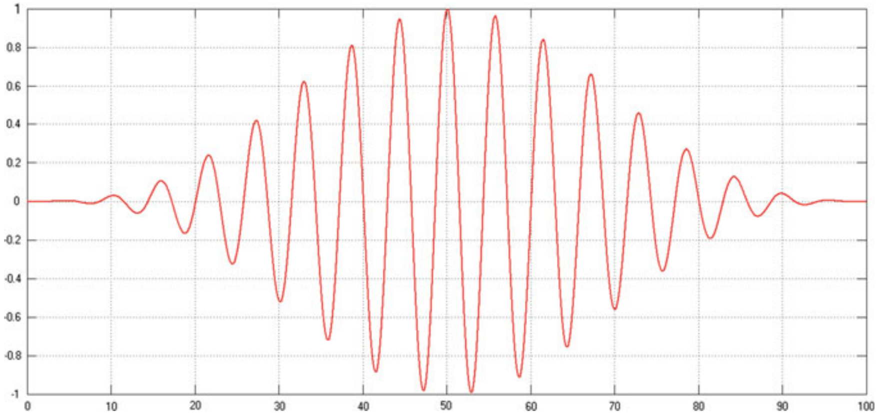

Fig. 2 The ultrasonic signal model

4 Signal Compression with Algorithm Based on Calculation of the Rate of Signal Change

The next algorithm is based on the calculation of the rate of change of input signal. In accordance with the rate of change of the signal, the sampling rate of the analog signal into a digital code is calculated. Therefore, the higher is the rate of change of a signal, the higher is the sampling rate, and vice versa. Thus, in the absence of a signal and at low rates of change of the signal (rate tends to zero), the sampling rate is very small and tends to zero; therefore, the conversion of such insignificant parts of the signal into a digital code will not performed.

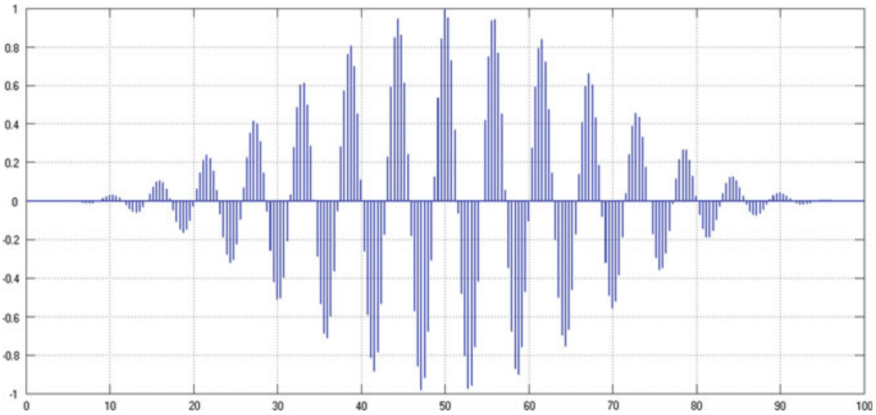

Fig. 3 The ultrasonic signal compressed with linear time quantization algorithm

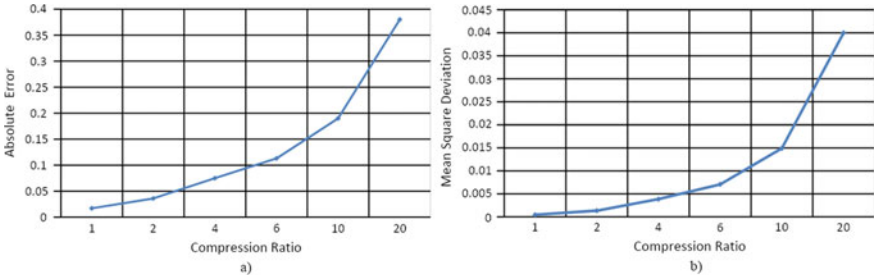

Fig. 4 Absolute error (**a**) and mean square deviation (**b**) versus compression ratio of signal (Fig. 3)

To sample input analog signal the voltage-to-frequency converter (VFC) was implemented in the model, which provides an output frequency accurately proportional to its input voltage.

Figure 5 demonstrates the performance of the algorithm of the progressive compressing.

Progressive compressing was applied to an ultrasonic echo-signal (Fig. 2). Resulting signal is presented in Fig. 6. The number of samples M was varied from 7000 to 350, which corresponded to a change of the compression ratio k in the range from 1 to 20. The graphs absolute error and mean square deviation of the reconstructed signal versus compression ratio were obtained (Fig. 7).

The modeling shows slower increase in absolute error as well as in mean square deviation for varied compression ratio in comparison with results of compression modeling with linear time quantization algorithm (Fig. 4). Compression ratio $k = 20$ showed less than 10% value of absolute error and mean square deviation less than 0.02.

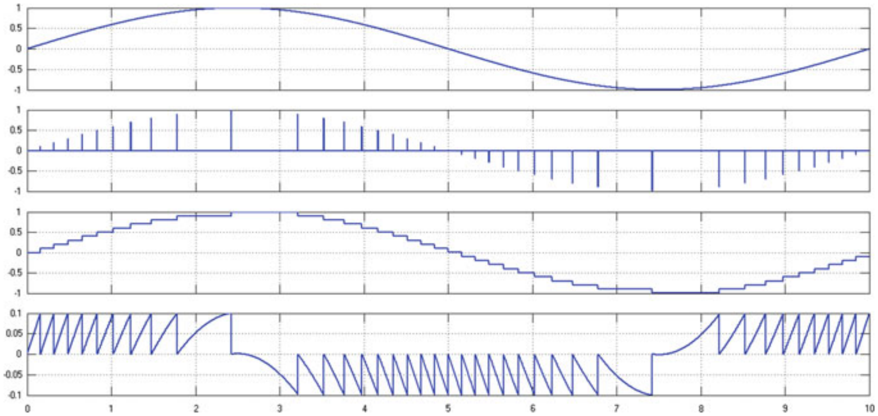

Fig. 5 Progressive compressing of sin-wave input signal: input sin-wave signal, sampled sin-wave signal, reconstructed signal, absolute error of reconstruction

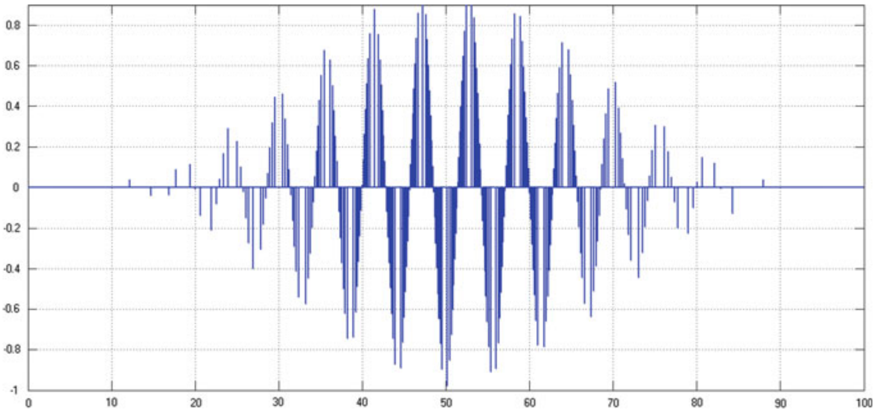

Fig. 6 The ultrasonic signal compressed with algorithm based on calculation of the rate of signal change

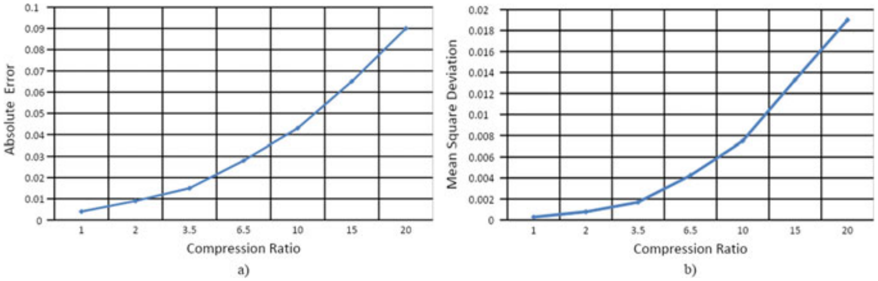

Fig. 7 Absolute error (**a**) and mean square deviation (**b**) versus compression ratio of signal (Fig. 6)

5 Signal Compression with Random Sampling Algorithm

In [9] authors offer algorithm of signal compression based on a choice in real time key points where extremes and points of the maximum curvature of function are presented. We will show that information losses in this case will be increased in more times rather than more samples are presented in signal.

For example, we will consider a model of the ultrasonic pulse well described by the formula:

$$y(t) = \sin \Omega t \sin^3 \omega t, \\ \Omega = 10, \omega = 0.3, t \in [0.001; 10] \tag{4}$$

Let 10,000 discrete values of this signal be total amount of the signal. We take random uniformly distributed M samples $y_i(t)$ from this signal (Fig. 8) calculated in Statistica 8.0 software [11].

Mean square deviation σ for 10 random samples is presented in Fig. 9. Compression ratio k is total amount of samples (10,000) divided on quantity of points in the sampled signal. As a result of nonlinear evaluation in the "Nonlinear Estimation" module of Statistica software it is found that mean square deviation of the restored signal from initial is inverse proportion to compression ratio:

$$\sigma(k) = 0.0038 + 0.00019/k - 0.0036/k^2 \tag{5}$$

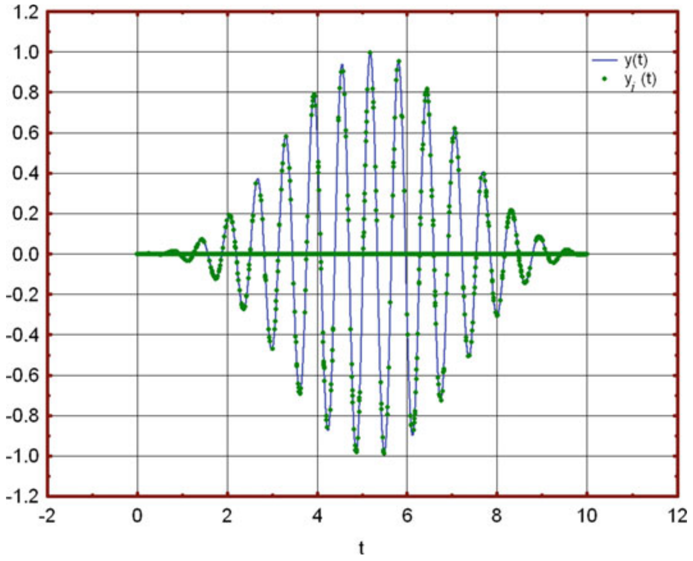

Fig. 8 The ultrasonic signal model

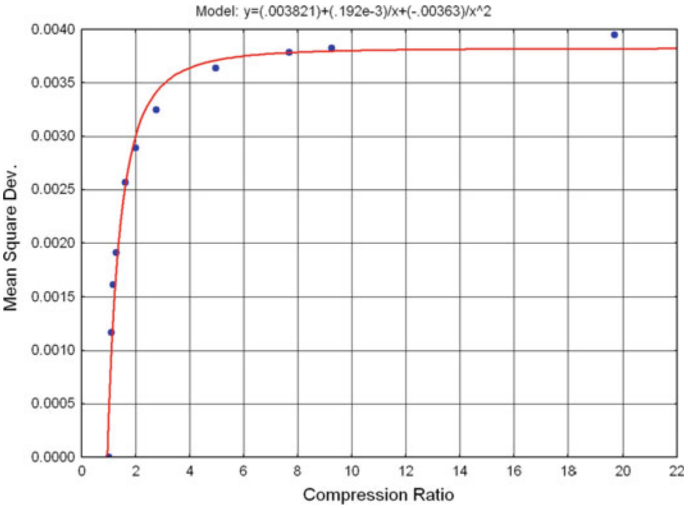

Fig. 9 The mean square deviation for random samples (Fig. 8)

At reduction of *M* quantity that is increasing of the compression ratio, the mean square deviation for samples will be sharply increased. Then in the domain of small volume of samples at compression of five times and more the mean square deviation changes a quite little, but information losses in this domain are already considerable. If we choose the key points that authors of [11] offer, the quantity of samples will be essential less than 2000 for our example that is compression ratio will be more than five times. It will catastrophically affect to the signal restoring accuracy. We will show it by restoration of the signal compressed twice. The initial values of frequencies Ω and $\boldsymbol{\omega}$ in the "Nonlinear Estimation" module was closed to true, $\Omega = 10.5$, $\omega = 0.35$. If compression ratio was less than two, the exact values Ω and $\boldsymbol{\omega}$ have been founded, but for compression more than twice *k* are essentially distinct from (4): $\Omega = 10.03$, $\omega = 0.397$ (Fig. 10).

Besides, the small deviation of the ultrasound signal amplitude from real is less critical for restoration losses, but some weakest deviation of frequency leads to essential distortions.

Form of curve described by (5) remains the same for any form of the ultrasonic signal. For example, the trapeze signal (Fig. 11) follows us the dependence resulted in Fig. 12.

Compression ratio more than 1.5–2 times for the trapeze signal form is inexpedient also due large error.

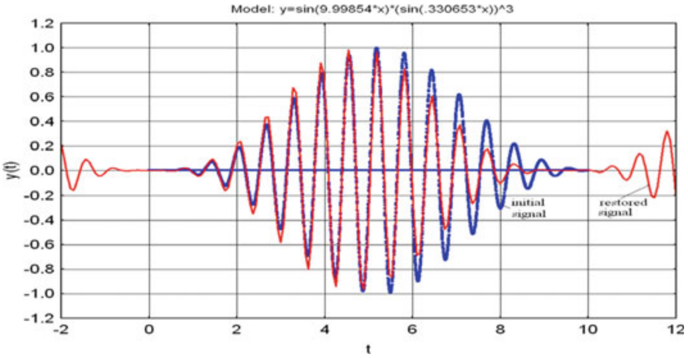

Fig. 10 Signal restoration by N = 5000 samples (red graph)

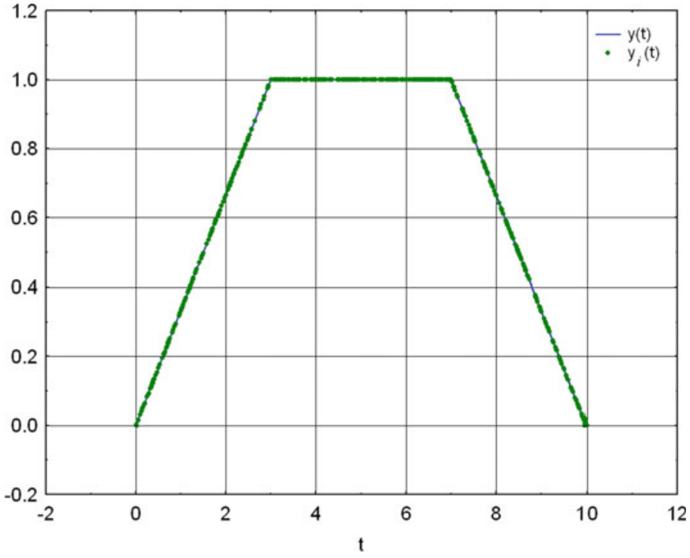

Fig. 11 The signal model

6 Conclusion

Compression of the ultrasonic echo-signal with algorithm based on calculation of the rate of signal change showed better appliance in the wide range of compression ratios (from 1 to 20). Thus, compression ratio k = 20 showed less than 10% value of absolute error and mean square deviation less than 0.02.

Compression algorithm with linear time quantization of ultrasonic signal showed good appliance only for low compression ratios (up to 5). Compression ratio k = 5 showed about 10% value of absolute error and mean square deviation near 0.005.

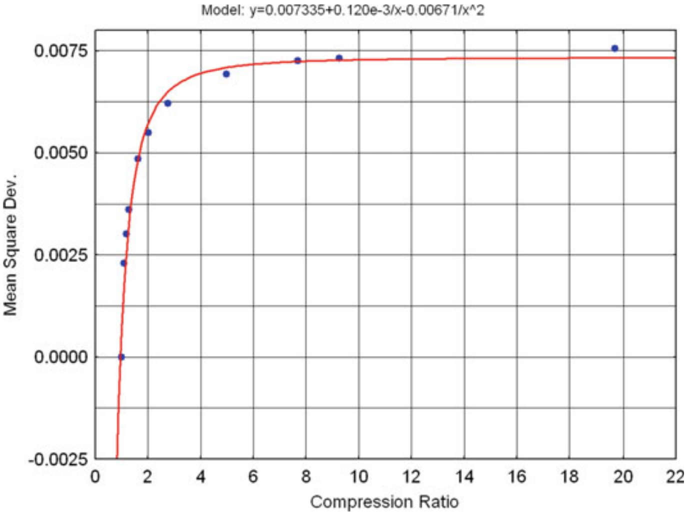

Fig. 12 The mean square deviation for random samples of signal (Fig. 11)

Signal compression with random sampling algorithm showed good rapid increase of mean square deviation for the compression ratios up to 2, but in a wide range of compression ratios (up to 22) mean square deviations does not exceed 0.0075.

References

1. Yang, G., Zhang, Q., Que, P.W.: Matching-pursuit-based adaptive wavelet-packet atomic decomposition applied in ultrasonic inspection. Russ. J. Nondestruct. Test. **43**, 62–68 (2007). https://doi.org/10.1134/S1061830907010093
2. Zhang, Q., Chen, T., Que, P., Xing, Y.: Compression of ultrasonic signals with the lifting scheme wavelet transform. Russ. J. Nondestruct. Test. **44**(7), 490–495 (2008). https://doi.org/10.1134/S1061830908070073
3. Rinkevich, A.B., Perov, D.V.: A wavelet analysis of acoustic fields and signals in ultrasonic nondestructive testing. Russ. J. Nondestruct. Test. **41**, 93–101 (2005). https://doi.org/10.1007/s11181-005-0134-5
4. Granichin, O.N., Pavlenko, D.V.: Randomization of data acquisition and $\ell 1$-optimization (recognition with compression). Autom. Remote Control **71**, 2259–2282 (2010). https://doi.org/10.1134/S0005117910110019
5. Zhiliang, B., Shili, Ch., Qiyang, X., Lecheng, J., Yanbo, Zh., Zhoumo, Z.: Compressive sensing of phased array ultrasonic signal in defect detection: simulation study and experimental verification. Structural Health Monitoring **17**(3), 434–449 (2018). https://doi.org/10.1177/1475921717701462
6. Donoho, D.: Compressed sensing. IEEE Trans. Inform. Theory **52**(4), 1289–1306 (2006). https://doi.org/10.1109/TIT.2006.871582
7. Tai, S.C.: ECG data compression by corner detection. Med. Biol. Eng. Comput. **30**, 584–590 (1992). https://doi.org/10.1007/BF02446789

8. Yurchenkov, V.A., Soldatov, A.I., Soldatov, D.A.: An application of the compressive sampling method for compressing and processing acoustic signals. Russ. J. Nondestruct. Test. **49**, 631–635 (2013). https://doi.org/10.1134/S1061830913110119
9. Antonenko, E.A., Katrich, V.A., Karpov, A.I., Mustetsov, N.P.: A method of the optimum data compression in the medical monitoring systems. ElectronComm **5**(88), 46–50 (2015). https://doi.org/10.20535/2312-1807.2015.20.5.70812
10. Mirmanov, A.B., Stukach, O.V.: The system problems in the microwave measurement while drilling telemetry for controlled drilling and modeling in Matlab Simulink. In: Proceedings of the International Conference on Mechanical Engineering, Automation and Control Systems (MEACS 2014), 6986885 (2014). https://doi.org/10.1109/MEACS.2014.6986885
11. Borikov, V.N., Stukach, O.V., Popova, E.A.: Control of the microplasma process in electrolyte solutions based on STATISTICA model. In: Proceedings of the IEEE International Siberian Conference on Control and Communications (SIBCON-2007), pp. 58–63 (2007). https://doi.org/10.1109/SIBCON.2007.371298

Mathematical Model of the Throughput of an IP Network Switching Node with a Non-constant Amount of Space in the Router RAM

Pavel Dunayev, Yermek Sarsikeyev, Olga Galtseva, and Gufana Narimanova

Abstract This paper offers a mathematical model that allows determining the performance and throughput of an IP network node under conditions when the amount of space in the router RAM is not constant, that is, in the case of overloads and a number of other factors. The Cisco Packet Tracer software package is used as a network emulator. The results of mathematical and simulation modeling are compared.

1 Introduction

IP network routers are important elements of the city's telecommunications infrastructure. They influence the bandwidth of the transmission channel. Their parameters, settings, amount of RAM (random access memory), etc. to a great extent determine the efficiency of the entire telecommunications network. Due to insufficient throughput of the IP node, the throughput of the entire network decreases, the packet service time increases, which increases the delay time of the IPTD (Internet Protocol Packet Transfer Delay) IP packet and the IPDV (Internet Protocol Packet delay variation) delay variation [1, 2]. According to the authors of the Chapter, based

---

P. Dunayev · Y. Sarsikeyev
Energy Department, JSC Kazakh Agrotechnical University Named After S. Seifullin,
62 Pobeda Avenue, 010000 Nur-Sultan, Republic of Kazakhstan
e-mail: dunayev.kz@mail.ru

Y. Sarsikeyev
e-mail: sarsikeyev.ermek@yandex.ru

O. Galtseva (✉)
School of Non-Destructive Testing, National Research Tomsk Polytechnic University,
30 Lenin Avenue, Tomsk, Russia 634050
e-mail: rabota2013tpu@mail.ru

G. Narimanova
Department of Innovation Management, Tomsk State University of Control Systems and
Radioelectronics, 40 Lenin Avenue, Tomsk, Russia 634050
e-mail: guftana@mail.ru

I. V. Minin et al. (eds.), *Progress in Material Science and Engineering*,
Studies in Systems, Decision and Control 351,
https://doi.org/10.1007/978-3-030-68103-6_8

on the above, increasing and evaluating the bandwidth of an IP node is a very urgent task.

Most of the known methods for assessing the throughput of IP networks are based on models in the form of a QN (Queuing Network), in which nodes display IP packet delays [3–5].

There are several methods for modeling telecommunications networks: physical, analytical, simulation, and combined. With the physical modeling method, the performance of the systems under study is measured in real time, i.e. an experiment is being performed. The result of this method is a model with high adequacy in a real system or network. Despite the advantages, this method has a drawback, i.e. the high cost of equipment for creating a model [6].

An analytical model is a set of analytical expressions that reflect functional dependencies between the parameters of a real system during its operation. Such models are used for simple systems with no requirements for high accuracy of the results obtained.

A simulation model is a computer program that reproduces events occurring in a real system. The result of the simulation model is the collected statistical data on important network characteristics [6].

The results of the experimental verification prove the correctness of the approach when drawing up the mathematical model, particularly, of taking into account the number of RAM space and the size of an IP packet. This condition distinguishes the constructed model from standard methods based on the QN.

2 Theoretical Part

In reality, IP networks show a situation when routers process a large number of IP packets of various sizes. The service or processing time for these packets depends on the switching matrix used. The switching matrix is the basis of any router since it is used to transmit packets from the input data port to the output one. Switching can be performed in several ways: memory switching, bus switching, and connection network switching (Fig. 1).

More complex interconnecting networks perform switching in several stages, which ensures simultaneous transmission of packets from different input ports to the same output port through a switching matrix [7].

The router may process 2 million or more packets per second [8–11].

For example, there may be either 5 thousand 64-byte IP packets or 10 thousand 32-byte ones at the same time. It is logical to assume that at all other things being equal if only 32-byte IP packets are used on routers, the performance will increase by 2 times since the amount of RAM space will 2 times increase. As is known, the throughput is measured in bits/s, thus, when talking about the number of packets per second, the authors mean the hardware performance. Therefore, with the declared hardware performance, the throughput should increase as the IP packet size increases.

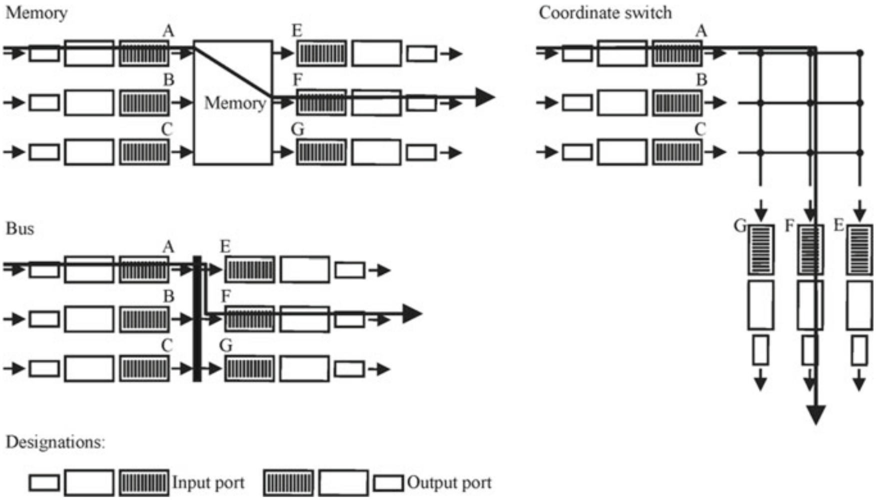

Fig. 1 Three ways to switch data

Thus, the count of the percentage of different sizes of information packets is very important for a more accurate calculation of the parameters of the IP network switching node.

Let us consider the simplest mathematical model of the performance of an IP network switching node.

Let us assume that there are two sizes of IP packets being service by the router: 1024 and 32 bytes each. The standard amount of RAM for the router selected for research, for the Cisco 2811 router in this case, is 256 MB. Therefore, the router can process 250 thousand 1024-byte packets within a certain time or 8 million 32-byte packets, or 200 thousand 1024-bytes packets and 1 million 600 thousand 32-byte packets, etc. Let us assume that the router's RAM is used as efficiently as possible. We also assume that the delay time is equal for all IP packet sizes (10–20 ms) [12].

Now, let us take a situation when the amount of space in RAM is not a constant but a discrete random variable. In this case, it is impossible to calculate the throughput of the switching node accurately by using standard methods.

If the case IP packets of the same size are sent, the performance may be calculated as follows

$$C_{IP} = M_R k_n \frac{1}{t_{serv}} \text{ [Packets/s]}, \tag{1}$$

where M_R is the amount of space in RAM or the number of packets being served, taking into account the size (250 thousand 1024-byte packets, 8 million 32-byte packets), k_n is the RAM inefficiency factor, and t_{serv} is the packet processing time (the delay introduced by the router).

For now, let us simplify by not taking into account the inefficiency factor of RAM use and assume it to be equal to one. When using 1024-byte IP packets, the performance will be equal to

$$C_{IP} = M_R \frac{1}{t_{serv}} = 250,000 \times \frac{1}{0.02} = 12.5 \times 10^6 \text{ [Packets/s]},$$

and in the case of using 32-byte IP packets

$$C_{IP} = M_R \frac{1}{t_{serv}} = 8,000,000 \times \frac{1}{0.02} = 400 \times 10^6 \text{ [Packets/s]}.$$

As can be seen, the performance of the switching node increased by 32 times when using packets of a smaller information size because the RAM space 32 times increased.

Let us determine what the performance will be if the router receives packets of different sizes at the same time. To be briefer, let us denote them “A” and “B”.

Let us assume that the information flow of IP packets arriving at the router looks like this (from right to left)

$$\text{AABBBABAB} \ldots,$$

where “A” is a 1024-byte packet and “B” is a 32-byte packet.

We will consider the occurrence of the current IP packet as an event independent from the occurrence of the previous one, and the information flow itself is infinite.

The probability that a randomly selected packet will be “A” is equal to P_A, and for the “B” packet, it is P_B.

Let us consider two hypotheses, H_1 and H_2. To simplify the calculations, let us take the following:

H_1—5 consecutive packets are of the “B” type; H_2—2 out of 5 packets are of the “A” type. In this case, the probability of hypotheses is $\boldsymbol{P}(\boldsymbol{H}_1) = \boldsymbol{P}_{\boldsymbol{B}}^5$, and $\boldsymbol{P}(\boldsymbol{H}_2) = 1 - \boldsymbol{P}_{\boldsymbol{B}}^5$. Since the total probability of hypotheses is equal to one, it means that they form a complete group of events.

Since the amount of space in RAM in the accepted case is a random variable, let us find its mathematical expectation

$$M = \sum_i X_i P_i = 3\left(1 - P_B^5\right) + 5P_B^5 = 3 + 2P_B^5.$$

By substituting the amount of space in RAM with its mathematical expectation in expression (1), we obtain the following.

$$C_{IP} = \frac{1}{t_{serv}}\left[3 + 2P_B^5\right],$$

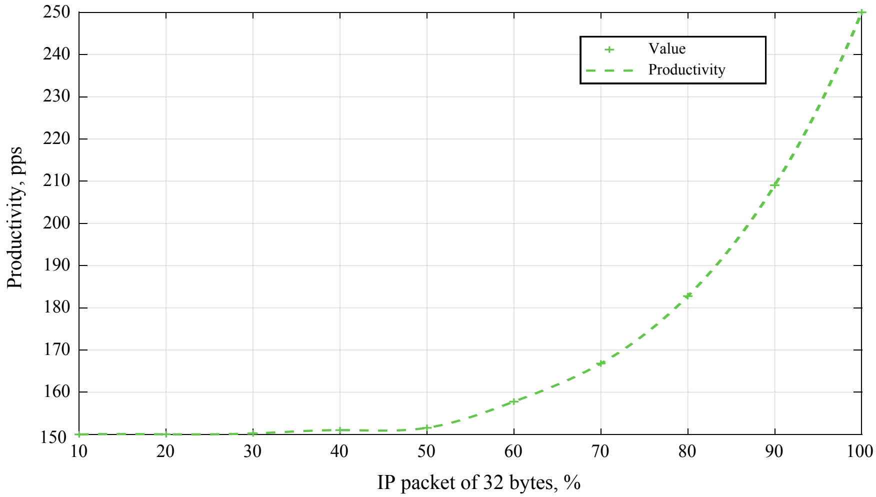

Fig. 2 Switching node productivity when servicing type "B" IP packets

and in the general case, if the inefficiency factor of use of the router RAM servicing space is taken into account, we obtain the following

$$C_{IP} = \frac{1}{t_{serv}}\left[3k_{250}\left(1 - P_B^5\right) + 5k_{8000}P_B^5\right] = \frac{1}{t_{serv}}\left[3k_{250} + (5k_{8000} - 3k_{250})P_B^5\right]$$

With 10% of processing of "B" packets, the performance is equal to $C_{IP} = 150.001$ [Packets/s].

As a percentage of the increase in the "B" IP packet service, the performance of the switching node is as follows (Fig. 2).

3 Experimental Part

Actually, it is almost impossible to verify the resulting mathematical model. In this regard, to verify the obtained mathematical model, a simulation model built in the Cisco Packet Tracer 7.3.0 data network simulator was used (Fig. 3).

The modeling process included several stages:

1. The transfer of the 1024-byte packet flow from PC2 to PC3 was provided with the help of a traffic generator.
2. An echo request (ping) with a 32-byte packet was sent from PC1 to PC3.
3. The echo request was repeated each time the number of 32-byte packets increased by 10%.

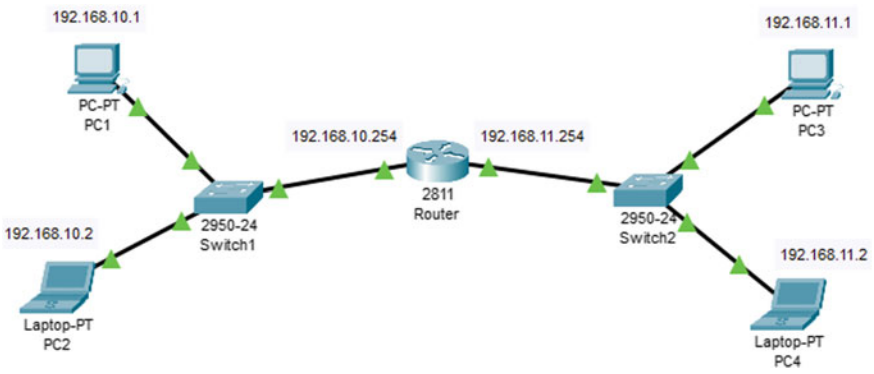

Fig. 3 Simulation model

A graphical representation of the results of the router performance and throughput simulation is shown in Fig. 4.

As can be seen from Figs. 2 and 4, the results of mathematical and simulation modeling of the router performance coincide, which indicates the adequacy of the obtained mathematical model. With 50% of 32-byte packets, the router performance and throughput are almost unchanged.

As a result of the simulation and its verification, let us derive a formula for determining the router throughput in a general form

$$B_{IP} = 8\sum_i \frac{M_R k_{ni}}{\max\left(t_{serv,i}\right)} P(H_i)\ [\text{Bit/s}], \tag{2}$$

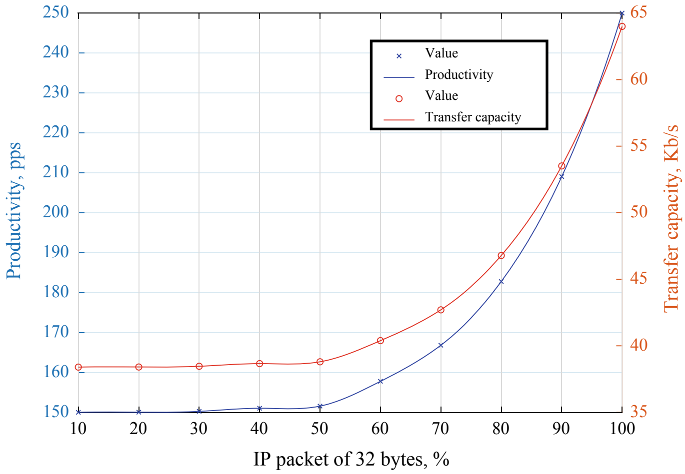

Fig. 4 Productivity and transfer capacity of the switching node in the simulation

where H_i is the hypothesis concerning the combination of IP packets of various size, $R(H_i)$ is the probability of the Hi hypothesis, M_{Ri} is the amount of space in RAM or the number of packets being serviced, $\max(t_{serv,i})$ is the maximum time delay introduced by the router.

4 Conclusion

Using this model, it is possible to calculate the performance and throughput of a router at a non-constant amount of RAM space. It should be noted that this model considers the switching node of an IP network only with sequential descent of packets. It also does not include a number of factors that significantly affect the router throughput, such as the method used to switch packets in the switching matrix of the router and queue formation [7], the size of the router buffer [13–16], and so on.

The development of a method for calculating the throughput of IP network switching nodes, taking into account the influencing factors, as well as mathematical and simulation modeling, are fundamental methods in the design and use of telecommunications networks.

Acknowledgements The research is carried out according the project with S. Seifullin Kazakh Agrotechnical University and within the framework of Tomsk Polytechnic University Competitiveness Enhancement Program grant.

References

1. Recommendation ITU-T Y.1541: Network performance objectives for IP-based services (2011). https://www.itu.int/rec/T-REC-Y.1541-201112-I/en
2. Recommendation ITU-T Y.1540: Internet protocol data communication service—IP packet transfer and availability performance parameters (2019). https://www.itu.int/rec/T-REC-Y.1540-201912-I
3. Fazio, P., Tropea, M., Voznak, M., De Rango, F.: On packet marking and Markov modeling for IP Traceback: a deep probabilistic and stochastic analysis. Comput. Netw. **182**, 107464 (2020). https://doi.org/10.1016/j.comnet.2020.107464
4. Dunayev, P.A., Ryabtsunov, SYu.: Statistical modeling of the IPTV network to estimate the channel throughput taking into account the packet service time. TUSUR Rep. **3**(20), 172–176 (2017)
5. Krishna, D.G., Raina, J.G.: Right buffer sizing matters: some dynamical and statistical studies on Compound TCP. Perform. Eval. **139**, 102095 (2020). https://doi.org/10.1016/j.peva.2020.102095
6. Kobylyansky, V.G., Sementsova, A.G.: The analysis of computer networks in the software package of cisco packet tracer. Tech. Sci. Theory Practice 39–46 (2017).
7. Kurose, D., Ross, K.: Computer networks: a top-down approach. E Publishing House, Moscow (2016)

8. Chrysos, N., Neeser, F., Gusat, M., Minkenberg, C., Denzel, W., Basso, C., Rudquist, M.R., Valk, K.M.: Large switches or blocking multi-stage networks? An evaluation of routing strategies for datacenter fabrics. Comput. Networks **91**, 316–328 (2015). https://doi.org/10.1016/j.comnet.2015.08.029
9. Alizadeh, M., Edsall, T.: On the data path performance of leaf-spine datacenter fabrics. In: Proceedings of the 21st Annual Symposium on High-Performance Interconnects, pp. 71–74 (2013). https://doi.org/10.1109/HOTI.2013.23
10. Andreades, P., Watts, P.M.: Low latency parallel schedulers for photonic integrated optical switch architectures in data center networks. In: Proceedings of the European Conference on Optical Communication, 2017 Sept, pp 1–3 (2017). https://doi.org/10.1109/ECOC.2017.8345961
11. Trevisan, M., Finamore, A., Mellia, M., Munafo, M., Rossi, D.: Traffic analysis with off-the-shelf hardware: challenges and lessons learned. IEEE Commun. Mag. **55**(3), 163–169 (2017). https://doi.org/10.1109/MCOM.2017.1600756CM
12. Vaton, S., Brun, O., Mouchet, M., Belzarena, P., Amigo, I., Prabhu, B.J., Chonavel, T.: Joint minimization of monitoring cost and delay in overlay networks: optimal policies with a markovian approach. J. Netw. Syst. Manage **27**(1), 188–232 (2017). https://doi.org/10.1007/s10922-018-9464-1
13. Appenzeller, G., Keslassy, I., McKeown, N.: Sizing router buffers. Comput. Commun. Rev. **34**(4), 281–292 (2004). https://doi.org/10.1145/1030194.1015499
14. Beheshti, N., Ganjali, Y., Ghobadi, M., McKeown, N., Salmon, G.: Experimental study of router buffer sizing. In: Proceedings of the ACM SIGCOMM Internet Measurement Conference, pp. 197–210 (2008). https://doi.org/10.1145/1452520.1452545
15. Surzhikov, A.P., Frangylyan, T.S., Ghyngazov, S.A.: A dilatometric study of the effect of pressing on the kinetics of compression of ultrafine zirconium doxide powders under thermal annealing. Russ. Phys. J. **55**(4), 345–352 (2012). https://doi.org/10.1007/s11182-012-9818-1
16. Wischik, D., McKeown, N.: Part I: buffer sizes for core routers. Computer Commun. Rev. **35**(3), 75–78 (2005). https://doi.org/10.1145/1070873.1070884

Investigation of the Liquid Flow on Rough Surfaces to Solve the Problems of Liquid Penetrant Testing

Irina Lobanova, Aleksey Vodopyanov, and Aleksey Kalinichenko

Abstract Cleanliness of the test surface is of particular importance in liquid penetrant testing. The surface cleanliness implies both the quality of surface cleaning from polluting substances, for example, oil, and the quality of its treatment, i.e. surface roughness. The surface roughness parameter increased to more than $Rz = 20\ \mu\text{m}$ can lead to unreliable test results since each groove on a rough surface will be a capillary for liquid spreading. Therefore, it will be difficult to completely remove the penetrant from the surface of the test object while removing its excess, which causes an indicator background of the surface and complicates defect detection. The study aims to determine the effect of liquid wettability on liquid penetrant testing results depending on the surface roughness. The paper proposes a mathematical model of liquid spreading on the rough surface depending on physicochemical properties of the liquid itself and material properties of the test object. The numerical modelling of the process is performed. The modelling results are confirmed experimentally, and statistical processing of the experimental results is performed.

1 Introduction

Liquid penetrant testing is currently one of the most effective methods of non-destructive testing to accurately identify defects on the surface of the investigated object, their length and direction. This method enables detection of defects with an opening of less than 1 μm in products made from different non-porous materials, such as plastic, glass, and magnetic and non-magnetic metals [1–3].

I. Lobanova (✉) · A. Vodopyanov · A. Kalinichenko
Division for Testing and Diagnostics, National Research Tomsk Polytechnic University,
30 Lenin Avenue, Tomsk, Russia 634050
e-mail: konarevai007@tpu.ru

A. Vodopyanov
e-mail: mariinsk888@yandex.ru

A. Kalinichenko
e-mail: lex-k@tpu.ru

I. V. Minin et al. (eds.), *Progress in Material Science and Engineering*,
Studies in Systems, Decision and Control 351,
https://doi.org/10.1007/978-3-030-68103-6_9

The main advantages of the method are:

- independence of test effectiveness on the product shape and geometry;
- ease of work performed;
- lack of need in complex and expensive equipment;
- method mobility;
- ability to detect defects on thin-walled parts with a thickness of 0.1–50 μm.

The method implies penetration of special liquids, flaw detection materials, into surface and through defects, which increase the light and color contrast of the defective area relative to the defect-free area during testing [4–8].

The quality of the flaw detection materials used depends on many parameters:

- properties of the materials included in the kit;
- technology used and testing conditions;
- ability of the kit to provide the required test sensitivity;
- surface state and the type of material of the test object [9];
- flaw detection kits include penetrant, cleaner and developer.

To ensure reliable detection of defects on the surface, penetrants used in testing should show good penetrating and wetting abilities [10, 11].

The penetration of liquids can depend on viscosity, density and polarity of the liquid, leakage and filtration properties, and roughness of the test surface [12, 13].

The surface roughness is considered as a combination of surface irregularities with relatively small steps within the base length.

On the one hand, the greater the roughness, the more distinctly its properties manifest themselves, which determines attraction or repulsion of the liquid from the surface. This effect can be attributed to the fact that at an edge angle less than 90° (for a smooth surface), the liquid penetrates into the cavities on the surface, similar to how it is absorbed into capillaries. This effect improves wetting of the test surface with liquid. If the contact angle is greater than 90°, liquid does not penetrate into cavities, which impairs wetting of the rough surface [14].

On the other hand, increased roughness improves liquid spreading, because each groove on the rough surface is a microchannel for liquid to spread. Therefore, some oils and fatty acids do not spread on a polished surface, but spread on the rough surface. Crack walls exhibit higher roughness parameters than the surface treated. Therefore, it should be expected that in clean crack cavities, liquids will show higher degree of wetting, and hence higher penetration [15, 16].

If the surface roughness is greater than the parameter $Rz = 20\ \mu\text{m}$, excess penetrant cannot be completely removed due to micro-grooves on the surface, which causes formation of a false indicator background and, hence, leads to unreliable testing results [17–20].

The study aims to determine the effect of wettability, namely, liquid spreading on the rough surface, on liquid penetrant testing results. The proposed program code increases the quality of studies aimed to determine the liquid flow in capillaries for research purposes, and it can be used to develop new flaw detection materials.

2 Program Description

A Wettability program was developed to reveal the effect of surface roughness on liquid spreading.

The program is based on the equation of liquid spreading on the rough surface, according to the so-called hydrodynamic viscous mode [2], in which the radius of the spreading spot is calculated using Eq. (1).

$$r = \sqrt[\frac{1}{4}]{\frac{4 \times \cos \Theta \times m}{\chi \times \pi \times \rho \times \eta \times K \times \sigma} \times t} \tag{1}$$

where r is the spot radius at time t (measured in m); θ is the contact angle of wetting (measured in degrees); K is surface roughness factor (dimensionless quantity); m is liquid droplet mass (measured in g); χ is the coefficient approximately equal to 10, which takes into account the increase in friction forces in the liquid due to the presence of the angular velocity of its flow (since each elementary trickle expands simultaneously when moving along the radius); ρ is liquid density (measured in g/cm^3); η is liquid viscosity (measured in Pa × s); σ is surface tension coefficient (measured in N/m).

The surface roughness factor was determined as the reciprocal of the arithmetic mean height of roughness Ra (2):

$$K = \frac{1}{R_a} \tag{2}$$

Figure 1 shows a block diagram of the developed program.

If the equation parameters are incorrectly set, the program displays an error message and asks to re-enter the data correctly.

The interface of the program for computer simulation of the effect of liquid spreading on the rough surface is shown in Fig. 2.

The left side contains the input and output windows of the task parameters. These windows are related to geometric and material parameters of the model and to parameters of the calculation method and graphical interpretation of the results. The first block contains the following parameters:

- mass of a liquid droplet (measured in g);
- liquid density (measured in g/cm^3);
- liquid viscosity (measured in Pa × s);
- wetting angle (measured in degrees);
- roughness factor (dimensionless quantity);
- time of observation (measured in s);
- surface tension coefficient (measured in N/m);
- the number of points is the parameter required to plot a common graph of modelling results with varied task parameters.

Fig. 1 Block diagram of the wettability program

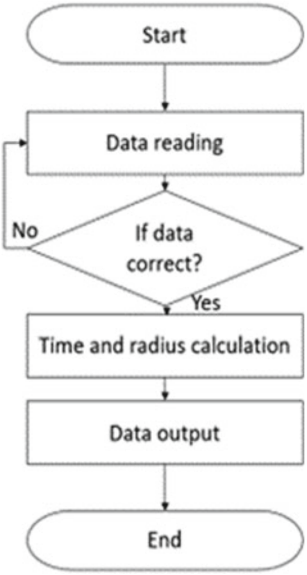

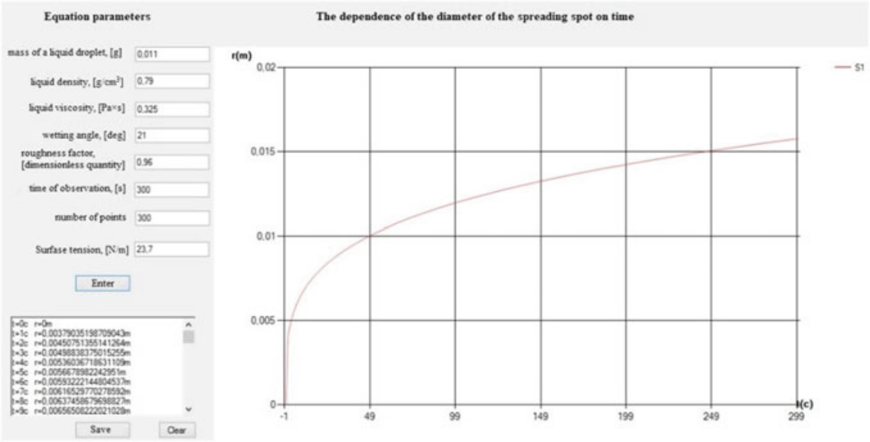

Equation parameters

mass of a liquid droplet, [g] 0.011
liquid density, [g/cm³] 0.79
liquid viscosity, [Pa×s] 0.325
wetting angle, [deg] 21
roughness factor, [dimensionless quantity] 0.96
time of observation, [s] 300
number of points 300
Surfase tension, [N/m] 23.7

```
t=0c  r=0m
t=1c  r=0.00379035198709043m
t=2c  r=0.00450751355141264m
t=3c  r=0.004988838375015255m
t=4c  r=0.00536036718631109m
t=5c  r=0.0056678982242951m
t=6c  r=0.00593222144804537m
t=7c  r=0.00616529770278592m
t=8c  r=0.00637458679698827m
t=9c  r=0.00656508222021028m
```

Fig. 2 Interface of the wettability program

An output field for intermediate results is in the lower left corner. The field is a simplified text editor that enables viewing of all intermediate values and operating them if necessary. The editor includes two columns—the current time value and radius of the spreading spot.

We have studied spreading of an acetone-based penetrant on plastic surface with various roughness areas. The roughness parameters Rz were 10, 20, and 30 μm.

Table 1 Values of the main equation parameters

Liquid	Droplet mass [g]	Liquid density [g/cm^3]	Liquid viscosity [Pa × s]	Wetting angle [deg]	Surface tension [H/m]
Acetone	0.011	0.79	0.325	21	23.7

Table 1 shows the values of the main equation parameters for acetone liquid and plastic material.

We have studied spreading of an acetone-based penetrant on plastic surface with various roughness areas. The roughness parameters Rz were 10, 20, and 30 μm.

These equation parameters were entered into the input windows of the Wettability program, and modeling of liquid spreading on the surface was performed with different roughness parameters.

3 Model Experiments

Table 2 presents the modeling results of the acetone-based penetrant spreading on a plastic plate with regard to various roughness parameters.

Graphical interpretation of the results is presented in Fig. 3.

The obtained curves indicate that the surface roughness affects the process of liquid spreading. The increased surface roughness leads to the increased size of the spreading spot; therefore, liquid spreads better on the rough surface.

Table 2 Modeling results of dependence of liquid spreading on time

D [mm] t [s]	Rz = 10 [μm]	Rz = 20 [μm]	Rz = 30 [μm]
1	10.2	12.0	12.8
3	13.6	15.8	16.8
5	15.4	18.0	19.2
7	16.8	19.6	20.8
10	18.4	21.4	22.8
15	20.3	23.8	25.2
20	21.8	25.6	27.2
30	24.1	28.2	30.0
50	27.4	32.2	34.2
80	30.8	36.2	38.4
120	34.2	40.0	42.6
200	38.8	45.4	48.4
300	43.0	50.4	53.4
360	45.0	52.6	56.0

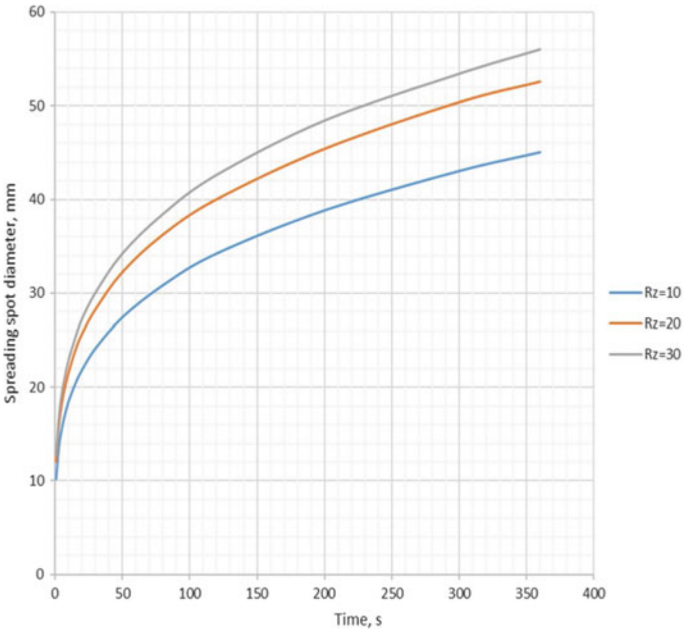

Fig. 3 Modeling results of liquid spreading on the rough surface

4 Experimental Study of Liquid Wettability

The following experiment was conducted to test the Wettability program.

Acetone-based penetrant was applied to a plastic plate with various roughness areas produced by machining the surface with sandpaper of different grain size, and liquid spreading was monitored for some time. The droplet volume was constant. The spreading time was recorded using a stopwatch. The spot diameter was measured using a caliper.

Figure 4 shows a plate with different roughness parameters and penetrant droplets applied.

Table 3 shows the experimental dependence of the penetrant spot spreading on the rough surface on time.

Figure 5 shows graphical interpretation of the results presented in the Table 3.

As can be seen from the graph, the larger the surface roughness parameter, the larger the liquid spot diameter.

The next stage was the penetrant testing performed on a plastic sample using a flaw detection kit. At the stage of removing excess penetrant from the test object surface, a false surface background occurred on the plate with the roughness area of Rz = 30 µm. This can be attributed to the capillary effect, that is each groove of the rough surface was a capillary through which the liquid propagated, which can lead to unreliable test results.

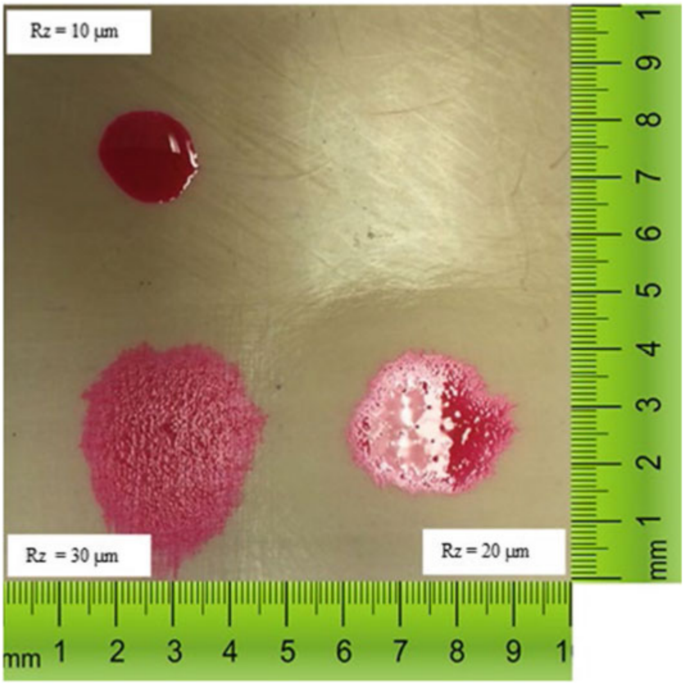

Fig. 4 Plate with penetrant droplets applied

Table 3 Experimental dependence of the diameter of the liquid spot spreading on time

D [mm] t [s]	Rz = 10 [μm]	Rz = 20 [μm]	Rz = 30 [μm]
1	9.7	9.9	11.2
3	12.2	14.5	14.6
5	13.6	17.0	17.0
7	14.6	18.9	18.9
10	15.4	20.9	20.8
15	17.1	22.8	23.3
20	18.4	24.1	25.3
30	19.9	26.1	28.0
50	21.7	28.9	31.5
80	23.8	31.4	35.0
120	25.9	33.7	38.9
200	29.8	36.3	42.4
300	31.9	38.8	45.3
360	33.5	40.7	47.4

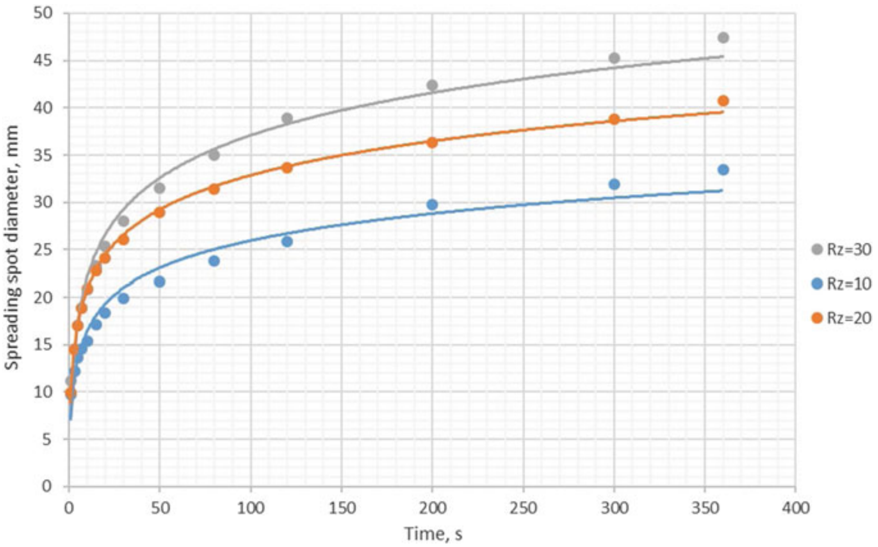

Fig. 5 Experimental dependence of the liquid spot spreading on time

After that, the modeling results were compared with the results of full-scale experiments of penetrant spreading on the rough surface.

The experimental results were statistically processed to determine the average value, standard deviation, and confidence interval. Figures 6, 7 and 8 present the graphs.

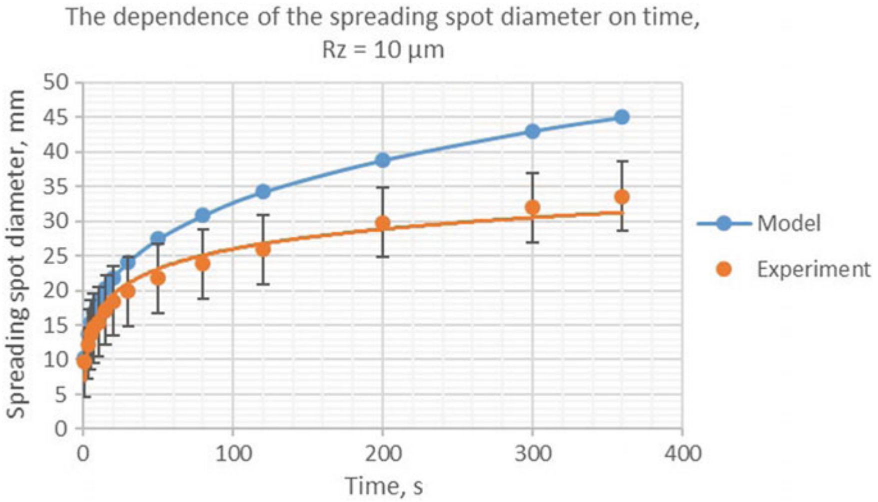

Fig. 6 Comparison of the modeling results with the experimental values at Rz = 10 µm

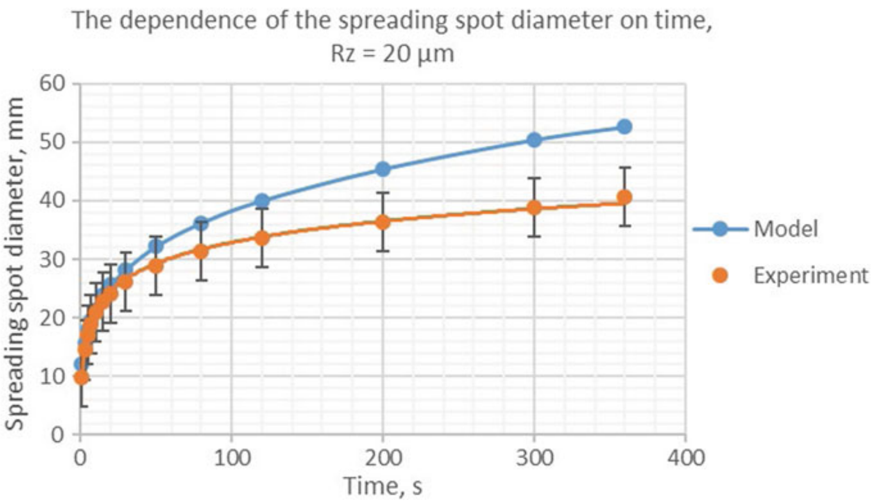

Fig. 7 Comparison of the modeling results with the experimental values at Rz = 20 µm

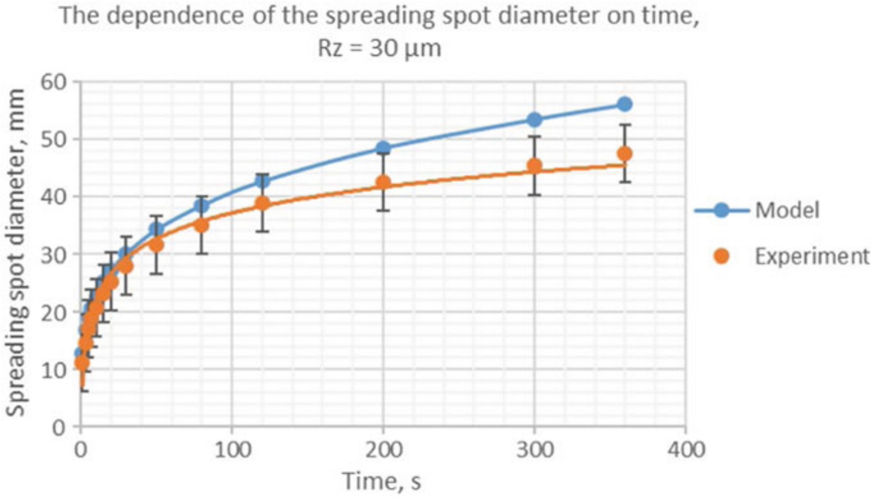

Fig. 8 Comparison of the modeling results with the experimental values at Rz = 30 µm

The curves obtained in modeling are within the confidence intervals, and thus they indicate the efficiency of the proposed mathematical model of liquid spreading on the rough surface at the initial stages of spreading.

5 Conclusion

Mathematical model of liquid spreading on the rough surface is based on the liquid spreading equation according to the hydrodynamic viscous mode.

Modeling of acetone-based penetrant spreading on a plastic plate with different surface roughness parameters is performed.

Efficiency of the mathematical model is confirmed experimentally.

Increase in the roughness parameter contributes to better liquid spreading on the surface.

Since each groove on the rough surface is a capillary through which liquid spreads, the penetrant cannot be completely removed from the surface at the stage of removing excess penetrant from the surface of the test object, which can cause invalid results of penetrant testing.

References

1. Gholizadeh, S.: A review of non-destructive testing methods of composite materials. Proc. Struct. Integrity **1**, 50–57 (2016). https://doi.org/10.1016/j.prostr.2016.02.008
2. Scott, I.G., Scala, C.M.: A review of non-destructive testing of composite materials. NDT Int. **15**(2), 75–86 (1982). https://doi.org/10.1016/0308-9126(82)90001-3
3. Kerber, M.L., Vinogradov, V.M., Golovkin, G.S.: Polymer composite materials. Properties Structure. Technology, Profession, St. Petersburg (2008)
4. Borovikov, A.S., Prokhorenko, P.P., Dezhkunov, N.V.: The physical basis of capillary flaw detection. Science and technology, Minsk (1983)
5. Zimon, A.D.: Fluid Adhesion and Wetting. Chemistry, Moscow (1974)
6. Prokhorenko, P.P., Migun, N.P.: Introduction to the Theory of Capillary Testing. Science and technology, Moscow (1988)
7. Rozina, M.V., Yablonik, L.M., Vasiliev, V.D.: Non-destructive testing in shipbuilding: Handbook of the flaw detector. Shipbuilding, Leningrad (1982)
8. Kanevsky, I.N., Salnikova, E.N.: Nondestructive Testing Methods: Textbook. Publishing House DVGTU, Vladivostok (2007)
9. Sergienko, A.A., Zhou, W.: Hydraulic resistance and heat exchange on a rough surface. Izvestiya Vysshikh Uchebnykh Zavedenij. Aviatsionnaya Tekhnika **4**, 49–51 (2004)
10. Glazkov, Y.A.: On the issue of evaluating the wetting ability of liquids for capillary flaw detection. Defectoscopy **11**, 57–62 (1990)
11. Sum, B.D., Goryunov, Yu.V.: Physico-Chemical Fundamentals of Wetting and Spreading, Mechanical Engineering, Moscow (1978)
12. Lobanova, I.S., Meshcheryakov, V.A., Kalinichenko, N.P., Kalinichenko, A.N., Kiseleva, M.S.: Modeling the penetration of liquids into the discontinuity of products from non-metallic materials. Polzunovsky Bull. **4**, 103–107 (2016)
13. Osipov, A.O., Osipov, O.P.: Problems of filtration and separation of anti-water-crystallization liquids during fuel pumping through filtered cardboards at low temperatures. Sci. Bull. MSTU GA **173**, 134–136 (2011)
14. Zhdanov, K.V., Erokhin, M.S., Stepkina, MYu., Zhirnov, A.A., Kudryashova, O.B.: Investigation of the effect of electrostatic surface charge on the wetting angle. Polzunovsky Bull. **2**, 222–226 (2016)
15. Pavlovskiy, V.A., Chistov, A.L., Shestov, K.V.: Flows modeling in pipes with rough walls. Marine Intell. Technol. **1**(4), 109–113 (2016)

16. Nikolaev, A.N.: Dynamics of film flow of a liquid in channels with large-scale regular roughness. Academenergo Labor **4**, 44–51 (2008)
17. Loytsyanskii, L.G.: Mechanics of Liquid and Gas. Science, Moscow (1987)
18. Volkov, V.I., Kozlov, D.U., Kirkolup, E.R.: Research of dynamics of liquid motion by capillary. Lett. Altai State Univ. **1**, 100–104 (2007)
19. Kanchukoev, V.Z., Karamurzov, B.S., Sozaev, V.A., Chernov, V.V.: Determination of the initial velocity and duration of motion of a fluid in capillaries. J. Eng. Phys. Thermophys. **76**, 49–53 (2003). https://doi.org/10.1023/A:1022907022849
20. Kamalov, R.F., Shamsutdinov, E.V., Vachagina, E.K.: Development of an experimental installation and study of the intensification of heat exchange in channels with a discrete-rough surface in the laminar flow of viscous media. Academenergo Labor **4**, 23–37 (2009)

Innovations in Technical Diagnostics and Materials Science

Diagnostics of Metal Nanopowders Produced by Electrical Explosion of Wires

Olga Nazarenko and Yulia Amelkovich

Abstract The features of using standard physicochemical methods of analysis for determining the basic characteristics of metal nanopowders are discussed. The methods for the analysis of the shape and size of particles, the value of the specific surface area, the particle size distributions, and parameters of chemical activity of metal nanopowders are considered. The combination of these diagnostic characteristics makes it possible to predict the technical properties of metal nanopowders and evaluate their qualities for use in technology. The experimental results of diagnostics of aluminum and tungsten nanopowders produced by the electric explosion of wires are presented.

1 Introduction

The development of engineering and technology is characterized by the transition to objects of the nanometer range (≤100 nm) to improve the physical, chemical, and mechanical characteristics of materials [1, 2]. Reducing the size of structural elements is one of the ways to impart qualitatively new properties to a substance, which allows a significant increase in product quality and an increase in the productivity of technological processes.

Nanopowders (NPs) can be obtained by various methods [3–5]. One of the promising methods for producing nanopowders is the electrical explosion of wires (EEW), which makes it possible to control the dispersed composition, physical, chemical, and other properties of the powders obtained [6–11]. The EEW process is characterized by a high energy density (>10^{14} W/s) and rapid heating (>10^{7} K/s) of the metal wire to high temperature (>10^{4} K) [6, 8]. The formation of nanodispersed

O. Nazarenko (✉) · Y. Amelkovich
Division for Testing and Diagnostics, National Research Tomsk Polytechnic University,
30 Lenin Avenue, Tomsk, Russia 634050
e-mail: olganaz@tpu.ru

Y. Amelkovich
e-mail: amely@tpu.ru

I. V. Minin et al. (eds.), *Progress in Material Science and Engineering*,
Studies in Systems, Decision and Control 351,
https://doi.org/10.1007/978-3-030-68103-6_10

particles during EEW occurs under highly nonequilibrium conditions. Due to the nonequilibrium conditions of production, electroexplosive NPs of metals have several unusual properties: after passivation, they are resistant to oxidation and sintering at room temperature and are characterized by high diffusion activity upon heating. The combination of unusual properties of electroexplosive NPs makes it possible to use them in the preparation of alloys and composite materials as additives that reduce the sintering temperature and reduce the interaction time, as reagents in the preparation of complex organic compounds and biologically active drugs, as modifiers of polymers for the preparation of functional materials, etc.

Metal NPs are metastable systems [8, 12, 13]. Even if NPs of metals are stored in an inert atmosphere, processes of recrystallization, diffusion sintering, diffusion of water reduction products, etc. occur simultaneously in them. The problems of the diagnostics of the metal NPs are associated with the instability of their properties and high reactivity, and difficulties arise in the interpretation of the results as well [14, 15]. The choice of diagnostic methods is not only a technical but also a theoretical problem. Diagnostic methods are necessary both for analysis of the properties of the nanomaterials, studying the effect of production conditions on their phase composition and structure, and for monitoring the characteristics of NPs as input raw materials in various nanotechnologies.

This work aims to substantiate the use of standard physicochemical methods of analysis and corresponding parameters for diagnostics of metal nanopowders. For testing, we selected aluminum (Al) and tungsten (W) nanopowders obtained by the electric explosion of wires in argon and nitrogen.

2 Experimental

Aluminum and tungsten NPs were produced on the installation UDP-4G. The operation of the installation is described in detail in [8, 16]. The conditions for the production of aluminum and tungsten NPs (d_w is the diameter of the wire, V is the charging voltage, e/e_s is the ratio of the specific energy input in the wire e to the sublimation energy of the wire material e_s, e_a/e_s is the ratio of the arc stage energy e_a to the sublimation energy of the wire material, kind of gas in the discharge chamber and pressure) and the characteristics of the dispersion of the obtained powders (S_{sp} is the specific surface area, $\bar{a}_s$ is the mean surface particle diameter) are presented in Table 1. The passivation with low oxidation by working gas +0.1 vol.% air was carried out after the production of the metal NPs to prevent their self-ignition after the contact with air.

The ohmic shunt and the S8-17 oscilloscope were used for current measurement. The voltage on the exploding wire was measured using the ohmic voltage divider. The phase composition of the final products was investigated by an X-ray diffractometer DRON-3.0 using CuKα-radiation. The size and shape of the particles were determined using a JSM-840 scanning electron microscope (SEM) and a Hitachi H-8100 transmission electron microscope (TEM). The reactivity of the powders was

Table 1 Electrical explosion conditions for aluminum and tungsten wires

Material of wire	d_w (mm)	V (kV)	e/e_s	e_a/e_s	Gas	P (Pa)	S_{sp} (m^2/g)	$\bar{a}_s$ (nm)
Al	0.35	24	1.5	0.4	Ar	1.5×10^5	12	120
W	0.2	22	1.1	0.5	Ar	1.5×10^5	3.9	79
W	0.3	23	0.4	1.1	N_2	1.5×10^5	1.9	164
W	0.3	23	0.7	0.8	N_2	1.5×10^5	1.7	183
W	0.3	23	0.4	0.9	N_2	0.3×10^5	2.6	120

investigated using an SDT Q600 thermal analyzer. The thermal analysis was carried out in a linear heating mode from 20 to 1000 °C at a heating rate of 10 °C/min in an air atmosphere. The particle size distributions were analyzed by the laser diffraction technique using a Malvern Mastersizer.

3 Results and Discussion

3.1 Disperse Composition and Particle Size Distribution

Disperse composition of powders is one of the most important parameters that determine their technical characteristics (bulk density, flowability, reactivity, etc.), and, consequently, the field of application. With an increase in the dispersion of metal NPs (with a decrease in the particle size below 100 nm), their activity increases [17, 18], but the content of metals in the particles also decreases. Powder particles obtained by the EEW method, as a rule, have a spherical shape, and the powders themselves are polydisperse systems. The particle size of electroexplosive NPs varies in a wide range: from 5×10^{-9} to 10^{-3} m. The production of metal NPs with a size less than 30 nm is inexpedient due to the low sintering temperature, instability to oxidation during passivation and agglomeration. In inert media, powders with a size less than 30 nm are sintered by a diffusion mechanism, and in chemically active media, they interact with an explosion. Therefore, the problem of finding the conditions for obtaining nanopowders that provide a high dispersion and narrow particle size distribution in the range of 30–60 nm is relevant and directly related to the problem of diagnostics of the disperse composition of NPs.

According to the SEM images, the aluminum NP consists of the particles with a diameter of ~100 nm (Fig. 1a) but it also contains the particles of both a larger diameter ~200 nm and a smaller diameter ~50 to 60 nm. The shape of the particles is close to spherical; there are separate agglomerates of particles that are partially sintered. Tungsten nanoparticles also have a shape close to spherical with a smooth surface [19, 20]. Figure 1b shows the SEM image of sample 3 from Table 1. It can be seen that most of the particles have a diameter of less than 100 nm.

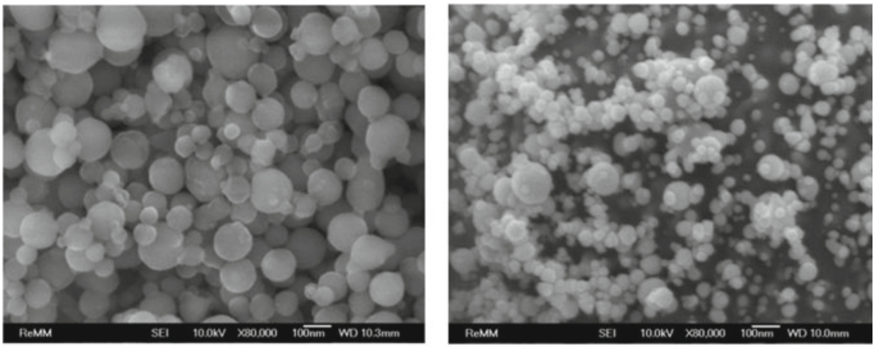

a) b)

Fig. 1 SEM images of aluminum **a** and tungsten **b** nanopowders

Figure 2a shows a TEM image of the aluminum nanoparticle. The aluminum nanoparticle consists of a metal core and an outer shell [16]. During the formation of nanoparticles under highly non-equilibrium conditions typical for EEW, a redistribution of impurities occurs in the surface layers and near-surface layers. In the process of cooling aluminum nanoparticles, refractory impurities, which were initially contained in the original wire (Fe, Mn, Cu), are concentrated in the near-surface layers. When the powders are passivated by slow oxidation of air, the gas-medium is desorbed, the air components are adsorbed, and a protective oxide-hydroxide layer is formed. Unlike coarse powders, the thickness of oxide-hydroxide layers on the metal nanoparticles ranges from 2 to 8 nm. Moreover, with a decrease in the particle diameter from 100 to 50 nm, the thickness of oxide-hydroxide layers decreases.

Figure 2b shows a TEM image of the tungsten nanoparticle (sample 2, Table 1).

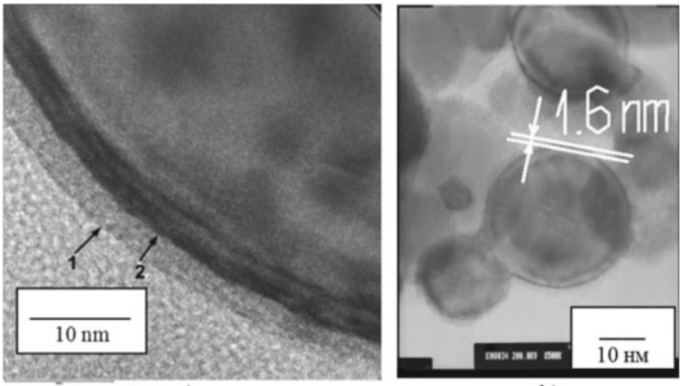

a) b)

Fig. 2 TEM images of aluminum **a** and tungsten **b** nanopowders

The thickness of the oxide layer on the tungsten nanoparticle is 1.6 nm [21, 22]. At such a thickness, the oxide layers are X-ray amorphous, which makes it difficult to determine their phase composition using X-ray phase analysis.

All electroexplosive powders are characterized by a three-modal particle size distribution, which is associated with the mechanism of destruction of the wires in the process of EEW and subsequent cooling of the primary products of the EEW [3, 16, 19]. Figure 3 shows the graphs of the particle size distribution for the tungsten NPs obtained by EEW.

The graphs of the particle size distribution make it possible to judge the effect of production conditions on the disperse composition of powders. When replacing the working gas from argon to nitrogen at a pressure of 1.5 × 10^5 Pa, the particle diameter corresponding to the first maximum on the distribution curve decreases from 0.686 to 0.169 μm, and the average particle diameter decreases from 2.404 to 0.694 μm (Fig. 3a, b). When using nitrogen as working gas, with a decrease in pressure from 1.5 × 10^5 to 0.3 × 10^5 Pa, the particle diameter corresponding to the first maximum did not change and was 0.169 μm, but the average particle diameter

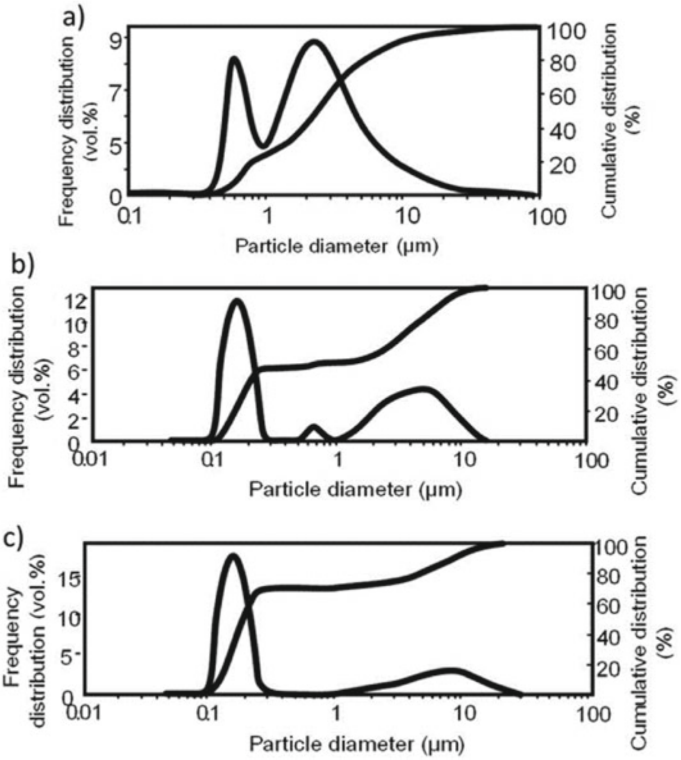

Fig. 3 Particle size distribution of tungsten nanopowders produced in **a** Ar, $P = 1.5 \times 10^5$ Pa, **b** N_2, $P = 1.5 \times 10^5$ Pa, **c** N_2, $P = 0.3 \times 10^5$ Pa

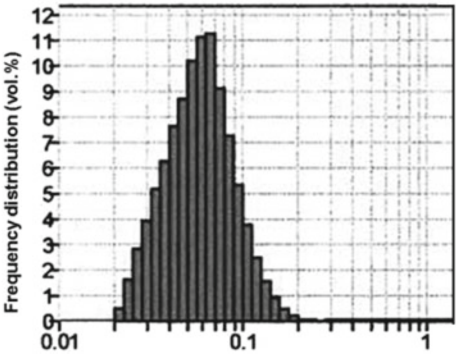

Fig. 4 Particle size distribution of tungsten nanopowder

in the powder decreases from 0.694 to 0.196 μm (Fig. 3b, c). The number of particles corresponding to the first maximum on the distribution curve increases accordingly.

It should be noted that there are no nanodispersed particles in the particle size distribution plots. This is explained by the peculiarities of the formation of electrical explosion products: in the process of the scattering of the wire destruction products, agglomerates are formed, the presence of which introduced an error in the measurements of the particle size of the powder by the laser diffraction technique. At the same time, electron microscopic studies (Fig. 2b) showed the presence of particles of the nanodispersed range. These results indicate the need for preliminary preparation of powders for the destruction of particle aggregates before analysis. The tungsten NP (sample 2, Table 1) was previously suspended in ethanol and sonicated (200 W, 22 kHz) for 15 min before analysis to determine the particle size distribution. According to the results obtained (Fig. 4), the tungsten NP has a relatively narrow particle size distribution in the range of 0.02–0.2 μm with a maximum of 0.06 μm [21, 22].

3.2 Reactivity Parameters

Differential thermal analysis (DTA) is used to test the stability of nanopowders and their mixtures to oxidation and chemical interaction [23–28]. Based on the DTA data, four parameters of chemical activity are determined. The parameters of the chemical activity of metal nanopowders are understood as the following values [24, 26]:

1. The temperature of oxidation onset t_o (°C) characterizes the thermal stability of nanopowders in the air; it is defined as the temperature at which an increase in the sample mass begins.
2. The maximum oxidation rate v_{max} (mg/s) characterizes the intensity/rate of weight gain and heat release during oxidation.

3. The degree of oxidation α (%) is determined for a given temperature range and characterizes the degree of conversion of the initial nanopowder into oxidation products.
4. Specific thermal effect or specific heat release Δ*H* (J/g) defines the amount of the heat released normalized to the mass of the nanopowder.

The practice has shown that the use of weighed portions of NPs of active metals, for example, aluminum, over 50 mg during DTA, led to combustion or melting of the crucible, combustion of the holder, and other undesirable effects. To reduce the thermal effects during the oxidation of nanopowders in air, it was recommended to use small weighed amounts of powders less than 10 mg.

According to DTA, when heated in air, aluminum NP is highly active (Fig. 5). The desorption of gaseous substances adsorbed on the surface of particles (~3 wt%) at the beginning of the heating is noticeable in the thermogravimetric (TG) curve. Then, there is a sharp increase in the rate of mass growth with a maximum at 630 °C (TG) and the release of heat (DTA).

The oxidation process of tungsten powders included three stages [19]. The presence of two maxima of heat release is associated with the polymodal particle size distribution: in the first place, the fraction of smaller particles is oxidized, and then the larger fraction is oxidized. Thermal activity parameters closely correlate with the dispersion of the studied powders and with the conditions for their preparation.

The parameters of the chemical activity of the studied aluminum and tungsten NPs, necessary for assessing the oxidation resistance, were determined from the data of thermal analysis and are presented in Table 2.

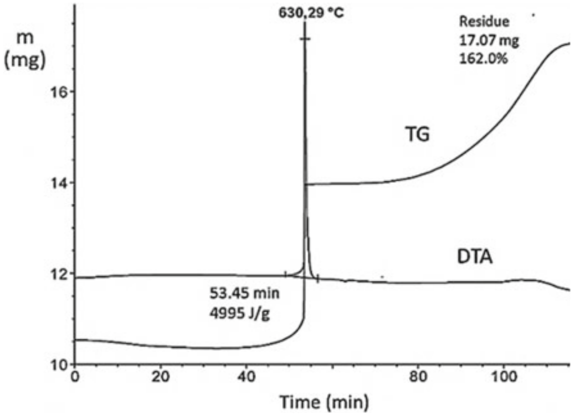

Fig. 5 TG–DTA curves of aluminum nanopowder, $m = 5$ mg

Table 2 Parameters of chemical activity of aluminum and tungsten nanopowders

Sample	t_o (°C)	α (%)	v_{max} (%/s)	Δ*H* (J/g)
Al	450	63.8	0.13	4995
W	370	24.1	0.03	3197

4 Conclusion

The possibility and some features of using standard physicochemical methods of analysis for the diagnostic of metal nanopowders are shown by the example of the analysis of aluminum and tungsten nanopowders obtained by the method of the electrical explosion of wires. The following methods were taken into consideration: the method of low-temperature adsorption of nitrogen, the method for determining the particle size distribution, electron microscopy, and thermal analysis. As a result of the application of these methods, metal nanopowders were characterized by the following characteristics: nanostructural characteristics (particle shape, size, particle surface condition, and specific surface area), particle size distribution, and parameters of chemical activity. The combination of these diagnostic features makes it possible to predict the technical characteristics of metal nanopowders and to select the powders of the required quality for use in nanotechnology.

References

1. Gogotsi, Y.: Nanomaterials Handbook. CRC Press, Boca Raton (2006)
2. Jeevanandam, J., Barhoum, A., Chan, Y.S., et al.: Review on nanoparticles and nanostructured materials: history, sources, toxicity and regulations. Beilstein J. Nanotechnol. **9**(1), 1050–1074 (2018). https://doi.org/10.3762/bjnano.9.98
3. Wang, Y., Xia, Y.: Bottom-up and top-down approaches to the synthesis of monodispersed spherical colloids of low melting-point metals. Nano Lett. **4**(10), 2047–2050 (2004). https://doi.org/10.1021/nl048689j
4. Bozon-Verduraz, F., Fiévet, F., Piquemal, J.-Y., et al.: Nanoparticles of metal and metal oxides: some peculiar synthesis methods, size and shape control, application to catalysts preparation. Braz. J. Phys. **39**(1A), 134–140 (2009). https://doi.org/10.1590/S0103-97332009000200002
5. Khan, I., Saeed, K., Khan, I.: Nanoparticles: properties, applications and toxicities. Arab. J. Chem. **12**(7), 908–931 (2019). https://doi.org/10.1016/j.arabjc.2017.05.011
6. Kwon, Y.S., Jung, Y.H., Yavorovsky, N.A., et al.: Ultra-fine powder by wire explosion method. Scr. Mater. **44**(8–9), 2247–2251 (2001). https://doi.org/10.1016/S1359-6462(01)00757-6
7. Kotov, Y.A.: The electrical explosion of wire: a method for the synthesis of weakly aggregated nanopowders. Nanotechnol. Russia **4**, 415–424 (2009)
8. Nazarenko, O.B., Gromov, A.A., Il'in, A.P. et al.: Electroexplosive nanometals. In: Gromov, A.A., Teipel, U. (eds.) Metal Nanopowders: Production, Characterization, and Energetic Applications, pp. 67–78. Wiley-VCH Verlag GmbH & Co. KGaA, Weinheim (2014)
9. Abdelkader, E.M., Jellis, P.A., Buckner, S.W.: Metal and metal carbide nanoparticle synthesis using electrical explosion of wires coupled with epoxide polymerization capping. Inorg. Chem. **54**(12), 5897–5906 (2015). https://doi.org/10.1021/acs.inorgchem.5b00697
10. Lerner, M.I., Glazkova, E.A., Lozhkomoev, A.S., et al.: Synthesis of Al nanoparticles and Al/AlN composite nanoparticles by electrical explosion of aluminum wires in argon and nitrogen. Powder Technol. **295**, 307–314 (2016)
11. Lázár, K., Varga, L.K., Kis, V.K., et al.: Electric explosion of steel wires for production of nanoparticles: reactions with the liquid media. J. Alloy. Compd. **763**, 759–770 (2018). https://doi.org/10.1016/j.jallcom.2018.05.32
12. Ivanov, G.V., Tepper, F.: "Activated" aluminum as a stored energy source for propellants. Int. J. Energetic Mater. Chem. Propul. **4**(1–6), 636–645 (1997)
13. Blackman, J.: Metallic Nanoparticles, Vol. 5, 1st ed. Elsevier, Oxford (2009)

14. Shuvalov, G.V., Klekovkin, I.V., Ilyin, A.P. et al: Scientific research on nanopowders diagnostics. In: Proceedings of the 6th International Forum on Strategic Technology (IFOST-2011), 49–51 (2011). https://doi.org/10.1109/IFOST.2011.6020962
15. Mourdikoudis, S., Pallares, R.M., Thanh, N.T.K.: Characterization techniques for nanoparticles: comparison and complementarity upon studying nanoparticle properties. Nanoscale **10**, 12871–12934 (2018). https://doi.org/10.1039/c8nr02278j
16. Kwon, Y.-S., Kim, J.-C., Ilyin, A.P., et al.: Electroexplosive technology of nanopowders production: current status and future prospects. J. Korean Powder Metall. Inst. **19**(1), 40–48 (2012)
17. Kwon, Y.S., Gromov, A.A., Ilyin, A.P., et al.: Passivation process for superfine aluminum powders obtained by electrical explosion of wires. Appl. Surf. Sci. **211**(1–4), 57–67 (2003). https://doi.org/10.1016/S0169-4332(03)00059-X
18. Gromov, A.A., Il'in, A.P., Teipel, U. et al.: Passivation of metal nanopowders. In: Gromov, A.A., Teipel, U. (eds.) Metal Nanopowders: Production, Characterization, and Energetic Applications, pp. 133–152. Wiley-VCH Verlag GmbH & Co. KGaA, Weinheim (2014)
19. Kwon, Y.-S., Kim, J.-C., Ilyin, A.P., et al.: Effect of electrical parameters and surrounding gas on the electroexplosive tungsten nanopowders characteristics. J. Korean Powder Metall. Inst. **19**(1), 49–54 (2012)
20. Ilyin, A.P., Nazarenko, O.B., Tikhonov, D.V.: Production of tungsten powders by electrical explosion of wires. J. Optoelectron. Adv. M. **10**(3), 645–648 (2008)
21. Gromov, A.A., Kwon, Y.S., Il'in, A.P., et al.: Specific features of the oxidation of a tungsten nanopowder. Russ. J. Phys. Chem. A **78**(9), 1484–1487 (2004)
22. Kwon, Y.S., Gromov, A.A., Ilyin, A.P., et al.: Features of passivation, oxidation and combustion of tungsten nanopowders by air. Int. J. Refract. Hard. Met. **22**(6), 235–241 (2004). https://doi.org/10.1016/j.ijrmhm.2004.06.005
23. Kwok, Q.S.M., Fouchard, R.C., Turcotte, A.M., et al.: Characterization of aluminum nanopowder compositions. Propell. Explos. Pyrotech. **27**(4), 229–240 (2002)
24. Gromov, A., Ilyin, A., An, V. et al.: Characterization of aluminum powders: I. Parameters of reactivity of aluminum powders. Propell. Explos. Pyrotech. **27**(6), 361–364 (2002)
25. Kwon, Y.S., Moon, J.S., Ilyin, A.P., et al.: Estimation of the reactivity of aluminum superfine powders for energetic applications. Combust. Sci. Tech. **176**(2), 277–288 (2004). https://doi.org/10.1080/00102200490255992
26. Gromov, A., Ilyin, A.: Characterization of aluminum powders: II. Aluminum nanopowders passivated by non-inert coatings. Propell. Explos. Pyrotech. **31**(5) 401–409 (2006)
27. Dilmukhambetov, E., Espolov, T., Ospanova, M., et al.: Reactivity to oxidation of metal nanopowders after electron irradiation. J. Mater. Sci. **2**(1), 175–181 (2013)
28. Sun, Y., Sun, R., Zhu, B., et al.: Thermal reaction mechanisms of nano- and micro-scale aluminum powders in carbon dioxide at low heating rate. J. Therm. Anal. Calorim. **124**(3), 1727–1734 (2016). https://doi.org/10.1007/s10973-016-5284-2

Influence of the Insulation Defects Size on the Value of the Wire Capacitance

Galina Vavilova, Vladislav Yurchenko, and Li Keyan

Abstract The study focuses on detection of defects in the single-core electrical wire insulation by changing the linear capacity of the electric wire. Numerical simulation was performed to create defects that are difficult to implement in practice. In the study, models of the following defects were created: local thinning of the wire insulation, eccentricity, foreign inclusion in the wire insulation. During the study, the depth and length of the 'local thinning' defect in the wire insulation, the shift of the core center relative to wire the center, length and thickness of the 'foreign inclusion' defect were varied. As a result, absolute and relative values of the geometric dimensions of the defects that cause a significant change in the wire capacitance are revealed. A significant deviation of the capacitance is taken at the level of 5% deviation from the nominal value of the capacitance of a defect-free wire in accordance with the requirements of normative and technical documentation and the accuracy of device for in-process testing of the wire capacitance. The paper reports the results of the initial study. Further research is required to increase the reliability of the models used.

G. Vavilova (✉)
Division for Testing and Diagnostics, National Research Tomsk Polytechnic University, 30 Lenin Avenue, Tomsk, Russia 634050
e-mail: wgw@tpu.ru

V. Yurchenko
Department of Information Technology and Security, Karaganda Technical University, 56 Ave. Nursultan Nazarbayev, Karaganda 100027, Republic of Kazakhstan
e-mail: jurchenkovv@mail.ru

L. Keyan
Inspection Business Department, National Lighting Test Center, No. 3 A, Dabeiyaochangpo Village, Chaoyang District, Beijing 100020, China
e-mail: 393678364@qq.com

I. V. Minin et al. (eds.), *Progress in Material Science and Engineering*,
Studies in Systems, Decision and Control 351,
https://doi.org/10.1007/978-3-030-68103-6_11

1 Introduction

Electrical wires are widely used in various industries. The wire quality has a direct impact on the quality and safety of the products in which it is used. In the minimum optional, a simple single-core wire is a metal core and polymer insulation applied over it [1–3].

The main indicator of the wire quality is the absence of defects in its design [4]. A defect is understood as any nonconformity of a product with established requirements [5, 6].

The presence of any even minor defect causes deviation from its nominal geometric and electrical parameters. At the production stage, an electric wire can include various types of defects [6–8]: local thinning or increased outer diameter of the insulation, foreign inclusions in the insulation, porous insulation, eccentricity, etc.

In wire manufacturing [9], defects should be detected at the yearly stage in order to timely improve the technological process, which will reduce the economic costs of cable product manufacturing. During the technological process, defects can be detected through the change in the linear capacity of the wire [7, 8, 10, 11].

The study of the effect of the geometric parameters of different defects on other parameters of electrical wires will allow their timely in-situ detection. The aim of the study is to determine geometric dimensions of insulation defects, which significantly impact the change in the electric wire linear capacity.

2 Wire Model

A detailed study of wire samples with different types of defects of different sizes. A number of reasons hampers creation of the bank of wire samples:

- resources are required to create an extensive bank of wire samples with defects;
- not all types of defects can be created artificially, in particular to ensure the variability of the geometric parameters of defects.

These problems can be partially solved through modeling [12–14], which reduces the cost of creating a large volume of real samples with different geometric dimensions of defects and simultaneously increases the study efficiency due to a variety of models of defects of various types and sizes [13].

A single-core wire can be regarded as a cylindrical capacitor (Fig. 1), which consists of a metal core diameter d and polymer insulation diameter D [15]. The core surface is considered as the first capacitor plate. Voltage is applied to the outer surface of the insulation, and this boundary is considered as the second capacitor plate. The inter-plate space is filled with dielectric, which is the insulation material of the wire [16, 17].

The capacity of the capacitor can be calculated using a well-known equation [18]:

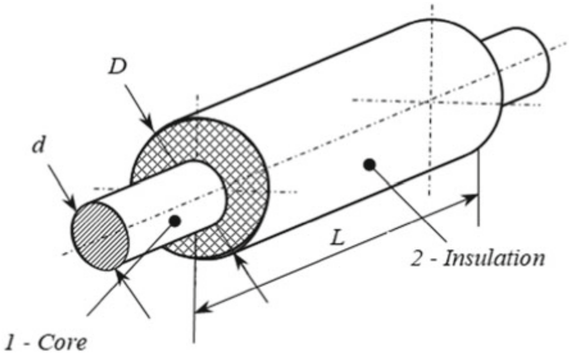

Fig. 1 Model and appearance of the wire

$$C = \frac{2\pi \cdot \varepsilon \cdot \varepsilon_0 \cdot L}{\ln\left(\frac{D}{d}\right)}, \tag{1}$$

The research object f is a mathematical model of a single-core wire with a core diameter $D = 1$ mm and an insulation diameter $d = 3$ mm. The wire insulation is polyethylene with dielectric constant ε = 2.3. The wire model length is equal to the length of the measuring electrode of the device for in-process testing of the wire capacitance ($L = 20$ cm) [9, 10, 18].

The capacitance of a defect-free wire of the specified dimensions is $C = 23.28$ pF. This value is taken as nominal.

3 Insulation Defects

Defects change geometric dimensions of the wire, and hence, they affect the capacitance value. The deviation of the capacitance in the presence of a defect is recorded relative to the nominal value—the capacitance of the defect-free wire. In accordance with the requirements of normative and technical documentation [19–22] and the accuracy of device for in-process testing of the wire capacitance [9, 10, 18], a significant change in the capacitance is taken at the level of 5% of the deviation from the nominal capacitance of the defect-free wire, which corresponds to $C_1 = 21.85$ pF and $C_2 = 24.15$ pF.

The types of defects modeled in the study are as follows:

- local thinning of the wire insulation (external defect);
- eccentricity (displacement of the core center from the wire center);
- foreign inclusion in wire insulation (intrinsic defect).

3.1 Local Thinning of the Wire Insulation

Figure 2 shows a defect model—local thinning of the wire insulation. The defect depth is determined by the $2h_x$ change in the insulation outer diameter D in the defect area. In the defect area, the insulation diameter is $D_d = D - 2h_x$.

In the presence of this defect, the sample can be divided into 3 sections: two sections of length L_1 and L_2 with the initial insulation diameter D and one section of length l_x with a smaller insulation diameter D_d. To simplify calculations, the defect boundaries are assumed sharp.

The capacity for each section is calculated by Eq. (1) separately, with regard to the geometric dimensions of each section. The capacity value for each section is indicated C_{sec1}, C_{sec2} and C_{sec3}, respectively (Fig. 2).

The total length of all wire sections corresponds to the total length ($L = 20$ cm) of the wire sample.

The general equation for calculating the wire capacity takes the form:

$$C = \frac{2\pi \cdot \varepsilon_0 \cdot \varepsilon \cdot (L_1 + L_2)}{\ln\left(\frac{D}{d}\right)} + \frac{2\pi \cdot \varepsilon_0 \cdot \varepsilon \cdot l_x}{\ln\left(\frac{D_d}{d}\right)} \qquad (2)$$

Numerical modeling was used to carry out the studies.

Figure 3a shows dependence of the wire capacitance with the *local thinning of the wire insulation* on changes in the defect length in the range from 0 to 5 cm at constant depth $hx = 0.5$ mm. Figure 3b shows dependence of the relative error in the changed wire capacitance on relative changes in the volume of the defective wire. To compare the results of the study, the concept of *the wire nominal volume* should be introduced, which corresponds to the insulation volume of the non-defective wire. The nominal volume of the wire is calculated using the formula for the volume of the cylinder, with regard to the geometric dimensions of the core and wire insulation. The considered defects cause a decrease in the insulation volume.

In Fig. 3a, b, the horizontal line indicates the capacitance corresponding to the threshold value in the absolute and relative form (deviation ±5%), which can be observed in all the graphs given below.

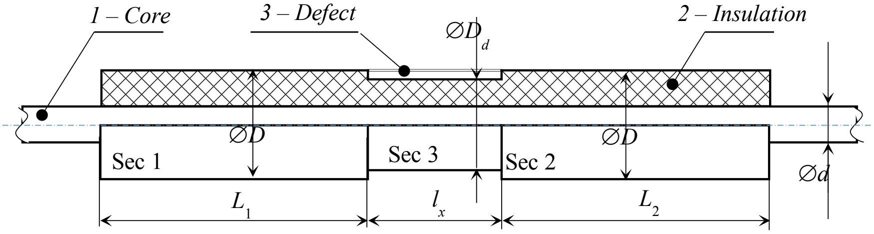

Fig. 2 Model of the defect Local thinning of the wire insulation

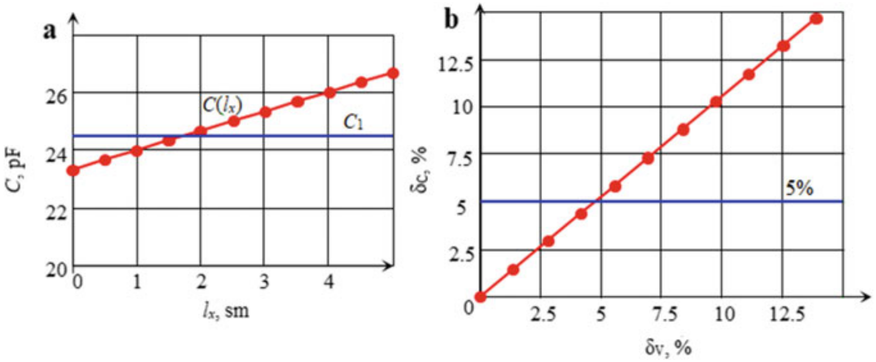

Fig. 3 Change in wire capacity **a** and relative error **b** in the presence of local length of the diameter (constant depth defect)

The defect *Local thinning of the diameter* increases the capacitance (Fig. 3). It should be noted that wire capacitance changes significantly when the defect length attains $l_x = 18$ mm and the volume of the wire insulation decreases by more than 4.5%.

Figure 4a shows dependence of the wire capacitance on changes in the defect depth in the range from 0 to 0.9 mm at constant length $l_x = 10$ mm. Figure 4b shows dependence of the relative error of the wire capacitance on relative changes in the volume of the wire insulation.

Figure 4 shows that wire capacitance changes significantly at defect depth $hx = 0.65$ mm, which corresponds to changes in the wire volume by more than 3.3%.

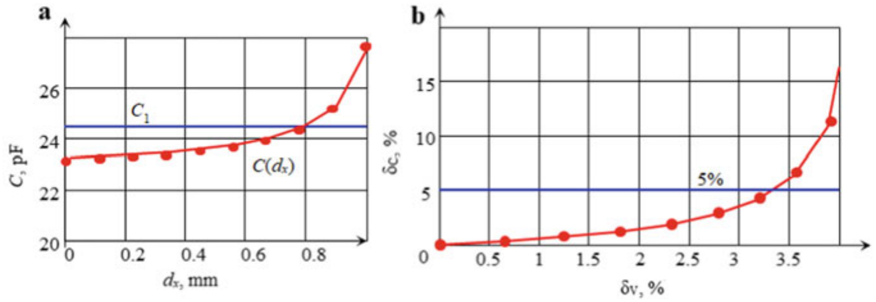

Fig. 4 Change in wire capacity **a** and relative error **b** in the presence of local thinning of the diameter (constant length defect)

3.2 Eccentricity

Eccentricity is deviation of the core center from the wire center [23, 24]. Figure 5 shows the *eccentricity* model and a graphical diagram for capacitance calculation.

Based on Eq. (1) and mathematical analysis [25–27] of data from Fig. 5b, the equation can be derived for dependence of the capacitance on the core displacement relative to the wire center:

$$C(m) = \frac{2\pi \cdot \varepsilon \cdot \varepsilon_0 \cdot l}{\ln\left(\frac{H_2 R}{H_1(m) \cdot r}\right)} \tag{2}$$

where $r = d/2$, $R = D/2$ are the core and insulation radii, mm; m is eccentricity, mm; $H1$,$H2$ are the distance from the axis to the center of the core and wire, respectively, mm (the selected point is on the insulation surface).

If we assume that $H_2 = R$, then $H1(m) = R - \text{m}$.

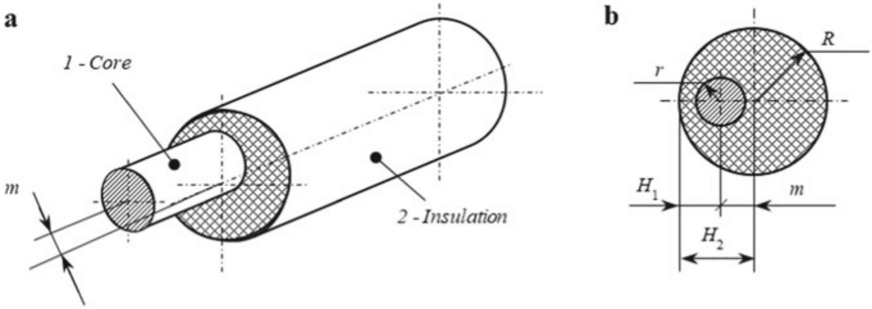

Fig. 5 Wire eccentricity: **a** general view, **b** incision

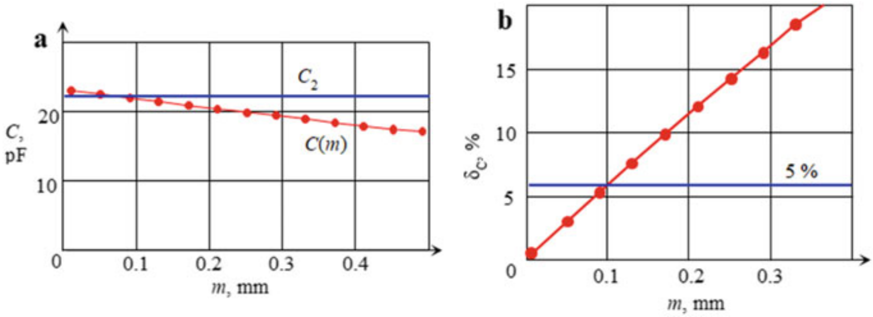

Fig. 6 Change in wire capacitance **a** and relative error **b** on wire eccentricity

Figure 6a shows dependence of the wire capacitance on the core displacement relative to the wire center *m* in the range from 0 to 0.5 mm. Figure 6b shows dependence of the relative error of the wire capacitance on the core displacement.

Figure 6 shows that eccentricity leads to a decrease in the wire capacitance. The threshold value of the wire capacitance is exceeded if eccentricity is more than 0.1 mm, which corresponds to 10% of the core diameter.

3.3 Foreign Inclusion

Figure 7 shows the *Foreign inclusion in wire insulation* model. Foreign inclusion is the presence of an air bubble, metal shavings or other object in the homogeneous structure of insulation [24, 27]. For ease of modeling, a section is taken inside the insulation along the entire circumference. The defect size is determined by the length l_x and the diameter of the defect inner D_2 and outer D_3 surfaces. The case is considered when the inner space of the defect is filled with air with a dielectric constant $\varepsilon_1 = 1$.

The wire capacitance of this defect can be calculated using a classical formula for a cylindrical capacitor (Eq. 1) with regard to recommendations provided in [28–30]. In this case, the wire sample capacity is calculated as the sum of capacities for each of the three sections (similar to *Local thinning of the wire insulation*). Section 2 is considered to be a multilayer cylindrical capacitor [30, 31], which comprises 3 insulation layers of known thickness: polyethylene—air—polyethylene. After conversion, the formula for calculating the capacity has the form:

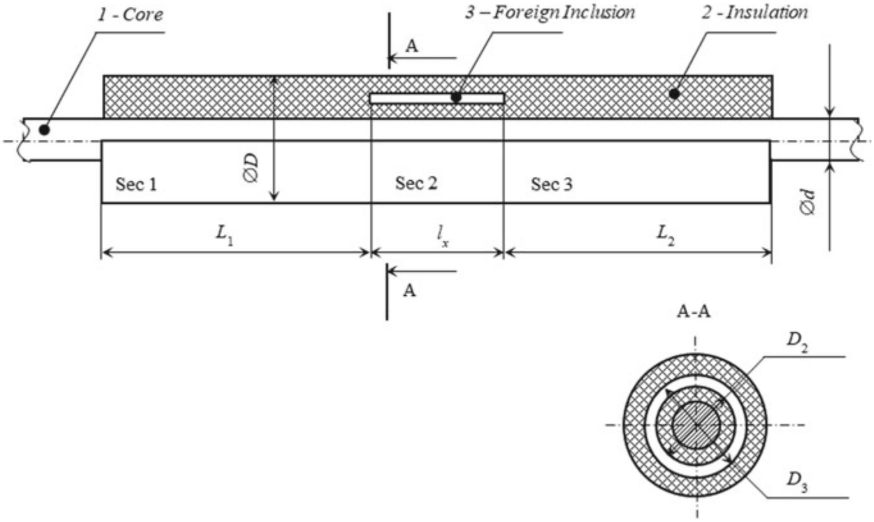

Fig. 7 Model of the *Foreign inclusion* defect

$$C = \frac{2\pi \cdot \varepsilon_0 \cdot (L_1 + L_2)}{\frac{1}{\varepsilon}\ln\left(\frac{D}{d}\right)} + \frac{2\pi \cdot \varepsilon_0 \cdot l_x}{\frac{1}{\varepsilon}\left(\ln\left(\frac{D_2}{d}\right) + \ln\left(\frac{D}{D_3}\right)\right) + \frac{1}{\varepsilon_1}\ln\left(\frac{D_3}{D_2}\right)}, \tag{3}$$

where d and D are diameters of the core and insulation, mm; D_2 and D_3 are diameters of the defect inner and outer surfaces, mm; L_1, L_2 are lengths of Sects. 1 and 3; l_x is the defect length (Sect. 2).

Figure 8 shows dependence of the capacitance and relative error on the length of the intrinsic defect in the range from 0 to 5 cm at a fixed defect thickness $h = D_3 - D_2 = 0.4$ mm.

Figure 8 shows that the *Foreign inclusion* defect decreases the capacity. The value of the wire capacitance attains threshold at a length of $l_x = 3$ cm and a fixed defect thickness $h = 0.4$ mm, which is more than 6% of the insulation volume of the defect-free wire.

Figure 9 shows the dependence and relative error of the capacitance on the thickness of the intrinsic defect h in the range from 0 to 0.5 mm at a fixed defect length $l_x = 3$ cm.

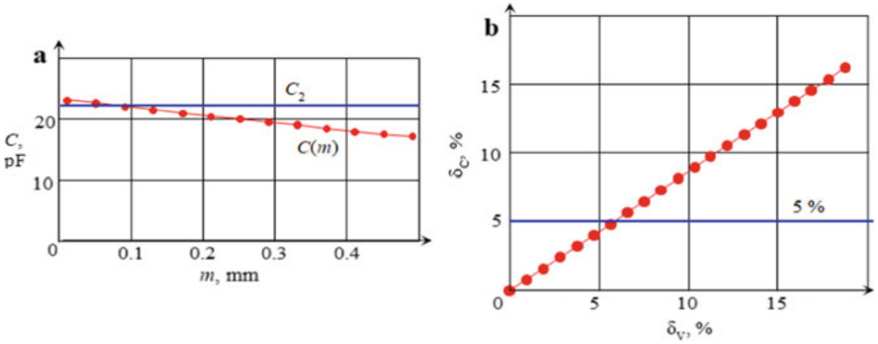

Fig. 8 Change in wire capacitance **a** and relative error **b** on changes in the length of the intrinsic defect

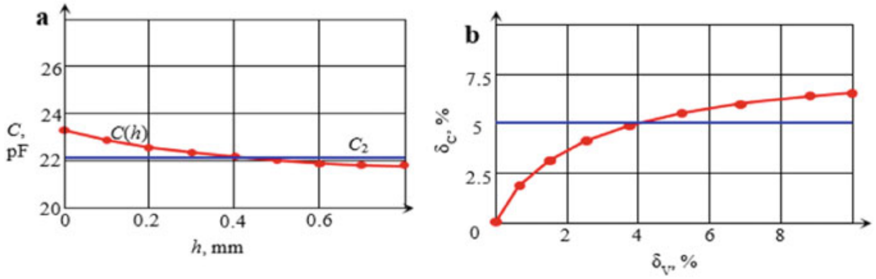

Fig. 9 Change in wire capacitance **a** and relative error **b** on changes in the thickness of the intrinsic defect

A significant change in the capacitance of the wire is observed when the thickness of the wire defect changes by more than 0.4 mm with a fixed length of the defect l_x = 3 cm (Fig. 9). This type of defect leads to a change in the wire insulation volume by more than 4% of the defect-free wire volume.

4 Conclusion

Modeling allows complex studies of the effect of various types of insulation defects on wire capacitance with no significant expenditures for creating a bank of samples.

The paper presents models of the following defects: eccentricity, local insulation thinning and foreign inclusion, which are quite difficult to investigate. In addition, it is almost impossible to provide variability of one of the geometric dimensions while the other one is constant.

The study has shown that defects cause changes in the capacitance. The wire capacitance can significantly change (by 5%) under the following conditions:

- 4.5% increase in the defect volume relative to the total volume of the wire at increased length of the defect, and 3.3% increase at the increased depth of the defect;
- eccentricity of 10% and greater of the core diameter value;
- 6% increase in the volume of the intrinsic defect relative to the total volume of the defect-free wire at increased length of the defect and 4% increase at increased thickness of the defect.

This study presents simplified models of defects since it is only the first stage of the research. Further research will focus on improving the reliability of the models. In addition, the effect of other types of defects and their geometric dimensions on wire capacitance will be investigated to show the possibility of detecting various types of defects during technological testing of wire capacitance.

References

1. Murty, P.S.R: Cables. In: Electrical Power Systems (Chap. 7), pp. 145–169 (2017). https://doi.org/10.1016/B978-0-08-101124-9.00007-3
2. Bryant, R.: Irradiation of cables, wires and heat shrinkables. Radiat. Phys. Chem. **174**, 108895 (2020). https://doi.org/10.1016/j.radphyschem.2020.108895
3. Furse, C., Haupt, R.: Down to the wire. IEEE Spectr. **38**(2), 35–39 (2001)
4. Wenbin, S., Ju, T., Cheng, P., Guodong, M., et al.: Improvement of insulation defect identification for DC XLPE cable by considering PD aging. Int. J. Electr. Power Energy Syst. **114**, 105409 (2020). https://doi.org/10.1016/j.ijepes.2019.105409
5. Drobny, J.G.: Polymers for Electricity and Electronics: Materials, Properties, and Applications. Wiley, New York (2012)

6. Ilie, S., Setnescu, R., Lungulescu, E.M., et al.: Investigations of a mechanically failed cable insulation used in indoor conditions. Polym. Test. **30**(2), 173–182 (2011). https://doi.org/10.1016/j.polymertesting.2010.11.016
7. Vavilova, G.V., Ryumkin, A.V.: Detection of insulation defects in the wire through measuring changes in its capacitance. IOP Conf. Ser.: Mater. Sci. Eng. **289**, 012017 (2018). https://doi.org/10.1088/1757-899X/289/1/012017
8. Jeon, J.C., Kim, J.-J., Choi, M.I., et al.: Detection and location of cable fault using improved SSTDR. Trans. Korean Inst. Electr. Eng. **65**(9), 1583–1589 (2016). https://doi.org/10.5370/KIEE.2016.65.9.1583
9. Severengiz, M.: Challenges and approaches for a continuous cable production. Proc. CIRP **40**, 18–23 (2016). https://doi.org/10.1016/j.procir.2016.01.040
10. Goldshtein, A.E., Vavilova, G.V., Mazikov, S.V.: Capacitance control on the wire production line. MATEC Web Conf. **79**, 01009 (2016). https://doi.org/10.1051/matecconf/20167901009
11. Paulter, N.G.: An assessment on the accuracy of time-domain reflectometry for measuring the characteristic impedance of transmission lines. IEEE Trans. Instrum. Meas. **50**(5), 1381–1388 (2017). https://doi.org/10.1109/19.963214
12. Kapranov, B.I., Vavilova, G.V., Volchkova, A.V., et al.: Mathematical modeling of tomographic scanning of cylindrically shaped test objects. IOP Conf. Ser.: Mater. Sci. Eng. **363**, 012015 (2018). https://doi.org/10.1088/1757-899X/363/1/012015
13. Kosar, V., Gomzi, Z.: Modeling of the power cable production line. Thermochim. Acta. **457**(1–2), 70–82 (2007). https://doi.org/10.1016/j.tca.2007.02.020
14. Abboud, L., Cozza, A., Pichon, L.: A matched-pulse approach for soft-fault detection in complex wire networks. IEEE Trans. Instrum. Meas. **61**(1), 1719–1732 (2012). https://doi.org/10.1109/TIM.2012.2187246
15. Surzhikov, A.P., Pritulov, A.M., Lysenko, E.N., et al.: Calorimetric investigation of radiation-thermal synthesized lithium pentaferrite. J. Therm. Anal. Calorim. **101**(1), 11–13 (2010). https://doi.org/10.1007/s10973-010-0788-7
16. Doskeyev, G.A., Edenova, O.A., Spivak-Lavrov, F.: Influence of the fringe field on moving of the charged particles in flat and cylindrical capacitors. Nucl. Instrum. Methods Phys. Res., Sect. A **645**(1), 163–167 (2011). https://doi.org/10.1016/j.nima.2011.01.132
17. Ravanamma, R., Muralidhara, R., Venkata, K.K., et al.: Structure and morphology of yttrium doped barium titanate ceramics for multi-layer capacitor applications. Mater. Today Proc. (2020). https://doi.org/10.1016/j.matpr.2020.07.646
18. Pulkkinen, J., Koivo, H.N., Zaramella, J.-C.: Capacitance/Diameter (C/D) Control in telephone cable insulation process. IFAC Proc. **29**(1), 725–729 (1996). https://doi.org/10.1016/S1474-6670(17)57747-2
19. Jing, D., Kang, L., Eileen, H.-J.: Energy monitoring and quality control of a single screw extruder. Appl. Energy **113**, 1775–1785 (2014). https://doi.org/10.1016/j.apenergy.2013.08.084
20. Hansson, S., Fisk, M.: Simulations and measurements of combined induction heating and extrusion processes. Finite Elem. Anal. Des. **46**(10), 905–915 (2010). https://doi.org/10.1016/j.finel.2010.06.004
21. Natheer, A.: Effects of cable insulations' physical and geometrical parameters on sheath transients and insulation losses. Int. J. Electrical Power Energy Systems **110**, 95–106 (2019) https://doi.org/10.1016/j.ijepes.2019.02.047
22. Ayokunle, A., Ademola, A., Lambe, M.A.: Predicting extrusion process parameters in Nigeria cable manufacturing industry using artificial neural network. Res. Article **6**(7), E04289 (2020). https://doi.org/10.1016/j.heliyon.2020.e04289
23. Loete, F., Zhang, Q., Sorine, M.: Experimental evaluation of the inverse scattering method for electrical cable fault diagnosis. IFAC-PapersOnLine **48**(11), 766–771 (2015). https://doi.org/10.1016/j.ifacol.2015.09.619
24. Ulf, B.: Extrusion User's Guide to Plastic (2nd ed., Chap. 20) pp. 177–203 (2019) https://doi.org/10.3139/9781569907351.020

25. Albert, L., Deschamps, F., Jolivet, A., et al.: A current synthesis on the effects of electric and magnetic fields emitted by submarine power cables on invertebrates. Mar. Environ. Res. **159**, 104958 (2020). https://doi.org/10.1016/j.marenvres.2020.104958
26. Halim, H., Phung, B.T., Fletcher, J.: Impact of electromagnetic fields on current ratings and cable systems. In: Proceeding of the 2014 International Conference on Smart Green Technology in Electrical and Information Systems (ICSGTEIS), 1–6 (2014). https://doi.org/10.1109/ICSGTEIS.2014.7038727
27. Kelly, A.L., Brown, E.G., Coates, P.D.: The effect of screw geometry on melt temperature profile in single screw extrusion. Polym. Eng. Sci. **46**(12), 1706–1714 (2003). https://doi.org/10.1002/pen.20657
28. Ballou, G.: Resistors, Capacitors, and Inductors. Handbook for Sound Engineers (4th ed., Chap. 10), pp. 241–272 (2008). https://doi.org/10.1016/B978-0-240-80969-4.50014-6
29. Lysenko, E.N., Surzhikov, A.P., Vlasov, V.A., et al.: Synthesis of substituted lithium ferrites under the pulsed and continuous electron beam heating. Nucl. Instrum. Methods Phys. Res., Sect. B **392**, 1–7 (2017). https://doi.org/10.1016/j.nimb.2016.11.042
30. Spivak-Lavrov, I.: Chapter two-analytical methods for the calculation and simulation of new schemes of static and time-of-flight mass spectrometers. Adv. Imag. Electron Phys. **193**, 45–128 (2016). https://doi.org/10.1016/bs.aiep.2015.10.001
31. Nizhegorodov, A.I., Bryanskikh, T.B., Gavrilin, A.N., et al: Testing a new alternative electric furnace for vermiculite concentrates heat treatment. Bulletin of the Tomsk Polytechnic University. Geo Assets Eng. **329**(4), 142–153 (2018)

New Factors of Reliability of Electric Furnaces for Vermiculite Firing with Mobile Base Plates

Anatoliy Nizhegorodov, Aleksey Gavrilin, Boris Moyzes, Kirill Kuvshinov, and Saule Sakipova

Abstract The article reviews measures to increase the reliable operation of electric furnaces for vermiculite concentrates firing over the entire period of their existence since 2003. A significant step forward in this research was the find that the implementation of suspended heating systems in the electric modules of furnaces, both types such as modular-triggering furnaces and in furnaces with mobile base plates, where the swelling process of the raw material is carried out during the process of its vibrotransportation in the thermal field of the heating system. The imbalance of inertial loads is an additional factor for reducing of operation reliability in furnaces with mobile base plates. The methods of their balancing, discussed in this research, provide the dynamic balance of all moving parts of these furnace units. A study of analytical models of temperature distribution, carried out in previous researchers of the authors, showed that uniform heating can only be achieved in systems with a variable interval for the placement of heaters. The research results carried out in this work at the accepted values of the minimum and maximum intervals show that,

---

A. Nizhegorodov
Department of Construction and Road-Making Machines and Hydraulic Systems, Irkutsk National Research Technical University, 83 Lermontov Street, Irkutsk, Russia 664074
e-mail: nastromo_irkutsk@mail.ru

A. Gavrilin · K. Kuvshinov
Division for Materials Science, National Research Tomsk Polytechnic University, 30 Lenin Avenue, Tomsk, Russia 634050
e-mail: tom-gawral@list.ru

K. Kuvshinov
e-mail: kuvshinov@tpu.ru

B. Moyzes (✉)
Division for Testing and Diagnostics, National Research Tomsk Polytechnic University, 30 Lenin Avenue, Tomsk, Russia 634050
e-mail: mbb@tpu.ru

S. Sakipova
Physical and Technical Faculty, E.A. Buketov Karaganda University, 56 Ave. Nursultan Nazarbayev, Karaganda 100027, Kazakhstan
e-mail: sesaule@mail.ru

I. V. Minin et al. (eds.), *Progress in Material Science and Engineering*,
Studies in Systems, Decision and Control 351,
https://doi.org/10.1007/978-3-030-68103-6_12

compared to the old systems located on the refractory base of the firing modules, the difference temperature decreases significantly, which proves the effectiveness of this approach.

1 Introduction

Constant work was being made by the improving of the electric modular launch furnaces for firing vermiculite concentrates and conglomerates since their introduction. The need to reduce the specific energy consumption of firing and increase their reliability remained relevant [1–6]. Modular-launch furnaces made it possible to achieve the minimum energy intensity of 170–175 mJ/m^3 [7], but due to a number of design aspects (the use of inclined modules with accelerating movement of raw materials, etc.), further reduction was not achieved.

Then an alternative concept of operation units for vermiculite firing (and other thermally activated bulk materials [8]) appeared. They were the electric furnaces with mobile base plates, which made it possible to bring the specific energy consumption of firing to 60–70 mJ/m^3.

The special features of new improved electric furnaces design are the follows:

- it allows to minimize operating space of the firing modules;
- implementation of quick-detachable suspension heating systems;
- it allows to transport the fired raw materials in the thermal field of the modules at a constant speed with a continuous flow of vermiculite concentrate particles [9–11].

These features make it possible to achieve high energy efficiency as well as make the units more competitive and help to operate at a their maximum reliability level.

The purpose of this work is to increase the reliability of the electric furnaces under consideration through the use of a new design of quick-detachable heating systems and dynamic balancing of the base plates [12–15].

2 Reliability Factors of Electric Furnaces for Vermiculites Firing

The experience gained during the production operation of the first modular-launch furnaces at the Kvalitet LLC enterprise in the city of Irkutsk made it possible to identify the causes of failures and find effective technical solutions that increased the reliability of their operation.

For example, let’s consider a three-module furnace with an additional “zero” non-electrified module (Fig. 1).

Fig. 1 Three-module furnace with an additional “zero” non-electrified module

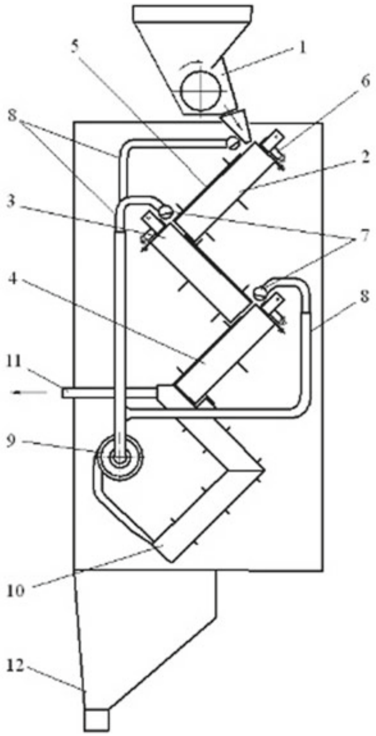

Vermiculite mica concentrate supplied by dispenser 1 passes through electric firing modules 2, 3, and 4, closed by thermo-covers 5. Using fastening heads 6, strip-type electric heaters with a surface heating temperature of 740–780 °C are installed on the edge of the modules. The strip-type electric heaters form longitudinal chambers (Fig. 2a), where vermiculite moves, being exposed to thermal radiation from both sides.

In the first design of the furnace, the heaters were located not on the edge, but flat, as it shown in Fig. 2b. Although the efficiency of transferring thermal energy to

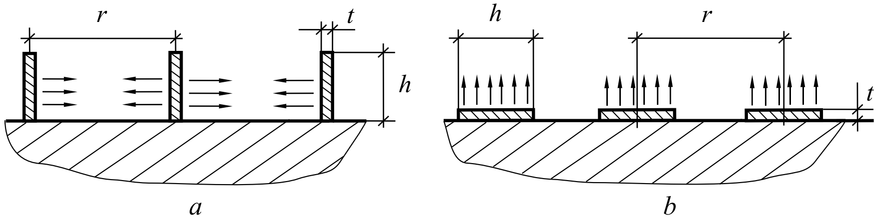

Fig. 2 Methods of installing strip electric heaters: *a*—on the edge, *b*—flat, *r*—installation step, *t*—thickness, *h*—width of heaters

Fig. 3 Soot deposit on strip heaters during firing concentrates of the Tatar deposit of vermiculite ores

expanded vermiculite in this method was somewhat greater, the failure rate of the furnace was very high due to the soot deposit (Fig. 3).

Suction pumps 7 (Fig. 1) located in the upper end parts of the modules, are connected by pipelines 8 with an exhaust fan 9. Due to the temperature difference and air traction that occurs in the slit-like spaces of the firing modules, the fine particles of vermiculite formed during its expansion are ejected and trapped suction pumps. A stream of hot air saturated with vermiculite dust passes through an additional module 10, heating it, and is discharged into the dust deposition and air purification system through the pipe 11.

The upper modules 2, 3 and 4 are connected sequentially, and the third lower electrical module is tightly attached to the "zero" module 10. The "zero" module 10 allows to use thermal exergy accumulated by vermiculite in electrical modules and the thermal radiation of small particles of vermiculite to complete the mechanical transformation (structure formation) of vermiculite at the absence of an external heat source. The tests results proved [4], that the use of such modules can reduce the energy consumption and energy intensity of firing by 10–20%.

The expanded product is poured into the hopper 12.

Failures in the operation of furnaces decreased significantly when heaters were installed on the edge, but this was only one of the factors of low reliability. There were congestions, the vermiculite flow stopped in the operating chambers because of the fragments collapse of the asbestos lining of thermal covers 5. It led to local overheating of the heaters and their burnout.

Another cause of failure was the interturn circuit due to the ingress of conductive objects into the furnace along with vermiculite concentrate.

We used felt as a thermally insulator for mullite-siliceous module covers, which is capable to maintain its properties at temperatures above 1380 °C. Application of felt allowed us to avoid the collapse of lining. Also any foreign objects were prevented to occur in the furnaces by pre-fractioning concentrates in drum sieves [8].

But all these measures reduced the failure rate by only 55–60%.

It turned out that the operation of the heating systems of the firing modules does not provide uniform heating of the refractory surfaces of the modules where the expanded vermiculite rolls. Obviously, for the same interval r of arrangement of heating elements (Fig. 2) the temperature in the central part of the module and on its

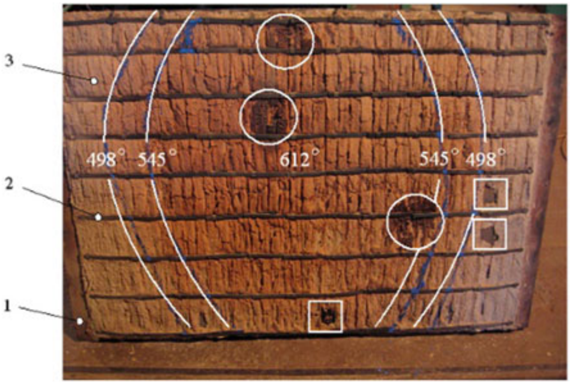

Fig. 4 Thermocover of the firing module: bottom view: 1—steel base, 2—lining fastening by strip nichrome, 3—lining of asbestos cord

periphery cannot be the same. Several researchers conducted studies and published works [16, 17], on the analytical models of the temperature distribution both on the refractory surface of the module and on the surface of the thermal cover. The temperature measurements were also taken on the surface of the thermal cover of one of the modules of the operating furnace. Figure 4 shows a thermal cover that has been in operation process at least 140 h. Here, the white lines indicate the approximate position of the isotherms with temperatures of 498 and 545 °C and the temperature in its central part 612 °C. Radiant energy flows from heaters and leaves traces which indicate that the temperature distribution is uneven on the refractory surface of the module. White circles outline the places where nichrome melted (1420–1460 °C). The squares indicate the places of peeling and falling out of the lining fragments mentioned above.

It is also obvious that burning out of heating elements due to soot deposit is the most difficult problem to resolve. The burnout mainly occurs in the center of the module, where the temperatures are highest. The problem remained unresolved. The surfaces of the cover and base, and most importantly, the of the heaters themselves which located in the central part, are getting heated more severely. Vermiculite concentrate always contains a small amount of associated minerals which have a relatively low melting point (vermiculite itself melts at temperatures from 1150 to 1350 °C, depending on its natural properties [18]). Quality of enrichment does not change the melting temperature. So when nichrome is overheated, the associated minerals adhere to its surface and form soot deposits (Figs. 3 and 4).

The suspended heating system allows to solve this problem and radically raises the reliability of electric furnaces for vermiculite firing to a new level (Fig. 5).

The difference is provided by the heaters 2 which are located above the base plate 1 under the thermal cover 3 and are held by special fasteners that have locks 4, hooks 5 and clamps 6 and provide the heaters are held with the same gap in relation to the base plate entire length. The heaters do not come into contact with the expanded grains of vermiculite and emit thermal radiation both to the bottom, to the processed raw materials, and up to the well-insulated module cover. The movement of the

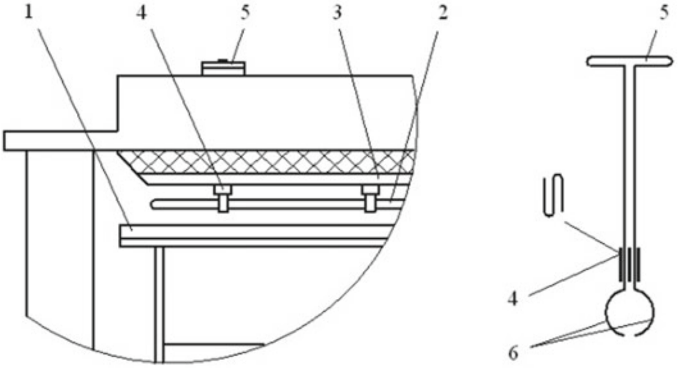

Fig. 5 Suspended heating system of wire heaters: fragment of the furnace firing module with a mobile base platform

concentrate in the heat field of the heaters is provided by non-symmetric vibrations of the base plate [9].

Let's consider one of the design options for an industrial electric furnace, consisting of six firing modules placed in two sections and, using its example, those technical solutions that will radically improve the reliability of such a furnace unit.

3 The Device of a Two-Section Six-Module Industrial Electric Furnace

Figure 6 shows a diagram of a two-section industrial furnace, consisting of six firing modules. It is a closed metal cabinet with insulated walls and door leaves (they are conventionally removed in Fig. 6). The furnace contains a common frame 1, mobile base plates 2 mounted on rollers 3 in the guide frames 4, spring-loaded on one side by coil springs 5 and non-linear elastic elements 6 on the other sides. Thermal covers 7 are mounted on modular units, and under them using special fasteners 8 are placed suspended electric heating grids 9.

Eccentric shafts are installed on each side of the furnace, which are driven through gear belt (or chain) gears 10 with a gear motor 11 with a rotation speed of 5–8 r/s.

The eccentrics 12 excites non-symmetrical vibrations of the base plates by means of tolls and springs 13 and with the help of non-linear elastic elements 6, which causes a vibro-transport effect [19] and provides one-way movement of vermiculite concentrate particles from the trays 16 of the hopper 14 under the heating grid 9 in the thermal field of the firing modules. The output of the expanded product occurs through trays 15.

In the process of oscillation of base plates, the significant inertia forces F occur. The forces F are determined by multiplying (N): $F = m_i \cdot a$, where m_i—is the mass

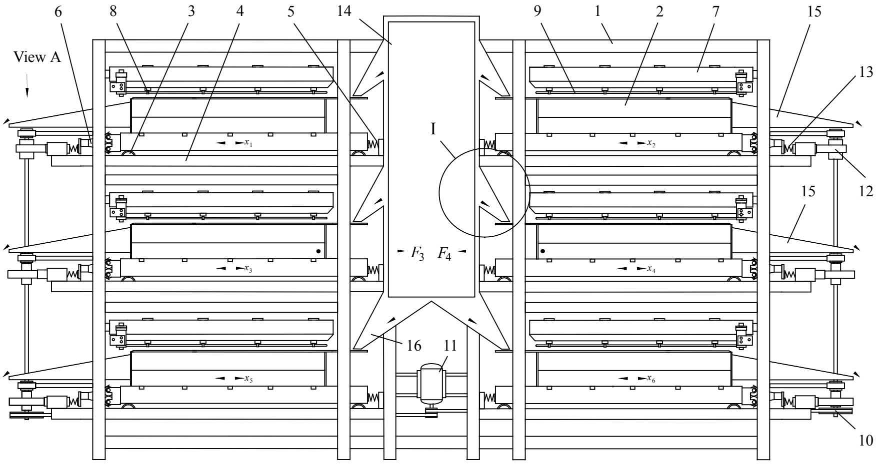

Fig. 6 Two-section six-module industrial electric furnace

of the *i*-th base plate with all elements attached to it, kg, and *a*—its vibration acceleration, m/c^2.

The synchronism and phase balance of oscillations of each pair of base plates is provided by the installation of eccentrics with a displacement of one relative to the other by 120° (Fig. 7a). This balances their multidirectional inertia forces T (N):

$$T = m\omega^2 e,$$

where m is the mass of the eccentric, kg, ω is the angular velocity of rotation of the shaft in rad/c, e is the eccentricity.

The inertia forces of the base plates F cause the high risk situation. These forces can lead to swinging of the entire furnace, to the appearance of sub- and super harmonics

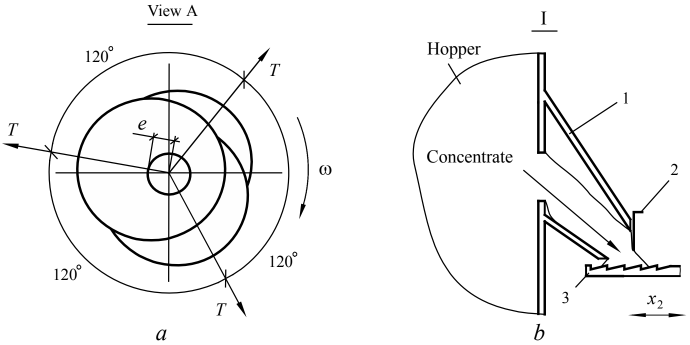

Fig. 7 Installation of eccentrics on the drive shaft with an angular pitch of 120° (**a**) and a diagram illustrating the dosage of vermiculite concentrate (**b**)

of its individual elements, and, in particular, to the excitation of vibrations of the rods of the heating grids 9. If the dynamic equilibrium of the entire system is not provided, then resonances or amplitude-modulated oscillations of individual heaters, their contacts and short circuits will occur. This happened when testing of a physical model of a single-phase furnace with a mobile base plate [8].

For balancing the base plates of each level, the eccentrics making them move vibrationally are set towards each other, and their shafts are connected by gear belt (or chain) gears 10 to the gear motor 11. This provides synchronous and antiphase oscillations of the base plates so that peak values of inertia forces F_3 and F_4, Fig. 6 are equal and directed oppositely. The dosing process of vermiculite concentrate in this furnace design is carried out from the common hopper through trays 1 equipped with adjustment flaps 2 using the base plates 3 themselves, due to the non-symmetry of their vibrations and the corrugated surface in zone "I" with a notch directed to the side of firing modules (Fig. 7b).

4 Results and Discussion

4.1 Redistribution of Thermal Power and Temperature of the Heating System

Let's turn to the main question about the distribution of thermal power and temperature of heaters in a suspended heating system (Fig. 5).

As it has been noted, burnout of heating elements due to soot deposit occurs most often in the central part of the module, where the temperatures are the highest. Not only the surfaces of the cover and refractory base, but also the heaters themselves, which are located in the central part, heat up more significantly. In the research [17] it is shown that in the pilot-industrial modular-firing furnace with belt heaters made of nichrome, the temperature differential was from 1119 °K in the center of the module to 910 °K along the sides with a discrepancy of 23%.

One heater 1 (Fig. 8) is an elongated U-shaped element of two rods, only here they are all made as a single heating grid with two ends for connection to the electrical network using fixing heads 2. The heaters are held by special clamps 3 under the thermal cover.

The design of the heating grid is such that the interval r_a between the rods of the first (extreme) heater a is half the interval r_b of the central heater b.

If there are only n intervals, then, on average, an increase in one interval between the rods will be (mm):

$$\Delta = \frac{r_b - r_a}{n}.$$

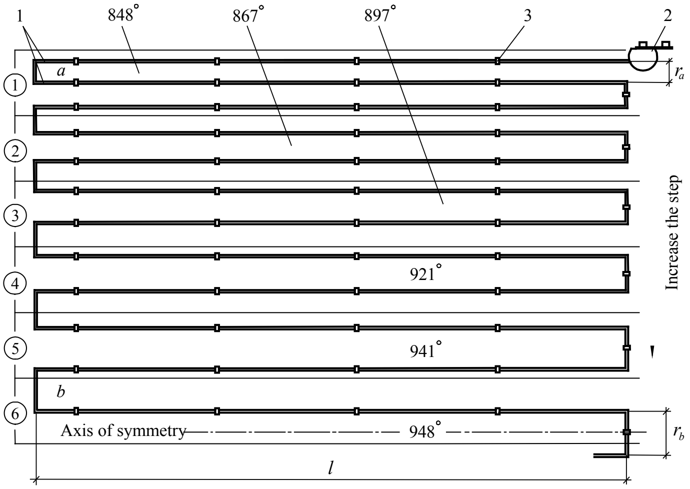

Fig. 8 Heating grid with variable spacing between rods

Let's set the values of the intervals $r_a = 22$ mm and $r_b = 44$ mm. Then the increase in each interval at $n = 11$ will be equal to $\Delta = 2$ mm.

With a heater length l equals to 400 mm, the total length of the heating grid can be calculated (mm):

$$l_\Sigma = 24 \cdot l + 2 \cdot (11 \cdot r_a + 55 \cdot \Delta + r_b),$$

moreover, the term of the obtained expression $2 \cdot (11 \cdot r_a + 55 \cdot \Delta + r_b)$, will determine the width of the firing module, which in this case will be equal to 792 mm, and the total length of the heating grid—10,392 mm or 10.39 m.

All initial parameters: $r_a = 22$ mm, $r_b = 44$ mm, $\Delta = 2$ mm, $l = 400$ mm and $n = 11$ are not taken by chance. The total length of 10.39 is approximately equal to the total length of the heaters of the prototype of the electric furnace with a mobile base plate. The experimental results are given in [20]. In this case, the cross-sectional area of the tape heaters was 10 mm^2.

Then it can be taken the values of the current values of the current $I = 79$ A and voltage $U = 162$ V, at which the maximum productivity and minimum density of expanded vermiculite were achieved [8], to calculate the consumed electrical power (W):

$$N = I \cdot U = 79 \cdot 162 = 12798.$$

Let us determine the value of the specific power (referred to the total length) (W/m):

$$N_l = \frac{N}{l_\Sigma} = \frac{12798}{10.39} = 1232.$$

Neglecting the end sections of the heating grid (r_a, $r_a + \Delta$ … and r_b), let's find the power per rod (W):

$$N_\text{o} = N_l \cdot l = 1232 \cdot 0.4 = 493. \tag{1}$$

The thermal power emitted by a single rod can be found by the formula obtained by the analytical method of balance fluxes [21] (W):

$$Q_\text{o} = \left[\varepsilon\sigma \mathrm{T}_\text{o}^4 f(1 + \rho_\text{o}\varphi_{\text{o}1}) + \rho_\text{o} Q_2(\rho_\text{o}\varphi_{\text{o}1}\varphi_{21} + \varphi_{2\text{o}}) + \rho_\text{o} Q_3(\rho_\text{o}\varphi_{\text{o}1}\varphi_{31} + \varphi_{3\text{o}})\right], \tag{2}$$

where ε is the nichrome heater blackness level, σ is the Stefan-Boltzmann constant [10], ρ_o is the reflectivity of the heater, $\varphi_{\text{o}1}$, φ_{21}, $\varphi_{2\text{o}}$, φ_{31} and $\varphi_{3\text{o}}$ are the angular coefficients that take into account the reflected radiation falling on a single heater, on the surface of the module base ($\varphi_{2\text{o}}$), on the surface of the thermal cover ($\varphi_{3\text{o}}$), to the adjacent heater from the surface of the thermal cover(φ_{21} и φ_{31}), Q_2 и Q_3—are the power of the heat reflected radiation from the surface of the base and thermal cover, respectively [22–25].Taking into account the losses during the conversion of electrical power into heat, the heat power emitted by a single rod can be found using the Formula (1),

$$W : Q_\text{o} = 0.92 \cdot N_\text{o}, \tag{3}$$

where 0.92 is the approximate value of the loss factor [21]. Then the thermal power determined by the Formula (3) will be equal to 454 W [26].

To determine the nature of the distribution of heat power, let us combine half of the heating grid (taking into account its symmetry) with the marking of the surface of the firing module in the form of zones 1, 2 … 6 of the same size, circled (Fig. 8). Let's see how many heating rods will be in the indicated zones: 1st zone—three rods, 2nd zone—two rods, two rods in zones 3, 4 and 5, and in zone 6—one rod. This means that the first zone has 1362 W of thermal power, the second, third, fourth and fifth zones have 908 W each, and the sixth only 454 W.

Figure 9 shows the distribution of heat power by the indicated zones: broken line Q. But this is just a "zonal model", because heat energy cannot be distributed discretely, therefore, a smoothing line with average values of heat power is shown here. In the first zone—1220 W, in the second, third, fourth and fifth zones—1000 W and in the sixth zone 650 W. It should be noted, that the indicated values of the average thermal power are radiation of the heaters into the surrounding space. Some of these flows fall on the base of the module and the thermal cover in its own zone, the rest to adjacent zones, including adjacent heaters [27–30].

So, in the structure of the Formula (2): its terms reflect:

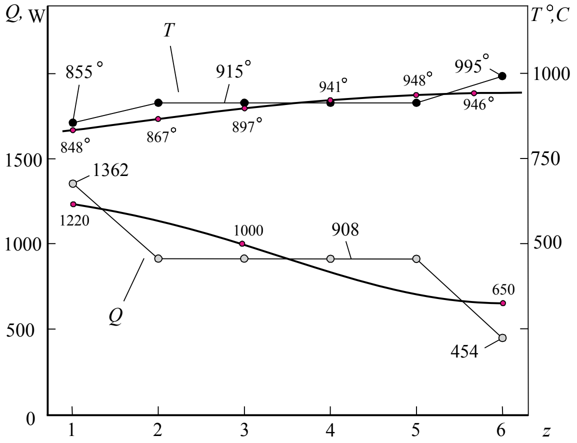

Fig. 9 Distribution of thermal power and heaters temperature by zones of their location (z is the ordinal number of the zone)

- $\varepsilon\sigma\mathrm{T}_{\mathrm{o}}^4 f\rho_{\mathrm{o}}\varphi_1$—is the fraction of reflected thermal radiation falling on the heating element from the surface of the adjacent heater;
- $\rho_{\mathrm{o}}Q_2(\rho_{\mathrm{o}}\varphi_{\mathrm{o}1}\varphi_{21}+\varphi_{2\mathrm{o}})$—is the fraction of the reflected thermal radiation falling on the heating element from the surface of the refractory base of the module;
- $\rho_{\mathrm{o}}Q_3(\rho_{\mathrm{o}}\varphi_{\mathrm{o}1}\varphi_{31}+\varphi_{3\mathrm{o}})-\rho_{\mathrm{o}}Q_2(\rho_{\mathrm{o}}\varphi_{\mathrm{o}1}\varphi_{21}+\varphi_{2\mathrm{o}})$—the fraction of the reflected heat radiation falling on the heating element from the surface of the module's thermal cover.

It still does not take into account the flows of thermal radiation from distant heaters and the corresponding sections of the surfaces of the base and thermo-cover, which reach the surface of a single heater. But all these fractions of the reflected radiation, as shown by the calculations carried out in [17], are approximately 10–12% of the intrinsic radiation of the heater. Therefore, the calculation of heater temperatures was carried out using a simplified formula:

$$Q_o=\varepsilon\sigma\mathrm{T}_{\mathrm{o}}^4 f,$$

solved with respect to T, °K:

$$\mathrm{T}=\left(\frac{Q_o}{\varepsilon\sigma\mathrm{T}_{\mathrm{o}}^4 f}\right)^{\frac{1}{4}}.$$

Figure 9 by the broken line at the top, shows the distribution of the average temperature values converted to degrees Celsius, three heaters in the first zone—855 °C, two heaters in zones 2, 3, 4 and 5–915 °C and one heater in the sixth zone—995 °C. And although the temperatures of the heaters just change discretely from one to the other, they cannot be the same in the second, third, fourth and fifth zones. To find the approximate values of the average temperatures of the heaters, a smoothing (averaging) line is shown here, indicating the average values of T by zones: 848 °C (1121 °K), 867 °C, 897 °C, 941 °C, 948 °C and 946 °C (1219 °K). The temperature ratio of the heaters, expressed in Kelvin degrees, in the sixth zone and the first is 1.0875, therefore, in the sixth zone, the temperature is 9% higher than the average temperature for the three heaters located in the first zone.

The temperature difference in the new heating system with variable spacing of heaters has become smaller (9% vs. 23%), which proves the effectiveness of this approach.

5 Conclusion

In the previous designs of heating systems, in which tape heaters were located on the refractory surface of the firing modules, the expanded vermiculite concentrate was constantly in contact with them. It led to blockages and the soot deposits. This, in turn, led to local overheating, melting of nichromium and furnace failure.

Because of the lower location of the heating system, inter-turn short-circuits occurred when conductive objects entered the furnace together with vermiculite concentrate.

The use of the suspended heating system, where wire heaters hang over the raw material to be fired, eliminated all these factors and significantly increased the reliability of the furnace units.

But the operation of suspended heating systems also has some peculiarities—they do not provide uniform heating of the refractory surfaces of the modules, along which the expanded vermiculite concentrate moves, and the temperatures of the heaters from the side sections of the modules to their center increase markedly.

The research of analytical models of temperature distribution, carried out in the early works of the authors, suggested that uniform heating can be provided only in heating systems with a variable interval of installation of heaters.

The research carried out in this work at the given values of the minimum (22 mm) and maximum (44 mm) intervals and with an increase in the heater spacing to 2 mm showed that, compared with the old heating system, the temperature difference decreased from 23 to 9%. This demonstrates the effectiveness of this approach. In addition, the difference in heating temperatures of the surface of the bases of the firing modules decreases.

In furnaces with movable base plates, the unbalance of inertial loads became another factor reducing reliability. The developed methods of their balancing, shown in the present work, make it possible to provide dynamic equilibrium of all movable parts of new furnace units.

References

1. Ding, F., Gao, M., Wang, J., Shen, T., Zang, W.: Tuning wettability by controlling the layer charge and structure of organo-vermiculites. J. Ind. Eng. Chem. **57**, 304–312 (2018). https://doi.org/10.1016/j.jiec.2017.08.037
2. Figueiredo, S.: The influence of acid treatments over vermiculite based material as adsorbent for cationic textile dyestuffs. Chemosphere **153**, 115–129 (2016). https://doi.org/10.1016/j.chemosphere.2016.03.004
3. Mo, K.H., Lee, H.J., Liu, M.Y.J., Ling, T.C.: Incorporation of expanded vermiculite lightweight aggregate in cement mortar. Constr. Build. Mater. **179**, 302–306 (2018). https://doi.org/10.1016/j.conbuildmat.2018.05.219
4. Karatas, M., Benli, A., Toprak, H.A.: Effect of incorporation of raw vermiculite as partial sand replacement on the properties of selfcompacting mortars at elevated temperature. Constr. Build. Mater. **221**, 163–176 (2019). https://doi.org/10.1016/j.conbuildmat.2019.06.077
5. Zhang, Y.N., et al.: Development and thermochemical characterizations of vermiculite $SrBr_2$ Composite sorbents for low-temperature heat storage. Energy **115**, 120–128 (2016). https://doi.org/10.1016/j.energy.2016.08.108
6. Ahirrao, N.S., Bhosle, S.P., Nehete, D.V.: Dynamics and vibration measurements in engines. Proc. Manuf. **20**, 434–439 (2018). https://doi.org/10.1016/j.promfg.2018.02.063
7. Shyamal, S., Swartz, C.L.E.: Real-time energy management for electric arc furnace operation. J. Process Control **74**, 50–62 (2019). https://doi.org/10.1016/j.jprocont.2018.03.002
8. Nizhegorodov, A.I., Gavrilin, A.N., Moyzes, B.B.: Improving the technology for processing sungulite vermiculite conglomerates. Bulletin of the Tomsk Polytechnic University. Geo Assets Eng. **330(4)**, 98–109 (2019). https://doi.org/10.18799/24131830/2019/4/230
9. Fuks, L., Herdzik-Koniecko, I.: Vermiculite as a potential component of the engineered barriers in low- and medium-level radioactive waste repositories. Appl. Clay Sci. **161**, 139–150 (2018). https://doi.org/10.1007/s13762-017-1597-3
10. Bryanskikh, T.V., Kokourov, D.V.: Energy efficiency of electric furnaces with movable floor in firing of vermiculite concentrates of different size groups. Refract. Ind. Ceram. **58**, 368–373 (2017). https://doi.org/10.1007/s11148-017-0113-0
11. Zvezdin, A.V., Bryanskikh, T.B.: Considering adaptation of electrical ovens with unit-type releasing to peculiarities of thermal energization of mineral raw materials. IOP Conf. Series: Mater. Sci. Eng. **168**(1), 012003 (2017). https://doi.org/10.1088/1757-899X/168/1/012003
12. Lysenko, E.N., Surzhikov, A.P., Vlasov, V.A., et al.: Synthesis of substituted lithium ferrites under the pulsed and continuous electron beam heating. Nucl. Instrum. Methods Phys. Res., Sect. B **392**, 1–7 (2017). https://doi.org/10.1016/j.nimb.2016.11.042
13. Surzhikov, A.P., Frangulyan, T.S., Ghyngazov, S.A.: A thermoanalysis of phase transformations and linear shrinkage kinetics of ceramics made from ultrafine plasmochemical $ZrO_2(Y)$-Al_2O_3 powders. J. Therm. Anal. Calorim. **115**(2), 1439–1445 (2014). https://doi.org/10.1007/s10973-013-3455-y
14. Surzhikov, A.P., Pritulov, A.M., Lysenko, E.N., Sokolovskii, A.N., Vlasov, V.A., Vasendina, E.A.: Influence of solid-phase ferritization method on phase composition of lithium-zinc ferrites with various concentration of zinc. J. Therm. Anal. Calorim. **109**(1), 63–67 (2012). https://doi.org/10.1007/s10973-011-1366-3
15. Gvozdkova, S.I., Shvartsburg, L.E.: Analysis of sources and methods for reducing noise by minimizing vibrations of engineering technological processes. Proc. Eng. **206**, 958–964 (2017). https://doi.org/10.1016/j.proeng.2017.10.578
16. Nizhegorodov, A.I., Zvezdin, A.V.: Study of an electric furnace physical model for firing vermiculite with a “zero” module. Refract. Ind. Ceram. **57**(3), 246–251 (2016)
17. İşçi, S.: Intercalation of vermiculite in presence of surfactants. Appl. Clay. Sci. **146**, 7–13 (2017)
18. Ritz, M., Zdrálková, J., Valášková, M.: Vibrational spectroscopy of acid treated vermiculites. Vib. Spectrosc. **70**, 63–69 (2014). https://doi.org/10.1016/j.vibspec.2013.11.007

19. Contreras-Serna, J., Rivera-Solorio, C.I., Herrera-García, M.A.: Study of heat transfer in a tubular-panel cooling system in the wall of an electric arc furnace. Appl. Therm. Eng. **148**, 43–56 (2019). https://doi.org/10.1016/j.applthermaleng.2018.10.134
20. Nizhegorodov, A.I., Bryanskikh, T.B., Gavrilin, A.N., Moyzes, B.B., Gradoboev, A.V., Vavilova, G.V., Tlusty, J., Tuzikova, V.: Testing a new alternative electric furnace for vermiculite concentrates heat treatment. Bulletin of the Tomsk Polytechnic University. Geo Assets Eng. **329(4)**, 142–153 (2018)
21. Xu, W., Zhang, J., Zhang, R.: Application of multi-model switching predictive functional control on the temperature system of an electric heating furnace. ISA Trans. **68**, 287–292 (2017). https://doi.org/10.1016/j.isatra.2017.02.001
22. Viti, C., Hirose, T.: Thermal decomposition of serpentine during coseismic faulting: Nanostructures and mineral reactions. J. Struct. Geol. **32**(10), 1476–1484 (2010)
23. Santamaria, A., Faleschini, F., Giacomello, G., et al.: Dimensional stability of electric arc furnace slag in civil engineering applications. J. Clean. Prod. **205**, 599–609 (2018). https://doi.org/10.1016/j.jclepro.2018.09.122
24. Sutcun, M.: Influence of expanded vermiculite on physical properties and thermal conductivity of clay bricks. Ceram. Int. **41**, 2819–2827 (2015). https://doi.org/10.1016/j.conbuildmat.2019.07.080
25. Kariya, J., Ryu, J., Kato, Y.: Development of thermal storage material using vermiculite and calcium hydroxide. Appl. Therm. Eng. **94**, 186–192 (2016). https://doi.org/10.1016/j.applthermaleng.2015.10.090
26. Lozano-Lunar, A., et al.: Safe use of electric arc furnace dust as secondary raw material in selfcompacting mortars production. J. Clean. Prod. **211**, 1375–1388 (2019). https://doi.org/10.1016/j.jclepro.2018.12.002
27. Soleimanimehr, H., Nategh, M.J., Najafabadi, A.F., Zarnan, A.: The analysis of the Timoshenko transverse vibrations of workpiece in the ultrasonic vibration-assisted turning process and investigation of the machining error caused by this vibration. Precis. Eng. **54**, 99–106 (2018)
28. Paczkowski, T., Troszyński, A.: The effect of multidirectional vibration on electrochemical machining. Proc. Manuf. **22**, 41–48 (2018). https://doi.org/10.1016/j.promfg.2018.03.008
29. Wang, Zh., Zhang, J.: Existence of periodic solutions for a class of damped vibration probl lems. CR MATH **356**(6), 597–612 (2018). https://doi.org/10.1016/j.amc.2008.10.020
30. Redko, V.V., Starikova, N.S., Redko, L.A., Vavilova, G.V.: Determination of sensitivity for in-process control of cable product insulation. IOP Conf. Ser.: Mater. Sci. Eng. **81**(1), 012083 (2015). https://doi.org/10.1088/1757-899X/81/1/012083

Complex Studies of the Innovative Vortex Burner Device with Optimization of Design

Askar Baubek, Alexandra Atyaksheva, Mikhail Zhumagulov, Nurlan Kartjanov, Inna Plotnikova, and Nataliya Chicherina

Abstract This article dwells on the scientific study of the vortical device for the efficient combustion of fossil fuels. The innovative burner device under investigation is based on principal of vortical motion of fuel air mixture. There is a precombustion chamber, where inflammation and partial combustion of the swirling flow takes place. Mathematical model has been developed and discussed in the article too, which enables to calculate the distribution of the tangential speed of the swirling flow, the distribution of the angular velocity, static pressure drop, and air resistance loss in the space of the vortical burner chamber (precombustion). The article also describes experiment on defining the geometric dimensioning of the burner discharge nozzle in relation to a combustion chamber. During the experiment, the exhaust nozzle was moved into the chamber. The recommended degree of deepening is 47–50% of the total length of the precombustion chamber.

A. Baubek
Department of Organization of Traffic Transportation and Operation of Transport, L. N. Gumiliyev Eurasian National University, 2 Street Satpayev, 010008 Nur-Sultan, Republic of Kazakhstan
e-mail: baubek.as@mail.ru

A. Atyaksheva
Department of Heat Power Engineering, Saken Seifullin Kazakh Agro Technical University, 62 Zhenis Avenue, 010011 Nur-Sultan, Republic of Kazakhstan
e-mail: sahsa77@mail.ru

M. Zhumagulov · N. Kartjanov
Department of Heat Engineering, L. N. Gumiliyev Eurasian National University, 2 Street Satpayev, 010008 Nur-Sultan, Republic of Kazakhstan
e-mail: Mikelike2000@yandex.ru

N. Kartjanov
e-mail: nurlan-k-e@yandex.kz

I. Plotnikova (✉) · N. Chicherina
School of Non-Destructive Testing, National Research Tomsk Polytechnic University, 30 Lenin Avenue, Tomsk, Russia 634050
e-mail: inna@tpu.ru

N. Chicherina
e-mail: chicherina@tpu.ru

I. V. Minin et al. (eds.), *Progress in Material Science and Engineering*,
Studies in Systems, Decision and Control 351,
https://doi.org/10.1007/978-3-030-68103-6_13

1 Introduction

The modern world is currently facing a large increase in fossil fuel consumption. As a result, the stocks of natural resources are reducing. Therefore, special attention is paid to improvement of the energy efficiency processes, including combustion technologies [1, 2]. One of the ways to increase the combustion efficiency is to create a vortex motion, for example, a tornado-like vortex motion [3]. This substantially improves mixing of fuel and oxidizer and, as a consequence, increases combustion of fossil fuel. Dynamic processes provide high-quality mixing. As noted in [4, 5], swirling flows are one of the most common ways to improve aerodynamics. Laboratory studies of vortex-tornadoes in gas are discussed in detail in [6]. The most complete review of experimental studies of vortex flows is provided in [7]. A mathematical model of the probability of potential firestorms is described in [8–12]. However, the problem of high aerodynamic resistance of burners, when the free area of the mixture flow sharply reduces and increases energy consumption by the air supply mechanisms, is still poorly studied.

The authors of the paper present the results of the study of a burner device with increased efficiency compared to its analogues. Efficiency is increased by using a tornado-like vortex motion at the beginning of combustion. The installation design features a part of the outlet nozzle protruding inward [13]. This design provides the conditions for appearance of a vortex of variable cross-section (mini-tornado) inside the burner. It increases the vortex flow rate and reduces the aerodynamic resistance at the burner outlet, because the flow is sucked into the outlet nozzle due to low pressure [14, 15]. The process occurs as a result of naturally induced vacuum in the axial section of the vortex. The study employed diesel fuel as the most convenient in laboratory conditions and water–oil emulsion [16]. This device was granted a patent for a useful model of the Russian Federation No. 128284 dated June 21, 2012 for “Device for fuel combustion” [17] and European patent EP No. 2684700 dated 09.24.2016 [18].

2 Materials and Methods

2.1 Modeling

Mathematical simulation of the actual burner was carried out to support the statements claimed in the patent [14], or as a counterbalance to them.

Numerical simulation of working process is performed for a preliminary study of the flow structure, the distribution of temperature, pressure, and velocities in different sections, and as a consequence of an assessment of the quality of mixing of fuel with an oxidizer in a vortex burner. Three-dimensional calculation of single-phase flow was carried out in the program complex of gas dynamics Ansys SFX. The design model was built in the CAD/CAM environment of the UG system. Stationary setting was considered in solving the problem. The grid was constructed using the finite volume method [19].

Mixing and partial combustion occurs in the burner, therefore numerical studies were carried out in several stages:

(1) a vortex motion mode was studied with replacement of the fuel stream with air with the possibility of producing the structure of a swirling flow in an axisymmetric limited volume;
(2) modeling of the working process in the fuel mode allowed to determine the influence of geometric and regime parameters on the value of temperature, pressure and flow rate.

The studies were based on experimental design created for laboratory investigation.

When performing numerical simulation of gas dynamics in a vortex device, a turbulent flow of a viscous incompressible gas in a Cartesian coordinate system was reviewed.

The system of nonstationary differential Navier–Stokes equations was used to describe the flow of fluid and gas [16, 17]:

$$\frac{\partial \overline{U}}{\partial t} + \frac{\partial \overline{E}}{\partial x} + \frac{\partial \overline{F}}{\partial y} + \frac{\partial \overline{G}}{\partial z} = 0 \tag{1}$$

where U—vector of conservative variables; E, F, G—flow vector, determined quantities.

At present, there are several approaches to the calculation of turbulent flows. The first of them is a direct numerical simulation of the Navier–Stokes system, which became possible due to the rapid growth of the performance of modern computer systems.

The second is the simulation of large vortex, which consists in solving the Navier–Stokes equations for large flows which are responsible for the transfer of pulse flows and modeling the smallest vortices (subgrid scale).

The approach to numerical modeling of turbulent flow consisting in solving the averaged Navier–Stokes equations (Reynolds equations) is more developed [14, 15]:

$$\begin{gathered}
\frac{\partial \overline{\rho}}{\partial t} + \frac{\partial}{\partial x_j}\left(\overline{\rho}\overline{U}_j\right) = 0 \\
\frac{\partial}{\partial t}\left(\overline{\rho}\overline{U}_i\right) + \frac{\partial}{\partial x_j}\left(\overline{\rho}\overline{U}_i\overline{U}_j\right) = -\frac{\partial \overline{P}}{\partial x_i} - \frac{\partial}{\partial x_j}\left(\overline{\tau}_y + \overline{\rho u_i''\overline{u}_j''}\right) \\
\frac{\partial}{\partial t}\left(\overline{\rho}\overline{H}\right) + \frac{\partial}{\partial x_j}\left(\overline{\rho}\overline{U}_j\overline{H}\right) = \frac{\partial \overline{P}}{\partial t} - \frac{\partial}{\partial x_j}\left(\overline{U}_i\overline{\tau}_y + \overline{u_i''\tau_y''} + \overline{Q}_j + \overline{\rho u_j''}\overline{H''}\right)
\end{gathered} \tag{2}$$

where ρ—density; P—pressure; U_i: and u_i''—components of average and pulsating velocity; η_{y}—the Reynolds stress tensor; $\rho\, u_j'' H''$—heat flow due to turbulent transfer.

The symbol «–» refers to the time-averaged parameters using the weight function (Favre averaging), «-»—refers to time-averaged parameters (Reynolds averaging), and «"» to the pulsating components.

$\tau_y = \overline{-\frac{2}{3}\mu\delta_y\frac{\partial U_j}{\partial x_j}} - \overline{\mu\left(\frac{\partial U_i}{\partial x_j} + \frac{\partial U_j}{\partial x_i}\right)}$—average stress tensor;
$\overline{Q}_j = -\lambda\frac{\partial\overline{T}}{\partial x_j}$—average heat flow according to Fourier's law;
$\overline{H} = \overline{h} + \frac{\overline{U}_j\overline{U}_i}{2} + k$—average total enthalpy;
$H'' = h'' + U_j \times u_j'' + k$—total pulsating enthalpy;
$k = \frac{\overline{u_i''u_j''}}{2}$—turbulent kinetic energy.

In the averaging process, an additional term $\overline{\rho u_i'' u_j''}$ appears in the equation of motion, which characterizes the effect of flux turbulence on combustion. This term has the mathematical form of a second-order tensor containing 9 elements, and acts like a voltage. Therefore, this tensor is called the Reynolds stress tensor. An additional term $\overline{\rho u_j'' H''}$ appears in the energy equation, which characterizes the heat transfer due to turbulent pulsations. The solution to the Reynolds equation system is to express the unknown turbulent pulsation components through their mean values.

To close the system of differential Eq. (2) we used the equation of state.

$p = p(\rho, T)$ form. Which, assuming that the gas is ideal, can be written as follows:

$$p = \rho RT \tag{3}$$

where R—universal gas constant.

Sutherland's formula was used to calculate the temperature-specific viscosity:

$$\frac{\mu}{\mu_o} = \left(\frac{T}{T_o}\right)^{3/2}\frac{T_o + S}{T + S} \tag{4}$$

where μ_{o} and T_{o} are dynamic viscosity and absolute temperature at normal atmospheric conditions, and S—is the Sutherland constant.

Flow of turbulent flows to solve the Reynolds equations split into two parts for using the hypothesis Boussinesq used [16, 17].

The turbulence flow *k-ε*, as shown by the practice of its use, predicts the stream in the primary flow well, but inaccuracies occurs near the wall. This is due to the fact that the transfer equation given above for *ε* is unsuitable within a viscous sublayer without the use of special damping or near-wall functions, which leads to an error in determining the characteristics of the boundary layer and an incorrect description of separated flows.

The model *k-ω*, on the contrary, well describes the wall, including detachment phenomena, but in the main flow it is sensitive to small perturbations of the value of *ω* at the input.

Based on the two models of turbulence *k-ε* and *k-ω* the SST model is created. Increased efficiency of the applied model is achieved by using the k-model in the interlayer. Such a model allows to resolve small-scale turbulence in the main stream.

Thus, there is no need to use complex wall functions, such as the logarithmic law of the wall, which has made it possible to extend the model's universality to flow regime and types.

Thus, there is no need to use complex wall functions, such as the logarithmic law of the wall, which has made it possible to extend the model's universality to flow regime and types.

According to the verified gas-dynamic calculations, for the closure of the system of Reynolds equations within task the optimal is the SST *k-ω model of turbulence*, the equations of which have the following form [14, 15]:

$$
\begin{aligned}
&\frac{\partial(\rho k)}{\partial t} + \frac{\partial\left(\rho U_j k\right)}{\partial x_j} - P_k - \beta''\rho k\omega + \frac{\partial}{\partial x_j}\left[\left(\mu + \frac{\mu_i}{\sigma_{k3}}\right)\frac{\partial k}{\partial x_j}\right] \\
&\frac{\partial(\rho\omega)}{\partial t} + \frac{\partial\left(\rho U_j \omega\right)}{\partial x_j} - a_3\frac{\omega}{k}P_k - \beta_3\rho\omega^2 \\
&+ \frac{\partial}{\partial x_j}\left[\left(\mu + \frac{\mu_i}{\sigma_{\omega 3}}\right)\frac{\partial \omega}{\partial x_j}\right] + (1 - F_1)2\rho\sigma_{\omega 2}\frac{1}{\omega}\frac{\partial k}{\partial x_j}\frac{\partial \omega}{\partial x_j}
\end{aligned}
\tag{5}
$$

Geometry of the computational domain is detailed in [16]. The model consisted of tangential input 1, flow part 2 and outlet nozzle 3, flooded into the flowing part to a depth of δ.

The computational grid for the flow region is a hybrid type grid in the internal space (tetragonal elements in the main flow, prismatic elements in the region near the exit section). The volume of the grid sampling was 760,000 knots, with thickening on the walls, corresponding to the nondimensional coordinates $y^+ = 1.5$.

2.2 *Results of Numerical Study and Considerations*

Figure 1 shows the simulation results for the pressure distribution in the burner device.

It shows that the pressure of the mixture of air fuel and their combustion products to the periphery increases and reaches a maximum at the surface of the vortex chamber body [13]. Vacuum is formed on the axis of the vortex chamber, which does not contradict the well-known theory of hydrodynamics. The outlet nozzle of the burner device has an internal protrusion—a depression inside the vortex chamber. This design feature was patented. Due to this feature, a variable-section vortex (mini-tornado) is created inside the chamber with a culminating narrowing in the inlet part of the exit nozzle. It is in this place that the lowest pressure occurs—the discharge at a level of 1.26×10^{-1} atm. Such a vacuum pressure ensures intensive absorption of combustion products into the outlet nozzle. The discharge along the axis of the vortex chamber has sufficient potential for sucking in additional fuel, if necessary. No auxiliary injection equipment is required. Additional fuel should be fed along the axis of the combustion chamber.

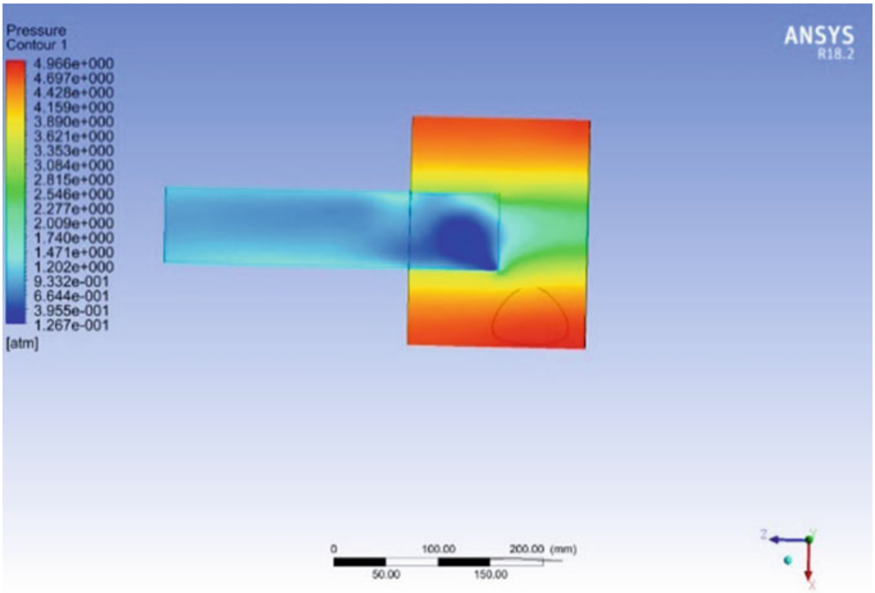

Fig. 1 Pressure distribution along the axial section (side view)

Similarly with pressure, Fig. 2 characterizes the temperature distribution in the burner device.

The temperature is distributed fairly evenly in the burner, which is certainly a positive factor. Considering both figures, it is clear that the temperature fluctuates between 750 and 850 °C. This temperature is sufficient for the primary thermal decomposition of fuel (evaporation and pre-gasification) and its pre-ignition and combustion. The figure shows that the temperature in the layers close to the burner body is generally lower. Therefore, the housing will not overheat under operating conditions and undergo significant thermal stresses. It is not necessary to use high-alloyed high-cost steels. The maximum temperatures are reached in the free space of the vortex chamber. It is necessary to address the issue of the ecological compatibility of the installation. The formation of nitrogen dioxide (NO_2) during combustion will be minimal, since the temperature level is not significant. Also, the reduction of the formation of nitrogen oxides is affected by the fact that products of incomplete combustion are formed in the burner space, which have a greater chemical affinity with oxygen and, as a consequence, restore nitrogen oxides to atomic and molecular nitrogen.

Figures 3, 4 and 5 show the distribution of velocities and zones of the highest velocities in the burner space. For information and convenience, in addition to the cross-sectional image along the axis, two images (vector and gradual) are displayed. It can be seen from the figures that the fuel–air mixture reaches the maximum swirling speed at the suction point at the outlet nozzle. This point of space is key, since it is in the entrance zone of the output nozzle that the deepest discharge takes place.

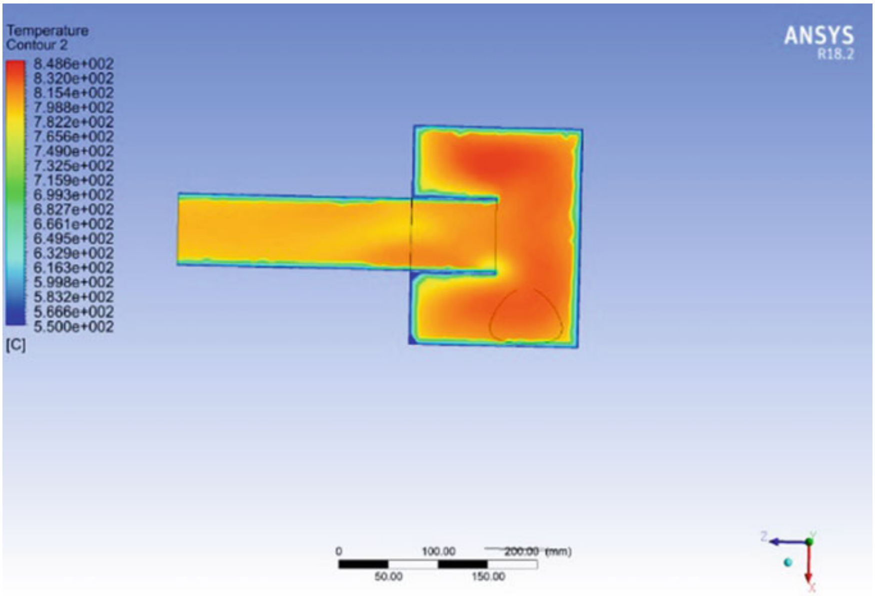

Fig. 2 Temperature distribution along the axial section (side view)

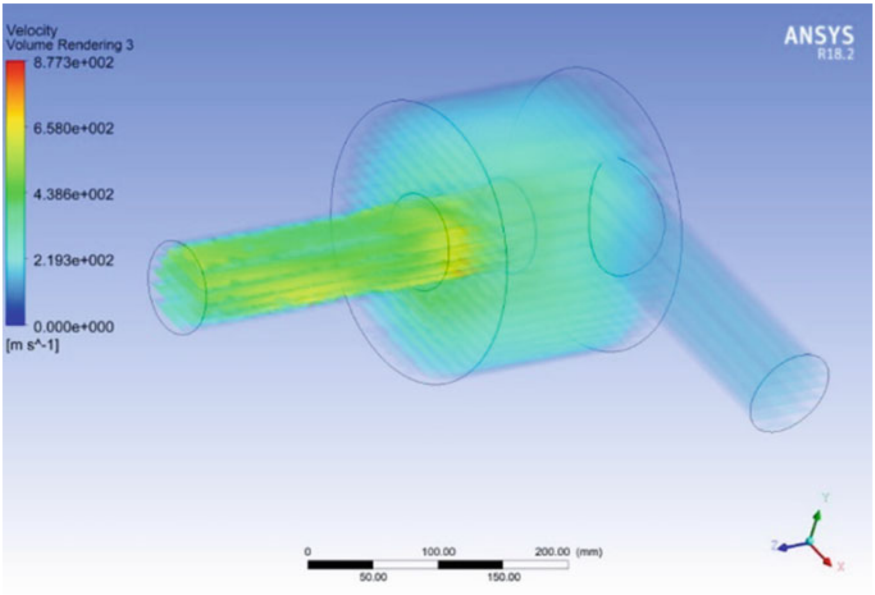

Fig. 3 Volumetric view of the distribution of speed inside the burner device

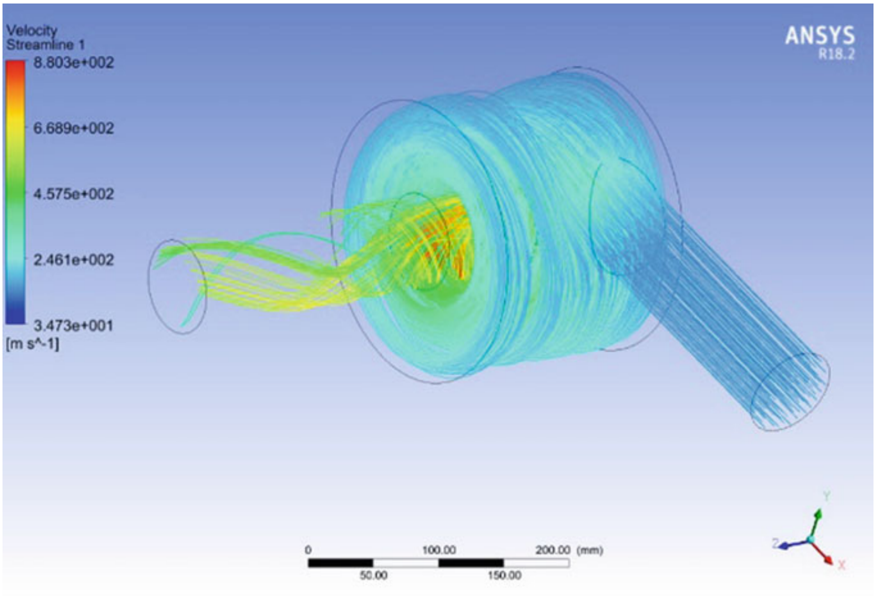

Fig. 4 Lines of speed direction inside the burner

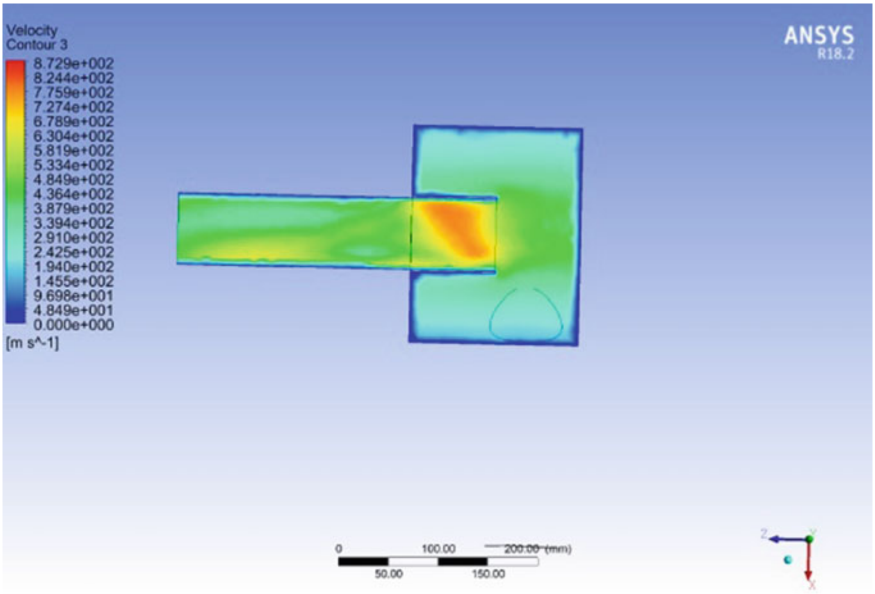

Fig. 5 Speed distribution contour in the burner

The potential energy of pressure is maximally transformed into the kinetic energy of the velocity. High speeds promote intensive mixing of fuel and oxidizer [3, 4]. As a consequence, we receive more effective combustion of the fuel–air mixture.

3 Results and Discussions

In order to test the proposed model for adequacy, the design was tested. Operation parameters, such as air and fuel consumption have been borrowed from the optimal values. These values were obtained by mathematical modeling described earlier.

Diesel fuel was taken:

Initial data:

- Type of fuel–Diesel fuel (winter).
- Content:

C (%)	H (%)	S (%)	O (%)	N (%)	NCV Q_i^r (MJ/kg)
86.3	13.3	0.3	0.05	0.05	42.4

- Initial temperature of fuel: $t_1 = 5$ °C (the experiment was carried out in winter).
- Fuel density: $\rho_f = 840$ kg/m^3.
- Initial temperature of air: $t_{a1} = 5$ °C.

The fuel is fed into the burner tangentially through the side inlet. At the same time air is supplied.

Inside the main chamber the flow swirls, the mixture is heated and partially burned. Thus, the flow is narrowed and then the flow is accelerated. This fact has a positive effect on the mixture formation of fuel and oxidizer.

Sequence of testing refers. The experiment was carried out in 4 stages:

1. Fuel supply to the main fuel channel with tangential twist. tangential twist occurs naturally and spontaneously.
2. Fuel ignition. To carry out this stage an ignition device is needed. It can be an electric spark or a small igniter torch. We used an electric spark.
3. Air volume selection. Combustion air flow was controlled by the gate position. Quantity of air supplied until steady burning (Fig. 6).
4. Measurements. The measurement has been made according to the followingindicators:
   - Temperature at the epicenter of combustion. The main measuring device is a quasi-monochromatic vanishing filament pyrometer (Fig. 7). The maximum temperature measurement limit is 5000 °C. Tungsten rods were installed in order to successfully take readings of radiation along the direction of the flame. The rods created an obstacle and glowed under the influence of the flame. Further, the rods begin to generate radiation equivalent in temperature to the radiation of the flame [20].

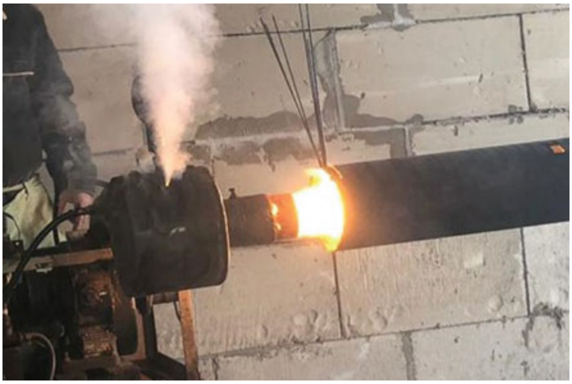

Fig. 6 Burner in operation

Fig. 7 Disappearing-filament optical pyrometer

- Air—fuel flow mix pressure in precombustion chamber and fuel pressure. Elastic-element pressure gage with a tubular spring were used to measure the pressure.
- Electricity consumption current for fuel and air pump supply.
- Fuel and air consumer. Fuel consumer determined using a measuring container and a stopwatch. Air consumer by the readings of the gas meter.

The values obtained are presented in Table 1.

The experimental value of the temperature 1520 °C exceeds the model values (Fig. 2). This is because the flame measurements were taken from outside the burner. At this point, the air - fuel mixture is supplemented with air from the environment.

Table 1 Measurement result

Measurement value	Reported value	Unit measure
(1) Temperature of combustion, t_c	1527	°C
(2) Amperage of fan motor, I	1.32	A
(3) Air–fuel mix flow pressure, P_m	0.36	kgf/sm^2
(4) Inlet fuel pressure, P_f	1.23	kgf/sm^2
(5) Consumption of fuel, B_f	0.091	l/s
(6) The same	0.0079	kg/s
(6) Consumption of air, V	0.13	kg/s

This process provokes afterburning. In doing so noted that the main combustion occurs outside, while the inside is pre-ignited by the lean mixture [21].

Performance calculation. As a result, according to the test results using the data obtained:

1. Burning capacity:

$$Q = B_f \cdot Q_i^r \cdot \eta = 300 \text{ kW},$$

   were $\eta = 0.9$—performance factor of burning. Factor accept by standard.
2. Excess air factor $\alpha = 1.2$ according to Table 1.
3. Flue gas mass flow. The calculation of the combustion products volumes was carried out according to the normative formulas for calculating the volumes of diatomic, triatomic gases and water vapor [16].

$$V_g^{20} = 0.1088 \text{ m}^3/\text{sec};$$
$$m_g = V_g^{20} \cdot \rho_g = 0.129 \text{ kg/s}.$$

   were ρ_g—density of products combustion, kg/m^3.
   The data were obtained at a temperature of 20 °C.
   Density of products combustion ρ_g depend on temperature t_g:

$$\rho_g = \frac{1}{0.787322521209717 + 0.00279036234132946 \cdot t_g}$$

   Gas density at 20 °C is equel to $\rho_{20} = 1.186$ kg/m^3;
   Gas density at 1520 °C is equel to $\rho_{1520} = 0.11986$ kg/m^3.
   Respectively:
   Gas specific volume at 20 °C is equel to $\nu_{20} = 0.843$ kg/m^3;
   Gas specific volume at 1520 °C is equel to $\nu_{1520} = 5.029$ kg/m^3;
   Flow rate at 1520 °C:

$$V_{\mathrm{g}}^{1520} = V_{\mathrm{g}}^{20} \cdot_{\mathrm{g}} = 0.64\ \mathrm{m}^3/\mathrm{sec}.$$

4. Velocity of power fluid (burning velocity):

$$\upsilon = \frac{4 \cdot V_{g}^{1520}}{\pi \cdot d^2} = 168\frac{\mathrm{m}}{\mathrm{s}}$$

were d—exit diameter, *m.*

The values of the velocities obtained in the experiment are perfectly combined with the values obtained in the model (Fig. 5).

In general, combustion gases go through a thermal expansion process. This significantly increases the gas volumetric flow rate and, accordingly, the velocity. The relationship of velocity to temperature is shown in the diagram, according Fig. 8.

5. Import power of fan motor:

$$N = I \cdot U = 286\ \mathrm{W},$$

were U—power tension, V.

6. Heat release rate:

Heat release rate (kW/m^3) precombustion chamber:

$$\frac{Q}{V_f} = \frac{B \cdot Q_i^r \cdot \eta}{V_f} = 56200.82\frac{\mathrm{kW}}{\mathrm{m}^3}$$

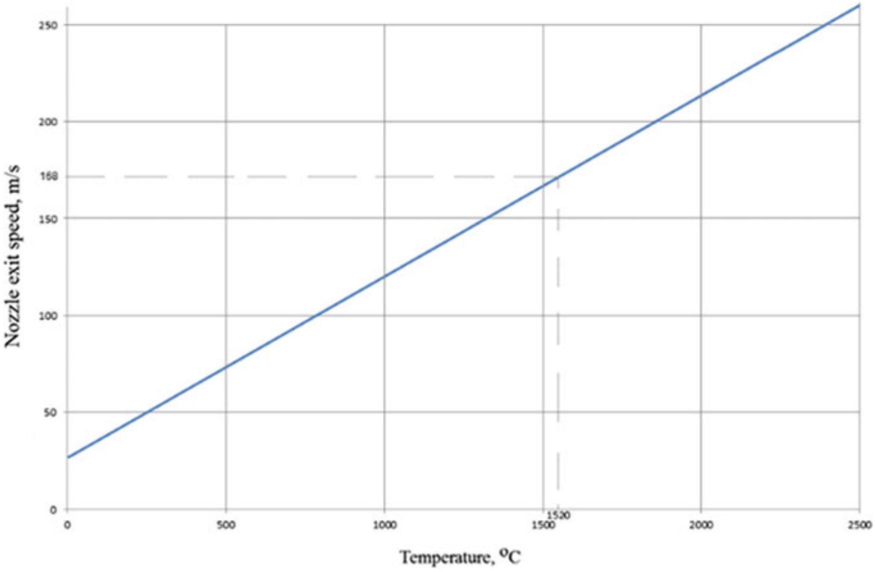

Fig. 8 The dependence of the velocity on temperature

were V_f—volume of combustion chamber, m^3.

Heat release rate natural circulation boiler usually chosen equal to 140–150 kW/m^3 for boilers designed for burning coal. For gas-oil boilers 200–230 kW/m^3, for gas-tight boilers a little higher [22, 23].

Thus, the proposed burner device has a thermal voltage 240 times higher than the standard furnaces of steam boilers.

A detailed experimental analysis of the aerodynamic characteristics of the burner is described in [16]. Based on this, we will not describe the process, but give only the main conclusions.

As a result, it is possible to draw a logical conclusion: the use of the output nozzle as a protruding part inside the combustion chamber positively affects the aerodynamic characteristics of the fuel–air mixture. As the protrusion increases, the pressure within the chamber decreases due to a general reduction in energy consumption on the fan. For the experimental sample in question, the optimal position of the exit nozzle inside the chamber is 80 mm, which is 47% for a total length of 170 mm.

4 Conclusion

The analysis of the results shows the design features of the outlet nozzle of the burner have a positive effect on the formation of a combustible mixture and lead to a decrease in the aerodynamic resistance of the flow at the outlet.

1. With the help of the Ansys SFX software complex, pressure, temperature and velocity distributions have been obtained in the vortex space of the patented burner device. Areas of the space of the burner device have been determined, which actively involved in the aerodynamics of the vortex. The most significant element is the outlet nozzle (nozzle) of the combustion chamber.
2. Areas of high speeds for improved mixture formation have been determined;
3. The peculiarities of the aerodynamic structure of concentrated vortex motion in a cylindrical chamber have been established, which consist in the formation of a mini-tornado with a vertex directed into the nozzle with a minimum aerodynamic drag of the vortex chamber with a given twist of the flow with tangential air entry from the individual supercharger;
4. The reliability of the presented mathematical model has been experimentally confirmed.
5. The necessity of changing the inner part of the outlet nozzle has been grounded. The recommended degree of penetration was 47–50% of the total length of the burner chamber.
6. This device is capable of effectively heating the fuel–air mixture before combustion due to the presence of a vortex combustion chamber. This contributes to the stable operation of the combustion chamber in cold temperatures.

The high combustion temperature in the investigated device (over 1500 °C) allows us to consider the presented vortex burner as a highly efficient generator of thermal energy. Such a generator can be used for various technologies.

The high velocity of combustion products at the outlet of the vortex burner has a high kinetic potential for conversion into other types of energy. The velocity of combustion products increases from 26 to 168 m/s (approximately 6.5 times) due to an increase in temperature from 5 to 1520 °C.

The high concentration of the air fuel mixture in the precombustion zone allows fuel to be burned at high thermal stresses conditions, which exceed typical values by hundreds of times.

Acknowledgements The research is carried out at L. N. Gumiliyev Eurasian National university Republic of Kazakhstan and Tomsk Polytechnic University within the framework of Tomsk Polytechnic University Competitiveness Enhancement Program grant.

References

1. Surzhikov, A.P., Frangulyan, T.S., Ghyngazov, S.A., Lysenko, E.N.: Investigation of oxidation processes in non-stoichiometric lithium-titanium ferrites using TG analysis. J. Therm. Anal. Calorim. **102**(3), 883–887 (2010). https://doi.org/10.1007/s10973-010-0912-8
2. Jenkins, B., Mullinger, P.: Industrial and Process Furnaces: Principles, Design and Operation, 2nd edn. Elsevier, Oxford (2014)
3. Grishin, A.M., Matvienko, O.V.: Numerical investigation of the formation of a convective column and a fire tornado by forest fires. J. Eng. Phys. Thermophy. **87**(5), 1080–1093 (2014). https://doi.org/10.1007/s10891-014-1110-5
4. Beer, J. M., Chiger, N. A.: Combustion Aerodynamics. Krieger Pub Co, USA (1983)
5. Alekseenko, S.V., Kuibin, P.A., Okulov, V.L.: Theory of concentrated vortices. An introduction. Springer, Berlin (2007)
6. Shtym, K.A., Solov'eva, T.A.: Conversion of KVGM-100-150 boilers to cyclone-swirl burning of gas. Ther. Eng. **62**(3), 202–207 (2015). https://doi.org/10.1134/S0040601515020093
7. Bengtsson, L., Lighthill, J.: Intense Atmospheric Vortices. Springer, Berlin (1982)
8. Piquet, J.: Turbulent Flows: Models and Physics. Springer, Berlin (1999)
9. Nizhegorodov, A.I., Gavrilin, A.N., Moyzes, B.B.: Application and production technology of thermal activation products of serpentine minerals from industrial wastes. Bull. Tomsk Polytech. Univ. Geo Assets Eng. **329**(5), 67–75 (2018)
10. Ievlev, V.M.: Numerical Simulation of Turbulent Flows. Science, Moscow (1990)
11. Kireev, V.I., Volnovsky, A.S.: Numerical Simulation of Gasdynamic Flows. Publishing house of MEI, Moscow (1991)
12. Grishin, A.M., Matvienko, O.V., Rudi, Y.A.: Mathematical modeling of gas combustion in a twisted jet and of the formation of a fiery whirlwind. J. Eng. Phys. Thermophy. **82**(5), 906–913 (2009). https://doi.org/10.1007/s10891-009-0278-6
13. Matvienko, O.V., Fil'kov, A.I., Grishin, A.M.: Computational investigation of the transport of burning particles. J. Eng. Phys. Thermophy. **89**(5), 1315–1324 (2016). https://doi.org/10.1007/s10891-016-1494-5
14. Kim, M., Oh, J., Lee, C.: Study on combustion and emission characteristics of marine diesel oil and water-in-oil emulsified marine diesel oil. Energies **11**(7), 1830 (2018). https://doi.org/10.3390/en11071830

15. Menter, F.R.: Two-equation eddy-viscosity turbulence models for engineering applications. AIAA J. **32**(8), 1598–1605 (1994). https://doi.org/10.2514/3.12149
16. Baubek, A., Zhumagulov, M., Kartjanov, N., Sadykova, S., Arpabekov, M.: Experimental test of water-oil emulsion combustion. E3S Web Conf. **178**, 01012 (2020). https://doi.org/10.1051/e3sconf/202017801012
17. Baubek, A., Baubek, N.: Patent for the utility model of the Russian Federation No. 128284 (2012)
18. Baubek, A., Baubek, N.: Device for burning fuel. European Patent 2864700
19. Van Doormal, J.P., Raithby, G.D.: Enhancements of the simple method for predicting incompressible fluid flows. Numer. Heat Transf. **7**(2), 147–163 (1984). https://doi.org/10.1080/01495728408961817
20. Ganapathy, V.: Industrial Boilers and Heat Recovery Steam Generators: Design, Applications, and Calculations: Design, Applications and Calculations Kindle Edition. Dekker, New York (2007)
21. Surzhikov, A.P., Frangylyan, T.S., Ghyngazov, S.A.: A dilatometric study of the effect of pressing on the kinetics of compression of ultrafine zirconium doxide powders under thermal annealing. Russ. Phys. J. **55**(4), 345–352 (2012). https://doi.org/10.1007/s11182-012-9818-1
22. Steam boilers (care and operation) a practical guide to the care and operation of superheaters, feed-water heaters, stokers, and other boiler accessories: and the efficient handling of steam boilers. American Technical Society, US (2017)
23. Alahmer, A., Yamin, J., Sakhrieh, A., Hamdan, M.A.: Engine performance using emulsified diesel fuel. Energy Convers. Manag. **51**(8), 1708–1713 (2010). https://doi.org/10.1016/j.enconman.2009.11.044

Cause Analysis of the Facility Failure Leading to the Explosion

Anna Vtorushina, Yuliya Anishchenko, and Elena Liukiiu

Abstract It is almost impossible to imagine human life without electrical energy in the modern world. The power industry is involved in many areas of human activity. Therefore, improving the reliability of the power supply facilities is a burning issue. This work studies a transformer substation located in an urban area. The research identified the main factors and causes leading to accidents in transformer substations located in urban areas. The fault tree of accidents leading to explosion or fire on transformer station is constructed and analyzed. The probability of the accident has been assessed by the expert method. It has been shown that the most likely causes are mechanical damage to the transformer oil tank and leakage of mineral oil through the welding joint. This work studies the worst scenario, which considers the most severe possible outcome. The calculation has been shown that residential and administrative buildings are located in possible damaged areas. To develop control measures a diagram bow tie was proposed. It presents the barriers aimed at preventing the causes and consequences of accidents.

1 Introduction

Power outages can cause major problems for people, business, social and health facilities, etc. In Russia, the annual electricity consumption is 1000 billion kW/h. To transmit electricity over long distances (from the generating station to a consumer), step-up and step-down transformer substations are used. Transformer substation is an electrical substation, which transforms voltage from high to low or vice

---

A. Vtorushina (✉) · Y. Anishchenko · E. Liukiiu
Division for Testing and Diagnostics, National Research Tomsk Polytechnic University,
30, Lenin Avenue, Tomsk, Russia 634050
e-mail: anl@tpu.ru

Y. Anishchenko
e-mail: ajv@tpu.ru

E. Liukiiu
e-mail: lenysya_1303@mail.ru

I. V. Minin et al. (eds.), *Progress in Material Science and Engineering*,
Studies in Systems, Decision and Control 351,
https://doi.org/10.1007/978-3-030-68103-6_14

versa. According to Rostechnadzor statistics, 39 accidents occurred at electric power facilities in 2018, and 33 of them took place at substations.

In Europe, the operating conditions of packaged transformer substations are also widely studied [1, 2]. For example, the article [3] analyzes the malfunctions of transformer substations with a voltage of 100–500 kV on the territory of European countries. The research considers the failures that occurred at 32 transformer substations from 2000 to 2010 in Great Britain, Austria, Spain, Germany, Netherlands, Switzerland, Denmark, and France. The experts of the working group developed a questionnaire to analyze the main failures of transformer substations. The survey showed that after a certain period of operation of transformer substations, the probability of failures did not increase. The failures are caused by the replacement of mainly old transformers. Since they are not serviced after failure these data cannot be used for modeling accidents. In contrast with similar survey results in 1983, the main cause of transformer failure for the analyzed period was transformer winding. Explosions or fires are mainly caused by bushing malfunctions [3].

A fire can also occur when transformer oil leaks through gaskets, holes in the fins of a radiator, or steel tanks, followed by ignition in the presence of an ignition source. Splash fires occur when mineral oil inside the tank heats up due to internal insulation failure. The temperature of the mineral oil inside the transformer tank increases, forming flammable vapor, which flows from the tank hole into the environment for a short period time [4].

Unfavorable weather conditions can also cause accidents at the transformer station [5]. While fire and explosion of the transformer is unlikely under normal weather conditions, they can potentially occur because of design errors, faulty equipment, or system overloads. Unexpected damage to transformers under unfavorable weather conditions can lead to overcharging, which causes heat and sparks enough for igniting the mineral oil. Boiling of mineral oil forms gases, which overpressure inside the sealed transformer and cause the rupture of the oil tank, the release of a huge amount of energy and heat radiation, and burning oil [6, 7].

Although the probability of fire or explosion of the transformer is relatively small, neglecting it can have serious consequences. Transformer fires are difficult to extinguish and control. Besides, the fire of transformer oil can spread to nearby equipment and buildings, posing a high risk [8].

To increase the safety of the transformer station operation, a risk-based approach can be used. It allows reducing the likelihood of accidents and (or) the severity of their consequences. This work is aimed at identifying the factors leading to transformer station accidents and proposing measures to reduce the likelihood and severity of their implementation.

This work studies the operation of the transformer substation (PS 110/35/10 kV) included two transformers (110/35/10 kV) with a capacity of 63 MVA located in Tomsk. The transformer substation is an industrial-purpose facility. The main processes are the reception, transmission, transformation, and redistribution of electrical energy. The PS 110/35/10 kV is designed to convert 110 kV electric energy to 35 kV and 10 kV. The 10 kV electric power is used to supply the future distribution and transformer substations (10/0.4 kV) of the various city facilities. 35 kV electric power is used as backup power for a lower voltage substation (PS 35/10 kV).

The substation is applied inside and consists of a close-coupled assembly made up of the following main parts:

- two three-phase power transformers (110/35/10 kV) with a capacity of 63 MVA each;
- closed distribution device (110 kV) designed according to the scheme «One working system of tires, divided by the switch» with 5 electric gas switches 110 kV (2-VL 110 kV, 2-inductory 110 kV, 1-sectional 110 kV), made by using the block-modular structures «BMK-Iset» and space reserve for 2 line cells 110 kV;
- prospective switchgear 35 kV designed according to the scheme «One working system of tires divided by the switch» with 5 vacuum switches 35 kV and space reserve for 2 line cells 35 kV;
- two arcing reactors of the installation connected via oil-immersed transformers with a power of 250 kVA each.

The substation is a two-storey building with a cable basement. The substation includes a panel of control, automation, and protection of equipment, an AC shield with two dry transformers of own needs at 630 kVA each, a DC panel with two accumulator batteries, room for current-limiting reactors, server room, communication room, premises for permanent duty personnel, KRU 10 kV with two cells 10 kV sections with a 10 kV vacuum breaker switch. Cells with 10 kV vacuum breaker switches are designed for each section: 1 input, 9 linear, 2 reserves, 1 for connecting arcing reactors, 1 for connecting auxiliary service transformers (AST), and 2 cells of voltage transformers (VT) of 10 kV. The maximum power of the receivers is 50 MW.

To prevent the spread of oil and fire escalation in case of an accident, an oil receiver, oil outlets, and an oil collector are provided. Working and emergency (evacuation, security) lighting is 220 V, while maintenance lighting of technical substation premises is 36 V. Incandescent and sodium lamps are used for lighting.

The number of permanent staff is 1. The operating mode of the substation is 24 h a day, 365 days a year. The total mass of one three-phase power transformer is 117200 kg. The total mass of oil is 30190 kg.

2 Results and Discussion

Accidents at transformer substations do not occur often, but the power outage of various facilities can cause great damage. The main reasons for accidents are human errors, equipment failure, electric circuit overload, failure of power system protection. As a result, they can cause such consequences as transformer fail, fire or (and) explosion of transformer substation, and a power outage.

The most common reason for accidents is a lightning strike, which can overload the transformer. Wires or equipment damage at various points of the electric grid can lead to an explosion. Corrosion and metal wear weaken the insulation of the transformer wires as well as other components, which can lead to transformer failure.

The excess heat or spark is enough to ignite the mineral oil in the transformer. Burning mineral oil creates an overpressure inside the sealed transformer, which leads to the rupture of the vessel, sparks, and flames.

The operation of the transformer substation does not include the storage, use, processing, transportation, or destruction of explosive and fire hazardous, chemically hazardous, biological, and radioactive substances and materials. However, power transformers contain transformer oil, which is a flammable substance.

The literature review [9–14] shows the following causes of accidents at complete transformer substations:

- Errors of electrical personnel, for example, not grounding the live part or voltage supply to faulty equipment. Poor repair or installation: poor adjustment of the commutator drives, insufficiently tightened contacts, factory defects in equipment, etc.
- Malfunction of the transformer substation protection system.
- Incorrect grounding. Single-phase ground faults in a 6–35 kV network are dangerous. The voltage on this phase drops to 0, and the other phases rise to a linear value, which creates an overvoltage. An electric arc breaks the bus insulation, insulation and wires melt.
- Lightning and switching overvoltage at the network. Such voltage drops lead to insulation failure and fires, so substations are equipped with lightning protection devices.

It is impossible to eliminate the technological disruption of the transformer substation. However, preventive measures can reduce the risk of accidents.

Various methods are used to estimate accident risk in different areas of the industry: event tree analysis [15, 16], fault tree analysis [17–19], bow-tie [20], and others [21, 22].

In this work to determine the causes and factors leading to the accidents at the transformer station the method «Fault tree analysis» was used [23]. Using event tree analysis, it is possible to present various scenarios, starting from the initial event, analyze the system, and calculate the probability of each scenario.

Based on statistics and data on the object of research, a model of accident development at the transformation station was proposed.

The analysis of cause and factors that can lead to the accident shows that the most damaging scenario includes an explosion and a possible fire in the transformer substation.

Table 1 presents typical initiating events and factors that can lead to an explosion at the transformer substation.

The most probable external influence that can lead to transformer overloading is a lightning strike. In this case, a voltage rises sharply and a transformer may fail immediately, which will lead to its explosion. A short circuit between third-party electricity systems and overhead transmission lines occurs due to a break in the contact wire and its hit on high-voltage lines. An inductive load increases because

Table 1 Typical initiating factors and events

Index	Event
A	The explosion of a transformer substation
M1	Overvoltage of the electrical network
M2	Transformer failure
M13	Lightning
B2	Short circuit between third-party electricity systems and overhead power lines
B3	Increasing of inductive load
B4	Accumulation of electrostatics in a dry environment
B5	Electromagnetic interference
B6	Arc fault in power lines
M3	Corrosion of metal
M4	Mineral oil leakage from the weld
M5	Short circuit in the working parts of the transformer
M6	Ignition of mineral oil in a transformer
M7	Poor repair/installation
M8	Malfunction of the transformer substation system
B7	Defective lightning rod
B8	Intergranular corrosion due to prolonged vibration of the active part of the transformer
B9	Impact of oxidizing transformer oil on metal
B10	Poor welded joints
B11	Mechanical stress destroying the weld
B12	The box is not ground in the valve body
B13	Poor-quality seals and gaskets of flange connections
M9	Loop closure
M10	Phase-to-phase short circuit. Short circuit on the case
B14	A spark
M11	Increased temperature in the transformer
B15	Ungrounded live parts
B16	Applying voltage to faulty equipment
B17	Poor switch drive alignment
B18	Insufficiently tightened contacts
B19	Defective equipment
B20	Ungrounded live parts
B21	Unconfigured network cutoff
B22	Overcurrent protection failure
B23	Malfunction of automatic transfer switches

(continued)

Table 1 (continued)

Index	Event
B24	Failure to turn on the emergency input switch and lack of control of transformer winding overheating
B25	Natural aging and insulation deprecation
B26	Systematic transformer overload
B27	Dynamic overload of the transformer
B28	Aging of insulation, oil wetting, and lowering of its level
B29	Transformer overvoltage
B30	Deformation of the transformer winding
B31	Overload transformer (high voltage in the primary winding)
B32	Poor core in the transformer
M12	Low level of mineral oil in the transformer
B33	Violation of the cooling system conditions because of poplar fluff getting into the transformer
B34	Mechanical damage to the integrity of the transformer oil tank
B35	Defective oil gauge

of high frequency of impulse voltages, parameters of the electrical network as well as switching equipment. Electrostatics accumulation in a dry environment forms a strong electrostatic field; its discharge can increase the voltage of the electrical network for a short time.

The transformer failure may be caused by metal corrosion, mineral oil leakage from the weld, short circuit, ignition of mineral oil in the transformer, poor-quality repair/installation, a malfunction of the transformer substation protection system.

Metal corrosion in the transformer may be caused by oxidizing oil impact on metal, while intergranular corrosion occurs from prolonged vibration in the transformer.

Mineral oil leakage from the welded joint occurs due to poor-quality welded joints, poor-quality sealed gaskets, mechanical stress, and insufficiently ground-in box in the valve body. Sparks and increased temperatures in the transformer are the reasons for mineral oil ignition in the transformer. In summer, poplar fluff clogs the transformer louvers, therefore the cooling conditions are violated and the transformer oil begins to heat up.

Ungrounded live parts, poor-quality repairs, insufficiently tightened contacts, poor adjustment of switch drives, the voltage supply to faulty equipment, defective equipment are poor-quality repair/installation of equipment.

A faulty transformer protection system is affected by ungrounded live parts, a faulty lightning rod, an unset network cutoff, a current protection failure at a certain time, a malfunction of the automatic transfer switch, as well as failure to turn on the emergency input switch, and lack of control of transformer winding overheating.

Transformer failure is also possible to be caused by a short circuit in the parts of the transformer. A turn circuit in a transformer is produced by natural aging and

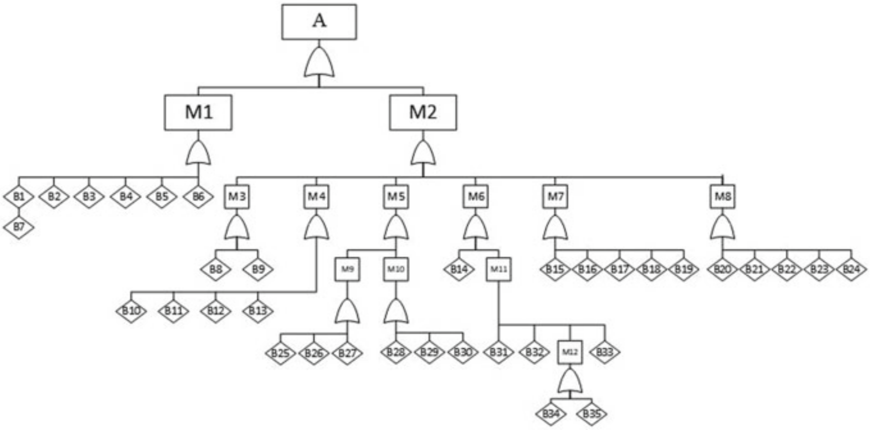

Fig. 1 Model of the accident development

insulation deprecation, systematic overloads, dynamic overloads. The reasons for a phase-to-phase short circuit are moist mineral oil, transformer overvoltage as well as transformer winding deformation.

The fault tree is built from the initial event. In this case, the transformer substation explosion was considered as the initial event. The final model of the accident development at a transformer substation is shown in Fig. 1.

The probability assessment was carried out by the method of expert judgments. Each branch of the reason tree is characterized by the probability of a specific event. To calculate the probability of the initial event, the logical operators must be taken into account.

The expert judgment method involves specialists who have knowledge and skills in a particular area. Usually, this method is used when there is no statistical data. To assess the probability of events, experts need to answer the questionnaire about the state of the object. Further, the expert questionnaires are processed and presented as tables, which include the qualitative characteristics of probabilities of each outcome event.

A group of 10 employees with extensive experience in operating similar substations was selected as experts. The experts needed to determine the probability of events leading to transformer failure on a 5-point scale. The questionnaire includes the events assigned a number from 1 to 25 and experts ranked them according to their experience and knowledge.

The experts ranked the following events: 1–Intergranular corrosion due to prolonged vibration of the active part of the transformer, 2–Impact of oxidizing transformer oil on metal, 3–Poor-quality seals and gaskets of flange connections, 4–Poor welded joints, 5–Mechanical stress causing the destruction of the weld, 6 –The box is not ground in the valve body, 7–Loop closure, 8–Phase-to-phase short circuit. Short circuit on the case, 9–Spark, 10–Increased temperature in the transformer (Overload transformer (high voltage in the primary winding)), 11–Increased temperature in the transformer (Poor core in the transformer), 12–Increased temperature in the transformer (Low level of mineral oil in the transformer), 13–Low level of mineral oil in the transformer (Mechanical damage to the integrity of the transformer oil tank), 14–Low level of mineral oil in the transformer (Defective oil gauge), 15–Increased temperature in the transformer (Violation of the cooling system conditions because of poplar fluff getting into the transformer), 16–Ungrounded live parts, 17–Applying voltage to faulty equipment, 18–Poor switch drive alignment, 19–Insufficiently tightened contacts, 20–Defective equipment, 21–Ungrounded live parts, 22–Unconfigured network cutoff, 23–Overcurrent protection failure, 24–Malfunction of automatic transfer switches, 25–Failure to turn on the emergency input switch and lack of control of transformer winding overheating.

The lowest rank was assigned to the least likely event and the highest rank - to the most likely event. The number of compared events depends on the reliability and accuracy of the results. The smaller the number of the events, the easier to distinguish their value for the expert. Thus, it is possible to rank the events reliably [24, 25]. After ranking the events it is necessary to assess the consistency of experts' opinions. In this work, Kendall's coefficient of concordance was estimated in the Statistica program and showed the consistency of the experts' opinion.

The events are assigned using the mid-rank method. The event with the lowest rank is the least likely to occur: $3.3 < 3.9 < 4.45 < 7.55 < 7.65 < 8.15 < 9.95 < 10.05 < 10.6 < 11.25 < 15.6 < 16.0 < 16.6 < 16.65 < 17.10 < 19.8 < 21.0 < 21.9 < 22.05 < 23.75 < 23.95 = > 1 = 2 = 9$, 4, 14, 8, 20, 25, 16, $6 = 7$, 15, 11, 23, 12, 18, 24, $3 = 22$, 17, 19, 21, 10, 5, 13.

The results of the analysis are presented in Fig. 2.

Thus, all events can be divided into groups:

- the most likely events: 21, 10, 5, 13. They include ungrounded live parts, increased temperature in the transformer (overload transformer (high voltage in the primary winding)), mechanical stress destroying the weld, low level of mineral oil in the transformer (mechanical damage to the integrity of the transformer oil tank);
- the least likely events: 1, 2, 9. They include intergranular corrosion due to prolonged vibration of the active part of the transformer, impact of oxidizing transformer oil on metal, spark.

The other events are medium probable.

The considered scenario of explosion and fire at the transformer station can lead not only to the destruction of the station but neighbor buildings and infrastructure. Therefore, it is necessary to estimate the damage effects and possible loss of this particular scenario.

An explosion of a three-phase power transformer can happen at the transformer substation. The total mass of the power transformer is 117.200 kg, gross oil weight is 30190 kg, the average radius from the explosion site to residential buildings is 100 m. Based on the calculation of partial pressures, the mass of the exploded substance is 30% of the total mass and is equal to 9057 kg.

1. Calculation of the thermal radiation intensity and the lifetime of the fireball.

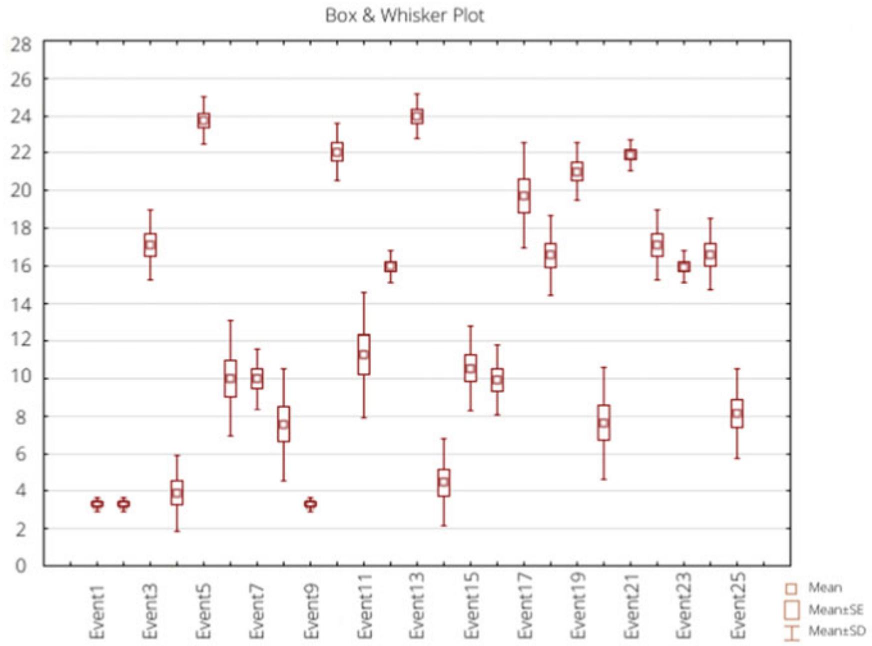

Fig. 2 Graphical representation of the expert judgment

To estimate the parameters of the explosion, it is necessary to calculate the thermal radiation intensity at a distance of 100 m (residential buildings, office buildings) and the lifetime of the fireball.

The results of the calculation show that the thermal radiation intensity is 31.86 kW/m^2. According to GOST R 12.3.047–2012 "Occupational safety standards system (SSBT). Fire safety of technological processes. General requirements. Methods of Control", this intensity could cause decomposition of wooden structures, carbonization of fabric, and rubber. Such thermal radiation intensity from 3 to 5 s could cause severe pain, from 6 to 8 s and 12 to 16 s—1st and 2nd degree burn correspondingly. The worker, serving the transformer substation, could die.

1. Determination of explosion area.
   To determine the explosion area, it is necessary to calculate the effect of the shock wave, which is estimated by the value of the overpressure in the shock wavefront. The overpressure for an explosion of 60,380 kg transformer oil at 100 m from residential buildings is presented in Table 2.

Table 2 Dependence of overpressure on a radius for a transformer explosion

R (м)	100	200	300	400	500
Overpressure (kPa)	109.34	31.26	16.23	10.82	8.03

To calculate the radius of the damaged areas, the interpolation method and data of Table 2 were used. The radius is the following: for an area of full destruction—176 m; for an area of severe destruction—208.38 m; for an area of medium destruction—274.92 m; for area of light destruction—429.39 m. Administrative buildings are located in the possible area of full destruction; residential buildings—in the possible areas of severe and medium destruction; production enterprise, construction, research as well as residential buildings—in the possible area of light destruction.

To analyze the existing control measures at the transformer station, the bow-tie method was used. This method focuses on the barriers between causes and hazardous events, hazardous events and consequences [26, 27]. The diagram presents preventive and reactive controls, which are designed to reduce the probability and severity of a risk (Fig. 3).

Thus, for the identified most probable events that can lead to an explosion of the transformer, preventive control measures were proposed. They are active protection elements; control of welded seams, mineral oil level; protection against corrosion, inspection, and control of repair/installation work, prevention of short circuits, continuous control and testing on the protection system of the transformer substation. According to the results of the expert assessment, special attention should be paid to the grounding of current-carrying parts during the operation of TP.

Protective grounding can be part of external lightning protection, as part of an overvoltage protection system. For transformer substations, modular or electrolytic grounding is performed. Natural ground electrodes are primarily used as ground electrodes. Since the transformer substation is a closed-type one, the resistance of the grounding device must comply with the current regulatory documentation. In

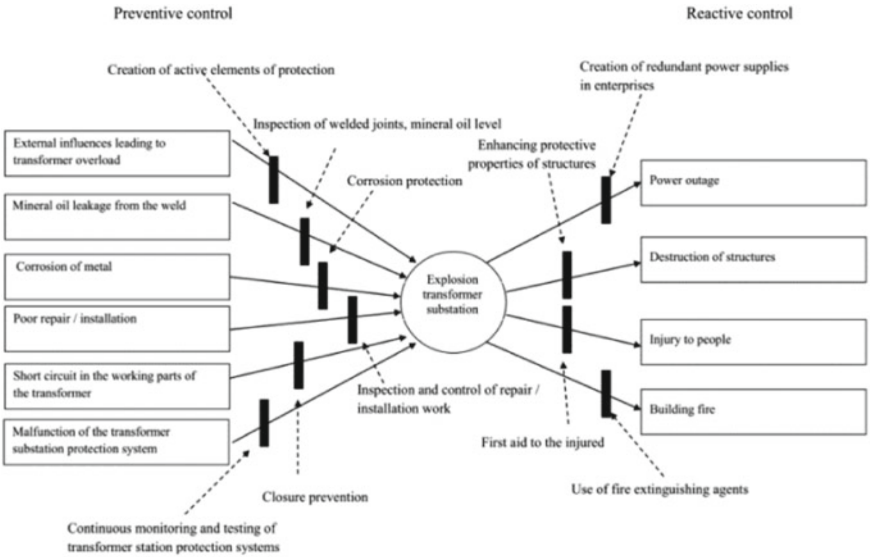

Fig. 3 Bow-tie analysis

Russia, grounding of current-carrying parts of a transformer substation must comply with the standard GOST 12.1.030-81 "Occupational safety standards system (SSBT). Electrical safety. Protective grounding. Zeroing".

To prevent overloading the transformer, namely high voltage in the primary winding, two power transformers must have equal short-circuit voltages (SC). Since the transformers in the substation operate in parallel, the load is unevenly distributed, the power is used in different ways and the power transformer is overloaded.

To reduce the negative effects of such factors as the level of mineral oil, it is recommended to replace the steel tank for transformer oil with a tank made of energy-absorbing material. The advantage of a tank made of energy-absorbing material is the ability to remain intact without damage under overpressure. Energy absorption takes place through successively deformable baffles, therefore, the mineral oil inside will receive minimal damage.

For example, the use of the TRANSFORMER PROTECTOR system prevents the explosion of the transformer oil tank. This system could help to reduce the pressure in the tank, to stop the release of explosive gases from the tank without the participation of air within a few milliseconds.

To decrease the consequences it is proposed to duplicate power supply systems or create backup power supplies for consumers, as well as strengthen the means of response in the case of an emergency, for example, the use of automatic fire extinguishing systems. The most acceptable system for extinguishing electrical equipment is gas or aerosol powder automatic fire extinguishing.

The use of more durable materials characterized by a low level of flammability can increase the protective properties of structures and reduce the damage from the fire or explosion.

Thus, in this work, based on the «bow-tie» method, barriers and controls were proposed to reduce the likelihood and damage of an explosion at a transformer station.

3 Conclusion

This study based on the analysis of literature data and a description of the operating transformer substation 110/35/10 kV SS with two 110/35/10 kV transformers with a capacity of 63 MVA. The fault tree of factors to explosion or fire at the transformer station is constructed and analyzed. The probability of the initial events was assessed by the method of expert judgment. The results of the expert assessment were checked for consistency; a high consistency of expert opinions was shown. It was presented that the most possible event is a mechanical damage to the transformer oil tank and mineral oil leakage from the weld. The paper considers the worst scenario. The explosion areas at a transformer substation were calculated and determined. The area of full destruction is 176 m, the area of light destruction is 429.39 m. Thus, it is shown that residential and office buildings are located in the possible area of full destruction. The bow-tie method was used to develop and propose control measures. Active protection elements; control of welded seams, mineral oil level; protection against corrosion, inspection, and control of repair/installation work, prevention of short circuits, continuous control and testing on the protection system of the transformer substation are the proposed preventive control measures. It is recommended to use natural grounding conductors as grounding. Power transformers must have equal short-circuit voltages to avoid overloading the transformers. To reduce the likelihood of mineral oil spreading, it is necessary to use energy-absorbing tanks. As measures of reactive control, it is proposed to use backup power supply systems for consumers, as well as to strengthen the forces and means of response in the event of an emergency. The strengthen the protective properties of structures could reduce the consequences of fire or explosion.

Acknowledgements The research is carried out at Tomsk Polytechnic University within the framework of Tomsk Polytechnic University Competitiveness Enhancement Program.

References

1. De Faria, H., Costa, J.G.S., Olivas, J.L.M.: A review of monitoring methods for predictive maintenance of electric power transformers based on dissolved gas analysis. Renew. Sustain. Energy Rev. **46**, 201–209 (2015). https://doi.org/10.1016/j.rser.2015.02.052
2. Sica, F.C., Guimarães, F.G., De Oliveira Duarte et al.: A cognitive system for fault prognosis in power transformers. Electr. Power Syst. Res. **127**, 109–117 (2015). https://doi.org/10.1016/j.epsr.2015.05.014
3. Tenbohlen, S., Jagers, J., Vahidi, F.: Standardized survey of transformer reliability: on behalf of CIGRE WG A2.37. In: International Symposium on Electrical Insulating Materials (ISEIM 2017), vol. **2**, pp. 593–596 (2017). https://doi.org/10.23919/ISEIM.2017.8166559
4. Liu, N., Gao, W.-S., Tan, K.-X., et al.: Construction and analysis of fault tree for large-scale power transformer. Zhongguo Dianli/Electr. Power **36**(11), 33 (2003)
5. Ward, D.M.: The effect of weather on grid systems and the reliability of electricity supply. Clim. Change **121**(1), 103–113 (2013). https://doi.org/10.1007/s10584-013-0916-z
6. Martin, D., Beckett, C., Brown, J., et al.: Analysis and mitigation of Australian and New Zealand power transformer failures resulting in fires and explosions. IEEE Electr. Insul. Mag. **35**(6), 7–14 (2020). https://doi.org/10.1109/MEI.2019.8878255
7. El-Harbawi, M., Al-Mubaddel, F.: Risk of fire and explosion in electrical substations due to the formation of flammable mixtures. Sci. Reports **10**(1), E6295 (2020). https://doi.org/10.1038/s41598-020-63354-4
8. Berg, H.-P., Fritze, N.: Risk and consequences of transformer explosions and fires in nuclear power plants. J. Konbin **23**(1), 5–16 (2012). https://doi.org/10.2478/jok-2013-0034
9. Amin, M., Schewe, P.F.: Preventing blackouts. Sci. Am. **296**(5), 60–67 (2007). https://doi.org/10.1038/scientificamerican0507-60
10. Wang, Y.-Y., Zhou, J.-J., Chen, W.-G., et al.: Assessment method for the reliability of power transformer based on fault-tree analysis. High Voltage Eng. **35**(3), 514–520 (2009)
11. Mustafina, R.M., Plotnikov, I.A., Plotnikova, I.V., et al.: Choice of parameters and stability of nonlinear vibration isolation device. J. Phys: Conf. Ser. **671**(1), 012046 (2016). https://doi.org/10.1088/1742-6596/671/1/012046
12. Plotnikova, I., Vedyashkin, M., Mustafina, R., et al.: Optimization of the stabilization system for electromagnetic suspension in active vibration isolation devices. MATEC Web Conf. **79**, 7 (2016). https://doi.org/10.1051/matecconf/20167901019

13. Wang, M., Vandermaar, A.J., Srivastava, K.D.: Review of condition assessment of power transformers in service. IEEE Electr. Insul. Mag. **18**(6), 12–25 (2002). https://doi.org/10.1109/MEI.2002.1161455
14. Liu, N., Gao, W., Tan, K., et al.: Simulation of maintenance period for power transformer based on fault tree. Gaodianya Jishu/High Voltage Eng. **29**(9), 19 (2003)
15. Bonvicini, S., Antonioni, G., Morra, P., et al.: Quantitative assessment of environmental risk due to accidental spills from onshore pipelines. Process Saf. Environ. Prot. **93**, 31–49 (2015). https://doi.org/10.1016/j.psep.2014.04.007
16. Alkhaledi, K., Alrushaid, S., Almansouri, J., et al.: Using fault tree analysis in the Al-Ahmadi town gas leak incidents. Saf. Sci. **79**, 184–192 (2015). https://doi.org/10.1016/j.ssci.2015.05.015
17. Liang, W., Hu, J., Zhang, L., et al.: Assessing and classifying risk of pipeline third-party interference based on fault tree and SOM. Eng. Appl. Artif. Intell. **2**, 594–608 (2012). https://doi.org/10.1016/j.ssci.2015.05.015
18. Marhavilas, P.K., Koulouriotis, D., Gemeni, V.: Risk analysis and assessment methodologies in the work sites: On a review, classification and comparative study of the scientific literature of the period 2000–2009. J. Loss Prev. Process Ind. **24**(5), 477–523 (2011). https://doi.org/10.1016/j.jlp.2011.03.004
19. Lee, W.S., Grosh, D.L., Tillman, F.A., et al.: Fault tree analysis, methods, and applications—a review. IEEE Trans. Reliab. **R-34**(3), 194–203 (1985). https://doi.org/10.1109/TR.1985.5222114
20. de Ruijter, A., Guldenmund, F.: The bowtie method: a review. Saf. Sci. **88**, 211–218 (2015). https://doi.org/10.1016/j.ssci.2016.03.001
21. Khan, F., Rathnayaka, S., Ahmed, S.: Methods and models in process safety and risk management: Past, present and future. Process Saf. Environ. Prot. **98**, 116–147 (2015). https://doi.org/10.1016/j.psep.2015.07.005
22. Dağsuyu, C., Oturakci, M., Kokangül, A.: A new approach to Fine-Kinney method and an implementation study. Alphanumeric J. **3**(2), 83–92 (2015)
23. Anishchenko, Yu.V., Vtorushina, A.N., Zadorozhnaya, T.A., et al.: Welding incident mitigation at mechanical engineering. Mater. Sci. Forum **927**, 6–12 (2018). https://doi.org/10.4028/www.scientific.net/MSF.927.6
24. Rae, A., Alexander, R.: Forecasts or fortune-telling: When are expert judgements of safety risk valid? Saf. Sci. **99**, 156–165 (2017). https://doi.org/10.1016/j.ssci.2017.02.018
25. Chhibber, S., Apostolakis, G., Okrent, D.: A taxonomy of issues related to the use of expert judgments in probabilistic safety studies. Reliab. Eng. Syst. Saf. **38**(1–2), 27–45 (1992). https://doi.org/10.1016/0951-8320(92)90103-R
26. Targoutzidis, A.: Incorporating human factors into a simplified «bow-tie» approach for workplace risk assessment. Saf. Sci. **48**(2), 145–156 (2010). https://doi.org/10.1016/j.ssci.2009.07.005
27. Badreddine, A., Romdhane, T.B., HajKacem, M.A.B., et al.: A new multi-objectives approach to implement preventive and protective barriers in bow tie diagram. J. Loss Prev. Process Ind. **32**, 238–253 (2014). https://doi.org/10.1016/j.jlp.2014.09.012

Designing of a Laboratory Complex for Spectral Analysis of Measurement Data of Different Materials

Renat Khamitov, Maria Kolchurina, Irina Kolchurina, Kira Ponomareva, and Inna Plotnikova

Abstract The article describes the process of development and testing of a laboratory complex for spectral analysis of measured data, which is based on a signal processing method based on measuring the frequency and amplitude of the signal (spectral method) with further evaluation using fast Fourier transform. The described laboratory complex consists of a spectrum analyzer connected to a personal computer with special software installed on it, a loudspeaker and a laser sensor. The this substantiates the relevance of the development, due to the fairly wide use of spectral analysis methods in science, technology and production, the advantages of using a laboratory complex in comparison with analogues were shown. the description of the experiments to measure the speed of objects, control their location, vibration measurement, the procedure of verification and calibration that is performed with the use of this complex, as well as the use of the system of automatic regulation and stabilization of production processes.

R. Khamitov
Department of Management, Kazan State Power Engineering University, 26 2nd South-West Street, Kazan, Russia 420034
e-mail: hamitov@gmail.com

M. Kolchurina · I. Kolchurina · K. Ponomareva
Department of Quality Management and Innovation, 42 Kirov Street, Novokuznetsk, Russia 654007
e-mail: kolchurina.masha@yandex.ru

I. Kolchurina
e-mail: ira-kolchurina@yandex.ru

K. Ponomareva
e-mail: kiraponomareva525@mail.ru

I. Plotnikova (✉)
School of Non-Destructive Testing, National Research Tomsk Polytechnic University, 30 Lenin Avenue, Tomsk, Russia 634050
e-mail: inna@tpu.ru

I. V. Minin et al. (eds.), *Progress in Material Science and Engineering*,
Studies in Systems, Decision and Control 351,
https://doi.org/10.1007/978-3-030-68103-6_15

1 Introduction

One of the important stages of the production process is the quality control of raw materials, semi-products and completed products, consisting of measurements—a process where the value of a feature is set—and further comparison of the measurement results with the specified parameters [1]. Depending on the specifics of the controlled parameter, it is possible to use different control methods, in particular, the spectral method [2, 3], non-destructive testing method [4, 5], its essence consists in determination of the spectral content (i.e. power frequency distribution) of a time series from a finite set of measurements using nonparametric or parametric methods [6, 7]. Nowadays this method is widely used in science and production; in particular, it is used in the assessment of product quality in food industry in the detection of chemical, biological and physical hazards [8], pharmaceuticals [9], the oil refining industry [10] and a number of other areas [11]. The reason for the high popularity of the spectral method is due to high visibility of the measurement results (the form the measurement results can be presented is the graph), it is easily to detect frequencies, the value of which is different from the standard values, and quickly identify and correct the fault during the process [12].

2 Research Method

Spectral analysis is a method of signal processing—material carriers of information,—based on the evaluation of the frequency and amplitude of the signal. There are various methods for estimating the vibration spectrum, one of which is the method based on using fast Fourier transform, which is based, in its turn, on representation of the original signal function from time as the sum of an infinite series of trigonometric functions with certain amplitudes and phases [13].

The Fourier series can be represented as: $f(x) = \sum_{k=-\infty}^{+\infty} X_n * e^{i*2\pi*\frac{k}{T}*x}$, where $f\ (x)$ is the function of the analyzed signal; k is the number of the trigonometric function; T is the segment where the function is defined; Xn is the complex amplitude of the signal n.

Graphically, the Fourier series is represented as a Fourier spectrum, where it is possible to trace the dependence of the signal amplitude on the frequency on it [14].

The method of signal processing by their representation in the form of Fourier spectrum underlies the work of modern spectrum analyzers-devices designed to observe and measure the relative energy distribution of electric (electromagnetic) oscillations in the frequency band [15]. Spectrum analyzer allows determining the frequency and amplitude of the analyzed signal. In general, the mechanism of its operation can be described as follows: the input of the analyzer receives a digital signal. The analyzer selects successive intervals from the signal, where the spectrum will be calculated, and converts the received signal using the Fourier transform [16].

The calculated spectrum is displayed as a graph of amplitude versus frequency. Spectrum analyzers allow measuring the signal frequency, its amplitude, power, modulation, distortion and noise, their using shows a complete picture of the signal nature and its characteristics, the knowledge of which is important for solving the problems facing modern science and technology [17, 18].

Currently, spectrum analyzers, in addition to converting a digital signal to an analog signal for subsequent processing, are able to convert an input digital signal read from various sensors into an analog signal for its subsequent transmission to analog electronic devices.

3 Description of the Installation

In the work, a laboratory complex was developed that allows spectral analysis of measurement data of various materials. The complex includes a computer with specialized software installed, a spectrum analyzer ZET 017-U4, a column and a RF 603 laser displacement sensor. It is also possible to additionally connect various sensors, for example, displacement sensors or force sensors, to one of the four analog–digital inputs of the analyzer Spectrum ZET 017-U4. The basic installation diagram is shown in Fig. 1.

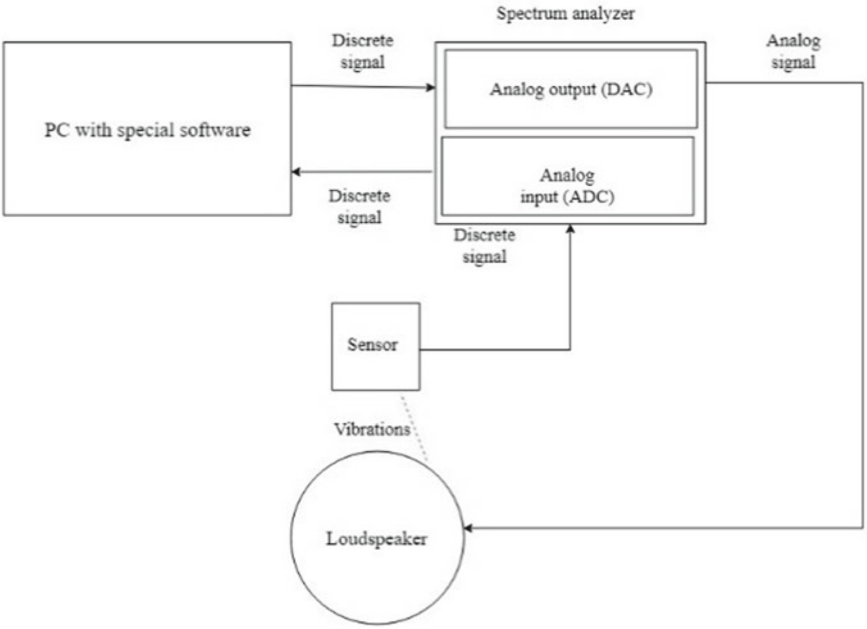

Fig. 1 Scheme of the laboratory complex

The spectrum analyzer used consists of two modules, such as an Analog output (DAC) and an Analog input (ADC). An ADC converts an analog signal into a digital one and is an analog output, and a DAC converts an analog signal into a digital one and is an analog output. The uncertainty of measurements made using the analyzer is best described by the Gaussian distribution, which indicates the possibility of using the analyzer for measurements with high accuracy. All analyzer settings are made on the computer, which is part of the laboratory complex, before starting work in a specialized software product, in which data is subsequently processed and the signal analyzed with its parameters determined.

Consider the algorithm of the laboratory complex for generation and spectral analysis of measurement information:

(1) a control command is sent to the generator from the computer via software by the USB interface to generate a specific waveform with a spectrum analyzer;
(2) the spectrum analyzer of the analog output transmits a signal to the column, which converts it into the form of vibrations, sounds or noise;
(3) the laser motion sensor reads vibrations from the column and transmits them to one of the four analog inputs of the spectrum analyzer;
(4) the received signal is converted by the ADC and fed to a computer in software that issues a report in the form of a measured signal.

To check the operability of the complex, a series of tests were conducted to generate a signal of a given frequency and amplitude in order to receive a filtered signal with the same parameters at the output. Part of the tests was carried out using one motion sensor; in other experiments, a second similar sensor was included in the laboratory complex. The set frequencies and voltage of the signals and the output parameters of the signals are shown in Table 1. The noise level in all experiments was equal to 0.001 mm.

In the first series of experiments a signal with a constant voltage of 7 V and frequencies equal to 1 Hz, 10 Hz, 50 Hz, 100 Hz, and 200 Hz, respectively, was supplied to the spectrum analyzer. At output in the first three experiments, a signal was obtained having a frequency similar to the frequency of the supplied signal (2 Hz, 9.8 Hz, 51 Hz), however, at frequencies exceeding 50 Hz, the noise component of the signal did not allow us to determine the useful signal read by the sensor. When exceeding the value of the frequency values of the signal mark at 50 Hz, the noise did not allow accurate measurements. According to the results of the experiments, we can conclude that the laboratory complex is advisable to use for tests performed at low frequencies. In these conditions, the installation allows you to take the necessary measurements and analyze the result using various software modes.

The laboratory complex also allows to produce flat, band, pink and defined noise at the DAC output. As we can see, the laboratory testing with using the laboratory complex is quite similar to real impacts, to which the specimen is exposed in the course of its operation.

Table 1 Experimental results

The frequency of the first harmonic [Hz]	The voltage of the first harmonic [V]	Second harmonic frequency [Hz]	Second harmonic voltage [V]	Frequency 1 of the RF sensor 603 [Hz]	Amplitude of 1 sensor RF 603 [mm]	Frequency 2 sensors RF 603 [Hz]	Amplitude 2 sensors RF 603 [mm]
1	7	–	–	2	0.100	–	–
10	7	–	–	9.8	0.200	–	–
50	7	–	–	51	0.250	–	–
100	7	–	–	–	0.001	–	–
200	7	–	–	–	0.001	–	–
1	2	10		1.9	0.024	10	0.032
1	2	50	5	2.1	0.025	49.5	0.030
10	2	10	5	10.1	0.024	9.9	0.031
10	2	50	5	10	0.025	50	0.029
10	2	100	5	–	0.001	–	0.001
10	2	100	5	–	0.001	–	0.001

4 Results and Considerations

The scope of this complex is wide enough, since the complex is based on the spectral method, which is widely used in various fields of modern science and technology. Thus, the assembly of various modifications of the laboratory complex allows it to be used to detect cracks in concrete and damage in building structures [19, 20], while continuously monitoring the tightness of various containers and pipelines.

It is also possible to use a laboratory complex to control the location of various objects and the speed of their movement, moreover, it is possible to measure values of both angular and linear velocities and values of displacements in the space of the studied object.

The developed laboratory complex can also be used in mechanical engineering during vibration analysis during dynamic testing of machines and various mechanisms. During this operation, a force sensor is connected to the spectrum analyzer through a charge amplifier and with its help vibrations emanating from moving parts of machines and mechanisms are measured.

It is possible to use the complex, creating systems for protecting production facilities based on voice recognition [21]. It is also advisable to include the laboratory complex under consideration in the equipment when conducting various scientific studies of the properties of substances and materials, as well as noted above, in assessing the quality of food products [22].

Another direction in which it is advisable to use this complex is the testing and calibration of vibration sensors by comparing the device to be verified with a reference device. To carry out this operation, verifiable sensors are connected to the spectrum

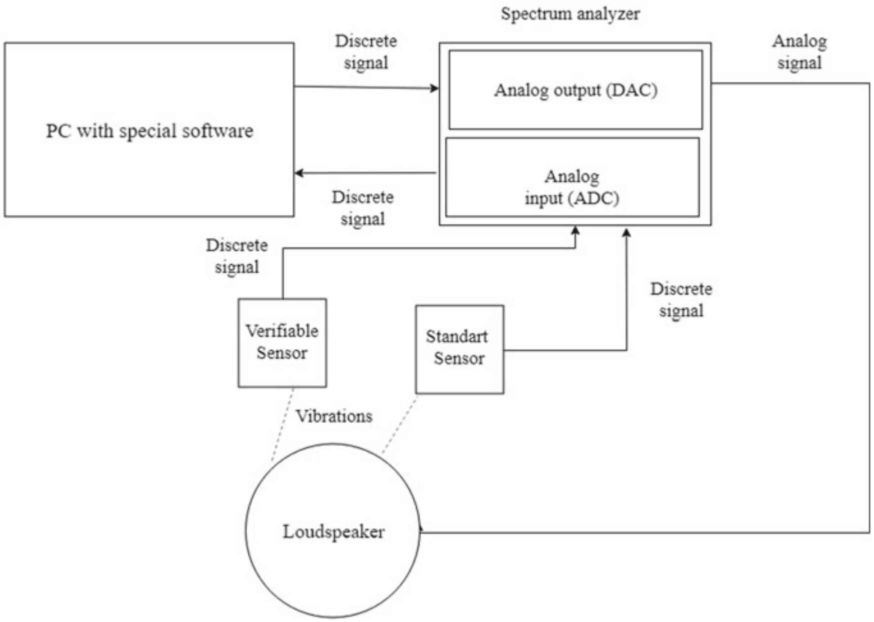

Fig. 2 Installation diagram for sensor verification

analyzer, which is installed on the loudspeaker. The installation diagram for sensor verification is shown in Fig. 2. On the computer, vibration parameters are set, which are reproduced by the loudspeaker, and the system is brought into operation and the device is automatically calibrated: the ADC receives signals from the reference and verified devices, transfers data to the computer, to the software, in which there is a comparison of the readings of devices, determination of the amplitude characteristic, the removal of the amplitude-frequency characteristics of the sensor being calibrated [23].

Based on the results of measurements and comparisons of instrument readings, a protocol is compiled containing information on the suitability of the sensor being verified. Since the verification procedure is carried out in automatic mode, its results are not affected by errors caused by the work of the employee performing the verification, due to high accuracy of measurements and the obtained results are achieved.

Presented laboratory complex can be used not only during control measurements, but also when creating automatic regulation and stabilization of production processes. At the same time, the laboratory complex takes a part of a proportional-integral-differentiating (PID) feedback regulator. PID control is carried out by applying a control signal to the control object, the value of which depends on the difference between the measured parameter and the set value, on the integral of the difference and on the rate of change of parameters. As a result, the PID controller transmits a signal providing such a state of the device at which the measured parameter is equal to the specified one, stable and maintained during the course of the process at a given level with fairly high accuracy. Because of the production process stability, labor productivity increases, product quality, process efficiency and effectiveness indicators increase, which is important in modern market economies and constant competition [21]. The control signal for the PID controller is determined by three components: proportional, integral and differential, and depends on how large the mismatch (proportional component) is, how long the mismatch (integral component) lasts, and finally, how quickly the mismatch (differential component) changes. The regulator can hold the set level or work on the set profile. Additionally, the software product of the complex can graphically display form the set level, the current value of the parameter, and the output signal.

5 Conclusion

In the course of the work, a laboratory setup was developed and implemented for the spectral analysis of measurable data of various materials with a fairly wide range of applications. In particular, it is possible to use the installation for conducting non-destructive testing in production, for detecting cracks in concrete, damage in building structures, with continuous monitoring of the tightness of various containers and pipelines, monitoring the location of various objects and the speed of their movement, during vibration analysis during dynamic tests machines and various mechanisms, during various scientific studies of the properties of substances and materials, in assessing the quality of food products, for the existence of verification of non-destructive testing means, as well as in the training of employees whose activities are directly related to the measurement and analysis of their results. A high degree of automation ensures high measurement accuracy, therefore it is advisable to include the developed laboratory complex in the laboratory base of industrial enterprises.

References

1. Kulz, M.: Mechanical Engineers Handbook, vol. 2: Design, Instrumentation, and Controls. Wiley, Hoboken (2015)
2. Surzhikov, A.P., Galtseva, O.V., Vasendina, E.A., Vlasov, V.A., Nikolaev, E.V.: Processing line for industrial radiation-thermal synthesis of doped lithium ferrite powders. IOP Conf. Ser.: Mater. Sci. Eng. **110** (1), 012002 (2016). https://doi.org/10.1088/1757-899X/110/1/012002
3. Im, S.B., Hurlebaus, S.: Non-destructive testing methods to identify voids in external post-tensioned tendon. KSCE C.E.J **16**(3), 388–397 (2012). https://doi.org/10.1007/s12205-012-1295-0
4. Li, N., Cao, M., Liu, K., He, C., Wu, B.: A boundary detecting method for post-tensioned pre-stressed ducts based on Q-factor analysis. Sens. Actuators, A **248**, 88–93 (2016). https://doi.org/10.1016/j.sna.2016.07.024

5. Krause, M., Milmann, B., Mielentz, F., Streicher, D., Redmer, B., Mayer, K., Langenberg, K.J., Schicker, M.: Ultrasonic imaging methods for investigation of post-tensioned concrete structures: a study of interfaces at artificial grouting faults and its verification. J. Nondestruct. Eval. **27**, 67–82 (2008). https://doi.org/10.1007/s10921-008-0033-5
6. Surzhikov, A.P., Pritulov, A.M., Lysenko, E.N., Sokolovskiy, A.N., Vlasov, V.A., Vasendina, E.A.: Calorimetric investigation of radiation-thermal synthesized lithium pentaferrite. JTAC **101**(1), 11–13 (2010). https://doi.org/10.1007/s10973-010-0788-7
7. Astanov, SKh., Kasimova, G.K., Sharipov, M.Z.: Optical systems for removal of polarization spectra. Eurasian Phys. Tech. J. **16**(31), 83–88 (2019). https://doi.org/10.31489/2019No2/83-88
8. Stoica, P., Moses, R.: Spectral Analysis of Signals. Prentice Hall, New Jersey (2005)
9. Fu, X., Ying, Y.: Food safety evaluation based on near infrared spectroscopy and Imaging a review. Crit. Rev. Food Sci. Nutr. **56**(1), 1913–1924 (2014). https://doi.org/10.1080/10408398.2013.807418
10. Roggo, Y., Chalus, P., Maurer, L., Lema-Martinez, C., Edmond, A., Jent, N.: A review of near infrared spectroscopy and chemometrics in pharmaceutical technologies. J. Pharm. Biomed. Anal. **44**(1), 683–700 (2007). https://doi.org/10.1016/j.jpba.2007.03.023
11. Yesbaev, A.N., Yessenbayeva, G.A., Ramazanov, M.I.: Investigation of the model for the essentially loaded heat equation. Eurasian Phys. Tech. J. **16**(1), 113–120 (2019). https://doi.org/10.31489/2019No2/105-112
12. Xu, S., Zhao, Y., Wang, M., Shi, X.: Comparison of multivariate methods for estimating selected soil properties from intact soil cores of paddy fields byViseNIR spectroscopy. Geoderma **310**, 29–43 (2018). https://doi.org/10.1016/j.geoderma.2017.09.013
13. Surzhikov, A.P., Pritulov, A.M., Lysenko, E.N., Sokolovskii, A.N., Vlasov, V.A., Vasendina, E.A.: Dependence of lithium-zinc ferrospinel phase composition on the duration of synthesis in an accelerated electron beam. J. Therm. Spray Technol. **110**(2), 733–738 (2012). https://doi.org/10.1007/s10973-011-1947-1
14. Doobae, J., Changmo, A., Jinsu, K., Gwangil, K.: Signal analysis of global financial crises using Fourier series. Physica A **526**, 1212015 (2019). https://doi.org/10.1016/j.physa.2019.04.251
15. Lizhe, T., Jean, J.: Discrete Fourier transform and signal spectrum Chap. 4 in digital signal processing (3rd ed.). Fund. Appl. 91–142 (2019). https://doi.org/10.1016/B978-0-12-815071-9.00004-X
16. Joseph, C., Joseph, J.C.: Practical Radio Frequency Test and Measurement: A Technician's Handbook. Newnes, New York (2002)
17. Meng, C., Hong, S., Xiaoshuai, P., Minzan, L., Qin, Zh., Man, Zh.: Spectrum analyzer development for oxidation diagnosis of Potato semi-finished products. IFAC-Papers On-Line **49**(16), 320–323 (2016). https://doi.org/10.1016/j.ifacol.2016.10.059
18. Turon, V,, Janik J., Spetik, R., Sovka, P., Vlcek, M.: Study of ADZT properties for spectral analysis. In: Proceedings of the 11th WSEAS International Conference on Signal Processing, Computational Geometry and Artificial Vision, and Proceedings of the 11th WSEAS International Conference on Systems Theory and Scientific Computation, pp. 171–176 (2011)
19. Franček, P., Petošić, A., Budimir, M., Hrabar, I.: Electrical resonance/antiresonance chaacterization of NDT transducer and possible optimization of impulse excitation signals width and their types. NDT E Int. **106**, 29–41 (2019). https://doi.org/10.1016/j.ndteint.2019.05.005
20. Chen, J., Wu, Y., Yang, C.: Damage assessment of concrete using a non-contact nonlinear wave modulation technique. NDT & E Int. **106**, 1–9 (2019). https://doi.org/10.1016/j.ndteint.2019.05.004
21. Sánchez-Aparicio, L.J., Bautista-De Castro, Á., Conde, B., Carrasco, P., Ramos, L.F.: Non-destructive means and methods for structural diagnosis of masonry arch bridges. Autom. Constr. **104**, 360–382 (2019). https://doi.org/10.1016/j.autcon.2019.04.021

22. Han, Z., Yang, S.: Analysis of voice of healthy aged persons with narrow band spectrum analyzer. Auris Nasus Larynx **17**(1), 45–48 (1990). https://doi.org/10.1016/s0385-8146(12)80020-4
23. Cheng, M., Sun, H., Pei, X., Li, M., Zhang, Q., Zhang, M.: Spectrum analyzer development for oxidation diagnosis of Potato semi-finished products. IFAC-Papers On-Line **49**(16), 320–323 (2016). https://doi.org/10.1016/j.ifacol.2016.10.059

Method of Polarizing Infrared Spectroscopy for Studying the Orientation of Protons in Protonated Crystals

Yury Borodin

Abstract A method of definition of the focused localization of protons in the protonated crystals is offered. The method is based on the shooting of infrared (IR) ranges in polarized light and the analysis of integrated IR of a strip of absorption of valent fluctuations of X–H bonds depending on the rotation angle of the polarization plane φ relatively crystallographic axis of the crystal. The direction of the dipolar moment of X–H bonds answers a maximum of this dependence. The results of the researches of flat samples of crystals of $LiNbO_3$ and $LiTaO_3$ are given. The places of localization and orientation volume proton-containing centers are shown. The use of polarizing IR spectroscopy of materials with impurity proton-containing centers is a convenient method of definition of localization and orientation of protons and allows to study of interaction with other ions. The operability of the offered method is confirmed with the coincidence of theoretical and experimental results.

1 Introduction

The protonation of crystals TiO_2, Al_2O_3, $KTaO_3$, $LiNbO_3$, $LiNbO_3$, and other substances is accompanied by a high concentration of H^+ ions in the layers, some of which are involved in the H-bond, and the other is included in the composition of stable centers. When protons are concentrated, the form of their oriented localization is, as a rule, proton-containing (PC) defect centers based on dipole complexes in one of the sublattices [1–4]. Ions H^+ are also localized in weakly oriented fragments X–H…X engulfed by the H-bond, providing their high mobility [5, 6]. In crystals with a hexagonal closest packing, this is associated with the formation of mobile PC centers, which ensure the formation of a denser proton lattice with a high level of induced elastic stresses [7–9].

Y. Borodin (✉)
School of Non-Destructive Testing, National Research Tomsk Polytechnic University, 30 Lenin Avenue, Tomsk 634050, Russia
e-mail: uryborodin@tpu.ru

I. V. Minin et al. (eds.), *Progress in Material Science and Engineering*,
Studies in Systems, Decision and Control 351,
https://doi.org/10.1007/978-3-030-68103-6_16

The low level of research on the localization of H^+ ions in the anionic sublattice, the orientation of PC centers, and the formation of quantum wells on their basis hinders the development of protonation and, consequently, the production of non-equilibrium materials with the re-constructing role of protons. Polarization studies make it possible to distinguish the behavior and orientation of H^+ ions concerning the site and impurity ions.

2 Experimental Procedures

It is known that the integrated intensity of the infrared (IR) absorption band is expressed [10] in the form:

$$A = \int lg(I_0/I)d\nu, \tag{1}$$

where I_0, I—transmission, respectively, related to the baseline on the contour of the absorption band.

The oscillator strength A' is expressed through A:

$$A' = 2,303A/Cd, \tag{2}$$

where C is the concentration of absorbing particles; d—sample thickness. Using the Overend formula [10], we get:

$$A' = K\frac{\pi N_A \nu'}{c_B^2 w_l}\frac{d\overrightarrow{p}}{dr}r_1, \tag{3}$$

where N_A is Avogadro's number; ν' is the observed frequency at the maximum of the absorption band; c_B is the speed of light in vacuum; w_l—vibrational coupling constant; $\overrightarrow{p}$—the vector of the dipole moment of the connection; r and r_1 are real and equilibrium internuclear distances.

For oscillations in a plane perpendicular to the direction of propagation of IR radiation with a random direction of the O–H bond in it, the value of K will be:

$$K = \frac{1}{\pi}\int_0^\pi \mathrm{Cos}^2\varphi d\varphi = 1/2, \tag{4}$$

where φ is the angle between the electrical component of the IR radiation and the direction of the vector $\overrightarrow{p}$. If the direction of the dipole moments is fixed within this plane, then $K = \cos^2\varphi$ or $A \sim \cos^2\varphi$ with the constancy of other parameters included in (4). The integral intensity of the absorption band is often approximated by an expression of the type $A \sim \cos^2\varphi$ (when recording IR spectra in polarized light), and the direction of the dipole moment of the bond corresponds to the maximum of this dependence. Strictly speaking, the direction of the dipole moment $\vec{p}$ in real cases does not always coincide with the direction of the internuclear distance, but this is true for the N–H and O–H bonds [10, 11].

The IR absorption band of stretching vibrations of O–H bonds in $LiNbO_3$, as shown [7, 8], splits into components 3470, 3482, and 3490 cm^{-1}, and in $LiTaO_3$—at 3486 and 3496 cm^{-1}. The low-component structure of the absorption bands of $LiNbO_3$ is associated in [12, 13] with three O…O distances perpendicular to the Z-axis of the plane and the predominant orientation of O–H bonds in it.

The IR absorption band of O–H bonds of bulk PC centers in most of the oxides under consideration has noticeable dichroism. Thus, in x-cut $LiNbO_3$ there is a noticeable absorption when the vector $\overline{E}$ is directed perpendicular to the Z-axis and is minimal when $\overline{E} \parallel Z$ (Fig. 1) [3]. A similar picture is observed for the y-cut $LiNbO_3$, and in the case of the z-cut absorption is practically independent of the orientation of the polarization plane relative to the X- and Y-axes. The contour of the absorption curve is well approximated by the Gaussian function, which makes it possible to calculate the contoured area of the integrated intensity A band using the relation:

$$A = [(\Delta D \Delta \nu \pi^{1/2})/2] ln2, \tag{5}$$

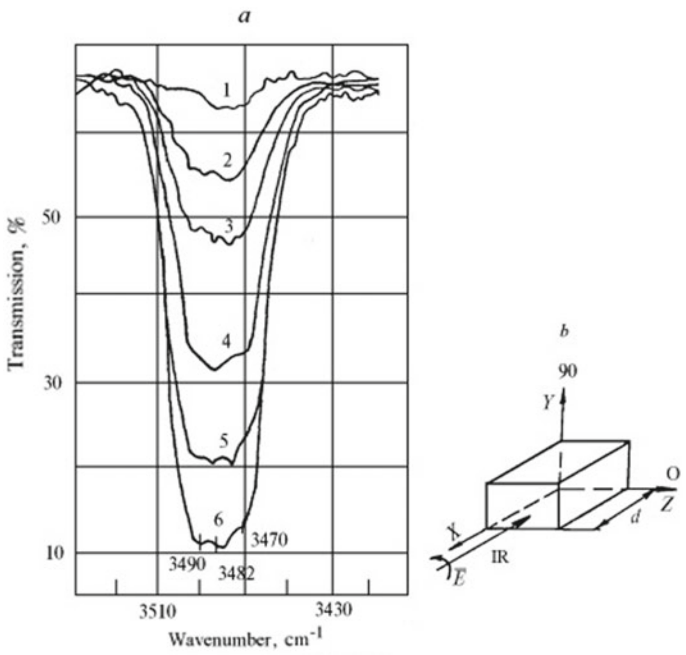

Fig. 1 Polarizing IR transmission: ***a*** $LiNbO_3$ crystals x-cut ($d = 23.5$ mm) at different angles between the z-axis and the IR radiation vector (deg.): 0 (1), 20 (2), 30 (3), 45 (4), 60 (5), 90 (6); ***b*** crystal layout

where ΔD and $\Delta \nu$ are, respectively, the change in optical density at the minimum of the absorption band relative to the baseline and its half-width (at $\Delta D/2$).

The data obtained in [7–9] on the change measured from one of the axes are approximated by a linear dependence $A = az + b$, where $z = \cos 2\varphi$ for $LiNbO_3$ *x*- and *y*-cuts.

3 Results and Discussion

For *z*-cut samples, this relationship is not observed and a type approximation is often used. The results of the optimization of the obtained linear dependences in the corresponding coordinates by the method of least squares are presented in [3, 8]. For $LiNbO_3$ *x*- and *y*-cuts, relation (5) is well satisfied, and the direction of O–H bonds is oriented within the z-plane (Fig. 2). In the case of *z*-cut samples, the direction of O–H bonds hasn't pronounced character and is isotropic. The rotation of the polarization plane for $LiNbO_3$ *x*- and *y*-cuts is performed with a step in 5°, *z*-cut –10°, the integral intensity was calculated from expression (5).

A possible place of localization of bulk PC centers in $LiNbO_3$ and $LiTaO_3$ is the oxygen plane along the boundary of (…) O_6- and LiO_6 octahedra. If the proton compensates, then it is located at the intersection of two empty octahedra parallel to the *z*-plane of the crystal. Other IR absorption bands in $LiNbO_3$ in the range from

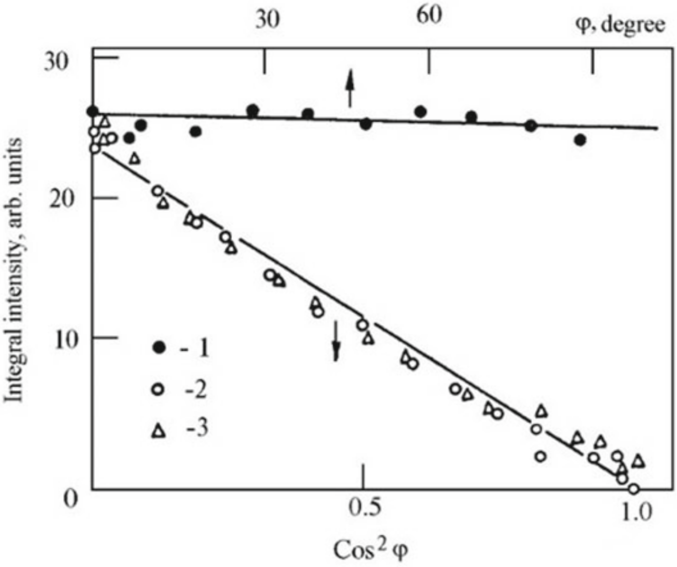

Fig. 2 Dependence of the integrated intensity of the bands with $\nu_{OH} = 3484\ cm^{-1}$ $LiNbO_3$ *z*– (1); *y*– (2); and *x*– (3) cuts from the angle between the *Z*-axis and the vector $\overline{E}$ of IR radiation

3000 to 4000 cm^{-1} aren't observed, and those shown in Fig. 2 data show almost complete orientation of O–H bonds within the z-plane of oxides.

The weakening of the strength of O–H bonds and the absence of other absorption bands in the region of 3000–3800 cm^{-1} suggests the formation of impurity PC centers on oxygen-vacancy dipoles with the direction of moments in the z-plane. The absorption band with a maximum at 3482 cm^{-1} in $LiNbO_3$, according to [12, 14], corresponds to the inter-oxygen distance in the OH…O fragment of more than 0.3 nm. Localization of PC centers on O^{*2-} ions of dipoles $Nb_{Li}^{3+} - O^{*2-}$ belonging simultaneously to (…) O_6–LiO_6 octahedra ($R_{O\ldots O} = 0.336$ nm) and compensation by protons formed in the form of associates (Nb_{Li}^{3+}, O^{*2-}, H^+) are proposed.

Annealing in vacuum at 100 °C $LiNbO_3$, accompanied by out-diffusion of Li_2O, leads to complete disappearance of IR absorption in the region of 3480 cm^{-1} and a shift of the band of stretching vibrations of O–H bonds to 3465 cm^{-1} [3, 9]. Reheating at 800 °C in a D_2O atmosphere is accompanied by absorption in the region of 2560 cm^{-1}, caused by stretching vibrations of O–D bonds. Condensation and removal of H^+ ions occur according to the reaction $2OH^- \rightarrow O^{2-} + H_2O$ with the release of water. In this case, the formation of electroneutral is possible, and absorption at ~500 nm is associated with electrons trapped by the deformed lattice [15].

In [10, 16], the oriented arrangement of H^+ ions and its isotopic analogs in the plane α-Al_2O_3 and TiO_2 (rutile) perpendicular to the C-axis with the IR absorption band of the valence vibrations of O–H bonds in the region of 3277–3279 cm^{-1} was established. Polarization IR spectroscopic studies of O–H, O–D and O–T bonds were carried out based on the model of an anharmonic oscillator and a linear hydrogen bond O–H…O. Weak absorption with a shoulder at 3266 cm^{-1} in α-Al_2O_3 is related to the orientation of the O–H bonds at an angle of +13 and –13° to the plane perpendicular to the *c*-axis. Weak absorption in the region of ~3000 cm^{-1} is associated with vibrations of O–H bonds in hydrogen-bonded O–H…O fragments [10]. Annealing in hydrogen doped with Ni^{3+} and Co^{3+} ions α-Al_2O_3 lowers the valence of impurities to +2, which indicates their partial compensation with protons.

In newly grown TiO_2 (rutile) crystals the concentration of O–H bonds reaches 2×10^{17} cm^{-3} [16]. IR absorption in the region of 3277 cm^{-1} and a weak band at 4350 cm^{-1} appear after treatment with TiO_2 in an H_2 medium at 500 °C for 5 h. The band at 3277 cm^{-1} at 20 °C has, as in the previously considered oxides, a dichroic appearance with the absorption coefficient at $\overline{E} \perp c$ several times greater than $\overline{E} \parallel c$. The large dichroism of the bands of O–H bonds in rutile shows that the H^+ ions are localized in the (001) plane. With decreasing temperature, in the whole class of oxides under consideration, the bands of stretching vibrations of O–H, O–D, and O–T bonds become narrower and shift to the high-frequency part of the spectrum.

Polarization studies of the orientation of O–H bonds in single-domain crystals $Ba_2Na_5NbO_{15}$ [17], $ZnWO_4$ [18], $SrTiO_3$ [19, 20], $BaTiO_3$ [21, 22] showed a character of IR absorption dichroism similar to the oxides considered above at different localization ions H^+. In $ZnWO_4$, where a significant misorientation of O^{*2-}—H^+ bonds is observed, doping with Fe, V and Sb (~10^{-5}–10^{-3} mol%) is accompanied by the appearance of dichroism in the IR absorption spectra up to room temperatures.

Thus, in $ZnWO_4$:Fe (4×10^{-4} mol.%), A wideband at 3420 cm^{-1} is replaced by a narrow symmetric line at 3445 cm^{-1}. Doping $BaTiO_3$ with iron (0.75 mol.%) leads not only to an increase in the content of H^+ ions but also to a complication of the shape of the IR spectra [2]. Along with a narrow band at 3485 cm^{-1} and two weak peaks in the polarization $\overline{E} \| c$ at 3483 cm^{-1} and 3510 cm^{-1}, broadbands that increase with Fe additions appear. The study of the structure and angular dependencies of the IR absorption bands of O–H bonds in $ZnWO_4$:Y and $ZnWO_4$:Sb indicates compensation of the excess charge of impurities in PC centers, which is confirmed by data on the deuteration of oxides. From the analysis of the polarization dependence of the line intensity at 3485.5 cm^{-1} in $BaTiO_3$: Fe, it was found that the H^+ ions in the lattice are located near the edges of oxygen octahedra, inclined to the tetrahedral axis [21].

Possible places of localization of H^+ ions can be judged by the action of temperature, pressure, or external electric field. In $SrTiO_3$, with a decrease in temperature below T_0 (105 K), polarization IR spectroscopy gives absorption bands identical to those of $LiNbO_3$ and $LiTaO_3$, due to the transition from a cubic lattice to a hexagonal lattice by rotating oxygen octahedra and doubling the unit cell (Fig. 3) [20]. In $SrTiO_3$ crystals of various origins, the O–H (O–D) stretching vibration band is in the region of 3495.7 (2581.6) cm^{-1} with a half-width at the maximum of 2.6 (1.9) cm^{-1}. Applying external pressure along different directions produces noticeable bands in the IR spectra at 94 K in the regions of 3506, 3514, and 3518 cm^{-1} (Fig. 3).

There is a large number of works on the influence of the type of the structural network, the content of OH bonds, internal stresses on the efficiency of creating $V^{+}_{O^{2-}} - O^{*2-}$– centers in amorphous α-SiO_2 [23]. Thus, in porous quartz glass at a sintering temperature of less than 573 K, SiOH groups appear as polar, and higher (≥400 °C) groups act as acidic. This transformation is catalytic, occurs near the glass pores, and is accompanied by significant changes in the luminescence intensity. The

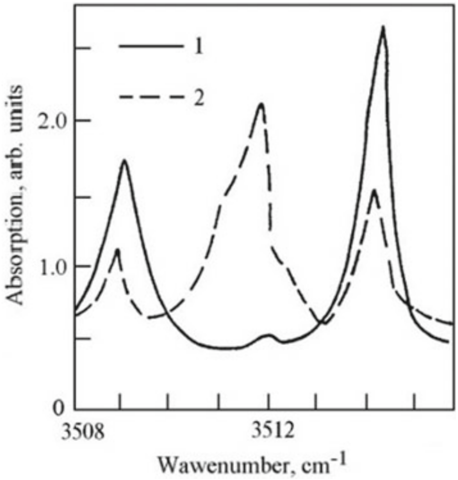

Fig. 3 Polarization IR absorption of $SrTiO_3$ at 94 K and pressure δ (110) = 64 N/nm^2 at different angles between the z-axis and the vector $\overline{E}$ of IR radiation: 0 (1) and 90° (2)

oriented character of the arrangement of H^+ ions in the region of thallium-containing centers in amorphous α-SiO_2 is facilitated by an elastically deformed tetrahedral environment [24]. A mechanism for the effect of densification on the generation of $V^{+}_{O^{2-}} - O^{*2-}$– centers under the action of ionizing radiation is proposed.

4 Conclusion

The possibility of using polarization IR spectroscopy to determine the orientation of protons in protonated crystals is shown. The direction of the dipole moment of the proton-containing centers can be related with a sufficient approximation to the direction of the internuclear distances of X–H bonds. Then the orientation of defect centers with a noticeable IR absorption band is put by following per under the vector of the change in the dipole moment, parallel to the component of the vector of the electromagnetic field of the polarized radiation. Polarization studies make it possible to isolate the behavior and orientation of H^+ ions concerning for to site electronegative ions and impurities. Stretching vibrations of X–H bonds show changes in the electric dipole moment along the molecular axis, and their symmetry lowers the symmetry of the site in the lattice and thereby gives information about the local environment.

Acknowledgements The work was performed at the expense of subsidies within the framework of the TPU Competitiveness Improvement Program.

References

1. Kappers, L.A., Sweeney, K.L., Hallibarton, L.E., Liaw, J.H.W.: Oxigen vacancies in lithium tantalate. Phys. Rev. B Condens. Matter **31**, 6793–6794 (1985). https://doi.org/10.1103/PhysRevB.31.6792
2. Kovacs, L., Foldvari, I., Cravero, I., Polgar, K., Capelleti, R.: An infrared absorption band caused by OH- ions in a $LiNbO_3$,: Mg Cr. Crystal. Phys. Lett. A **133**, 433–437 (1988). https://doi.org/10.1016/0375-9601(88)90931-0
3. Borodin, Yu.V., Sergeev, A.N.: The formation of nanocomposition structure in crystals. In: Proceedings of the 3rd International Forum on Strategic Technologies (IFOST-2008), pp. 174–176 (2008). https://doi.org/10.1109/IFOST.2008.4603001
4. Sweeney, K.L., Halliburton, L.E., Kappers, L.A.: Self-trapped electrons in lithium tantalate. Phys. Lett. A **116**(2), 81–84 (1986). https://doi.org/10.1016/0375-9601(86)90244-6
5. Endo, S., Chino, T., Tsuboi, S., Koto, K.: Pressure-induced transition of the hydrogen bond in the ferroelectric compounds KH_2PO_4 and KD_2PO_4. Nature **340**, 452–455 (1989). https://doi.org/10.1038/340452a0
6. Bates, J.B., Perkins, R.A.: Infrared spectral properties of hydrogen deuterium and thritium in TiO_2. Phys. Rev. B Solid State **16**, 3713–37229 (1977). https://doi.org/10.1103/PhysRevB.16.3713
7. Nazarenko, O.B., Sechin, A.I., Amelkovich, Yu.A.: Characterization of naturally aged iron nanopowder produced by electrical explosion of wires. Met. Mater. Int. (2019). https://doi.org/10.1007/s12540-019-00443-8

8. Borodin, Y.V.: Low-temperature nanodoping of protonated $LiNbO_3$ crystals by univalent ions. Tech. Phys. **60**, 107–111 (2015). https://doi.org/10.1134/S1063784215010065
9. Borodin, Y., Zadorozhnaya, T., Ghyngazov, S.: The effect of protonation on structural modification in layers. Mater. Sci. Forum **942**, 21–29 (2019). https://doi.org/10.4028/www.Scientific.net/MSF.942.21
10. Engstrom, H., Bates, J.B., Wang, J.C., Abraham, M.M.: Infrared spectral of hydrogen isotopes in α-Al_2O_3. Phys. Rev. **21**, 1520–1526 (1980). https://doi.org/10.1103/PhysRevB.21.1520
11. Chen, Y., Gonzalez, R., Schow, O.B., Summers, G.P.: Charge and mass transfer involving hydrogen in MgO crystals. Thermochemically reduced at high temperature. Phys. Rev. **B 27**, 1276–1282 (1983). https://doi.org/10.1103/PhysRevB.27.1276
12. Kovacs, L., Szalay, V., Capeletti, R.: T Stoichiomnetry dependence of the OH−absorption band in $LiNbO_3$crystals. Solid State Commun. **52**, 1029–1031 (1984). https://doi.org/10.1016/0038-1098(84)90503-9
13. Kovacs, L., Polgar, K.: Densiny measurements on $LiNbO_3$ crystals confirming Nb substitution for Li. Cryst. Res. Technol. **21**, K101–K104 (1986). https://doi.org/10.1002/crat.2170210629
14. Sokolov, N.D.: Hydrogen bond dynamics. Hydrogen bond. Science, Moscow (1981)
15. Jhans, H., Honig, J.M., Rao, C.N.R.: Optical properties of reduced $LiNbO_3$. J. Phys. C. Solid State Phys. **C 19**, 3649–3658 (1986)
16. Bates, J.B., Wang, J.C., Perkins, R.A.: Mechanism for hydrogen diffusion in TiO_2. Phys. Rev. B **19**, 4130–4139 (1979). https://doi.org/10.1103/PhysRevB.19.4130
17. Zhang, L., Chandler, P.J., Townsend, P.D.: Ion-implanted planar waveguides in barium sodium niobate. Appl. Phis. Lett. **53**, 544–546 (1988). https://doi.org/10.1063/1.100629
18. Foldari, J., Capeletti, R., Kappers, L.A., Gilliam, O.R., Watterich, A.: The role of OH-ions in the charge compensation of impurities in $ZnWO_4$ single crystals. Phys. Lett. A. **135**, 363–367 (1989). https://doi.org/10.1016/0375-9601(89)90009-1
19. Reeves, R.J., Jones, G.D., Syme, R.W.G.: Spectroscopy of $S_2F_2Pr^{3+}$ and CaF_2Pr^{3+}. Phis. Rev. B. **40**, 6475–6484 (1989). https://doi.org/10.1103/PhysRevB.40.6475
20. Weber, G., Kapphan, S., Wohlecke, M.: Spectroscopy of the O-H and O-D stretching vi-brations in $SiTiO_3$ under applied electric field and uniaxial stress. Phys. Rev. B Condens. Matter. **34**, 8406–8417 (1986). https://doi.org/10.1103/PhysRevB.34.8406
21. Jovanovic, A., Wohlecke, M., Kapphan, S., Maillard, A., Godefroy, G.: Infrared spectroscopy of hydrogen centers in undoped and iron-doped $BaTiO_3$ crystals. J. Phys. Chem. Solids. **50**, 623–627 (1989). https://doi.org/10.1016/0022-3697(89)90457-5
22. Owrutsky, J.C.: Summary of phisycal properties and crystal structure $BaTiO_3$. J. Chem. Phys. **83**, 5338–5341 (1985)
23. Cocito, G., Cognolato, L., Modone, E., Sorgo, B.: Hydrogen in fibers: a comparison between the aging and the simulated aging. J. Opt. Commun. **9**, 2–4 (1988)
24. Cammarata, R.C., Sieradzki, K.: Effects of surface stream on the elastic modul of thin films and superlattices. Phys. Rev. Lett. **2**, 2005–2008 (1989). https://doi.org/10.1103/PhysRevLett.62.2005

Visual Control Methods—The Basis of Quality Control

Ludmila Redko and Marina Yanushevskaya

Abstract The current information processing speed is very high. To effectively manage a company, information should be speedily processed to make timely decisions at all hierarchy levels, from managers to executors. Information visualization in these conditions significantly speeds up these processes and reduces risks. The quality management system of a modern company includes elements and methodology of various performance improvement concepts, such as risk management, total quality management, lean manufacturing, six sigma, and the theory of constraints. The emphasis in process organization is placed on visual methods. Despite the fact that visualization as a method is considered within the concept of lean manufacturing, there are methods for representing information in a visual form defined in other concepts. The paper discusses the use of the methodology for information visualization in terms of different quality management system concepts. A comparative analysis of modern concepts for improving performance, an overview of the methodology designed to display information in the quality management system in a visual form is made, and successful examples of using various methods of information visualization for quality management in companies are given.

1 Introduction

To improve performance and competitiveness, companies implement various performance improvement concepts. These concepts include Lean Manufacturing, Six Sigma, Knowledge Management, Risk Management, Strategic Management,

---

L. Redko
Division for Testing and Diagnostics, National Tomsk Polytechnic University,
30 Lenin Avenue, Tomsk 634050, Russia
e-mail: laredko@tpu.ru

M. Yanushevskaya (✉)
Faculty of Innovation Technologies, Tomsk State University of Control Systems and
Radioelectronics, 40 Lenin Avenue, Tomsk 634058, Russia
e-mail: vela2007@bk.ru

I. V. Minin et al. (eds.), *Progress in Material Science and Engineering*,
Studies in Systems, Decision and Control 351,
https://doi.org/10.1007/978-3-030-68103-6_17

Goldratt's Theory of Constraints, and Iwao Kobayashi's 20 Keys to Business Improvement Program. The most common are: quality management system based on ISO 9000 standards, lean manufacturing system and six sigma system. With regard to the development of quality management approaches, the quality management system based on ISO 9000 standards includes elements of strategic management, knowledge management and risk management. Modern concepts of performance improvement are described below according to the following criteria: definition; time of origin; key concepts; basic principles; the cyclic process used; scope of use in quality management; methods used.

2 Modern Concepts of Performance Improvement

2.1 QMS Based on ISO 9001: 2015 [1]

Definition: a concept for continuous improvement of activities and increasing the company competitiveness.

Formation: development of the first ISO 9000 standards in 1987.

Key concepts: quality—compliance of inherent characteristics with requirements; process—activity that transforms inputs into outputs; system—a combination of interrelated and interacting processes.

Basic principles:

- Customer focus.
- Leadership.
- Interaction of workers.
- Process approach.
- Improvement.
- Evidence-based decision making.
- Relationship management.

Cyclic process used: Plan-Do-Check-Act (PDCA) cycle, also known as the Deming Cycle, Shewhart cycle, Deming Wheel or Plan-Do-Study-Act.

Scope of use in quality management: achieving the objectives of the company in the field of quality by managing a system of interrelated processes.

Methods used:

- Quality control tools (histogram, Pareto chart, control chart, scatter chart, stratification, checklist, Ishikawa chart) [2].

- Quality management tools (affinity diagram, relationship diagram, tree diagram, matrix diagram, network diagram (Gantt diagram), process decision program chart (PDPC), prioritization matrix).
- Quality analysis tools (functional cost analysis, analysis of the causes and consequences of failures (FMEA analysis).
- Quality design tools (quality function deployment (QFD), theory of inventive problem solving).

2.2 Lean Manufacturing (LM)

Definition: a management concept based on elimination of all types of waste.

Formation: developed by Toyota in 1950, the concept founder is Taiichi Ohno.

Key concepts: muda (mura, muri)—losses, everything that does not add value to the product; value stream; the principle of pull production.

Basic principles:

- Strategic focus.
- Focus on creating value for the consumer.
- Organization of the value stream for the consumer.
- Continuous improvement.
- Pulling.
- Reduction of losses.
- Visualization and transparency.
- Priority security.
- Building a corporate culture based on respect for a person.
- Built-in quality.
- Fact-based decision making.
- Establishing long-term relationships with suppliers.
- Compliance with standards [3].

Cyclic process used: consists of five sequential steps:

- Determine the value of a specific product.
- Determine the value stream for this product.
- Provide a continuous flow of product value stream.
- Allow the user to pull the product.
- Strive for excellence.

Scope of use in quality management: Increasing the efficiency of activities by reducing losses in all processes.

Methods used:

- Process mapping.
- Kanban.
- Total productive maintenance.
- 5S system.
- Quick changeover (SMED).
- Kaizen.
- Poka-yoke—a method of avoiding mistakes [4].

2.3 Six Sigma

Definition: A management concept that focuses on improving quality by reducing variation in process parameters and achieving a planned quality level in terms of standard deviations (sigma).

Formation: developed by Motorola Corporation in 1980.

Key concepts: σ (sigma) is root-mean-square deviation; KPIs are key performance indicators of a company that help it achieve strategic and tactical goals.

Basic principles:

- Customer satisfaction.
- Definition of processes, their indicators and methods of process control.
- Teamwork and staff involvement.

Cyclic process used: DMAIC, Define—Measure—Analyze—Improve—Control [5].

Scope of use in quality management: Process control, improvement of process parameters based on the study and analysis of statistical data.

Methods used: Statistical methods of process management, descriptive statistics, methods of testing statistical hypotheses, graphs [6, 7].

All three concepts imply improving the quality of activities and reducing costs. All concepts use a cyclical process to identify a problem, study and fix it. These concepts differ in the field of their application in the company's quality management system and in a specific methodology.

At enterprises, these concepts are typically implemented in the following sequence: QMS ISO 9001, the lean manufacturing methodology starting with the 5S concept, then the 6 Sigma concept related to improvement projects.

The methodology of the three concepts overlaps, for example, all of the listed concepts employ statistical methods of information visualization and process control [8, 9].

All three concepts employ methods of visual information representation, however, the concept of visualization is defined in the concept of lean manufacturing only:

Table 1 Methods of information visualization in accordance with the stages of the PDCA cycle

Phase of PDCA cycle	ISO 9001	Method
P—plan, developing the system goals and its processes, identifying the resources required to achieve the results in accordance with customer's needs and company's policies, considering risks and opportunities	6	Process diagrams Goal matrices Risk register Visual representation of the required quality, work standards QFD
D—do, fulfillment of what was planned	7, 8	Outlining, color labeling, rational layout, information boards, process maps
C—check, monitoring and (where applicable) measuring the processes, products and services with regard to policies, objectives, requirements and planned actions and presenting the results;	9	A3 format of the report, descriptive statistics, Shewhart control charts
A—act, taking actions to improve performance to the necessary level	10	Statistical analysis, value stream maps, spaghetti diagrams

location of all tools, parts, production stages and information about the production system performance so that they could be clearly visible, and each participant in the production process could instantly assess the system state.

The following methods are used for visualization in the lean manufacturing: labeling; contouring; marking; color coding; information stand.

Visualization tools used in the lean manufacturing are the report in A3 format and andon [10, 11].

However, the integrated quality system exhibits great potential for visual information representation. Text can be converted into tables and color schemes, pictures and numbers can be presented in the form of graphs and diagrams. Visual information increases the speed and quality of decisions and reduces the number of errors.

The stages of the PDCA cycle as the simplest model of the system present in all the concepts have been taken to consider the methods of information visualization that can be used at various stages of the cycle (Table 1).

3 Results and Discussion

Let us consider an instrument-making enterprise with a quality management system that has employed a different quality management methodology for 15 years.

Since all stages of the PDCA cycle and the applied methodology cannot be considered within the scope of one paper, we take the analysis stage (Act) as an example.

Analysis of the manufacturing process using statistical methods and lean methodology.

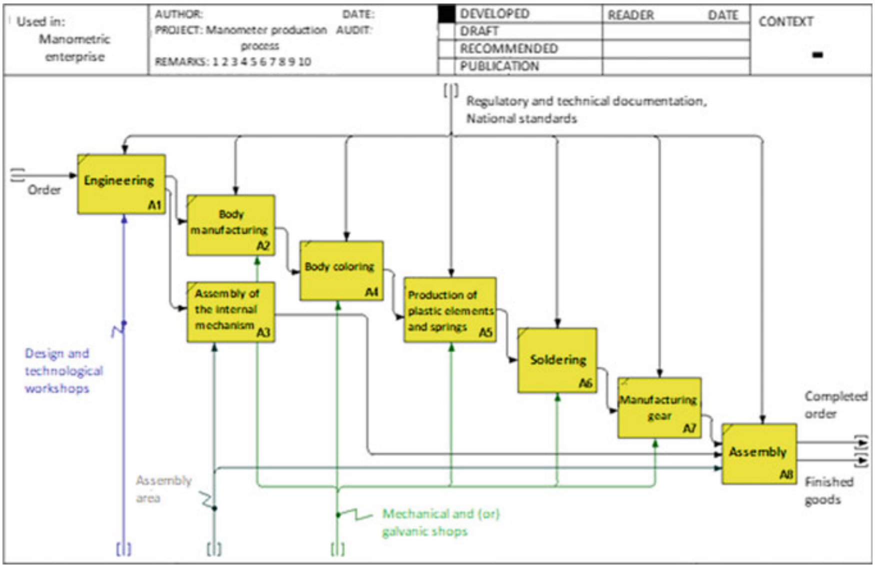

Fig. 1 Model of manufacturing process of measuring instruments

At the first stage, a diagram of the process was created (Fig. 1). This diagram shows the sequence of the process stages. Similar schemes can be used to analyze the process and train new employees.

Analysis of manufacturing process of measuring instruments.

Shewhart charts, X-MR charts and p-charts were used to study the stability of the manufacturing process in terms of non-compliances over the study period (Fig. 2).

The analysis of claims received from external consumers during the study period was carried out.

A total of 80% of all non-compliances are attributed to poor assembly, defects that occur during transportation, managers' errors, and others (Fig. 3).

An assembly site was chosen for further analysis.

A current state value stream map was developed (Fig. 4).

- value creation time—43% of the total time;
- non-productive time caused by:
- duration of storage of finished mechanisms on the site during the shift (27% of the total non-productive time);
- unused equipment downtime (23%);
- expectations of items due to their lack in stock (8%);
- excessive movement of working personnel (7%).

The production area and workplaces was analyzed using a spaghetti diagram. Workplaces are located irrationally, workers excessively move when switching from one operation to another (Fig. 5).

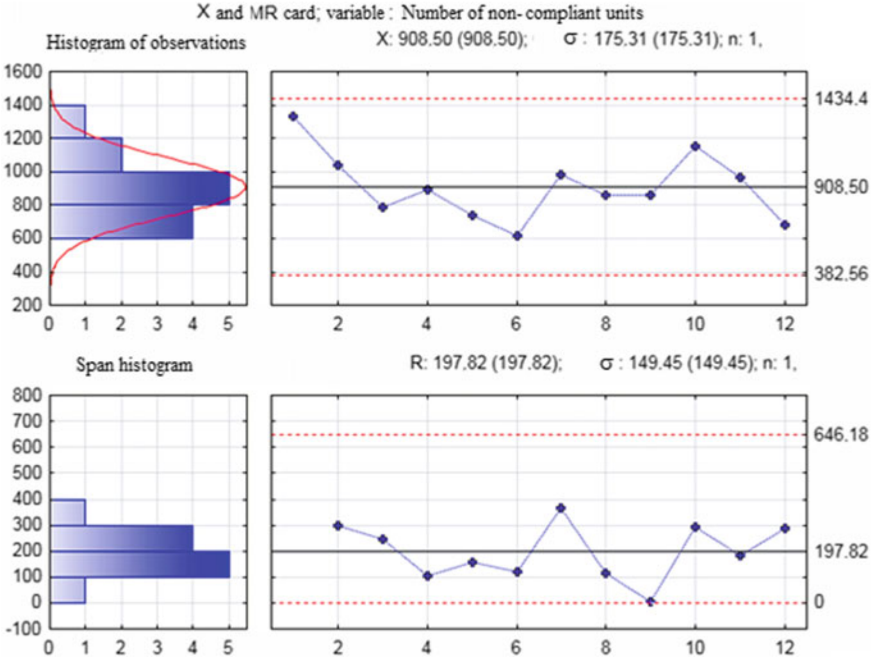

Fig. 2 X-MR chart by the number of non-compliances over the study period

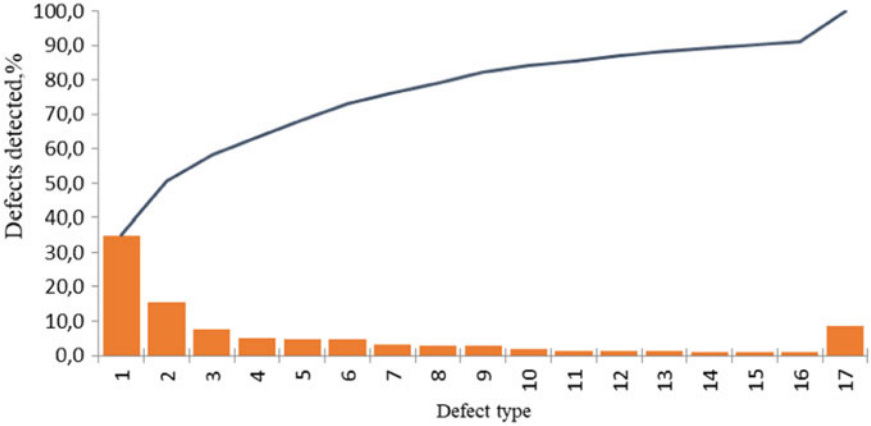

Fig. 3 Pareto chart by types of defects over the study period: 1—poor assembly; 2—defects caused by transportation; 3—managers; 4—errors; 5—others

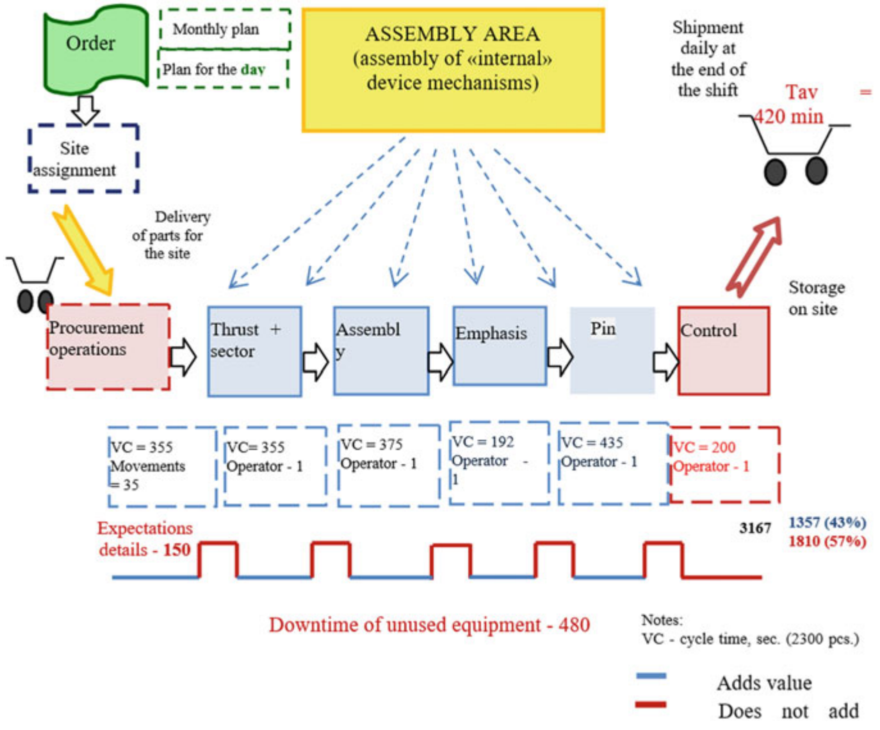

Fig. 4 Graphic representation of the current state value stream map

About 40% of equipment (and workplaces) are not involved in the production process. An excessive amount of unlabeled stocks, which hinders the search for necessary items. An excessive amount of empty containers that clutters the area.

A future state value stream map was created.

Value creation time—65% of the total time. Reduction of non-productive time:

- storage of finished mechanisms on the site during the shift (by 85%);
- unused equipment downtime (by 100%);
- expectations of items due to their absence in stock (by 86%);
- excessive movement of personnel (by 74%).

The identified incompliances were analyzed based on the results of control at the site. 80% of all incompliances were identified using the Pareto chart. Main reasons for appearance of these incompliances:

- negligence of personnel during technological operations;
- delivery of defective items by the supplier.

Based on the analysis, the following recommendations were made for applying the lean manufacturing methodology at the Assembly site:

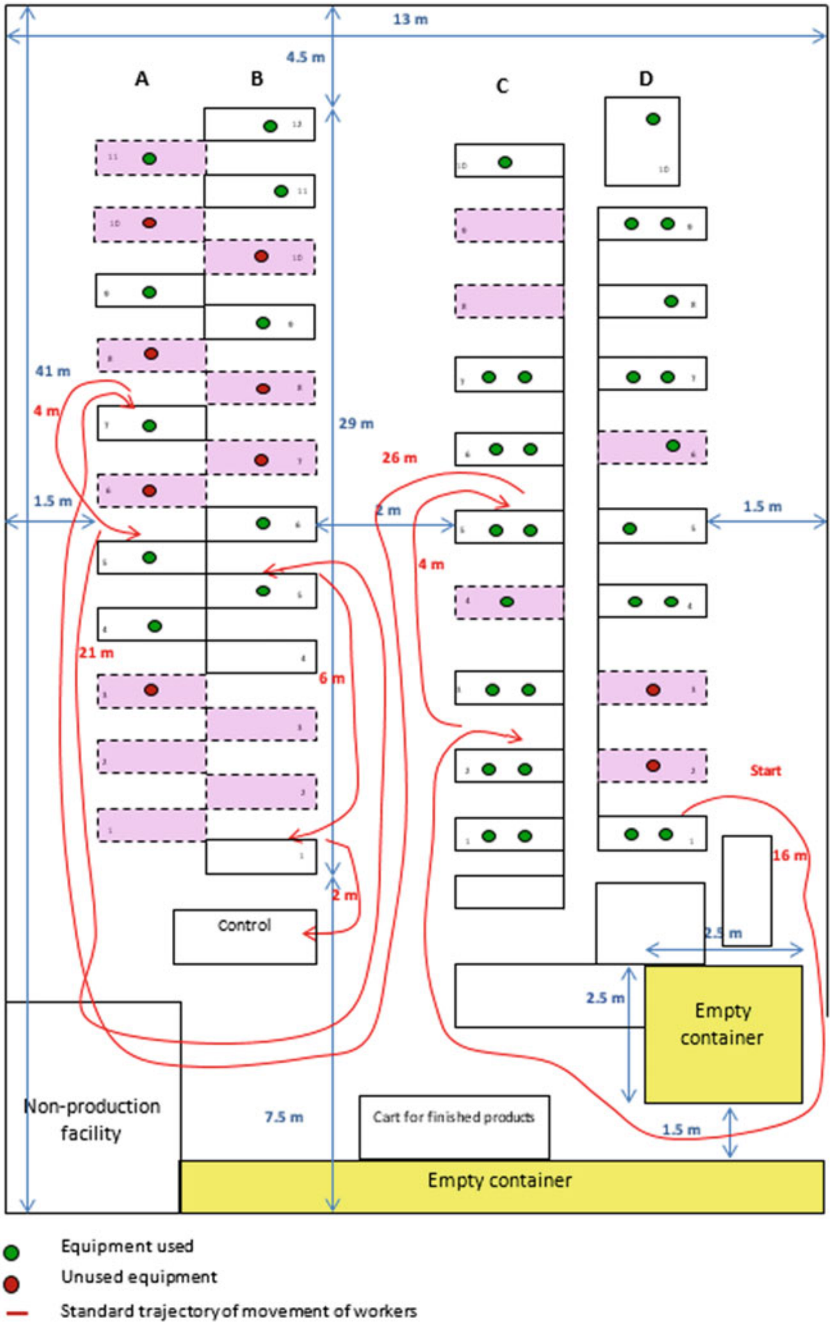

Fig. 5 Spaghetti diagram

- training of employees on the concept of lean manufacturing is required;
- the assembly site should be reconstructed based on the results of theь spaghetti diagram.

After the reconstruction, the following results were achieved:

- 1.5-fold reduction of the area occupied by production facilities (475 vs. 300 m^2);
- workplaces are located along the most frequent operations;
- working tables are placed parallel to each other with a passage between them;
- removal of unnecessary empty containers from the production area (except for the quantity required for 2 shifts, 250–300 pcs).

Using 5S elements and visualization at the assembly site.

Creation of a quarantine zone at the assembly site for unused items, tools and devices:

- use of red date tags by workers to indicate unused items;
- removal of unused items from the production premises.

Division of all items (tools, supplies) into frequently and rarely used. Fixing a specific place for each object.

Determination of the area for placing the cart with finished products, empty containers, and stocks using adhesive tape for marking the floor.

Labeling containers with stocks:

- labels must contain: item name, material, size or thickness.
- Maintaining order:
- cleaning is required at the end of each shift, put all tools in the right places;
- general cleaning at the end of the month.

Establishing a system for assessing (controlling) the order and appointing responsible persons:

- level 1—weekly control performed by the site foreman;
- level 2—control performed by the head of the mechanical assembly site during the round;
- control results (point and percentage system) are placed on stand 5S;
- photographs of ‘in the past/now’ and most active workers are placed on stand 5S.

Standardization of the assembly site:

- creation of a standard for each operation (in A4 format—a brief, understandable version in the form of diagrams);
- creation of a standard for the workplace (appearance and frequency of cleaning).

Creating a Kanban Board (Fig. 6).

Main results obtained after fulfillment of the recommendations:

- improved operational performance of the assembly process;
- reduced amount of defective mechanisms and reworking;
- improved organizational culture;

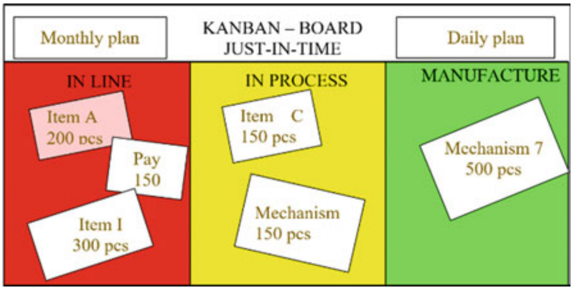

Fig. 6 Model of Kanban-board

- reduced production areas.

4 Conclusion

Information visualization methods are required for a more detailed analysis of the situation. In contrast to textually presented information, graphical methods provide more details about the situation under consideration and help understand the essence of the problem being solved. A generation grown up in the digital age thinks differently, and the graphic series is essential for the decision-making processes.

The paper discusses the use of information visualization methods that include three concepts applicable to the analysis stage of the PDCA cycle.

Despite the fact that methods of visual management are primarily associated with lean manufacturing, a number of improvement concepts are integrated into modern quality management. Each concept provides visual or graphical methods that enable effective management at all stages: planning, implementation, control, and analysis.

References

1. Leontyuk, S.M., Vinogradova, A.A., Silivanov, M.O.: Fundamentals of ISO 9001:2015. J. Phys. Conf. Ser. **1384**(1), 12068–12072 (2019). https://doi.org/10.1088/1742-6596/1384/1/012068
2. Narottama, M., Sharma, V.: Defect reduction in manufacturing industry using lean Six Sigma approach. Lect. Notes Mech. Eng. 19–30 (2020). https://doi.org/10.1007/978-981-15-1071-7_3
3. Cuellar-Valer, S., Gongora-Vilca, A., Altamirano-Flores, E.: Application of lean manufacturing in a Peruvian clothing company to reduce the amount of non-conforming products. Adv. Intel. Syst. Comp. **1253**, 481–487 (2020). https://doi.org/10.1007/978-3-030-55307-4_73
4. Maslova, O.P., Ilyina, T.A., Krichmar, V.A., Safronov, E.G.: Implementing lean manufacturing and solving motivation problems in Russian companies. Lect. Notes Netw. Syst. **139**, 384–391 (2020). https://doi.org/10.1007/978-3-030-53277-2_46
5. Jiang, H., Cao, Y.: Research on enterprise quality innovation of VE and DMAIC tool integrated application. In: Proceedings of the 2020 International Conference on E-Commerce and Internet Technology, pp. 372–375 (2020). https://doi.org/10.1109/ECIT50008.2020.00092

6. Siregar, K.: Quality control analysis to reduce defect product and increase production speed using lean six sigma method. IOP Conf. Ser. Mater. Sci. Eng. **801**(1), 456–463 (2020). https://doi.org/10.1088/1757-899X/801/1/012104
7. Sony, M., Antony, J., Park, S., Mutingi, M.: Key criticisms of six sigma: a systematic literature review. IEEE Trans. Eng. Manage. **67**(3), 950–962 (2019). https://doi.org/10.1109/TEM.2018.2889517
8. Popova, L.F., Yashina, M.N., Bocharova, S.V., Cherkashnev, R.Y.: Development of methodology of identification of the quality management system processes. Qual. Access Success **19**(164), 43–47 (2018)
9. Plotnikova, I.V., Redko, L.A., Chicherina, N.V.: The analysis of the process of complaints consideration using statistical methods of control. IOP Conf. Ser. Mater. Sci. Eng. **516**(1), 101–105 (2019). https://doi.org/10.1088/1757-899X/516/1/012013
10. Mikhailovsky, P., Plakhin, A., Ogorodnikova, E.: Lean management tools to improve the production system. Qual. Access Success **21**(176), 65–68 (2020)
11. Moskvicheva, E.L., Mukhametshina, A.M., Erofeyev, A.N., Savelyev, K.V.: Lean manufacturing—a method of managing a manufacturing enterprise. IOP Conf. Ser. Mater. Sci. Eng. **862**(4), 27–30 (2020). https://doi.org/10.1088/1757-899X/862/4/042051

Innovations in Biomedical Engineering

Test Signal Generator for High-Resolution Electrocardiography

Pavel Baranov, Diana Avdeeva, and Andrey Kolomeytsev

Abstract The paper presents the first results of developing a generator of test high-resolution electrocardiographic (ECG) signals for testing electrocardiographs and the ECG interpretation algorithms. The flowchart of this generator and the experimental results are given in this paper.

1 Introduction

Electrocardiography (ECG) is currently the only diagnostic equipment which provides global monitoring and screening of cardiovascular system pathology of outpatients and studies the electrical activity of the heart [1, 2]. Electrocardiographs operate at low frequencies from 0.05 to 75, 100, 150, and 250 Hz, and contain surge and muscle tremor suppressors [3].

Along with electrocardiographs, various algorithms of the ECG interpretation are used for computer data processing and establishing diagnosis. However, any hardware/firmware malfunction of electrocardiograph may result in serious injury of a patient, wrong diagnosis and, consequently, wrong treatment.

Thus, Bogun et al. [4] noted that in the ECG analysis of 442 (19%) of 1085 patients, the obtained data were not interpreted correctly. For 92 patients (24%), the doctor was unable to correct the misinterpretation when analyzing the ECG, which led to an inadequate treatment.

P. Baranov (✉) · A. Kolomeytsev
Department of Electronic Engineering, National Research Tomsk Polytechnic University, 30 Lenin Avenue, Tomsk, Russia 634050
e-mail: bpf@tpu.ru

D. Avdeeva
Research and Production Laboratory "Medical Engineering", National Research Tomsk Polytechnic University, 30 Lenin Avenue, Tomsk, Russia 634050
e-mail: avdeeva@tpu.ru

I. V. Minin et al. (eds.), *Progress in Material Science and Engineering*,
Studies in Systems, Decision and Control 351,
https://doi.org/10.1007/978-3-030-68103-6_18

It should be noted that a study of low amplitude potentials of the human heart in the frequency band over 250 Hz is of great importance for early diagnostics of cardiovascular system pathology [5–11]. According to Avdeeva, et al. [12], the spontaneous activity of myocardial cells registered on the surface of the thoracic cell in the frequency range from 0 to 10,000 Hz, is impulse in nature; the pulse amplitudes vary from 1 mkV to several tens of microvolts and the pulse duration ranges from 0.3 ms to tens of milliseconds.

Accordingly, the development of the existing models of the cardiac activity and the ECG interpretation algorithms based on the disease statistics obtained from typical electrocardiographs cannot be used, with a high degree of probability, for computer-aided diagnosis.

This work proposes a prototype test signal generator developed for high-resolution electrocardiography and algorithms for the ECG analysis.

2 ECG Test Signal Generator

For the development of advanced automated electrocardiographs, the test ECG signal generator must reproduce the following signals. DC voltage: –300 and 300 mV.

The root mean square (RMS) values 0.3 μV, 1.0 μV, 10 μV, 0.1 mV, 1 mV, 4 mV, 10 mV, 1 V and 5 V of sine-, triangle- and square-waveform alternating current can be varied within the frequency span of 0.5–500 MHz, 500 MHz–500 Hz, and 500–1000 Hz with increments of 0.5 MHz, 10 MHz and 0.1 Hz, respectively.

The output voltage of an artificial ECG: from ±500 μV to ±10 mV; amplitude discretization: 5 μV at a sampling frequency ranging from 30 to 360 pulses per minute; ST segment displacement: 10–2.05 mV; adjustment of the amplitude, width and position of electrocardiographic waves in the QRS complex.

The flowchart of the test ECG signal generator depicted in Fig. 1, meets the requirements indicated above.

As can be seen from Fig. 1, the test ECG signal generator consists of the following functional units:

- secondary power source (SPS) is designed to supply DC to AC 220 V 50 Hz voltage power for the circuit elements of the generator (UVDD = 15 V, UVSS = –15 V, UVCC = 5 V);
- the reference voltage source (RVS) is used to create the reference voltage for the digital-to-analog converter (DAC);
- from the reference voltage, the DAC generates a unipolar, constant-amplitude signal of the specified frequency;
- buffer operational amplifier (BOA 1) is designed for the test signal shift relative to zero;
- multiplying digital-to-analog converter (MDAC) is used to attenuate the test signal by 1–100 times;

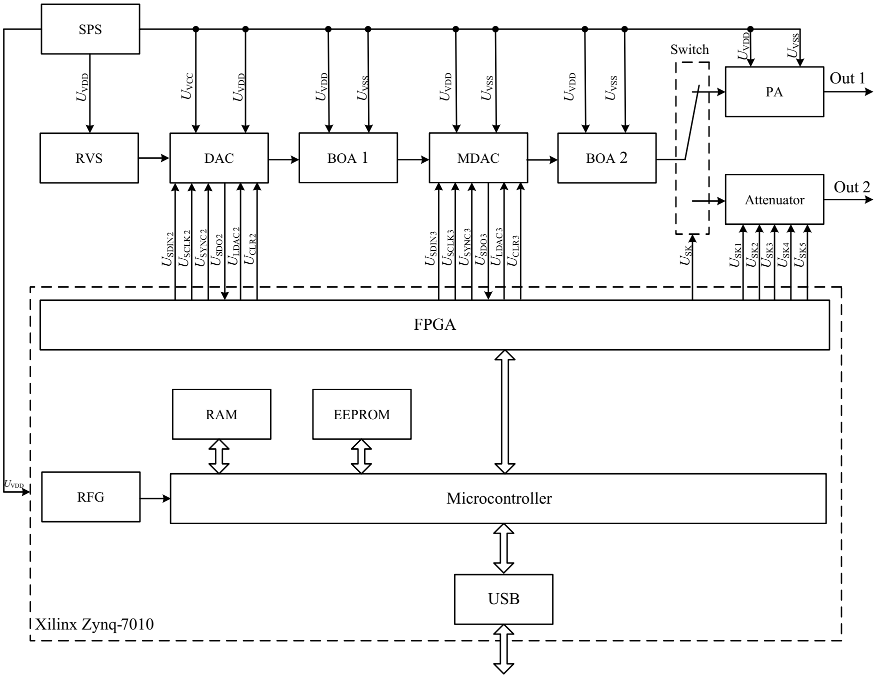

Fig. 1 Flowchart of the test ECG signal generator

- buffer operational amplifier (BOA 2) is designed to adapt the MDAC output to the inputs of the power amplifier (PA) and attenuator;
- the switch is used for automated switching of the generator outputs;
- the PA is designed to amplify the current test signal and adapt the generator output to low impedance loads;
- the attenuator is used to attenuate the test signal and provide 0.3 V, 1.0 V, 10 V, 0.1 mV, 1 mV, 4 mV, 10 mV RMS values and the output voltage of the artificial ECG varying from ±500 μV to ±10 mV;
- a myRIO-1900 (National Instruments, USA) device with Xilinx Zynq-7010 FPGA module functions as a logic software and logic hardware;
- dynamic random-access memory is used as a RAM unit;
- non-volatile memory is provided by electrically erasable programmable read-only memory (EEPROM);
- a 40 MHz reference frequency generator (RFG) is used for clocking the microcontroller and the field programmable logic device (FPGA).

Based on the LabVIEW system-design platform, customized software is developed to generate test signals and control the generator operation. The LabVIEW consists of two parts: the top-level program based on a host computer, namely a Test Signal Generator virtual device, and the low-level program based on the NI myRIO 1900 target device. The application running on the host computer is responsible for the user interface, while the application running on the target device utilizes the DDS-based FPGA for the continuous test signal reproduction with a quick frequency agility. The model described in [13] is used to generate an ECG period of signal. Figure 2 illustrates the user interface for the generator control.

Figures 3–7 present the output waveforms of the sampled signals of the prototype signal generator using the ECG recorder with nanoelectrodes [12].

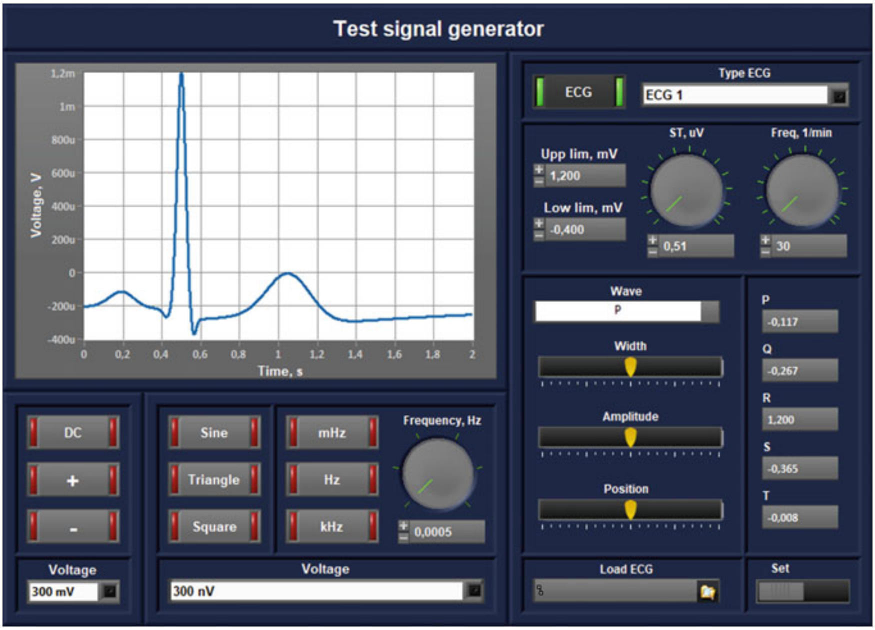

Type ECG: ECG 1

Upp lim, mV: 1,200

Low lim, mV: -0,400

ST, uV: 0,51

Freq, 1/min: 30

Wave: P

P: -0,117

Q: -0,267

R: 1,200

S: -0,365

T: -0,008

Frequency, Hz: 0,0005

Voltage: 300 mV

Voltage: 300 nV

Fig. 2 User interface for the generator control

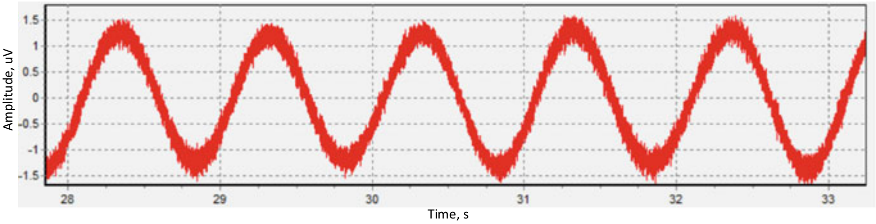

Fig. 3 Sine waveform. RMS: 1 μV. Frequency: 1 Hz

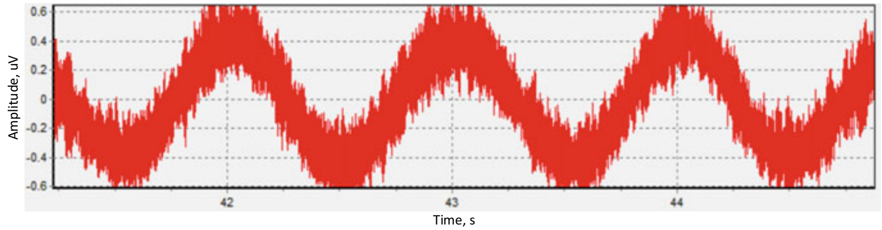

Fig. 4 Sine waveform. RMS: 300 nV. Frequency: 1 Hz

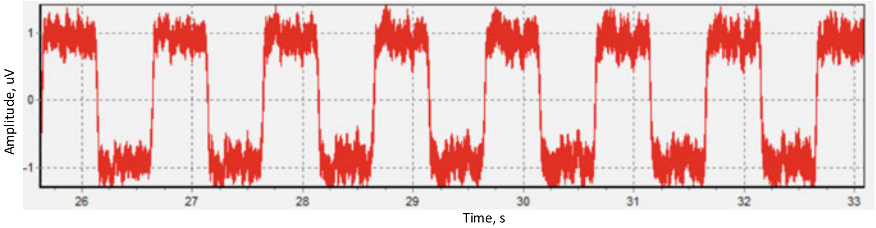

Fig. 5 Square waveform. RMS: 1 μV. Frequency: 1 Hz

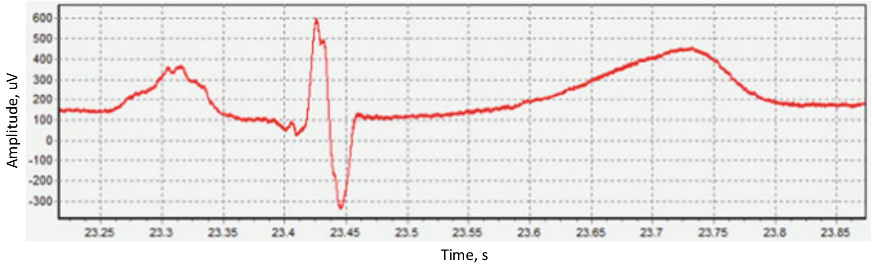

Fig. 6 One ECG period of signal

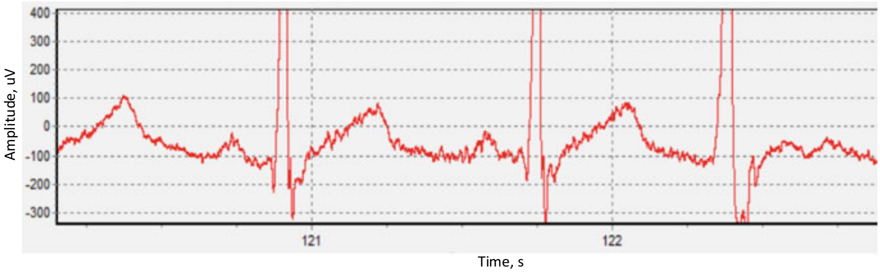

Fig. 7 ECG signal

3 Conclusions

From the outcome of our investigation it is possible to conclude that the proposed test signal generator provided a reproduction of the following signals. DC voltage: –300 mV and 300 mV. The RMS values 0.3 μV, 1.0 μV, 10 μV, 0.1 mV, 1 mV, 4 mV, 10 mV, 1 V and 5 V of sine-, triangle- and square-waveform alternating current varied within the frequency span of 0.5–1000 Hz with increments. The output voltage of an artificial ECG: from ±500 μV to ±10 mV; amplitude discretization: 5 μV at a sampling frequency ranging from 30 to 360 pulses per minute. In our future research we intend to improve the accuracy of the signal reproduction.

Acknowledgements The research is funded by Grant № MK-873.2020.8 of the President of the Russian Federation.

References

1. Wellens, H.J.J., et al.: Risk stratification for sudden cardiac death: current status and challenges for the future. Eur. Heart J. **35**, 1642–1651 (2014). https://doi.org/10.1093/eurheartj/ehu176
2. Ebrahimzadeh, E., Pooyan, M.: Early detection of sudden cardiac death by using classical linear techniques and time-frequency methods on electrocardiogram signals. J. Biomed. Sci. Eng. **04**, 699–706 (2011). https://doi.org/10.4236/jbise.2011.411087
3. Gulizia, M.M., et al.: ANMCO/AIIC/SIT consensus information document: definition, precision, and suitability of electrocardiographic signals of electrocardiographs, ergometry, Holter electrocardiogram, telemetry, and bedside monitoring systems. Eur. Heart J. Suppl. **19**, 190–211 (2017). https://doi.org/10.1093/eurheartj/sux031
4. Bogun, F., et al.: Misdiagnosis of atrial fibrillation and its clinical consequences. Am. J. Med. **117**(9), 636–642 (2004). https://doi.org/10.1016/j.amjmed.2004.06.024
5. Bae, M.H., et al.: Erroneous computer electrocardiogram interpretation of atrial fibrillation and its clinical consequences. Clin. Cardiol. **35**(6), 348–353 (2012). https://doi.org/10.1002/clc.22000
6. Abdelghani, S.A., Rosenthal, T.M., Morin, D.P.: Surface electrocardiogram predictors of sudden cardiac arrest. Ochsner J. **16**, 280–289 (2016)
7. Moreira, J.O., et al.: The signal-averaged electrocardiogram of atrial activation in patients with or without paroxysmal atrial fibrillation. Arq. Bras. Cardiol. **87**(5), 564–569 (2006). https://doi.org/10.1590/S0066-782X2006001800003
8. Frances, R.J.: Low noise level unmasks late potentials on signal-averaged electrocardiography. Exp. Clin. Cardiol. **15**, 61–64 (2010)
9. Priori, S.G., et al.: ESC Guidelines for the management of patients with ventricular arrhythmias and the prevention of sudden cardiac death. Eur. Heart J. **36**, 2793–2867 (2015). https://doi.org/10.1093/eurheartj/ehv316
10. Trobec, R., Tomašic, I., Rashkovska, A., Depolli, M., Avbelj, V.: Body sensors and electrocardiography. Springer, New York (2018)
11. Cakulev, I., et al.: Confirmation of novel noninvasive high-density electrocardiographic mapping with electrophysiology study: implications for therapy. Circ. Arrhythm Electrophysiol. **6**(1), 68–75 (2013). https://doi.org/10.1161/CIRCEP.112.975813

12. Avdeeva, D.K., Ivanov, M.L., Yuzhakov, M.M., Turushev, N.V., Kodermiatov, R.A., Maksimov, I.V., Zimin, I.A.: Novel high-resolution nanosensor-based measuring equipment for ECG recording. Measurement **146**, 215–229 (2019). https://doi.org/10.1016/j.sna.2019.06.023
13. Simulate ECG Express VI. Avaluable at https://zone.ni.com/reference/en-XX/help/373696B-01/lvbiomed/bio_sim_ecg/

Vibration Installation for Research of Erythrocytes Agglutination

Marina Shulgina, Alexander Aristov, and Yulia Rozenbaum

Abstract Proposed a method for establishing a human blood group based on the light flux registration passing through blood samples in the form of drops. In them there is a process of agglutination of red blood cells. This article describes the design of the vibrating installation, which will be used to study the vibration modes of droplet samples in order to find the necessary frequency and amplitude of vibrations for better detection of agglutinates during blood typing.

1 Introduction

Each person has one of four blood groups according to the AB0 classification system [1]. They differ depending on the presence or absence of certain proteins in the blood (alpha and beta agglutinins), as well as the presence of specific antigens on the erythrocyte membrane, which are indicated by the letters A and B [2, 3]. The determination of human blood groups is an important step before blood transfusion, making it possible to establish which blood type will be administered to the patient. Transfusion of mismatched blood groups can lead to the development of complications after transfusion of blood components [4]. In emergency situations, when a person's life depends on it, it is necessary to immediately transfuse blood. Although an in-place analysis is desirable for an appropriate blood transfusion procedure, most traditional methods and tools lack the required usability or tolerance. Blood typing tests have traditionally been carried out manually, using methods such as slide and

---

M. Shulgina · A. Aristov (✉) · Y. Rozenbaum
Division for Electronic Engineering, National Research Tomsk Polytechnic University, 30 Lenin Avenue, Tomsk, Russia 634050
e-mail: aristov@tpu.ru

M. Shulgina
e-mail: minika666@yandex.ru

Y. Rozenbaum
e-mail: julia-rozz@mail.ru

I. V. Minin et al. (eds.), *Progress in Material Science and Engineering*,
Studies in Systems, Decision and Control 351,
https://doi.org/10.1007/978-3-030-68103-6_19

tube agglutination tests. Red blood cell agglutination is caused by an immune reaction between red blood cells and antibodies against the corresponding blood group. Typically, when typing a blood sample, agglutination is detected by human eyes or by imaging methods.

Recently, a sufficient number of fully automated blood analysis devices have been developed that work in blood centers and large hospitals. These facilities have several advantages, the most important of which are high transmittance in mass analysis and good sensitivity. However, none of these devices can give results in a short time. These systems are stationary, have large dimensions and high cost. Therefore, to enable analysis to determine the blood group remotely from clinical laboratories, the development of a portable, inexpensive and sensitive device for typing blood samples is required.

Currently, a lot of research is underway to develop automated methods for determining blood groups. For example, scientists from Austria Ferraza et al. [5] were able to develop a special software tool based on image processing methods using a CCD-camera that can detect the occurrence of agglutination in the studied samples.

Maxime Hueta, Myriam Cubizollesa, Arnaud Buhot from France also worked on a similar topic [6]. They developed an integrated microfluidic chip that contains dried anti-A or anti-B reagents for typing inside their microchannel. A drop of blood in the analysis falls into this channel. Then, by video recording, the agglutination is visualized inside the biochip.

The publications of Japanese scientists Hiroki Ashiba, Makoto Fujimaki, Koichi Awazu [7] described a new method based on the detection of agglutination using an optical waveguide-sensor (waveguide-mode sensors). Using it, the reflectance spectrum of the initial blood and blood mixed with reagents containing antibodies for group affiliation was measured. Measurements based on the waveguide sensor showed the potential for detecting weak agglutination, which is difficult to distinguish with the human eye.

In the articles [8], domestic developments of methods for the automatic determination of agglutination are presented. Tarkhov N. S., Stekacheva V. L. In their work, when developing a portable device, they use the fact that in the course of agglutination reactions, a change in the density of the substance occurs and pressure increases on the piezoresonance sensor, which is used as a sensitive element.

One of the first publications devoted to the acousto-optic method for detecting red blood cell agglutination was the work of Alipov et al. [9]. The method is based on a combination of the action of ultrasound on the reaction mixture “blood-serum-physiological solution” with its optical sounding. The mechanism of interaction of the blood-serum mixture with ultrasound is considered in detail in articles by Dubrovsky et al. [10, 11]. It is also worth mentioning the method of determining the blood group using impedancemetry. The principle of their method is to detect changes in impedance during blood agglutination with coliclones [12].

2 Methodology

We also conduct research aimed at developing a simple, inexpensive, fast-performing, automated method for recording the hemagglutination reaction that occurs when conducting a blood typing study. To register the agglutination reaction, we are considering a method based on photometry of blood samples in the form of lying drops [13, 14]. Figure 1 shows the optical design of this study.

To accelerate the formation of erythrocyte aggregates, droplet blood samples mixed with an agglutinating agent have a mechanical effect in the form of horizontal vibration. Hydrodynamic flows that occur in a drop of blood during vibration lead to a more rapid association of individual red blood cells into large clusters (in the case of specific agglutination in the sample).

Initially, a reaction mixture of blood and a solution of cyclones represents a highly scattering medium. Reducing the dispersion of the medium, due to the formation of red blood cell agglutinates, leads to an increase in the transmittance of blood samples. In addition, as a result of vibrational flows, a clot of agglutinated erythrocytes separates from the transparent liquid part of the reaction medium and a significant part of the droplet becomes practically transparent to optical radiation.

And since the drop has a spherical surface, it begins to focus the light flux passing through it onto the photodetector installed in the focus position of the drop-lens.

During these processes, the intensity of the light flux arriving at the photodetector in the presence of agglutination increases more than 10 times with respect to the initial moment of the reaction time. In the absence of agglutination, dispersion of the sample occurs and the light transmission of such a drop does not change significantly.

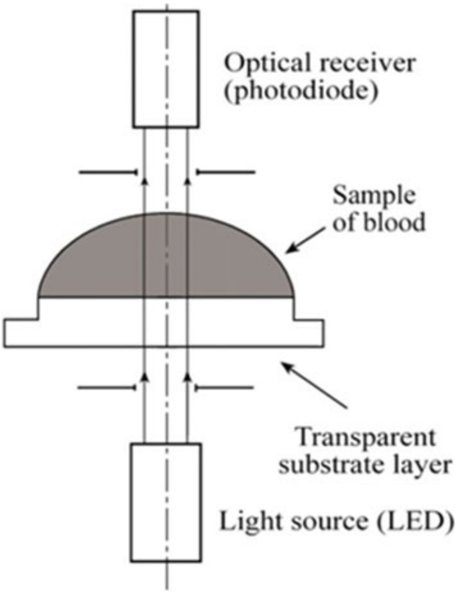

Fig. 1 Photometry method of droplet samples

Fig. 2 Laboratory layout of a system for generating droplet vibrations

Based on this registration technique, we conducted experimental studies on blood typing. These studies showed the possibility of sufficiently reliable identification of samples in which red blood cell agglutination occurred. In addition, during the studies, it was noted that the nature of the vibrational effects (frequency and amplitude of oscillations) on the drop sample of blood in which the agglutination process takes place affects the rate of erythrocyte agglutinate formation and the nature of the final conglomerates formed from agglutinating red blood cells. And this, in turn, leads to a different nature of the behavior of the optical curves recorded during the photometry of droplets. Therefore, the problem arose of finding the necessary frequency and amplitude of the vibrational impact on the drop to provide the best mode for detecting agglutination during blood typing.

The vibrational part of the installation used in our studies was assembled on the basis of the electromagnetic focusing unit CD-ROM (Fig. 2).

Since this system is based on an electromagnetic drive and it is characterized by a dependence of the oscillation amplitude on the frequency of the exciting signal, and this did not allow us to conduct a comparative analysis of agglutination at different frequencies. Therefore, to conduct experimental studies to determine the necessary parameters of vibrational effects on a drop, the task arose to develop a vibrational platform suitable for such studies.

3 Results

To achieve this goal were put forward requirements for the design of a vibrating installation:

- the amplitude of the platform oscillations should be in the range from 0.3 to 3 mm;
- the oscillation frequency of the platform can vary from 1 to 50 Hz;
- the speed of vibrational vibrations should be from 1 to 200 mm/s.

Since at this stage of research there were no requirements for the dimensions of this device, it was decided to use a stepper motor as a drive device.

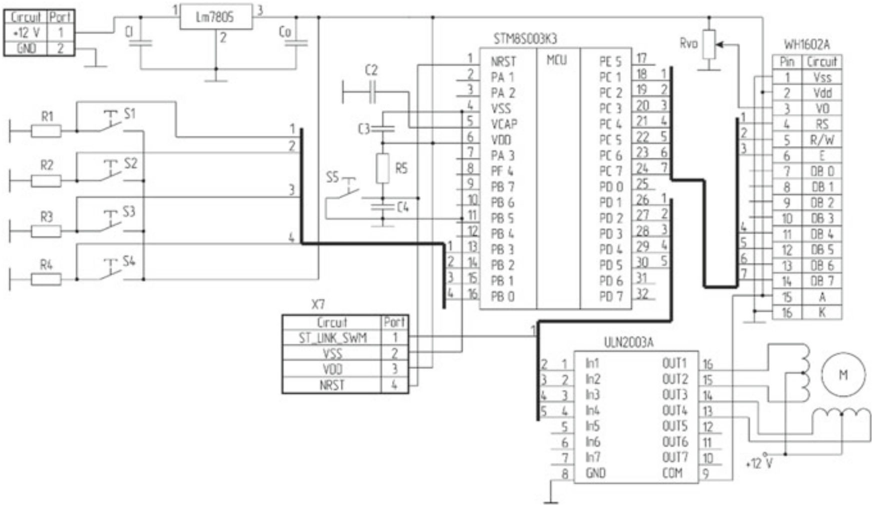

Circuit	Port
+12 V	1
GND	2

X7

Circuit	Port
ST_LINK_SWM	1
VSS	2
VDD	3
NRST	4

WH1602A

Pin	Circuit
1	Vss
2	Vdd
3	V0
4	RS
5	R/W
6	E
7	DB 0
8	DB 1
9	DB 2
10	DB 3
11	DB 4
12	DB 5
13	DB 6
14	DB 7
15	A
16	K

Fig. 3 Schematic diagram of the control of the vibration unit

According to our proposed device design, a screw drive by a stepper motor creates a reciprocating movement of the carriage, with cuvettes with blood samples placed on it.

To change the amplitude and velocity of the platform, the stepper motor is given the number of steps and its rotation speed. The electrical circuit diagram for controlling this unit is shown in Fig. 3.

All microcircuits are powered through the LM7805 stabilizer. The control signals to the stepper motor come from the microcontroller. The STM8S003K3T6 microcontroller was selected [15], because it has the necessary number of input / output ports, low power consumption, and compatibility with microcontrollers of more modern series. This makes it possible to further improve the device by using a more powerful STM microcontroller with a large number of input/output ports, which allows the use of more peripheral devices. It is also planned to introduce signals from optical measuring channels through the controller to register the optical parameters of droplet samples.

The device uses a unipolar stepper motor with a pitch of 1.8°. To coordinate a stepper motor with a microcontroller, a driver is required, in our case it is a ULN2003 driver. The controls are buttons S1–S4, by pressing of which the operator can change the amplitude and frequency of vibration, as well as the speed of the carriage. The values of the motion parameters of the vibrating platform are displayed on the WH1602A LCD display.

The programming of the controller is carried out using the ST-LINK V2 programmer. It is compatible with the STM32 and STM8 line controllers, allowing you to step-by-step execute the microcontroller program and monitor the values of all registers, which greatly facilitates the work with the project.

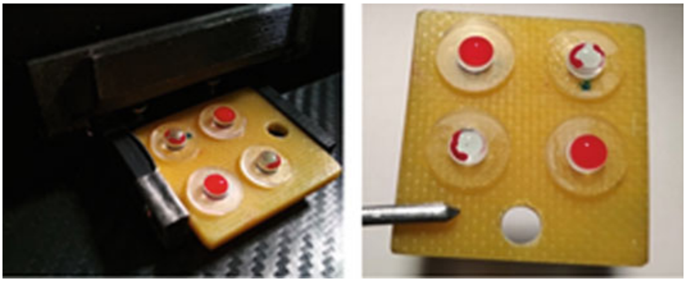

Fig. 4 Separation of a clot of agglutinated red blood cells from the clear liquid portion of the reaction medium

This device has been assembled and technical tests performed. The tests confirmed the specified technical requirements for this device and the possibility of conducting experimental studies on it.

Figure 4 shows a photo of a vibrating platform cuvette holder with blood samples located on it.

The photo reflects the result that can be observed visually in blood samples after vibration of the samples in the device. In blood samples, where cell agglutination has occurred, the central region of the drop is cleared from agglutinates. In blood samples where there is no agglutination, the medium remains cloudy.

4 Conclusions

In the future, using this setup, experiments will be conducted to find the most suitable vibration mode. The task of the research is to identify vibration modes in which the process of erythrocyte agglutination will occur faster and it will be better to optically detect samples where there is agglutination, from blood samples where this process is not observed.

Accordingly, with the proper experimental procedure, the correct selection of the parameters of the optical measuring system, the parameters of the vibration platform, corresponding to the analytical processing of the data, it is possible to obtain a sufficiently high sensitivity of our method, which will make it possible to assess the presence of erythrocyte agglutinates with a high degree of reliability even in samples with weak agglutination.

References

1. Misevic, G.: ABO blood group system. Blood Genom. **2**(2), 71–84 (2018). https://doi.org/10.46701/APJBG.2018022018113
2. Dean, L., Dean, L.: Blood groups and red cell antigens. NCBI, USA (2005)
3. Watkins, W.M.: The ABO blood group system: historical background. Transf. Med. **11**(4), 243–265 (2001). https://doi.org/10.1046/j.1365-3148.2001.00321.x
4. Reid, M.E., Mohandas, N.: Red blood cell blood group antigens: structure and function. Semin. Hematol. **41**(2), 93–117 (2004). https://doi.org/10.1053/j.seminhematol.2004.01.001
5. Ferraz, A., Carvalho, V., Soares, F.: Development of a human blood type detection automatic system. Proc. Eng. **5**, 496–499 (2010). https://doi.org/10.1016/j.proeng.2010.09.155
6. Huet, M., Cubizolles, M., Buhot, A.: Real time observation and automated measurement of red blood cells agglutination inside a passive microfluidic biochip containing embedded reagents. Biosens. Bioelectron. **93**, 110–117 (2017). https://doi.org/10.1016/j.bios.2016.09.068
7. Ashiba, H. et al.: Hemagglutination detection for blood typing based on waveguide-mode sensors. Sens. Bio-Sens. Res. **3**, 59–64 (2015). https://doi.org/10.1016/j.sbsr.2014.12.003
8. Tarhov, N.S., Stekacheva, V.L.: Portable device for rapid -diagnosis of blood group. J. Izvestiya Tula State University. Tech. Sci. (12–1), 9–18 (2014)
9. Alipov, A.N., Vaninskii, V.Z., Denisov, L.B., Donskov, S.I., Doubrovskii, V.A., Zav'yalov, E.N., Knyaz'kov, N.N.: The method for determining the agglutination reaction, USSR Invention Certificate No. 1683760. (1987)
10. Doubrovski, V.A., Medvedeva, M.F.: Acousto-optical method of blood typing (Part 1). Photometric and statistical methods for image processing. Biomed. Eng. **50**(1), 10–14 (2016). https://doi.org/10.1007/s10527-016-9577-3
11. Medvedeva, M.F., Doubrovski, V.A.: The application of digital image analysis for blood typing: the comparison of anti-A and anti-B monoclonal antibodies activity with standard hemagglutinating sera. Proc. SPIE **10336**, 10333609 (2017). https://doi.org/10.1117/12.2268367
12. Chen, L.L., Liao, Q., Hu, X., Zhang, G.Z.: New method for blood type detection based on bioelectrical impedance analysis technology and its system implementation. Jiliang Xuebao/Acta Metrologica Sinica **35**(4), 403–408 (2014). https://doi.org/10.3969/j.issn.1000-1158.2014.04.21
13. Aristov, A., Nosova, E.: Method of evaluation of process of red blood cell sedimentation based on photometry of droplet samples. Med. Biol. Eng. Comput. **55**(4), 621–630 (2017). https://doi.org/10.1007/s11517-016-1542-5
14. Aristov, A.A., Nosova, E.V., Soldatov, A.N.: Use of lying drop photometry for clinical laboratory diagnostics. Biomed. Eng. **50**(5), 314–317 (2017). https://doi.org/10.1007/s10527-017-9645-3
15. Microcontroller of the STM8S family. Available at: https://www.st.com/resource/en/datasheet/stm8s003f3.pdf. Accessed 15 Sept 2020

New Approaches to Stratification of Patients by the Level of Sudden Cardiac Death Risk Using the Data on Energies of Cardiac Micropotentials Obtained by Nanosensor-Based Hardware and Software Complex

Diana Avdeeva, Ivan Maksimov, Wenjia Guo, Maxim Ivanov,
Nikita Turushev, Mikhail Yuzhakov, Stepan Enshin, Sergey Mazikov,
Ekaterina Marchenko, and Mariya Balakhonova

Abstract The problem of human cardiovascular diseases is one of the critical health problems. The most serious aspect is sudden cardiac death (SCD). A new method and approaches to recording micropotentials by the nanosensor-based hardware and

---

D. Avdeeva · W. Guo · M. Ivanov · N. Turushev · M. Yuzhakov (✉) · S. Enshin · S. Mazikov
Laboratory for Medical Engineering, National Research Tomsk Polytechnic University, 7
Savinykh Street, Tomsk, Russia 634050
e-mail: libra@tpu.ru

D. Avdeeva
e-mail: diana.avdeeva@mail.ru

W. Guo
e-mail: guowenjia@mail.ru

M. Ivanov
e-mail: lydoz@mail.ru

N. Turushev
e-mail: nvtur90@mail.ru

S. Enshin
e-mail: stepanomt@mail.ru

S. Mazikov
e-mail: s-mazikov@mail.ru

I. Maksimov
Department of Emergency Cardiology, Cardiology Research Institute, Tomsk National Research
Medical Center of the Russian Academy of Sciences, 111a Kievskaya Street, Tomsk, Russia
634050
e-mail: miv@cardio.tsu.ru

E. Marchenko
Laboratory of Medical Alloys and Shape Memory Implants, National Research Tomsk State
University, 40 Lenin Avenue, Tomsk, Russia 634050
e-mail: 89138641814@mail.ru

I. V. Minin et al. (eds.), *Progress in Material Science and Engineering*,
Studies in Systems, Decision and Control 351,
https://doi.org/10.1007/978-3-030-68103-6_20

software complex are elaborated for dynamic personalized monitoring of the heart. Tables with data on functioning of the patient's heart during multiple examinations are automatically generated in one Excel file. The study presents results on cardiac micropotentials in groups 1A—volunteers died from cardiogenic shock, and 1B—volunteers with acute myocardial infarction (AMI) survived. Relative average values of the total energy for all time intervals are given in the following amplitude ranges: (0.5–1.0) μV; (1.1–3.0) μV; (3.1–5.0) μV; (5.1–20.0) μV in a dynamic pattern. The results are divided into 3 ranges: the total energy value of more than 150%, less than 50% and in the range of (50–150)%. The most significant changes in the micropotential energy by a factor of (4, 5) can be observed in the range of (5.1–20) μV. It is shown that the excess of the micropotential energy over 150% and the decrease in the micropotential energy below 50% are predictors of SCD.

1 Introduction

Diseases of the human cardiovascular system are some of the critical health problems recognized by scientists all over the world [1]. According to Eurostat reports, the number of patients in Europe attained 11.3 million [2]. In 2018, the American Society of Cardiology reported the projected proportion of people suffering from cardiovascular disease (CVD) to increase to 45% of the total US population [3]. An increased number of patients is associated with general aging of the population, improved effectiveness of methods for controlling infectious diseases and changed rhythm of people's lives that causes bad health habits.

CVD is dangerous since its course is asymptomatic until transition to acute forms that often end in death. Widespread prevalence and lack of awareness of people about the state of their body and the need to change the lifestyle in the early stages of the disease result in high mortality from CVD worldwide.

The most serious problem in mortality from CVD is the phenomenon of sudden cardiac death (SCD). SCD refers to nonviolent death due to circulatory dysfunction incompatible with life without symptoms preceding the event.

Around 4 to 5 million people per year die from sudden cardiac death worldwide [4]. Studies of various scientific groups have shown a significant number of SCD episodes among deaths from various pathologies of the cardiovascular system, most of which were coronary heart disease, cardiomyopathy and Cardiac channelopathies [4]. In statistical review [5], the prevalence of SCD after myocardial infarction (MI) attacks during 1 year, 5 and 10 years is (7–20%), (24–38%), and (40–56%), respectively. In various cardiomyopathies, the proportion of SCD cases ranges from 2 to 4% [6].

M. Balakhonova
Department of Cardiology, Siberian State Medical University, 2 Moskovsky Trakt, Tomsk, Russia 634050
e-mail: maria_balahonova@mail.ru

Knowing one of the causes of SCD, the number of deaths could be reduced by preventing cardiac arrest using a wearable implantable pacemaker, which proved to be very effective in combating this phenomenon [7]. Nevertheless, indications for this treatment are still controversial due to the ambiguity of the existing criteria for stratification of people by risk groups [8].

Methods currently used for classification of sudden cardiac death do not allow accurate identification of risk groups and correctly recommended treatment. For example, according to the statistics provided by the DANISH study, a group of people at risk of SCD did not actually need to undergo prescribed pacemaker implantation and were unnecessarily exposed to postoperative risks. At the same time, 80% of cases of cardiac arrest outside hospitals occurred in people who were not prescribed pacemaker implantation [9].

Thus, the group of people most vulnerable in stratification of the population includes patients without obvious signs of CVD, since health services and the group of people themselves remain unaware of the upcoming event and cannot take preventive measures against SCD. Thus, development of new methods and systems for stratification of the population for predisposition to episodes of SCD is critical at the global level.

The main methods to detect the presence of predictors of SCD in humans are reported in [4, 6, 8, 10]:

- medical history,
- heart imaging techniques,
- genetic testing,
- serological testing,
- electrocardiographic examination,
- studies of autonomous tonus,
- electrophysiological examination.

The most common diagnostic criterion for assessing the occurrence of SCD is the value of the left ventricular ejection fraction (LVEF) obtained by echocardiographic examination. LVEF reflects the performance of the left heart ventricle. This parameter is critical for determining indications for pacemaker implantation (PI) [11]. However, studies show that an isolated use of LVEF is insufficient for both stratification of the population and indications for PI implantation [11], since not all cardiac pathologies that cause SCD are followed by the change in the volume of blood ejected from the heart, and a group of people with low LVEF (less than 35%) accounts for 4.3% of cases of threatening arrhythmias, and only one third of all cases result in SCD [12]. In addition, echocardiographic examination is prescribed only in case of signs of CVD in medical history and are not used for annual examination of the population [11], which makes them useless for stratification of people without symptoms of heart disease.

To visualize the heart, the MRT method is used to obtain an image of fibrous tissue in various parts of the heart indicating the cardiomyopathy and causing life-threatening rhythm disturbances.

Despite the clarity of imaging techniques, they can only be used as an auxiliary means of SCD stratification due to high cost and laborious diagnostic process. This makes them of little use for groups without severe CVD symptoms.

Electrophysiological (EP) examination is invasive recording of the myocardium during electrical stimulation either with or without additional drug stimulation. The importance of EP study as a SCD risk stratification factor is particularly notable in the study of patients after myocardial infarction [13].

Electrocardiographic examination methods are important in the SCD stratification, since they allow the study of a large group of people with minimal consumption of time, money and labor resources, including that within the framework of clinical examination of the population. In addition, these methods yield a large number of parameters available for statistical analysis.

Analysis of the literature revealed the following significant markers of risk detected by ECG:

- abnormal duration of the QRS complex [13],
- block of His bundles [14],
- fragmented QRS complexes [15],
- high heart rate (HR),
- T-wave width (Tpeak-Tend) [16],
- microvolt T-wave alternations (mTWA) (from cycle to cycle) [13],
- changes in the composition of cardiac late potentials [10],
- change in the ST-segment during Holter monitoring (HM) [13],
- change in the QT-segment and its variance, HM [13],
- change in the T-wave shape, HM [13],
- the angle between the QRS and T vectors.

One of the new parameters for prediction of an episode of SCD in humans is the duration and morphology of the QRS complex. QRS duration is significant in assessing risk factors in people with bundle branch block (BBB), especially in men [17].

A fragmented QRS complex found on a conventional electrocardiogram is a sign of abnormal ventricular depolarization and, according to one theory, it is caused by scars on the heart and formation of fibrous tissue, as well as changed functioning of tissue ion channels [18]. The QRS fragmentation curve is a complex split in one or more points with new teeth formed.

An increased heart rate (HR) at rest is one of the signs of dysregulation of the sympathetic system, which is used as a criterion for SCD stratification. For example, in [19], a study was conducted among risk groups of SCD, where a number of deaths were found to grow at increased heart rate at rest.

Microvoltage T-wave alternations (mTWA) are some of the subtle parameters on the ECG, representing small changes in the amplitude and morphology of the wave from one cycle to another.

However, the overall diagnostic value of this criterion remains in question for the entire population due to conflicting results of statistical studies, and it requires further additional assessment [5].

The duration of the T-wave (Tre) is determined as the duration of the interval from the wave peak to its end. In a standard 12-lead ECG, this parameter showed itself as one of the evaluation criteria for stratification of patients by SCD signs. According to [20], the risk of mortality increases significantly with every increase of 10 ms in the Tre duration with the minimum significant limit starting from 85 ms.

Scientists used this parameter for stratification of SCD risk groups and noted that, although this parameter can be used as an independent factor, its full potential can be revealed only in combination with other parameters, such as elongation of the QT segment and QRS complex [16].

The QT interval is also one of the predictors of SCD.

Another ECG parameter used for SCD risk stratification is the presence of late ventricular potentials (LVV) [21], which are studied using signal-averaged electrocardiography (SAECG). Late micropotentials are low-amplitude (less than 20 μV) high-frequency (above 20–50 Hz) components in the final fragment of the QRS complex. LVV is currently determined by statistical Simson's method of the QRS complex of the ECG recorded using orthogonal leads (X, Y, Z) with bidirectional digital filtering in the frequency range from 40 to 250 Hz. This method employs a set of similar cardiocycles (about 500), since the method implies synchronization of cardiocycles along the R wave and their summation with subsequent averaging. The total value $\sqrt{}(X^2 + Y^2 + Z^2)$ of the parameters is analyzed for the signs of LVV. The parameters that are significant in the analysis of potentials are as follows: the duration of the averaged QRS–totQRS complex, the rms amplitude of the last 40 s of the averaged QRS–RMS-40 complex, the duration of potentials with amplitude of less than 40 μV at the end of the averaged QRS complex.

A QRS complex duration of more than 114 ms plays the role of an independent prognostic factor in the diagnosis of life-threatening arrhythmias, and that exceeding 120 ms indicates the risk of developing ventricular fibrillation and sustained atrial tachycardia. For other significant parameters, the boundary values are: LAS-40 of more than 38 ms, RMS-40 of less than 20 μV. In case, two of the three parameters are detected, the method indicates SCD risk [21].

Dysfunction of the autonomic nervous system with decreased regulatory activity of the vagus nerve is often associated with the development of life-threatening arrhythmias, especially after MI cases in humans [22].

The analysis of studies of predictors and predictive models showed that prediction of SCD is still an urgent problem actively being solved by the scientific community of clinicians. Most of the studies conducted are aimed at stratification of SCD cases in groups with known signs of CVD and focus little on patients without pronounced symptoms, which leaves the bulk of the population and people involved in sports, who, despite their healthy appearance, may be exposed to SCD, especially at young age without adequate treatment [23].

Thus, in stratification of the population, the group of people most vulnerable are currently patients without obvious signs of CVD, since the health services and the group of people themselves remain unaware of the upcoming event and cannot take preventive measures against SCD. Thus, the relevance of new methods and systems for stratification of the population for predisposition to episodes of SCD is critical at the global level.

Methods of stationary electrocardiography are mainly designed for short-term studies in conditions of a cardiologist's office or a hospital ward. However, most episodes of cardiac abnormalities occur outside the hospital during daily activities, including dangerous arrhythmic episodes leading to SCD [24]. To record these episodes, it is necessary to use wearable devices recording outside the premises of clinics in patient's daily life [25–27].

Advanced communication technologies and computers provided new technical solutions to improve mobile ECG devices. Among the types of mobile ECG devices, the following categories are of greatest interest: ambulatory electrocardiographs (AE) and activity trackers.

The Holter cardiograph is the earliest and most commonly used device for long-term monitoring of cardiovascular activity.

Activity trackers are a separate class of devices designed to track biological parameters of the human body in real time. Modern trackers are made as a wristwatch with a sensor module that records parameters of the human body and transmits it to the user's smartphone.

The devices considered earlier showed that modern development of medical diagnostic technologies shows a tendency towards advanced and increased variety of medical wearable devices. The development of information and communication technologies (ICT) greatly promotes this area. As a result, portable telemetry systems were designed for long-term monitoring of heart activity, referred to as MCOT (mobile cardiac outpatient telemetry system) in the English-language literature. The system provides remote interaction between the patient's electrocardiographic data and medical personnel during a long-term monitoring outside the hospital [28].

There is a tendency to increase the duration of heart exanimation and ensure the continuity of recording during the entire exanimation process.

The main technical parameters of known wearable technical devices are as follows:

- amplitude range from 30 μV to 10 mV;
- frequency range from 0.05 to 100 Hz;
- sampling frequency from 128 to 1024 Hz;
- number of channels from 1 to 3;
- weight from 16 to 110 g.

The existing equipment for continuous dynamic monitoring of the state of the human heart functions in standard frequency ranges, shows low resolution, and contains filters that limit signals in both low and high frequencies.

New methods and high-resolution technical means operating in extended amplitude and frequency ranges are being created for human heart examination to develop methods for assessing the state of the human cardiovascular system [29–32].

In [33], a nanosensor-based hardware and software complex (HSC) is described. It is capable of recording cardiac micropotentials without filtering and averaging electrical cardiac signals with a level of 1 μV, in the frequency range from 0 to 10,000 Hz, and with a sampling frequency of 64,000 Hz. HSC has undergone preliminary clinical studies in volunteers. In [33, 34], it was shown that sensitivity and metrological characteristics of the nanosensors are higher in comparison with those of silver-chloride electrodes.

The aim of the study is creation of new methods and approaches based on non-invasively recorded cardiac micropotentials for dynamic personalized monitoring of the heart activity.

2 Methods

Before the recordings processing, ‘extraneous’ components such as artefacts, electrical interference, electromagnetic interference, and others should be excluded from the ‘useful’ signal. A specially developed program [33] is used for signal processing (Fig. 1).

This program eliminates concentrated interferences while maintaining a continuous spectrum and eliminates the intrinsic noise of the HSC.

A computational module has been developed to automatically generate Excel tables with processed results of the Holter ECGs recorded from the chest (leads 1–3) using the nanosensor-based HSC.

Figure 2 presents a block diagram of the automation algorithm for statistical data generation.

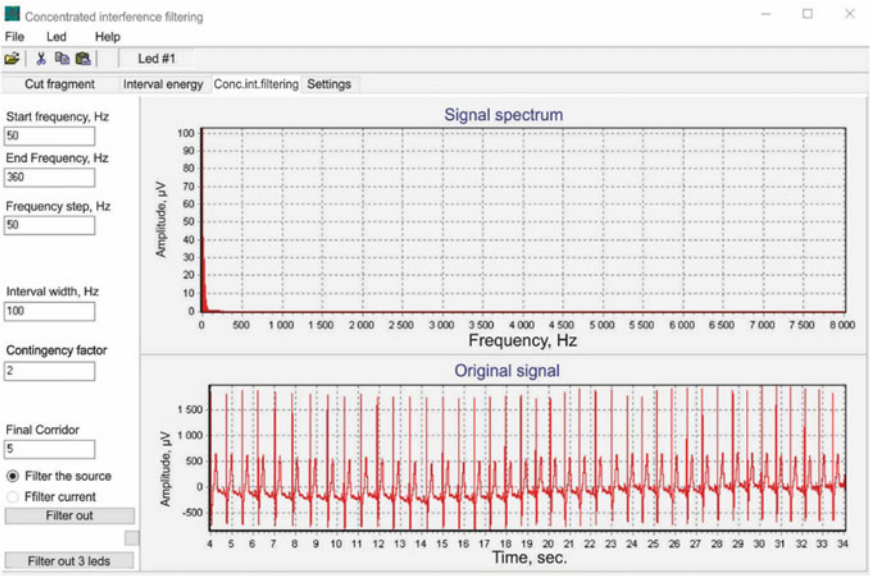

Start frequency, Hz: 50
End Frequency, Hz: 360
Frequency step, Hz: 50
Interval width, Hz: 100
Contingency factor: 2
Final Corridor: 5
● Filter the source
○ Ffilter current

Fig. 1 Signal processing window

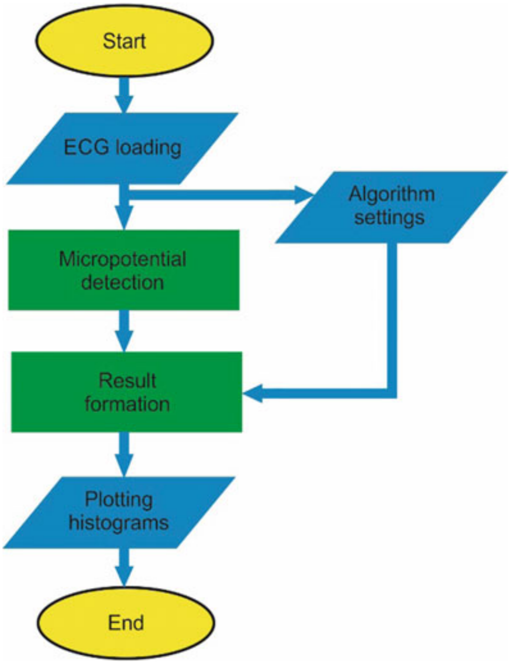

Fig. 2 Block diagram of the automation algorithm for statistical data generation

The first stage of the algorithm is loading of an ECG signal and an Excel file with rows and columns formed for filling the data. To speed up the program, the ECG signal is loaded without displaying in graphs, since this process requires significant computing power. The loaded Excel file can or cannot contain data. If the table contains data, the program finds the cells for filling the data. The method for opening an Excel file is implemented through the OLE Variant variable designed to operate with the settings and table data using the program code.

To speed up the algorithm, at the stage of detecting micropotentials an algorithm for finding micropotentials was implemented for the entire signal duration with no graphical display of the result. Similar to the ECG file loading, the display of data can be specified in the settings when detecting micropotentials.

The next stage includes the main part of the developed program module. Since a large number of ECG recordings are being processed, it is required not only to speed up the loading and detection algorithm but also to generate results for further statistical analysis of the data. To accomplish this task, the obtained results were divided into sections (intervals). Initially, the detection algorithm yields a result from 200 on the time scale and from 1000 on the amplitude scale. These data show the accuracy of the detection algorithm with a time increment of 0.1 ms and an amplitude of 0.1 μV. Given these data, the total number of different positions can attain 200,000 in one of 3 leads only, which hinders determination of the diagnostic value of the results. Therefore, the time scale was divided into 20 intervals with an increment of 1 ms, and the amplitude scale fell into 6 intervals: (0.5–1.0); (1.1–3.0);

(3.1–5.0); (5.1–20.0); (20.1–50.0); (50.1–100) μV. These intervals were selected experimentally to identify areas that indicate features of the heart. This method reduced the number of different positions to 120. In addition, the program additionally divided the time scale into 3 intervals: (0.1–3) ms, (3.1–7) ms, (7.1–20) ms to study changes in the dynamics of micropotentials in extended time and amplitude intervals: (0.5–1.0); (1.1–3.0); (3.1–5.0); (5.1–20.0); (20.1–50.0); (50.1–100) μV.

The tables provide the number of micropotentials and their energy in the specified amplitude-time intervals for 3 leads and the examination date. As a result, tables with data on the state of the volunteer's heart during multiple examinations can be presented in one Excel file. This method is becoming a new tool for monitoring and preventing changes in the state of the patient's heart. Moreover, data on micropotentials that reflect a spontaneous activity of myocardial cells ensure early identification of the heart disease symptoms.

3 Results

To assess the diagnostic value of the recorded cardiac micropotentials, they were studied in two groups of volunteers: group 1A involved 6 volunteers who died from cardiogenic shock, and group 1B involved 10 volunteers with previously documented acute myocardial infarction. Figures 3, 4, 5, 6, 7 and 8 show the results of study for

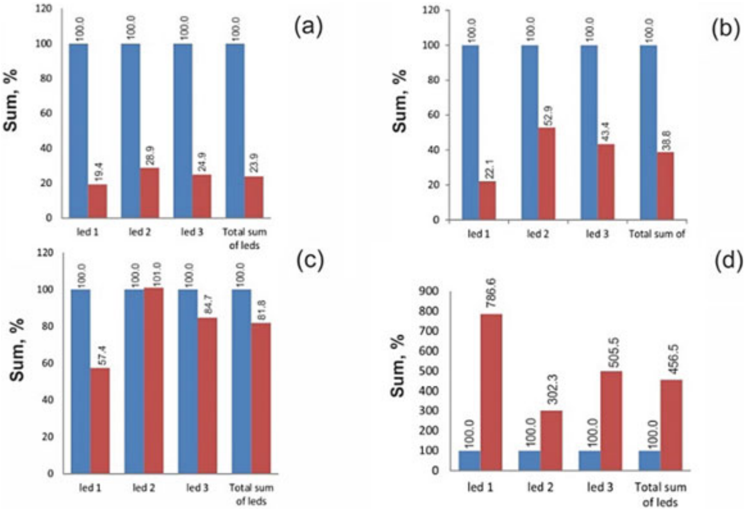

Fig. 3 Volunteer 1, group 1A, recording 1—04.05.2014, recording 2—06.08.2015, out of hospital SCD after 6 months; amplitude intervals: **a** (0.5–1) μV; **b** (1.1–3) μV; **c** (3.1–5) μV; **d** (5.1–20) μV; range of more than 150%

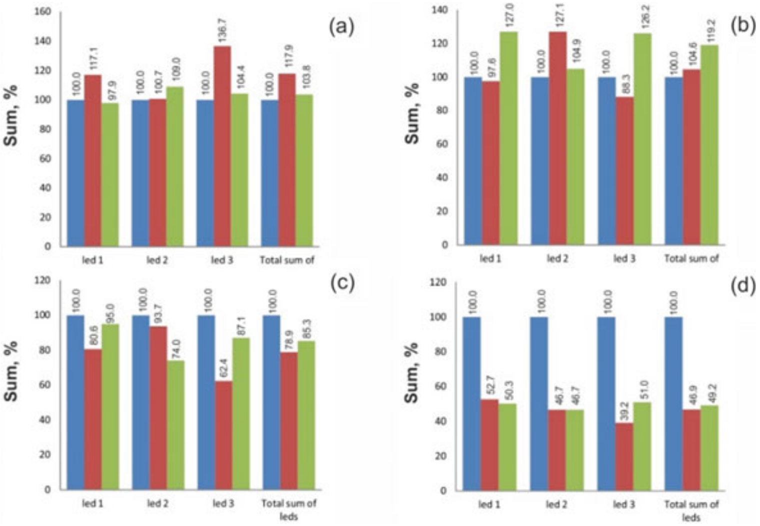

Fig. 4 Volunteer 2, group 1A, recording 1—11.03.2016, recording 2—14.03.2016, recording 3—06.04.2016, a day before death; amplitude intervals: **a** (0.5–1) μV; **b** (1.1–3) μV; **c** (3.1–5) μV; **d** (5.1–20) μV; range of less than 50%

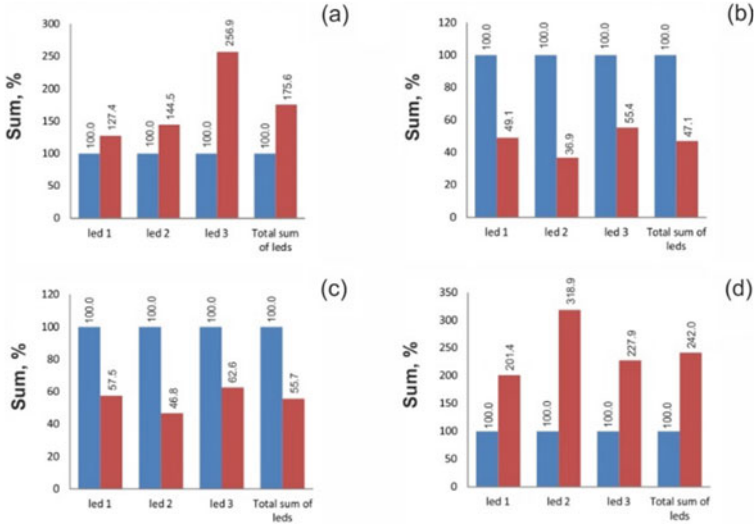

Fig. 5 Volunteer 3, group 1A, recording 1—25.04.2016, recording 2—10.05.2016, a day before death; amplitude intervals: **a** (0.5–1) μV; **b** (1.1–3) μV; **c** (3.1–5) μV; **d** (5.1–20) μV; range of more than 150%

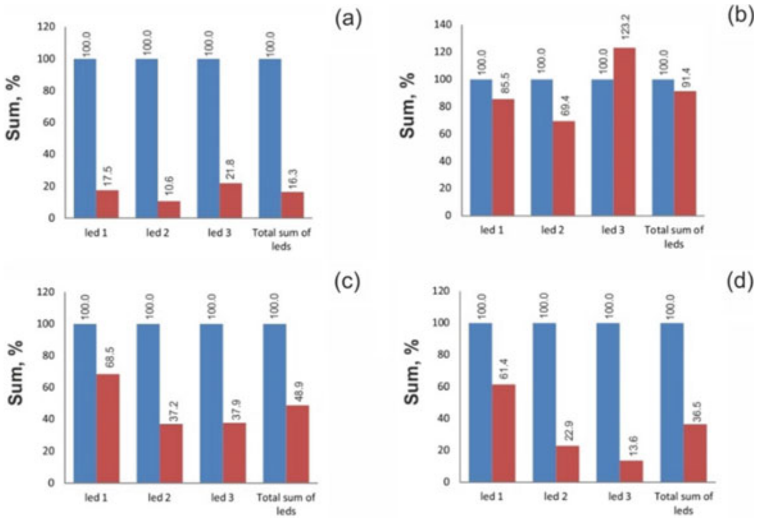

Fig. 6 Volunteer 4, group 1A, recording 1—27.04.2016, recording 2—28.04.2016, a day before death; amplitude intervals: **a** (0.5–1) μV; **b** (1.1–3) μV; **c** (3.1–5) μV; **d** (5.1–20) μV; range of less than 50%

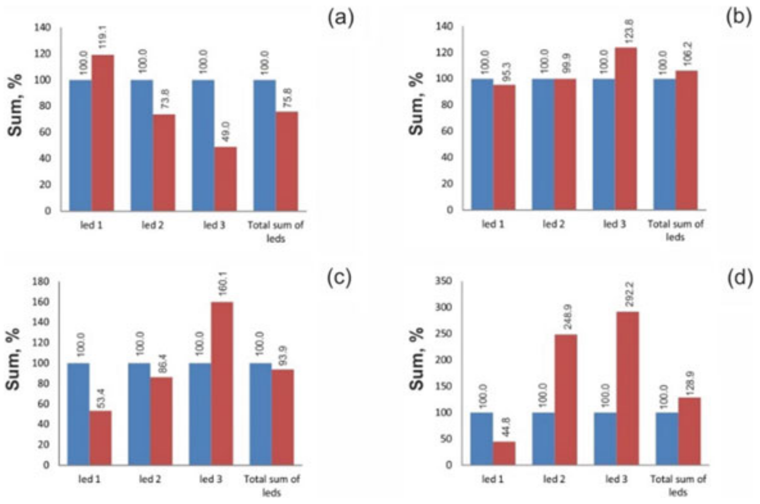

Fig. 7 Volunteer 5, group 1A, recording 1—14.11.2017, recording 2—16.11.2017, a day before death; amplitude intervals: **a** (0.5–1) μV; **b** (1.1–3) μV; **c** (3.1–5) μV; **d** (5.1–20) μV; lead 1—range of less than 50%; leads 2 and 3—more than 150%, total sum of leads—from 50% to 150%

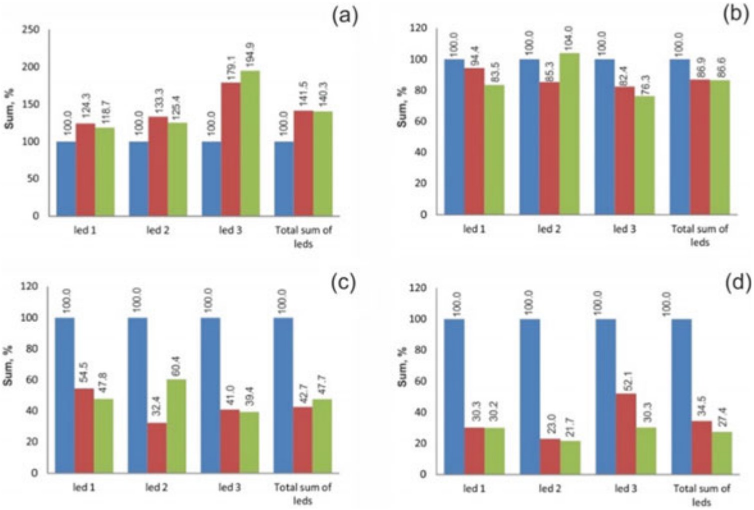

Fig. 8 Volunteer 6, group 1A, recording 1—14.11.2018, recording 2—16.11.2018, recording 3—19.11.2018, a day before death; amplitude intervals: **a** (0.5–1) µV; **b** (1.1–3) µV; **c** (3.1–5) µV; **d** (5.1–20) µV; range of less than 50%

group 1A, and Figs. 9, 10, 11, 12, 13, 14, 15, 16, 17 and 18 present the results of study for group 1B.

Preliminary medical studies were conducted in Tomsk Research Institute of Cardiology. Each volunteer signed an informed consent (Clinical studies were approved by the local ethical committee on biomedical ethics at the Research Institute of Cardiology protocol #147 dated 28.06.2016). The volunteer was informed about the regime and procedures for examination and treatment, according to the regulations on the

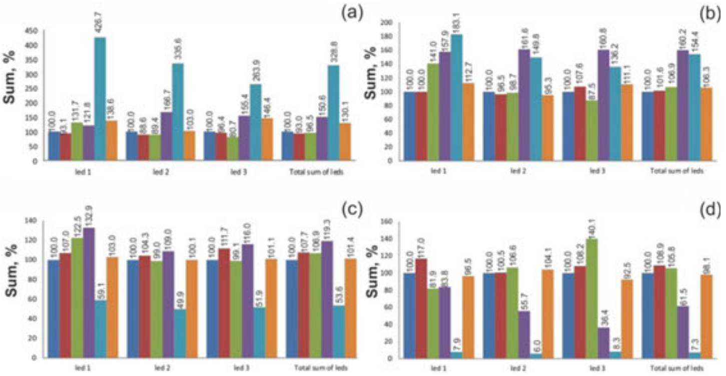

Fig. 9 Volunteer 1, group 1B, recording 1—12.03.2015, recording 2—20.03.2015, recording 3—26.03.2015, recording 4—08.04.2015, recording 5—28.04.2015, recording 6—04.06.2017; amplitude intervals: **a** (0.5–1) µV; **b** (1.1–3) µV; **c** (3.1–5) µV; **d** (5.1–20) µV; range (50–150)%

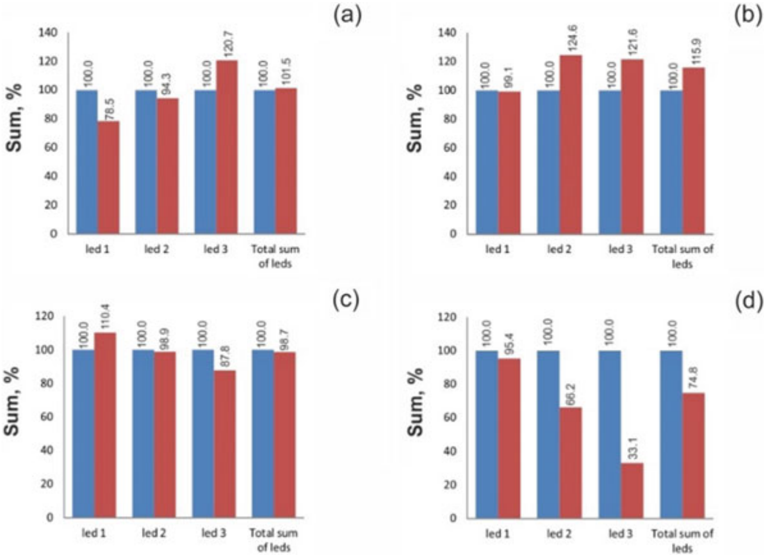

Fig. 10 Volunteer 2, group 1B, recording 1—10.02.2016, recording 2—17.02.2016, amplitude intervals: **a** (0.5–1) μV; **b** (1.1–3) μV; **c** (3.1–5) μV; **d** (5.1–20) μV; range (50–150)%

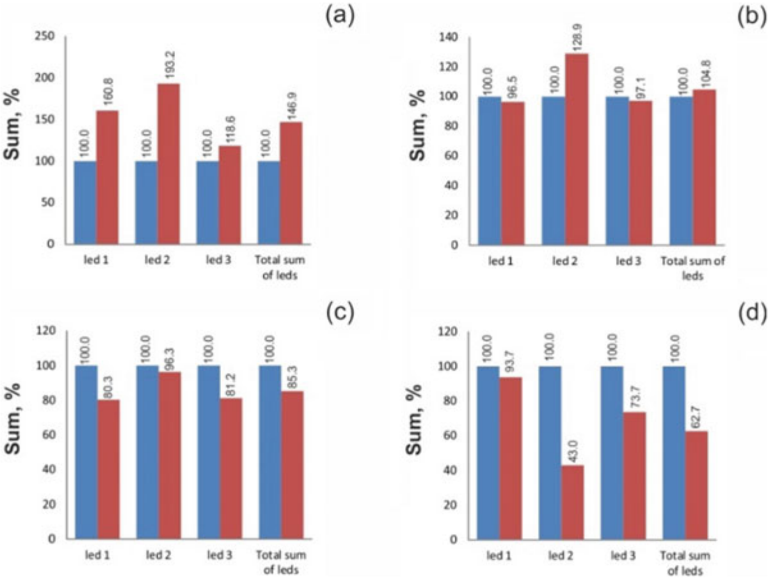

Fig. 11 Volunteer 3, group 1B, recording 1—10.02.2016, recording 2—17.02.2016, amplitude intervals: **a** (0.5–1) μV; **b** (1.1–3) μV; **c** (3.1–5) μV; **d** (5.1–20) μV; range (50–150)%

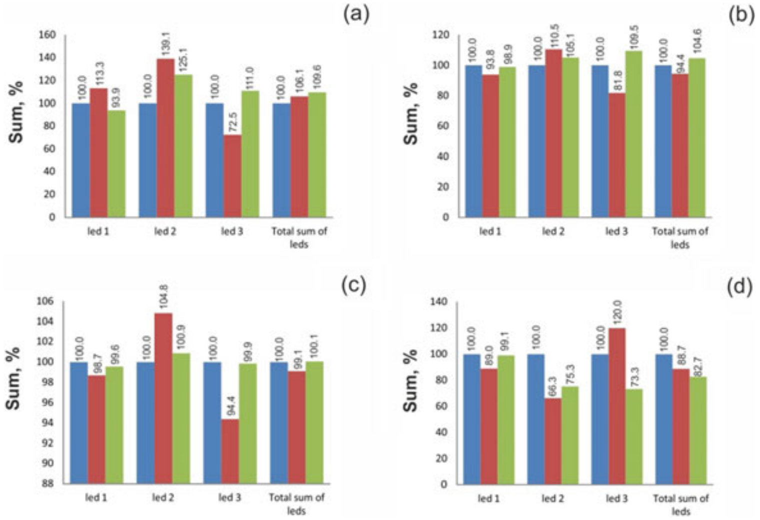

Fig. 12 Volunteer 4, group 1B, recording 1—24.02.2016, recording 2—26.02.2016, recording 3—09.03.2016; amplitude intervals: **a** (0.5–1) µV; **b** (1.1–3) µV; **c** (3.1–5) µV; **d** (5.1–20) µV; range (50–150)%

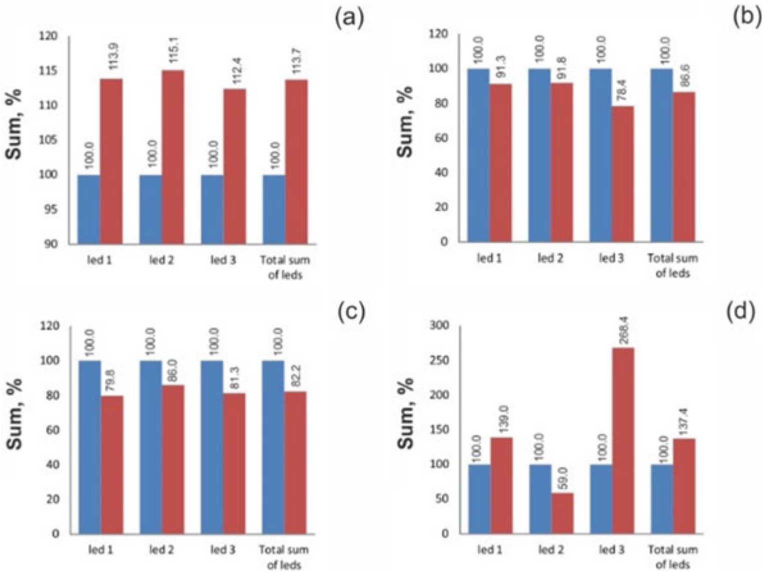

Fig. 13 Volunteer 5, group 1B, recording 1—10.02.2016, recording 2—11.03.2016, amplitude intervals: **a** (0.5–1) µV; **b** (1.1–3) µV; **c** (3.1–5) µV; **d** (5.1–20) µV; range (50–150)%, lead 3—range (5.1–20) µV – more than 150%

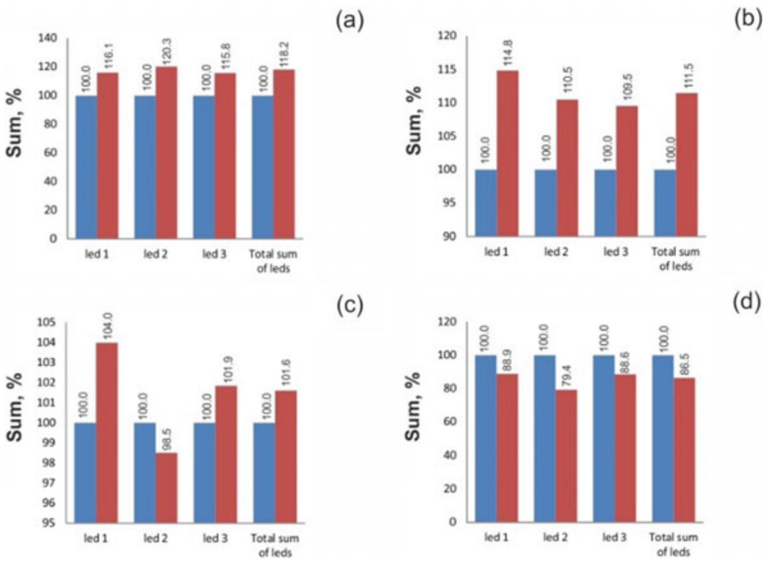

Fig. 14 Volunteer 6, group 1B, recording 1—16.03.2016, recording 2—18.03.2016, amplitude intervals: **a** (0.5–1) μV; **b** (1.1–3) μV; **c** (3.1–5) μV; **d** (5.1–20) μV; range (50–150)%

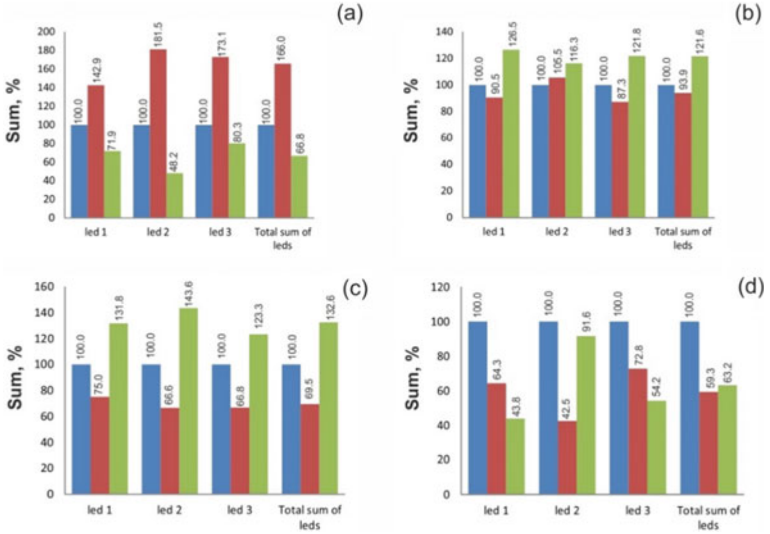

Fig. 15 Volunteer 7, group 1B, recording 1—29.03.2016, recording 2—06.04.2016, recording 3—15.04.2016; amplitude intervals: **a** (0.5–1) μV; **b** (1.1–3) μV; **c** (3.1–5) μV; **d** (5.1–20) μV; range (50–150)%

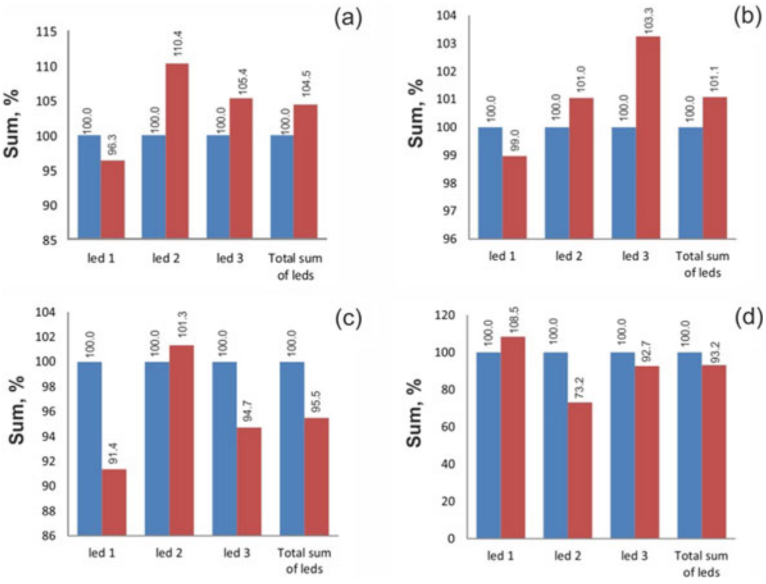

Fig. 16 Volunteer 8, group 1B, recording 1—14.04.2016, recording 2—22.04.2016, amplitude intervals: **a** (0.5–1) µV; **b** (1.1–3) µV; **c** (3.1–5) µV; **d** (5.1–20) µV; range (50–150)%

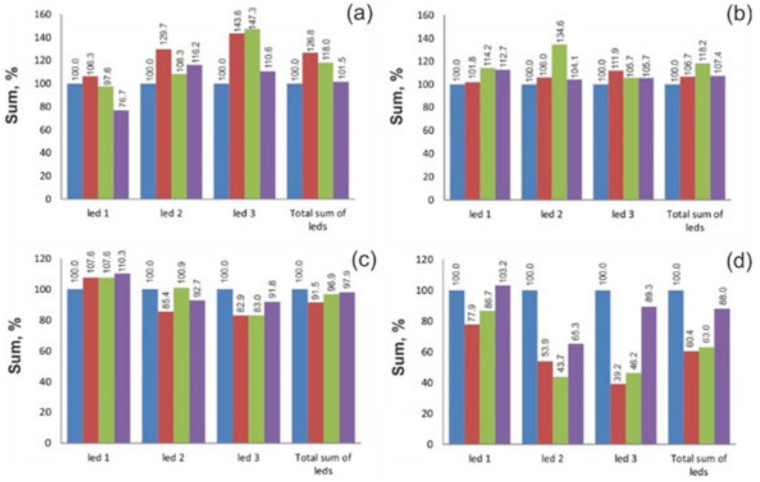

Fig. 17 Volunteer 9, group 1B, recording 1—17.04.2016, recording 2—25.04.2016, recording 3—06.06.2016, recording 4—04.06.2017; amplitude intervals: **a** (0.5–1) µV; **b** (1.1–3) µV; **c** (3.1–5) µV; **d** (5.1–20) µV; range (50–150)%

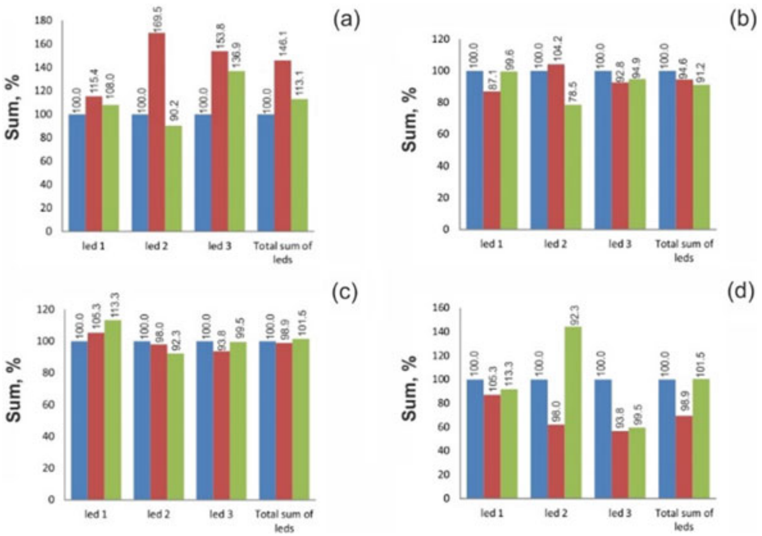

Fig. 18 Volunteer 10, group 1B, recording 1—28.04.2016, recording 2—15.05.2016, recording 3—20.06.2016; amplitude intervals: **a** (0.5–1) μV; **b** (1.1–3) μV; **c** (3.1–5) μV; **d** (5.1–20) μV; range (50–150)%

procedure for hospitalization in Tomsk Research Institute of Cardiology (information leaflets/consents (order of the Chief Medical Officer of the Research Institute of Cardiology #12 of June 06, 2014). The confidentiality of the volunteers surveyed is respected.

The ECG was recorded using three leads from the chest at rest according to Holter's system.

Figures 3, 4, 5, 6, 7, 8, 9, 10, 11, 12, 13, 14, 15, 16, 17, 18 show the relative average values of the total energy for all time intervals in the following amplitude intervals: (0.5–1.0); (1.1–3.0); (3.1–5.0); (5.1–20.0) μV in the dynamics of study. The result of examination 1 is taken as 100%. The total energy for 3 leads is determined, and the ratio of the results for subsequent studies to the energy determined during examination 1 (in %) is calculated. The results are grouped into 3 ranges: the value of the total energy for all time intervals is more than 150%, less than 50% and ranges from 50% to 150%.

4 Discussion

In group 1A (lethal outcome), Volunteer 1, Fig. 3, died from SCD outside the hospital 6 months after the last examination. There were no symptoms, postmortem examination confirmed the presence of signs of acute coronary insufficiency. The greatest

(4, 5)-fold changes in the energy of micropotentials could be observed within the range (5.1–20) μV.

Volunteers (2–6) were examined in the hospital and died from cardiogenic shock. In Volunteers 2, 4, and 6, the micropotential energy decreased by more than 50%, and in Volunteers 1, 3, and 5, the micropotential energy exceeded 150%.

In group 1 B (acute myocardial infarction volunteers, but survivors of myocardial infarction, comparison group), all 10 volunteers exhibited micropotential energies in the range of (50–150)%.

5 Conclusion

The study yields the following conclusions:

- The developed method for real time recording micropotentials without filtering and averaging using the nanosensor-based HSC is of high new diagnostic value.
- The energy of micropotentials index shows the state of the heart muscle.
- The energy of micropotentials exceeding 150% and the energy of micropotentials decreased by more than 50% are SCD predictors.

Acknowledgements The research was financially supported by the Federal Targeted Program Research and Development in Priority Fields of S&T Complex of Russia in 2014–2020 the Agreement No. 14.578.21.0032 dated 05.06.201, the unique identifier of the contract: RFMEF157814X0032. The study was carried out at Tomsk Polytechnic University within the framework of Tomsk Polytechnic University Competitiveness Enhancement Program.

Conflicts of Interest

The authors declare that they have no conflicts of interest.

References

1. Abtahi, D., Kpaeyeh, J., Gold, M.: Risk stratification of sudden cardiac death: a multi-racial perspective. Int. J. Hear. Rhythm. **1**, 24–32 (2016). https://doi.org/10.4103/2352-4197.191479
2. Cardiovascular diseases statistics. EuroStat. Available at: https://ec.europa.eu/eurostat/statistics-explained/index.php/Cardiovascular_diseases_statistics#Deaths_from_cardiovascular_diseases
3. Benjamin, E.J.: Heart disease and stroke statistics—2018 update: a report from the American heart association. Circulation **137**(12), e67–e492 (2018). https://doi.org/10.1161/CIR.0000000000000558

4. Osman, J., Tan, S.C., Lee, P.Y., Low, T.Y., Jamal, R.: Sudden Cardiac Death (SCD)—risk stratification and prediction with molecular biomarkers. J. Biomed. Sci. **26**(1), 39–39 (2019) doi:10.1186/s12929-019-0535-8
5. Waks, J.W., Buxton, A.E.: Risk Strat. Sudd. Card. Death After Myocard. Infarct. **69**(1), 147–164 (2018). https://doi.org/10.1146/annurev-med-041316-090046
6. Akhtar, M., Elliott, P.M.: Risk stratification for sudden cardiac death in non-ischaemic dilated cardiomyopathy. Curr. Cardiol. Rep. **21**(12), 155 (2019). https://doi.org/10.1007/s11886-019-1236-3
7. Kober, L., et al.: Defibrillator implantation in patients with nonischemic systolic heart failure. N. Engl. J. Med. **375**(13), 1221–1230 (2016). https://doi.org/10.1056/NEJMoa1608029
8. Chugh, S.S., Uy-Evanado A.: Improved prediction of sudden cardiac death risk. Circ.: Cardiovasc. Imaging **9**(8), (2016). https://doi.org/10.1161/circimaging.116.005133
9. Lopera, G., Curtis, A.B.: Risk stratification for sudden cardiac death: current approaches and predictive value. Curr. Cardiol. Rev. **5**(1), 56–64 (2009). https://doi.org/10.2174/157340309787048130
10. Wellens, H.J.J., et al.: Risk stratification for sudden cardiac death: current status and challenges for the future. Eur. Hear. J. **35**(25), 1642–1651 (2014). https://doi.org/10.1093/eurheartj/ehu176
11. Holkeri, A., et al.: Predicting sudden cardiac death in a general population using an electrocardiographic risk score. Heart **106**(6), 427–433 (2020). https://doi.org/10.1136/heartjnl-2019-315437
12. Oehler, A., Feldman, T., Henrikson, C.A., Tereshchenko, L.G.: QRS-T angle: a review. Ann. Noninvasive Electrocardiol. **19**(6), 534–542 (2014). https://doi.org/10.1111/anec.12206
13. Liew, R.: Sudden cardiac death risk stratification—an update. Eur. Cardiol. **10**(2), 118–122 (2015). https://doi.org/10.15420/ecr.2015.10.2.118
14. Wasfy, M.M., Hutter, A.M., Weiner, R.B.: Sudden cardiac death in athletes. Methodist DeBakey Cardiovasc. J. **12**, 73–130 (2016). https://doi.org/10.14797/mdcj-12-2-76
15. Masarone, D. et al.: Risk stratification of sudden cardiac death in patients with heart failure: an update. J. Clin. Med. **7**(11), (2018). https://doi.org/10.3390/jcm7110436
16. Kurl, S., Mäkikallio, T.H., Rautaharju, P., Kiviniemi, V., Laukkanen, J.A.: Duration of qrs complex in resting electrocardiogram is a predictor of sudden cardiac death in men. Circulation **125**(21), 2588–2594 (2012). https://doi.org/10.1161/CIRCULATIONAHA.111.025577
17. Brenyo, A., Pietrasik,, G., Barsheshet, A., Huang, D., Polonsky, B., McNitt, S., Moss, A., Zareba, W.: QRS fragmentation and the risk of sudden cardiac death in MADIT II. J. Cardiovasc. Electrophysiol. **23**(12), 1343–1348 (2012). https://doi.org/10.1111/j.1540-8167.2012.02390.x
18. Take, Y., Morita, H.: Fragmented QRS: what is the meaning? Indian Pacing Electrophysiol. J. **12**(5), 213–225 (2012). https://doi.org/10.1016/S0972-6292(16)30544-7
19. Zipes, D.P., Jalife, J., Stevenson, W.G.: Cardiac electrophysiology: from cell to bedside, 7th edn. Elsiver, UK (2017)
20. Patel, S.I. et al.: QT prolongation and sudden cardiac death risk in hypertrophic cardiomyopathy. Acta Cardiol. **74**(1), 53–58 (2019). Doi:https://doi.org/10.1080/00015385.2018.1440905
21. Simson, M.B.: Use of signals in the terminal QRS complex to identify patients with ventricular tachycardia after myocardial infarction. Circulation **64**(2), 235–242 (1981). https://doi.org/10.1161/01.CIR.64.2.235
22. Stein, P.K., Kleiger, R.E., Rottman, J.N.: Differing effects of age on heart rate variability in men and women. Am. J. Cardiol. **80**(3), 302–305 (1997). https://doi.org/10.1016/S0002-9149(97)00350-0
23. Rosengarten, J.A., Scott, P.A., Morgan, J.M.: Fragmented QRS for the prediction of sudden cardiac death: a meta-analysis. EP Europace **17**(6), 969–977 (2015). https://doi.org/10.1093/europace/euu279
24. Müller, D., Agrawal, R., Arntz, H.-R.: How sudden is sudden cardiac death? Circulation **114**(11), 1146–1150 (2006). https://doi.org/10.1161/CIRCULATIONAHA.106.616318
25. Ivanov, M.L. et al.: Wearable nanosensor-based hardware and software complex for dynamic cardiac monitoring. J. Phys.: Conf. Ser. **1327**, (2019). https://doi.org/10.1088/1742-6596/1327/1/012029

26. Peter, Z., Alena, G.: Ambulatory arrhythmia monitoring. Circulation **122**(16), 1629–1636 (2010). https://doi.org/10.1161/CIRCULATIONAHA.109.925610
27. Rashkovska, A., Depolli, M., Tomašić, I., Avbelj, V., Trobec, R.: Medical-grade ECG sensor for long-term monitoring. Sensors **20**(6), (2020). https://doi.org/10.3390/s20061695
28. TelePatch CardiacMonitor PM750. Available at: https://medicompinc.com/wp-content/uploads/2017/04/TelePatch_User-_Manual.pdf
29. Rybalka, S., Yuzhakov, M., Ivanov, M., Dang Kuang N., Kodermjatov, R., Wenjia, G., Maksimov, I., Zimin, I.: Methods and approaches for automatic processing and storage of high-potential electrocardiogram registered by hardware and software complex on nanosensors. MATEC Web Conf. **155**, (2018). https://doi.org/10.1051/matecconf/201815501008
30. Giorgio, A., Rizzi, M., Guaragnella, C.: Efficient detection of ventricular late potentials on ECG signals based on wavelet denoising and SVM classification. Information **10**(11), 328 (2019). https://doi.org/10.3390/info10110328
31. Kodermyatov, R., Ivanov, M., Yuzhakov, M., Kuznetsov, V., Yuzhakova, M., Timofeeva, E.: Development of a high-resolution apparatus to monitor physiological state of a person undergoing extreme conditions. MATEC Web Conf. **48**, 05004 (2016). https://doi.org/10.1051/confmatec/20164805004
32. Escalona, O.J., Mendoza, M., Villegas, G., Navarro, C.: Real-time system for high-resolution ECG diagnosis based on 3D late potential fractal dimension estimation. Comput. Cardiol. **38**, 789–792 (2011)
33. Avdeeva, D.K., Ivanov, M.L., Yuzhakov, M.M., Turushev, N.V., Kodermiatov, R.A., Maksimov, I.V., Zimin, I.A.: Novel high-resolution nanosensor-based measuring equipment for ECG recording. Measurement **146**, 215–229 (2019). https://doi.org/10.1016/j.measurement.2019.06.023
34. Yuzhakov, M.M. et al: Research into spontaneous activity of myocardial cells under normal and pathological conditions using the hardware and software complex based on nanosensors. IOP Conf. Ser.: Mater. Sci. Eng. **457**, (2018). https://doi.org/10.1088/1757-899X/457/1/012013

Search for the Frequency of Ultrasonic Exposure to Intensify Drug Treatment of Gallstone Disease

Ekaterina Dikman, Yuliya Zyuzkova, Irina Nam, Andrey Kolomeytsev, and Anatoly Chirev

Abstract The chapter describes the search for the frequency of ultrasonic vibrations using the COMSOL Multiphysics interactive environment for the treatment of gallstone disease using a technique based on the ultrasonic intensification of drug dissolution of calculi. The found frequency is the most effective, but at the same time it does not have an excessive thermal effect on the skin surface in contact with the emitter.

1 Introduction

Currently, there is an increase in the incidence of cholelithiasis which causes the formation of stones in the gallbladder. The reasons for the increasing prevalence of the disease are malnutrition, lifestyle changes, physical inactivity, poor ecology, hereditary factors, and improved diagnosis of the disease.

The treatments available today are imperfect. They can have a lot of contraindications and postoperative complications (cholecystectomy), can be dangerous in the presence of large calculi due to the likelihood of blockage by fragments of the bile

---

E. Dikman (✉) · Y. Zyuzkova · I. Nam · A. Kolomeytsev
Division for Electronic Engineering, National Research Tomsk Polytechnic University, 30 Lenin Avenue, Tomsk, Russia 634050
e-mail: eka.dikman@gmail.com

Y. Zyuzkova
e-mail: yaz6@tpu.ru

I. Nam
e-mail: iphn@tpu.ru

A. Kolomeytsev
e-mail: aak65@tpu.ru

A. Chirev
Department of General Medicine, Siberian State Medical University, 2 Moskovsky Trakt, Tomsk, Russia 634055
e-mail: kaf.fak.hir@ssmu.ru

I. V. Minin et al. (eds.), *Progress in Material Science and Engineering*,
Studies in Systems, Decision and Control 351,
https://doi.org/10.1007/978-3-030-68103-6_21

ducts (extracorporeal shock wave lithotripsy) or require long-term treatment and significant monetary costs (drug therapy) [1–3].

Thus, another method is needed, which will be more effective and safer than all available. This method is the ultrasonic intensification of drug dissolution of gallbladder calculi. Percutaneous ultrasound exposure will accelerate the diffusion between bile with a drug containing ursodeoxycholic acid dissolved in it and cholesterol calculus [2, 3].

The purpose of this study is to select the parameters of ultrasonic exposure, namely the vibration frequency, which will be most effective, but at the same time not exert excessive thermal effects on the skin surface in contact with the emitter.

2 Gallstone Disease: Etiology and Treatment Methods

2.1 Physiology of the Gallbladder

The gallbladder is a hollow organ of the human digestive system, located in a special bed near the lower part of the right lobe of the liver and representing a thin-walled pear-shaped or conical reservoir with a volume of 30–70 ml. On average, in an adult, the length of the gallbladder is 7 cm, and the width is 3 cm.

Bile accumulates and concentrates in the gallbladder. Bile is a complex aqueous solution secreted by liver cells that has a specific odor and yellow, brown or greenish color. Consists of 80% water and 20% of substances dissolved in it (bile acids, salts, proteins, etc.). In the human body, the formation of bile and its subsequent secretion is the only way to remove certain molecules and ions.

Cholelithiasis (cholelithiasis) is a disease in which stones (calculi) form in the gallbladder, bile ducts, which prevent the free flow of bile and contribute to the development of various infectious processes [3, 4].

2.2 Pathogenesis of Gallstone Disease

In the biliary tract, two types of stone formation are distinguished: primary and secondary. Primary cholesterol stones are formed because of the precipitation of cholesterol.

Secondary stone formation, as a rule, is the result of blockage of the bile ducts during gallstone disease or scarring, which contribute to the development of an ascending infection from the lumen of the gastrointestinal tract.

2.3 Methods of Treatment of Cholelithiasis

Today there are several different types of cholelithiasis treatment, both nonsurgical and surgical.

One of the most common non-surgical methods of treating gallstones is litholytic or drug therapy. With cholesterol calculi in the gallbladder and there are contraindications to surgical treatment or the patient's refusal to operate, he is prescribed drugs containing chenodeoxycholic or ursodeoxycholic acids, the action of which is directed directly to dissolving the stones. This method of treatment has the following disadvantages: the duration of treatment (up to two years) and the inability to dissolve large stones, as well as stones present in the gallbladder in large quantities [4, 5].

Another non-surgical method is extracorporeal shock wave lithotripsy. The destruction of gallstones occurs because of exposure to a focused ultrasonic shock wave. After crushing, the fragments, the size of which allows them to freely pass through the narrow cystic duct, are independently removed from the gallbladder. Larger fragments are unable to leave the gallbladder and remain inside, which is a disadvantage of this method of treatment.

Cholecystectomy is a surgical operation to remove the gallbladder, which, despite the development of non-surgical methods, remains the main treatment for cholelithiasis. The main disadvantages of this method are the trauma of the abdominal wall, possible complications, a long recovery period, and restrictions on physical activity after surgery, and so on [4–6].

Thus, at present there is a need to use a method of treatment that combines the advantages of those already known.

3 Biological Effects of Ultrasound

Once in the human body, ultrasound affects not only the irradiated organs or tissues. The main factors of ultrasound action are mechanical, physicochemical and thermal factors.

The mechanical action of ultrasound is based on the effect of alternating acoustic pressure, as a result of which tissue micro-massage occurs at the cellular level. Under the influence of ultrasound, the conductivity of ion channels of cell membranes changes and micro flows of metabolites in the cytosol and organelles increase, and the permeability of cell and intracellular membranes increases.

Physicochemical action is due to the presence of mechanical resonance, which increases the speed of movement of molecules, enhances their decomposition into ions, changing the isoelectric state, and entails the formation of new electric fields, the appearance of free radicals and various products of sonolysis of biological solvents. In addition, under the influence of this effect, local stimulation of biochemical and physicochemical processes in tissues occurs, metabolism is activated, and the pH value of tissues changes.

The thermal effect of ultrasound is manifested in the conversion of mechanical energy into thermal energy, which increases the temperature of the tissues. The main heat is concentrated at the interface between tissues with different acoustic impedances, in the tissues that most absorb ultrasonic energy (bone, nerve), as well as in places with insufficient blood supply, since the blood removes heat during its movement.

In addition, ultrasound has the ability to destroy the cell walls of many pathogenic microorganisms. Based on this, we can conclude that ultrasound has a bactericidal effect.

Based on the above, we can say that the ultrasound effect in general has a beneficial effect on the human body and its individual parts for therapeutic and prophylactic purposes [7–9].

Any device for ultrasound therapy consists of a generator of electrical oscillations, to the oscillatory circuit of which a piezoelectric transducer is connected. The transducer is placed in a separate special knob, called the emitter, connected to the device itself by means of a cable.

For the wave to travel through the base without attenuation, its thickness must be an integer number of half-waves.

The second electrode is the knob body, to which the braided shield of the supply cable is connected.

Piezo transducers made of barium titanate ceramics are widely used in ultrasonic therapeutic devices. It is small crystals sintered at high temperatures and has a polycrystalline structure. Barium titanate is much cheaper than quartz, and has a lower voltage value required exciting ultrasonic vibrations.

Treatment is usually carried out by applying the surface of the knob to the area to be treated [9, 10].

Previous studies have shown [11], that at a frequency of 880 kHz studies (standard frequency for ultrasonic physiotherapy in Russian) ultrasound at intensities over 0.4 W/cm^2 of skin is heated to a physical model.

4 Simulation of Tissue Heating Caused by Focused Ultrasound

A model was created in COMSOL Multiphysics interactive environment to demonstrate tissue heating caused by focused ultrasound. It is necessary to register the minimum frequency at which a soft tissue burn occurs in the zone of contact with the emitter during 30 min of therapy.

When the ultrasound passes through the tissue volume, some of the energy of the primary acoustic field is absorbed locally by the tissue and converted into heat. This leads to an increase in temperature, the value of which depends on the physical properties of the medium (acoustic absorption coefficient, density and specific heat of the substance), properties of the ultrasonic device (beam geometry), as well as

Table 1 General parameters for simulation

Description	Name	Expression
Displacement amplitude of transducer	d0	0.41 μm
Initial temperature value	T0	309.75 K
Source frequency	f0	Variable
Absorption coefficient of water	alpha_water	0.025 1/m
Absorption coefficient of skin	alpha_skin	17.27 1/m
Absorption coefficient of fat	alpha_fat	4.6 1/m
Absorption coefficient of muscle	alpha_muscle	11.5 1/m

the frequency and time-averaged acoustic intensity of the acoustic field. The actual temperature rise that can occur also depends on the conductivity and convective properties of the tissue, such as the rate of blood flow in that area. When exposed for 30 min, a burn occurs at a temperature of 47 °C or 320.15 K.

This work assumes the simulation of two physical processes: acoustic pressure and heat transfer in biological tissues. In COMSOL Multiphysics, the necessary general settings have been configured (Table 1).

Further, geometric constructions of the objects under study were performed. For this, the average values of the thickness of the skin, fat layer, and muscle tissue of a person were used (Fig. 1).

It was necessary to adjust the parameters of the effect of acoustic pressure on areas of biological tissues and areas filled with water, depending on the absorption coefficient of ultrasound in these media, as well as the parameters of heat transfer in biological tissues.

Then materials were selected from the proposed library or manually created for the corresponding objects: water, skin, fat, muscle.

The next step was to generate a mesh on the object, which is necessary for modeling acoustic pressure and thermal processes. Since this work involved two physical processes with different properties, it will be necessary to build two different meshes (Figs. 2 and 3). To simulate the acoustic pressure, the mesh size had to be comparable to the ultrasound wavelength.

Calculations were performed using the above constructions. It turned out that the ultrasound frequency at which the skin surface temperature exceeded the permissible one was 950 kHz (Fig. 4). With this value and with its increase, a soft tissue burn occurs (Fig. 5).

Below are diagrams of the temperature distribution inside the object at frequencies above and below the found one. So, at a frequency of ultrasonic vibrations of 880 kHz, the maximum temperature does not reach 318 K, which indicates the safety of exposure with such parameters (Fig. 6). At a frequency of 1 MHz, the temperature

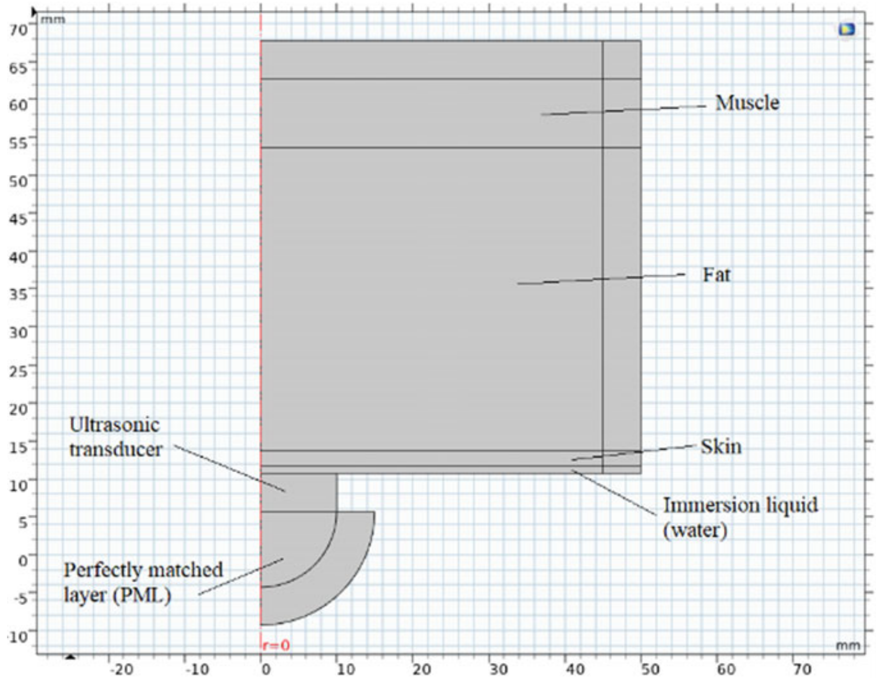

Fig. 1 Geometry of acoustic source and biological tissues

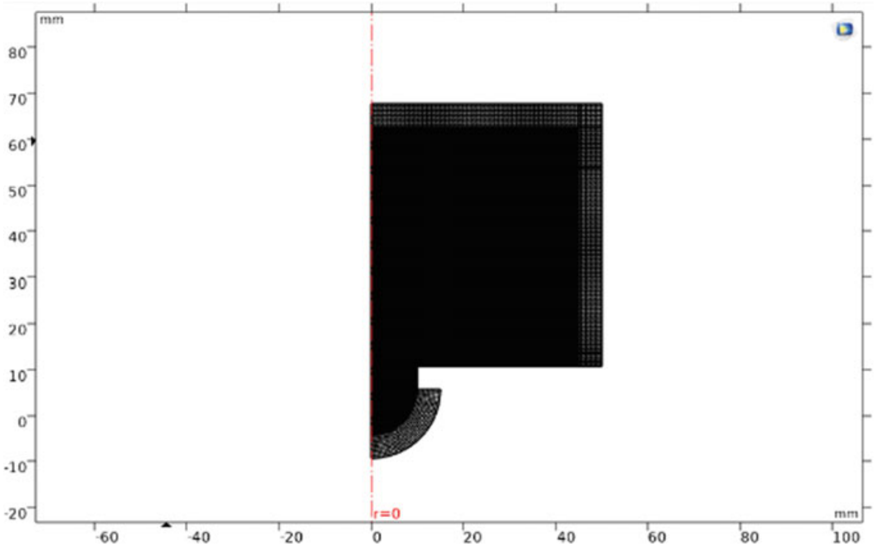

Fig. 2 Mesh for pressure acoustics simulation

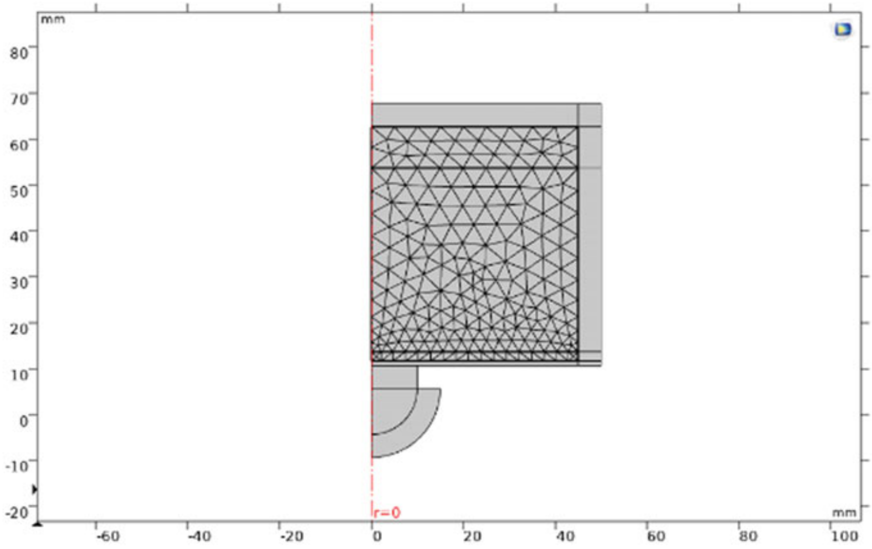

Fig. 3 Mesh for thermal simulation

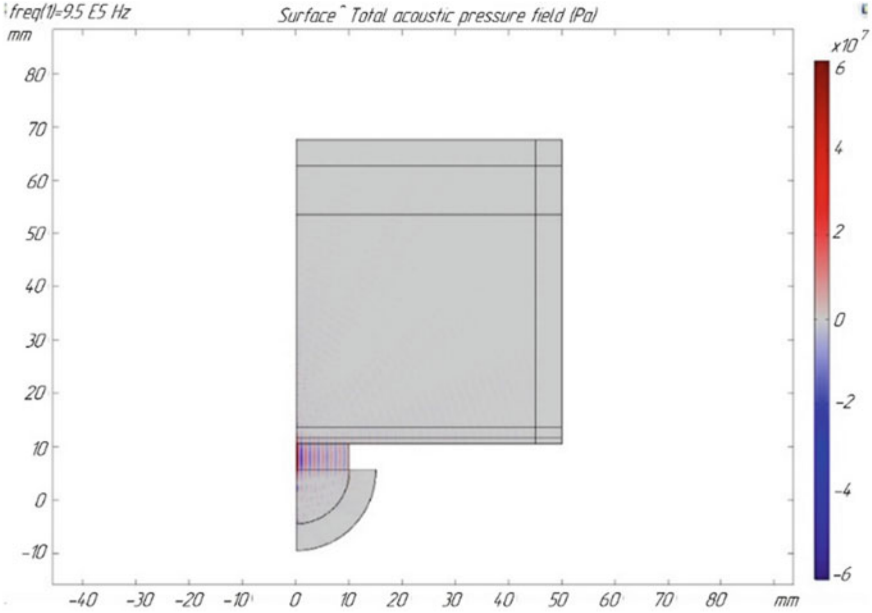

Fig. 4 The acoustic pressure field in the water and tissue domains for source frequency of 950 kHz

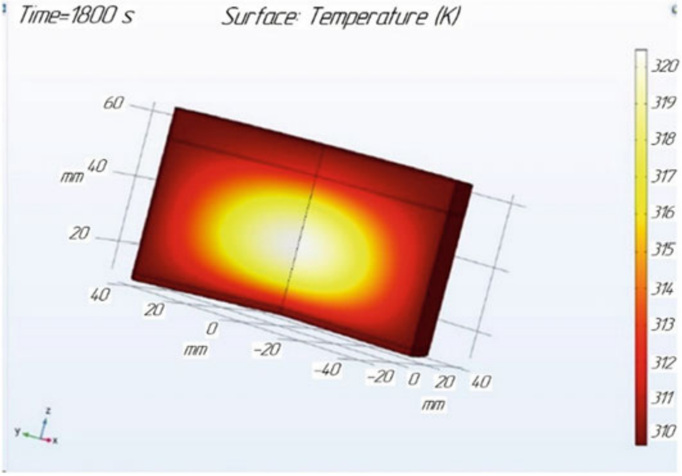

Fig. 5 Surface plot of the temperature rise in the tissue after 30 min insonation for source frequency of 950 kHz

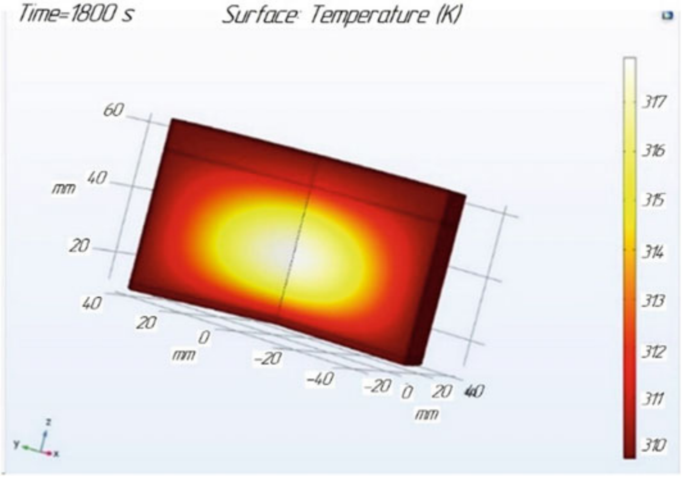

Fig. 6 Surface plot of the temperature rise in the tissue after 30 min insonation for source frequency of 880 kHz

is much higher than permissible, and, accordingly, it is dangerous to use it for these purposes (Fig. 7).

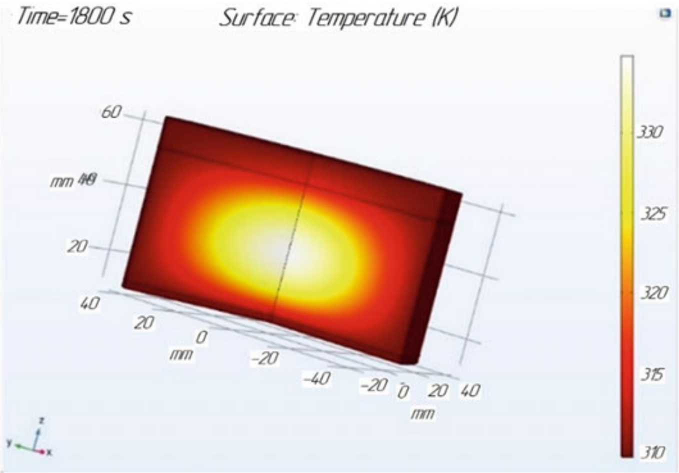

Fig. 7 Surface plot of the temperature rise in the tissue after 30 min insonation for source frequency of 1 MHz

5 Conclusion

In the course of the work, a model was created that demonstrates the heating of tissue, which is caused by exposure to focused ultrasound. The model allows two studies. First, the analysis of the propagation of acoustic pressure with the subsequent construction of its field and amplitude profile. Secondly, the heat source calculated for solving the first problem can be used in further modeling and analysis of the processes of heating and cooling of tissues of a living organism.

Such work can be carried out to reduce the risks of mechanical damage or overheating of healthy tissues when the emitter of the physiotherapeutic apparatus is applied pointwise, as well as for more accurate focusing and calculation of ultrasonic exposure, which will be necessary and sufficient to achieve the set goals.

The result of the work done was to find the frequency of ultrasound, which cannot be exceeded in order to prevent overheating and burns of the human skin. This frequency was 950 kHz. Thus, it is advisable to choose a radiator with a resonant frequency that will be less than the found one, but large enough for the ultrasonic effect to be effective.

References

1. Portincasa, P., Moschetta, A., Palasciano, G.: Cholesterol gallstone disease. Lancet **368**(9531), 230–239 (2006). https://doi.org/10.1016/S0140-6736(06)69044-2
2. Guarino, M.P., Cocca, S., Altomare, A., Emerenziani, S., Cicala, M.: Ursodeoxycholic acid therapy in gallbladder disease, a story not yet completed. World J. Gastroenterol. **19**(31), 5029–5034 (2013). https://doi.org/10.3748/wjg.v19.i31.5029

3. Jones, M.W., Genova, R., O'Rourke, M.C.: Acute Cholecystitis. In: StatPearls [Internet]. Treasure Island (FL): StatPearls Publishing; 2020 January. Available from: https://www.ncbi.nlm.nih.gov/books/NBK459171/
4. Portincasa, P., Ciaula, A.D., Bonfrate, L., Wang, D.Q.: Therapy of gallstone disease: what it was, what it is, what it will be. World J. Gastrointest. Pharmacol. Ther. **3**(2), 7–20 (2012). https://doi.org/10.4292/wjgpt.v3.i2.7
5. Keus, F., De Jong, J.A., Gooszen, H.G., Van Laarhoven, C.J.H.M.: Laparoscopic versus open cholecystectomy for patients with symptomatic cholecystolithiasis. Cochrane Database Syst. Rev., CD00623 (2006). https://doi.org/10.1002/14651858.cd006231
6. Wang, T., Luo, H., Yan, H.T., Zhang, G.H., Liu, W.H., Tang, L.J.: Risk factors for gallbladder contractility after cholecystolithotomy in elderly high-risk surgical patients. Clin. Interv. Aging **12**, 129–136 (2017). https://doi.org/10.2147/CIA.S125139
7. Vel'sher, L.Z., Podkolzin, A.A., Stakhanov, M.L., Gorchak, YuYu., Zharov, V.P., Menyaev, YuA, Zmievskoi, G.N., Rozhdestvin, V.N.: A combined method for wound treatment based on exposure to low-intensity radiation and ultrasound. Biomed. Eng. **37**(5), 262–267 (2003). https://doi.org/10.1023/B:BIEN.0000012493.24634.03
8. Izadifar, Z., Babyn, P., Chapman, D.: Mechanical and biological effects of ultrasound: a review of present knowledge. Ultrasound Med. & Biol. **43**(6), 1085–1104 (2017). https://doi.org/10.1016/j.ultrasmedbio.2017.01.023
9. Snehota, M., Vachutka, J., Haar, G., Dolezal, L., Kolarova, H.: Therapeutic ultrasound experiments in vitro: review of factors influencing outcomes and reproducibility. Ultrason. **107**, 106167 (2020). https://doi.org/10.1016/j.ultras.2020.106167
10. Novikov, A.A., Klyuev, V.I., Reznik, L.B.: New high-amplitude ultrasonic apparatuses with adaptive systems for therapy and surgery. Biomed. Eng. **41**(4), 205–206 (2007). https://doi.org/10.1007/s10527-007-0046-x
11. Dikman, E., Soldatov, A., Chirev, A.: The study of the possibility of drug dissolution of gallbladder calculi. Sens. Rev. **40**(3), 363–366 (2020). https://doi.org/10.1108/SR-12-2019-0301

Engineering of Humic Acids in Biostimulants of Plant Growths

Olga Tchaikovskaya, Vlada Chaidonova, Natalya Yudina, and Inna Plotnikova

Abstract The generalization of literature data and the results of our scientific research over many years has led to the conclusion that physicochemical effects on natural organic materials can be key in the manifestation of their biological activity to reduce the toxicity of pollutants in the environment and improve plant growth. The bioactive properties of humic substances were studied using luminol-dependent luminescence and bioluminescence. It was shown that humic substances have the highest physiological activity for germination of wheat seeds at the concentration of 0.01 g/l. Possible to reduce the concentration of humic substances by the mechanoactivation or the UV-irradiation. The results of this work are promising for the development of approaches for the biological recultivation of polluted or depleted lands using humic preparations isolated from peat. The evaluation of morpho-physiological responses of wheat and the enzyme activity of a soil in presence of an irradiated humic acids were discussed.

1 Introduction

The relevance of the study is because of the conservation of biological resources, their rational and careful use. The development of the efficient technologies will provide the growing population of the globe with food and environmentally friendly

---

O. Tchaikovskaya · V. Chaidonova
Department of Physics, Tomsk State University, 36 Lenin Avenue, Tomsk, Russia 634050
e-mail: tchon@phys.tsu.ru

N. Yudina
Laboratory of Oil Rheology, Institute of Petroleum Chemistry of the Siberian Branch of the Russian Academy of Sciences, 3 Academichesky Avenue, Tomsk, Russia 634021
e-mail: natal@ipc.tsc.ru

I. Plotnikova (✉)
Department of Control and Diagnostics, National Research Tomsk Polytechnic University, 30 Lenin Avenue, Tomsk, Russia 634050
e-mail: inna@tpu.ru

I. V. Minin et al. (eds.), *Progress in Material Science and Engineering*,
Studies in Systems, Decision and Control 351,
https://doi.org/10.1007/978-3-030-68103-6_22

products. At the beginning of 2010, Russia was on the 3rd place in the world in grain exports (after the United States and the European Union) and on the 4th place in the world in wheat exports (after the United States, European Union and Canada). However, in the world there is a problem of depletion and pollution of soils due to agricultural activity. Therefore, there is the task of improving the quality of fertile land without the use of chemical reagents.

Humic substances (HS) are a natural organic compound, is a product that is formed during the decomposition of plant and animal residues under the action of microorganisms and abiotic environmental factors. It is necessary to note that HS can absorb light and transfer light energy to other components of aqueous solutions, inducing the transformation of contaminating molecules [1–5].

HS and their most important constituent—humic acids (HA)—are natural organic formations widely distributed in soils and peats, in coals and shales, in marine and lake sediments, in the waters of rivers and mineral springs. Recently, in connection with the widespread prevalence of humic substances in the biosphere, their importance in plant life, the question arose of studying the antioxidant activity of these compounds. The degree of antioxidant activity of a substance is largely determined by its ability to bind free radicals, that is, antiradical activity [6].

Scientists all over the world are currently engaged in unraveling the mechanism of the effect of humic substances on natural processes and searching for ways to positively influence humic fertilizers on crop growth. The authors [7–11] indicate that the amino acid or humic acid component of organic fertilizers is the main effective component in their stimulating effect on the growth and quality of plants. The authors [12] studied the effect of biostimulants of various origins on enhancing the formation of roots, cuttings and plant growth. It was found that fertilizers of plant origin, in comparison with synthetic ones, increase plant growth and do not change their genotypes. The size of the dissolved HA molecules affects the quality of drinking water. In addition, HA interact easily in water with substances of inorganic nature. Using the luminescence decay method, the researchers [13] studied the Eu (III) complexes with fulvic acids. The results showed that the quenching mechanism depends on the ionic strength, which determines the complex formation and the fate of Eu (III) in natural waters containing humic substances. Observations have shown that interaction at short distances leads to the complexation of Eu (III) with fulvic acids. Along with this, there may be interaction at a further distance, which leads to repulsion between Eu (III) and fulvic acids. These interactions can affect the overall mechanism of plant nutrient absorption.

Phenol derivatives and herbicides are one of the largest groups of environmental pollutants due to their presence in many industrial effluents. A number of species of microorganisms possess enzymatic systems that are applicable to the decomposition of various aliphatic and aromatic toxic compounds [14–17]. Studies [18] were aimed at studying the effect of humic acids on the efficiency of degradation by microbial types of phenolic compounds and herbicides in water. The potential environmental significance of such studies is shown.

The purpose of this work was to study the effect of modification of humic acids to improve the growth of wheat using humic fertilizers.

2 Experimental

2.1 Humic Acid

2.1.1 Nature of Humic Acids

Humic substances [19] are widely distributed in nature and are one of the main organic components of soil, water, coal, peat, sapropel. Soil humic substances occur after chemical and biological decomposition of plant and animal residues by microorganisms. The resulting products have a complex chemical structure that is more stable than the starting materials. Humic substances are not a well-defined class of organic compounds. Their differences are based on differences in solubility in aqueous solutions at different pH levels. The main humic fractions are humic acid, fulvic acid and humin [20]. They contribute to soil fertility—a fact that has been recognized since ancient times. Although humic acids are strongly associated with soils and are resistant to microbial metabolism and, therefore, have a very long half-life in soils, they are depleted from soils as a result of wind and water erosion and leaching with water [21]. Therefore, it is important to replenish them in order to preserve or improve the fertility of the soil.

As humic acids were studied from 1786 (when they were first extracted by Archard from peatlands in Germany [22]), their importance became clearer. They are not only important for soil fertility, but are also precursors of kerogen, peat, asphalt, bitumen, oil and coal. They affect the agricultural environment, forming complexes with metals and organic matter that can change the toxicity of heavy metals [23], pesticides and herbicides.

For many decades, it was believed that humic acids are formed in soils as a result of microbial conversion of plant lignins. However, before the 1980s there were no experimental results confirming that humic acids were probably formed before the plant matter reached the soil, despite the fact that they were isolated and realized their importance as early as 1786 in Germany. A serious omission and leading to a poor understanding of how the content of humic acids in soils can be maintained or increased for optimal fertility. However, in the study [19] using fluorescence spectrophotometry, it was demonstrated that humic acids are formed in an aging plant and algal substance before they reach the soil, where they are then firmly bound to it and also become resistant to the metabolism of microorganisms. Humic acids are removed from the soil by wind and water erosion, as well as leaching with water, which means that the reserves in the soil should be regularly replenished. As previously [1], it was shown that the soil can be replenished or enriched with humic acids by processing plant and algal substances or by adding external sources of decomposed vegetable or algal substances, such as composts, mulch, peat and brown coal [19].

In addition to this problem, for 200 years of research of humic substances, their chemical nature is still not clear and the (bio) chemistry of formation of these substances is one of the least studied aspects of the chemistry of humus and one of the most interesting. In the study [20] it was shown that:

(1) Humic acids can be formed as a result of various chemical and biochemical processes involving many high and low molecular weight plant components.
(2) The role of lignin in the formation of humic substances seems overvalued. Lignin and degraded lignins may be co-extracted with humic acids or may be associated with humic acids, but they do not make a significant contribution to the resistant part of humic acids.
(3) Other more resistant plant components, such as the highly aliphatic biopolymer present in the cuticles of plants and suberin, can represent important components of the structure of humic acid.

During the past 150 years, the structures of natural organic compounds have generally been clarified over the decades after their discovery. The situation with humic acids, by contrast, was completely different [24]. Even in the mid-1980s, there were disputes on such basic issues as whether humic acids are predominantly aliphatic or aromatic [25]. From the late 1800s, and especially from the 1920s, it is generally accepted that humic acids are formed as a result of the microbial conversion of plant lignins in the soil.

In 1797, humic acids were extracted from plant matter [26], but, apparently, there is no other such message until 1987 [27], when it was done by chance. In 1989 [28] and 1991, we first reported that humic acids are present in an aging plant and algal substance, which means that they enter the soil before any suspected microbial transformation of plant lignins. Since then, similar results have been obtained [29, 30]. More recently [31] humic acids have been isolated from maize plants at different stages of maturity, and it was concluded that humic acids originate from the preservation of plant tissue.

2.1.2 Humic Acids Samples

The objects of investigation is humic acids (HA) isolated from the upper sphagnum high bogpeat by extraction with 0.1 N NaOH solution. Has have been purified according to the protocol of the International Humic Substances Society. The concentration of HA in solutions was 1 mg/l at pH = 10–11. For comparison, a commercial preparation of the Aldrich HA was used too. To study the chemiluminescence, 0.1 ml of a solution of luminol (0.003 M) was selected in the presence of NaOH (0.3 M). Oxidation was carried out in a buffer medium (sodium tetraborate). The volume of the added buffer was 2.88 ml. The test solution had pH = 11. After thorough mixing, the quartz cuvette (l = 1 cm) with the resulting solution was placed in a cuvette compartment with a thermostat (T = 25 °C). To accelerate the reaction, a catalyst was introduced into the system—10 µl of phthalocyanine from a solution with a concentration of 0.5 g/l. Then hydrogen peroxide (10 µl from a solution with a concentration of 0.1 M) was introduced into the system. After that, add 10 µl of HA from the solution with a concentration of 0.01 g/l to the cuvette. The spectra of the chemiluminescence of luminol, the kinetics of the reaction at a wavelength of 425 nm before and after the addition of HA were obtained. The spectra were recorded using a standard technique on the scanning spectrofluorimeter Cary Eclipse (Varian).

2.2 UV-Irradiation

Irradiation of 50 ml of a solution of 0.01 g/l HA was carried out in a beaker for 2–32 min with constant stirring on a magnetic stirrer. The distance from the lamp to the solution was h = 8.5 cm. As sources of UV radiation for photochemical transformation, we used a pulsed U-type barrier discharge excilamps with working KrCl (the wavelength of irradiation: λ_{rad} ~ 222 nm) molecules: parameters were $\Delta\lambda = 5$ nm, peak power density 18 mW/cm^2, average radiation power of 1.6 kW, $f = 200$ kHz, and pulse duration 1 μs. The incident light intensity at 222 nm was at 2×10^{15} photons $\times$ cm^{-2} $\times$ s^{-1}. The intensity values exclude the possibility of multiphoton processes and photoionization in the studied systems [32–35].

It is necessary to note that HA can absorb light and transfer light energy to other components of aqueous solutions, inducing the transformation of contaminating molecules [36]. It was found that HA can act as photosensitizers when irradiated with light with wavelengths greater than 290 nm [37]; HA able to produce reactive oxygen species after irradiation and photoinduce the transformation of pesticides. At the same time, there are conflicting data on the interactions of HA and organic ecotoxicants in the process of photolysis of complex solutions of pollutants [38]. Thus, it is reported that, under the action of UV irradiation (λirr = 313 nm), with the addition of HA, the phototransformation efficiency of para-cresol varies only slightly. At the same time, under the action of sunlight in the presence of HA, the efficiency of photolysis increases dramatically. There are facts that indicate that HA can act as inhibitors of photoreactions: it is necessary to note that under the action of UV irradiation in the presence of HA, the quantum yield of phototransformation of benzopyrene, quinoline and benzoquinoline decreases [39–41].

2.3 Chemiluminescence Spectroscopy

To establish the role of HA in the oxidative process, chemiluminescence of luminol was chosen, the luminescence of which is associated with the formation and transformation of free radicals and redox processes [37]. The sensitivity of this method allows it to be used to determine the formation and consumption of free radicals. The method is not directly determining the concentration of radicals, but the reaction rate at which they are formed. The intensity of chemiluminescence is proportional to the rate of formation of radicals. The matrix solutions of HA with a concentration of 1 g/L were prepared by mixing a sample of a dry preparation with a calculated volume of 0.1 N NaOH solution. The solutions under test were prepared from matrix solutions by diluting with water to 0.01 g/L.

The antiradical activity of HA before and after irradiation was analyzed in the chemiluminescence reaction of luminol on a Cary Eclipse spectrofluorometer (Varian, Australia) in the Chemiluminescence and Kinetics modes. Luminol solutions (Aldrich company) prepared from a dry sample in a solution of alkali 0.1 n. NaOH. To 0.1 ml of luminol (C = 0.003 m.) Was added 2.87 ml of a buffer solution of 0.01 m of sodium tetraborate (pH = 9.18) and 10 μl of phthalocyanine (C = 0.5 gl -1) as a catalyst for the reaction. After thorough mixing, the quartz cuvette (l = 1 cm) with the solution was placed in the cuvette compartment of the device with a thermostat (t = 25 °C). Then, 10 μl of hydrogen peroxide from a solution with a concentration of 0.1 m was added to the system, kept for 1 min, and then 10 μl of HA from a solution with a concentration of 0.01 gl -1 was added to the cuvette. The total volume of the test solution remained constant and was 3 ml. Chemiluminescence spectra and the dependence of luminol luminescence on time at a wavelength of 425 nm in the presence of HA before and after irradiation were obtained.

2.4 Biotesting of Humic Acids

The physiological activity of humic fertilizers was assessed by their influence on the germination readiness (percentage of germinated seeds for 3–4 days) of wheat of the non-genetically modified Samurai variety, its root length, wheatgrass height, and its biomass using a standard technique described in [41]. The change in soil fertility under the action of HA was studied by the example of enzymatic activity of universal neutral soil. The soil catalase activity was determined by the gasometric method. Polyphenoloxidase, peroxidase, and urease activity of soil were determined by photocolorimetric methods. Statistical processing of data based on the results of 3 sets of experiments with 3 replicates was carried out using standard methods.

Catalase activity was determined by the gasometric method by the volume of released oxygen. This method based on measuring the rate of decomposition of hydrogen peroxide when interacting with the soil. The amount of released oxygen is fixed for 1 min at a temperature of 18–20 °C (unit: ml of oxygen per 1 g of soil).

Peroxidase activity was determined by the formation of purpurogallin by the photocolorimetric method at a wavelength of 508 nm. After incubation, the extract of the soil filtrate was mixed with a freshly prepared 1% pyrogallol solution and 0.5% hydrogen peroxide solution (unit: mg of purpurogallin per 100 g of soil).

The activity of the polyphenol oxidase action was determined by the formation of purpurogallin from pyrogallol, in the same way as the peroxidase activity, but without the addition of hydrogen peroxide (unit: mg of purpurogallin per 100 g of soil.

Urease activity was determined as follows. A sample of the extract obtained from 2 g of soil was mixed with a solution of phosphate buffer with a volume of 5 ml and 10% urea solution with a volume of 5 ml. Then the sample was incubated for 3 h.

After that, the sample was centrifuged with potassium chloride. Urease activity was determined by optical density on a spectrophotometer at a wavelength of 480 nm. Urease activity is expressed in units of measurement: mg NH_3 per 1 g of soil per 1 h.

2.5 Bioluminescence Measurements

To assess the toxicity of aqueous solutions it is customary to use biological tests. As biotests, lower organisms are commonly used - bacteria, algae, crustaceans, etc. In the course of biotesting, some physiological function of the organism is being monitored (lifetime, mobility, etc.). The results of biotesting are characterized by integrity and non-specificity: the impact of all chemical compounds present in the test solution is taken into account, usually not additively, in changing only one function of the test organism. It is believed that the results of toxicity monitoring using simple organisms can be extrapolated to complex organisms, including humans.

The most convenient and promising are biotests based on marine luminescent bacteria [37]. Luminescence intensity used as a physiological function in bioluminescent tests. These biotests are characterized by a high speed of analysis (1–3 min), good sensitivity, and the possibility of instrumental registration and quantitative assessment of toxicity [37]. Therefore, in this work, we consider it expedient to use a bioluminescent bioassay to monitor the toxicity of solutions subjected to UV irradiation and treatment with humic acids.

The toxicity of solutions was evaluated using a bioluminescent biotest Microbiosensor 677F based on the lyophilized luminescent bacteria Photobacterium phosphoreum, produced at the Institute of Biophysics of the Siberian Branch of the Russian Academy of Sciences (Krasnoyarsk, Russia) [36]. The method of determining toxicity is based on the suppression of the luminescence function of marine luminous bacteria. The analysis uses 109 microbial cells, which guarantees the averaged statistically significant toxicity assessment.

An important advantage of a bioluminescent sensor is the ability to quantify organic substances dissolved in water by the magnitude of the change in the level of emission. Bioluminescent measurements were performed on a chemiluminometer (Angstrom, Novosibirsk, Russia), which consists of a cooled photomultiplier with an amplifier controlled from a personal computer and a thermally stabilized eight-position cuvette compartment and allows measuring the total radiation intensity in the range of 400–700 nm in counting mode photons. In the control experiment, the intensity of bioluminescence was compared with the intensity of bioluminescence in the presence of phenol at a concentration of $C = 4 \times 10^{-5}$ M. The toxicity of the solutions was estimated by the bioluminescent index $B = I/I0$, where I0 is the intensity of bioluminescence of the control sample, I is the intensity of bioluminescence of bacteria in the solution with toxic compound or after UV irradiation. The degree of detoxification of solutions after exposure was characterized by the detoxification coefficient: $K = Beff/B0$, where B0 is the value of the bioluminescent index of the solution with the toxicant; Beff—the maximum value of the bioluminescent index of the solution when HA is added, or under the action of UV irradiation.

2.6 Mechanoactivation

Samples of peats were mechanically activated in a planetary mill in the presence of 8 wt% of solid sodium hydroxide as follows: the rotational speed of the drums was 1820 rpm and the centrifugal acceleration was 600 m/s^2. The grinding bodies were 8–10 mm diameter Grade SHKH 15 steel balls. The weight of one drum charge with grinding balls was 0.2–0.5 kg, the sample weight was 15–20 g, and treatment time was 2 min. Shock-shear action was accompanied by grinding and disordering of sample structure, which facilitates the subsequent extraction of HA [42].

3 Results and Discussions

3.1 Chemiluminescence Analysis

The intensity of chemiluminescence decreases (Fig. 1) noteworthily in the presence of unirradiated HA, and decreases by more than 6 times when the HA is irradiated for 32 min. This may be due to the formation under the action of ultraviolet free radicals of HA, which contribute to quenching the chemiluminescence reaction of luminol.

From the dependence of the intensity of chemiluminescence on the irradiation time, it was found that the luminescence emission time is maximal upon addition of HA irradiated for 8 min (Table 1). The general form of the luminescence kinetics corresponds to the exponential law. The luminescense decay of luminescence in the

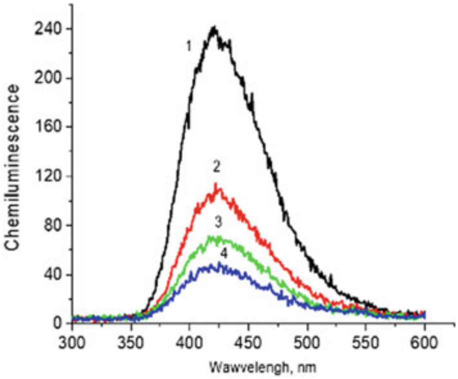

Fig. 1 Spectra of chemiluminescence of luminol (1): 2—in the presence of unirradiatedHA; 3—in the presence of HA, irradiated for 2 min, 4—in the presence of HA, irradiated for 32 min

Table 1 Dependence of the time of chemiluminescence of luminol on the composition of the reaction mixture and UV irradiation of a KrCl excilamp

No	Solution	Reaction time, min
1	luminol	0.96
2	luminol + HA without irradiation	2.43
3	luminol + HA after mechanoactivation	3.0
4	luminol + HA irradiated for 2 min	3.18
5	luminol + HA irradiated for 8 min	6.18

presence of irradiated humic acids can be divided into two components-a fast one (up to 1 s) and a slow one (up to several minutes). According to the results of the work, it can be concluded that the intermediate products of photo-oxidation of humic acids of molecular nature are the source of extinguishers of chemiluminescence of luminol.

The obtained quantitative characteristics can be used to develop methods for monitoring the peroxide oxidation of pollutants in water and detailing the mechanisms of their phototransformation in the presence of HA, which will be the subject of further research.

3.2 *Bioluminescent Analysis*

Bioluminescent monitoring of water toxicity showed (Table 2) that UV irradiation of water changes the level of toxicity. The aqueous solution after UV treatment for 32 min almost completely inhibits the bioluminescence of bacteria: K = 0.1. The addition of humic acids to water after UV irradiation with a KrCl excilamp at a concentration of 0.01 g/l reduces the toxicity level after this exposure several times (K = 0.8). Mechanoactivation of humic acids does not affect the bioluminescent level of toxicity.

Table 2 Bioluminescent index and level of toxicity of aqueous solutions containing humic acids (C = 0.01 g/l) excited by various sources

No	Radiation source, exposure time	Solution	K	Toxicity level
1	No	Water	1	Non-toxic
2	No	HA	1	Non-toxic
3	No	Phenol	0.15	Extra-toxic
4	KrCl excilamp, 2 min	Water	0.45	Medium
5	KrCl excilamp, 2 min	HA	0.95	Non-toxic
6	mechanoactivation	HA	1	Non-toxic

The bioluminescent index and the level of toxicity of the bioluminescence of bacteria in the water and water + HA systems after activation. The results showed that the addition of HA does not affect the level of toxicity of water (Table 2, No. 1–3). However, a shift in the bioluminescence maximum from 470 nm to 490 nm was observed with the addition of HA to water. It is known that the blue fluorescent protein (lumasin-protein), always present in luminescent bacteria, is responsible for bioluminescence with a maximum at 470 nm, while the chromophore associated with the enzyme of the bioluminescent reaction, luciferase, corresponds to the maximum emission at 490 nm. Most likely, the addition of the Ledger displaces metabolic processes in bacteria and leads to a change in the emitter. UV irradiation of water leads to an increase in the level of toxicity (Table 2, No. 4). Addition of irradiated HA does not lead to an increase in water toxicity (Table 2, No. 5), as well as preliminary mechanoactivation of the HA (Table 2, No. 6) behaves.

3.3 Biotesting of Humic Acids

The results of biotestingof HA with germination of wheat seeds are shown in Figs. 2 and 3. The greatest physiological activity of HA was manifested at a concentration in the solution of 0.01 g/l: the energy of seed germination was activated, the green mass and root mass increased. An increase in the concentration of HA in the solution causes their aggregation and, obviously, decreases the physiological activity. The maximum physiological activity of HA after mechanoactivation is noted at a lower concentration of 0.005 g/l.

The creation of soil fertility is unthinkable without the participation of microorganisms. Microorganisms process organic and mineral compounds, continuously synthesizing new metabolic products. Among them—enzymes, vitamins, amino acids, auxins and chelates [43], which play a significant role in the processes of

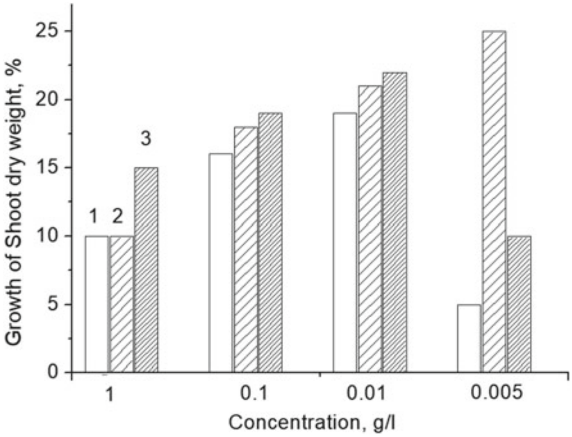

Fig. 2 Results of biotesting of humic acids obtained for germination of wheat seeds: 1—HA, 2—mechanoactivated HA, 3—HA after 2 min exposure of KrClexcilamp irradiation

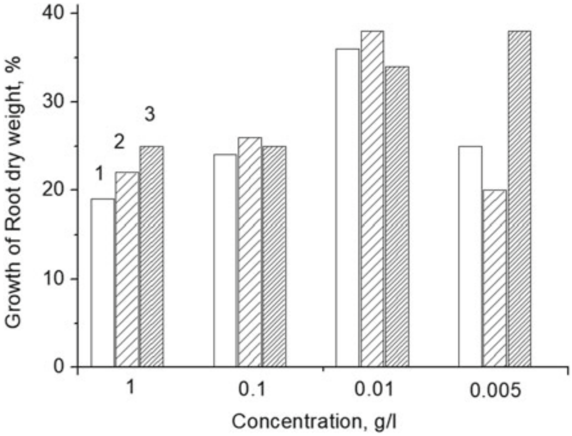

Fig. 3 Results of biotesting of humic acids obtained for germination of wheat seeds: 1—HA, 2—mechanoactivated HA, 3—HA after 2 min exposure of KrClexcilamp irradiation

increasing soil fertility and plant nutrition. An important indicator of soil fertility is enzymatic activity. Catalase plays a significant role in the oxygen balance of the soil. The main oxidoreductases that catalyze the process of humus formation are polyphenol oxidase and peroxidase. The activity of urease is an important indicator of the intensity of soil nitrogen mobilization processes.

With the use of HA, the activity of all the enzymes studied increases by 1.5–2.5 times in comparison with the control at the end of the experiment. The greatest effect was on HA after mechanical activation and UV irradiation (Table 3).

Table 3 Effect of humic acids on the enzymatic activity of the soil

Sample of soil	Enzyme activity			
	Catalase, ml O2/(g soil per min.)	Polyphenoloxidase, mg quinone	Peroxidase, mg quinone	Urease, mg NH3
Soil (S)	0.4 ± 0.1	0.12 ± 0.01	0.21 ± 0.02	0.29 ± 0.02
After 20 days				
S + H2O	0.8 ± 0.2	0.17 ± 0.02	0.26 ± 0.01	0.37 ± 0.01
S + HA[a]	2.1 ± 0.2	0.29 ± 0.01	0.39 ± 0.04	0.55 ± 0.02
S + HA (C = 5 mg/L) after MA[b]	2.6 ± 0.2	0.40 ± 0.02	0.49 ± 0.03	0.81 ± 0.04
S + HA after UV-irradiation for 2 min	3 ± 0.2	0.35 ± 0.02	0.39 ± 0.03	0.71 ± 0.04

[a] Concentration of HA C = 0.01 g/l
[b] MA – mechanoactivation

Humic preparations are characterized by a certain physiological effect, which increases the overall unspecific resistance of plants, which enhances growth, especially of the root system, and then of the aboveground mass. The functional groups –COOH and –OH in the structure of HA have a protonophore effect and are stimulators of plant growth and respiration. The entry of HA into the intracellular space of plants is associated with their adsorption and transformation on the surface of the roots. Consequently, macrostructural properties of HA and physiological activity are interrelated values.

4 Conclusion

Analysis of the obtained results showed that when plants are treated with a solution of humic acids, it is possible to induce immunity in plants; Since seed treatment causes biochemical changes in tissues. Treatment preserves the level of peroxidase in seedlings at a sufficiently high level, which allows the plant to protect itself from diseases at the stage of development, when immunity is lowered. And a solution of humic acids from peat can be a new form of biological plant protection. The restoration of depleted or contaminated soils with substances of natural origin leads to the resistance of plants to diseases and pests and determines high yields of crops and its stability. The development of ways to effectively solve this problem is of great economic importance. Humic acid-based fertilizers can effectively improve nutrient absorption and plant use. The use of humic fertilizers in the form of an aqueous solution by foliar application ensures the best performance of wheat plants. It is possible to improve wheat productivity compared to a decrease in fertilizer in terms of most growth characteristics, yield and grain quality, if irradiated or mechanically activated humic acids are used in fertilizers.

Acknowledgements Work was supported by the Tomsk state university academic D. I. Mendeleev fund programme (project number 8.1.20.2018) and The Tomsk State University competitiveness improvement programme.

References

1. Merényi, G., Lind, J.: Role of a peroxide intermediate in the chemiluminescence of luminol. A mechanistic study. J. Am. Chem. Soc. **102**(18), 5830–5835 (1980). https://doi.org/10.1021/ja00538a022
2. Merényi, G., Lind, J.: Luminol chemiluminescence: chemistry, excitation, emitter. Luminescence **5**(1), 53–56 (1990). https://doi.org/10.1002/bio.1170050111
3. Bastos, E.L., Romoff, P., Eckert, C.R., Baader, W.J.: Evaluation of antiradical capacity by H_2O_2-hemin-induced luminol chemiluminescence. J. Agric. Food Chem. **51**, 7481–7488 (2003). https://doi.org/10.1021/jf0345189

4. Kubo, H., Toriba, A.: Chemiluminescence flow injection analysis of reducing agents based on the luminol reaction. Anal. Chim. Acta **353**(2–3), 345–349 (1997). https://doi.org/10.1016/s0003-2670(97)87796-3
5. Popov, I., Lewin, G.: Photochemiluminescent detection of antiradical activity. VI. Antioxidant characteristics of human blood plasma, low-density lipoprotein, serum albumin and amino acids during in vitrooxidation. Luminescence **14**(3), 169–174 (1999). https://doi.org/10.1002/(sici)1522-7243(199905/06)14:3%3c169::aid-bio539%3e3.0.co;2-k
6. Kudryasheva, N.S., Nemtseva, E.V., Sizykh, A.G., Kratasyuk, V.A., Visser, A.J.W.G.: Estimation of energy of the upper electron-excited states of the bacterial bioluminescent emitter. J. Photochem. Photobiol. B: Biol. **68**(2–3), 88–92 (2002). https://doi.org/10.1016/s1011-1344(02)00360-3
7. Peymaninia, Y., Valizadeh, M., Shahryari, R., Ahmadizadeh, M.: Evolution on morpho-physiological responses of wheat genotypes against drought stress in presence of a leonardite derived humic fertilizer under greenhouse condition. J. Anim. Plant Sci. **22**(4), 1142–1149 (2012)
8. Albiach, R., Canet, R., Pomares, F., Indelmo, F.: Organic matter components, aggregate stability and biological activity in a horticulture soil fertilized with different rate of two sewage sludges during ten years. Biores. Technol. **77**, 109–114 (2001). https://doi.org/10.1016/s0960-8524(00)00166-8
9. Molasadeghi, V., Shahryari, R.: Grouping bread wheat genotypes under terminal drought in the presence of humic fertilizer by use of multivariate statistical analysis. Adv. American-Eurasia J. Agric. Environ. Sci. **5**(3), 510–515 (2011)
10. Molasadeghi, V., Valizadeh, M., Shahryari, R., Imani, A.: Evalution og drought tolerance of wheat genotypes using stress tolerance indices at presence of potassium humate. Adv. American-Eurasia J. Agric. Environ. Sci. **10**(2), 151–156 (2011)
11. Peoa-Mendez, E., Havel, J., Patocka, J.: Humic substances compounds of still unknown structure: applications in agriculture, industry, environment, and biomedicine. J. Appl. Biomed. **3**, 12–13 (2005)
12. Monder, M.J., Kozakiewicz, P., Jankowska, A.: Anatomical structure changes in stem cuttings of rambler roses induced with plant origin preparations. Sci. Hortic. **255**, 242–254 (2019). https://doi.org/10.1016/j.scienta.2019.05.034
13. Kouhail, Y., Benedetti, M., Reiller, P.: Eu(III)–Fulvic acid complexation: evidence of fulvic acid concentration dependent interactions by time-resolved luminescence spectroscopy. Environ. Sci. Technol. **50**(7), 3706–3713 (2016). https://doi.org/10.1021/acs.est.5b05456
14. Gómez, M., Murcia, M.D., Gomez, E., Ortega, S., Sanchez, A., Tchaikovskaya, O.N., Bryantseva, N.G.: Modelling and experimental checking of the influence of substrate concentration on the first order kinetic constant in photo-processes. J. Environ. Manag.**183**(3), 818–825 (2016). https://doi.org/10.1016/j.jenvman.2016.09.033
15. Tchaikovskaya, O., Karetnikova, E., Sokolova, I., Mayer, G., Shvornev, D.: The phototransformation of 4-chloro-2-methylphenoxyacetic acid under KrCl and XeBr excilamps irradiation in water. J. Photochem. Photobiol. A: Chem. **228**(1), 8–14 (2012). https://doi.org/10.1016/j.jphotochem.2011.11.004
16. Tchaikovskaya, O., Karetnikova, E., Murcia, M.D., Gomez, M., Gomez, J.L.: Photodegradation of 2-methyl-4-chlorophenol in a KrCl exciplex flow-through photoreactor: a kinetic study. Desalinat. and Water Treat. **54**, 1862–1871 (2015). https://doi.org/10.1080/19443994.2014.891079
17. Hidalgo, A.M., Murcia, M.D., Gómez, M., Gómez, E., García-Izquierdo, C., Solano, C.: Possible uses for sludge from drinking water treatment plants. J. Environ. Eng. **143**(3), 777–780 (2017). https://doi.org/10.1061/(asce)ee.1943-7870.0001176
18. Nechaev, L., Tchaikovskaya, O.N., Sokolova, I.V., Savel'eva, A.V., Yudina, N.V., Mal'tseva, E.: Effect of simulated solar radiation on the interaction of humic acid with naphthalene. Russ. J. Appl. Chem. **86**(4), 510–514 (2013). https://doi.org/10.1134/s1070427213040095
19. Susic, M.: Replenishing humic acids in agricultural soils. Agronomy **6**, 45–51 (2016). https://doi.org/10.3390/agronomy6040045

20. Saiz-Jimenez, C., De Leeuw, J.W.: Chemical structure of a soil humic acid as revealed by analytical pyrolysis. J. Anal. Appl. Pyrol. **11**, 367–376 (1987). https://doi.org/10.1016/0165-2370(87)85042-8
21. Susic, M., Isdale, P.: Hydraulic and environmental modelling of coastal, estuarine and river waters. Gower Technical, Aldershot, UK (1989)
22. Mal'tseva, E.V., Nechaev, L.V., Yudina, N.V., Chaikovskaya, O.N.: Physicochemical and spectroluminescent properties of the humic acids of coals. Solid Fuel Chem. **51**, 3–8 (2017). https://doi.org/10.3103/s0361521917010062
23. Lysenko, E.N., Surzhikov, A.P., Vlasov, V.A., Nikolaev, E.V., Malyshev, A.V., Bryazgin, A.A., Korobeynikov, M.V., Mikhailenko, M.A.: Synthesis of substituted lithium ferrites under the pulsed and continuous electron beam heating. Nucl. Instrum. Methods Phys. Res. **392**, 1–7 (2017). https://doi.org/10.1016/j.nimb.2016.11.042
24. Humic Acid. More than two centuries of humic acid research—why so long? Available online: https://humicacid.wordpress.com/a-history-of-humic-acid-research (accessed on 14 July 2016)
25. Farmer, V.C., Pisaniello, D.L.: Against an aromatic structure for soil fulvic acid. Nature **313**, 474–475 (1985)
26. Vauquelin, C.: Sur une maladie des arbres qui attaque spécialement l'orme et qui est analogue à un ulcère. Ann. Chim. **21**, 39–47 (1997)
27. Frimmel, F.H., Bauer, H.: Influence of photochemical reactions on the optical properties of aquatic humic substances gained from fall leaves. Sci. Total Environ. **62**, 139–148 (1987). https://doi.org/10.1016/0048-9697(87)90493-1
28. Susic, M., Boto, K.G.: High-performance liquid chromatographic determination of humic acid in environmental samples at the nanogram level using fluorescence detection. J. Chromatogr. **482**, 175–187 (1989). https://doi.org/10.1016/S0021-9673(01)93218-2
29. Davies, G., Fataftah, A., Ghabbour, E.A., Jansen, S.A., Radwan, A., Raffauf, R.F.: Isolation of humic acid from the terrestrial plant Brugmansia sanguinea. Sci. Total Environ. **201**, 79–87 (1997). https://doi.org/10.1016/S0048-9697(97)84054-5
30. Adani, F., Spagnol, M., Genevini, P.: Biochemical origin and refractory properties of humic acid extracted from the maize plant. Biogeochemistry **78**, 85–96 (2006). https://doi.org/10.1007/s10533-005-2902-7
31. Nebbioso, A., Piccolo, A.: In: Xu, J.,Wu, J., He, Y., (eds.) Functions of natural organic matter in changing environment. Zhejiang University Press, Hangzhou, China, Springer, Dordrecht, The Netherlands, pp. 89–94 (2013)
32. Tchaikovskaya, O., Sokolova, I., Mayer, G., Karetnikova, E., Volostnov, D., Lipatnikova, E., Kuzmina, S.: The role of UV-irradiation pretreatment on the degradation of 2,4-dichlorophenoxyacetic acid in water. Luminescence **26**, 156–161 (2011). https://doi.org/10.1002/bio.1198
33. Tchaikovskaya, O.N., Sokolova, I.V., Mayer, G.V., Karetnikova, E.A., Nechaev, L.V., Tarasenko, V.F., Sosnin, E.A.: The use of modern UV radiation sources for the utilization of persistent toxic substances. Atmos. Ocean. Opt. **23**(1), 55–59 (2010). https://doi.org/10.1134/S1024856010010112
34. Surzhikov, A.P., Lysenko, E.N., Malyshev, A.V., Vlasov, V.A., Suslyaev, V.I., Zhuravlev, V.A., Korovin, E.Y., Dotsenko, O.A.: Study of the radio-wave absorbing properties of a lithium-zinc ferrite based composite. Russ. Phys. J. **57**(5), 621–626 (2014). https://doi.org/10.1007/s11182-014-0284-9
35. Surzhikov, A.P., Frangulyan, T.S., Ghyngazov, S.A.: A thermoanalysis of phase transformations and linear shrinkage kinetics of ceramics made from ultrafine plasmochemical ZrO2(Y)-Al 2O3 powders. J. Therm. Anal. Calorim. **115**(2), 1439–1445 (2014). https://doi.org/10.1007/s10973-013-3455
36. Boule, P.: Handbook of environmental chemistry, vol. 2. Part 2. Environmental photochemistry. Springer-Verlag, Berlin-Heidelverg (1999)
37. Chaikovskaya, O., Sokolova, I., Svetlichnyi, V., Kudryasheva, N., Fedorova, E.: Luminescent analysis of photoinduced detoxification of phenol in the presence of humic substances. J. Appl. Spectrosc. **73**(6), 829–833 (2006). https://doi.org/10.1007/s10812-006-0162-5

38. Hutzinger, O.: Handbook of environmental chemistry, vol. 2. Part B. Reactions and processes. Springer-Verlag, Berlin-Heidelverg (1982)
39. Izmailov, D., Demin, E., Vladimirov, Yu.: Determination of the activity of antioxidants by measuning the kinetics of chemiluminescence. Photobiol. exp. photomed. **2**, 70–76 (2011) (in Russian)
40. Surzhikov, A.P., Galtseva, O.V., Vasendina, E.A., Vlasov, V.A., Nikolaev, E.V.: Processing line for industrial radiation-thermal synthesis of doped lithium ferrite powders. IOP Conf Ser Mater Sci. Eng. **110**(1), 012002–012006 (2016). https://doi.org/10.1088/1757-899x/110/1/012002
41. Surzhikov, A.P., Pritulov, A.M., Lysenko, E.N., Sokolovskii, A.N., Vlasov, V.A., Vasendina, E.A.: Influence of solid-phase ferritization method on phase composition of lithium-zinc ferrites with various concentration of zinc. J. Therm. Anal. Calorim. **109**(1), 63–67 (2012). https://doi.org/10.1007/s10973-011-1366-3
42. Ivanov, A., Savel'eva, A., Yudina, N.: Transfomations of humic asids on the mechanical activation of peat under redox conditions. Solid Fuel Chem. **50**, 76–80 (2016). https://doi.org/10.3103/S0361521916020105
43. Surzhikov, A.P., Pritulov, A.M., Lysenko, E.N., Sokolovskii, A.N., Vlasov, V.A., Vasendina, E.A.: Dependence of lithium-zinc ferrospinel phase composition on the duration of synthesis in an accelerated electron beam. J. Therm. Anal. Calorimetry **110**(2), 733–738 (2012). https://doi.org/10.1007/s10973-011-1947-1